UCLA
UCLA Electronic Theses and Dissertations

Title
Climatic Effects of Black Carbon Aerosols over the Tibetan Plateau

Permalink
https://escholarship.org/uc/item/7dh9r29g

Author
He, Cenlin

Publication Date
2017

Peer reviewed|Thesis/dissertation

University of California

Los Angeles

Climatic Effects of Black Carbon Aerosols over the Tibetan Plateau

A dissertation submitted in partial satisfaction

of the requirements for the degree

Doctor of Philosophy in Atmospheric and Oceanic Sciences

by

Cenlin He

2017

ABSTRACT OF THE DISSERTATION

Climatic Effects of Black Carbon Aerosols over the Tibetan Plateau

by

Cenlin He

Doctor of Philosophy in Atmospheric and Oceanic Sciences

University of California, Los Angeles, 2017

Professor Kuo-Nan Liou, Co-chair

Professor Qinbin Li, Co-chair

Black carbon (BC), also known as soot, has been identified as the second most important anthropogenic emissions in terms of global climate forcing in the current atmosphere. Ample evidence has shown that BC deposition is an important driver of rapid snow melting and glacier retreat over the Tibetan Plateau, which holds the largest snow/ice mass outside polar regions. However, the climatic effects of BC over the Tibetan Plateau have not been thoroughly investigated in such a manner as to understand, quantify, and reduce large uncertainties in the estimate of radiative and hydrological effects. Thus, this Ph.D. study seeks to understand and improve key processes controlling BC life cycle in global and regional models and to quantify BC radiative effects over the Tibetan Plateau. First, the capability of a state-of-the-art global chemical transport model (CTM), GEOS-Chem, and the associated model uncertainties are systematically evaluated in simulating BC over the Tibetan Plateau, using in situ measurements of BC in surface air, BC in snow, and BC absorption optical depth. The effects of three key factors on the simulation are also delineated, including Asian anthropogenic emissions, BC aging process, and model resolution. Subsequently, a microphysics-based BC aging scheme that accounts for condensation, coagulation, and heterogeneous chemical oxidation processes is developed and examined in GEOS-Chem by comparing with aircraft measurements. Compared to the default aging scheme, the mi-

crophysical scheme reduces model-observation discrepancies by a factor of $\sim$3, particularly in the middle and upper troposphere. In addition, a theoretical BC aging-optics model is developed to account for three typical evolution stages, namely, freshly emitted aggregates, coated BC by soluble material, and BC particles undergoing further hygroscopic growth. The geometric-optics surface-wave (GOS) approach is employed to compute the BC single-scattering properties at each aging stage, which are subsequently compared with laboratory measurements. Results show large variations in BC optical properties caused by coating morphology and aging stages. Furthermore, a comprehensive intercomparison of the GOS approach, the superposition T-matrix method, and laboratory measurements is performed for optical properties of BC with complex structures during aging. Moreover, a new snow albedo model is developed for widely-observed close-packed snow grains internally mixed with BC. Results indicate that albedo simulations that account for snow close packing match closer to observations. Close packing enhances BC-induced snow albedo reduction and associated surface radiative forcing by up to 15% (20%) for fresh (old) snow, which suggests that BC-snow albedo forcing is underestimated in previous modeling studies without accounting for close packing. Finally, the snow albedo forcing and direct radiative forcing (DRF) of BC in the Tibetan Plateau are estimated using GEOS-Chem in conjunction with a stochastic snow model and a radiative transfer model. This, for the first time, accounts for realistic non-spherical snow grain shape and stochastic multiple inclusions of BC within snow in assessing BC-snow interactions. The annual mean BC snow albedo forcing is 2.9 W m^{-2} over snow-covered Plateau regions. BC-snow internal mixing increases the albedo forcing by 40–60% compared with external mixing, whereas Koch snowflakes reduce the forcing by 20–40% relative to spherical snow grains. BC DRF at the top of the atmosphere is 2.3 W m^{-2} with uncertainties of -70% – +85% in the Plateau. The BC forcings are further attributed to emissions from different regions.

The dissertation of Cenlin He is approved.

Laurent Pilon

Jochen Stutz

Qinbin Li, Committee Co-chair

Kuo-Nan Liou, Committee Co-chair

University of California, Los Angeles

2017

To my dear family ...

for the endless love and support

To my dear friends ...

for the great kindness, support, and friendship

that will last forever

Table of Contents

List of Tables

xxii

Acknowledgments

My deepest gratitude goes to my advisors, Professor Kuo-Nan Liou and Professor Qinbin Li, for their patient guidance, tremendous support, and constructive instruction in my Ph.D. study. Particularly, I would like to thank them for teaching me how to think critically, how to be an independent scientist, how to efficiently solve problems, and how to express myself logically and effectively. Without their enormous help, I would not come so far in atmospheric sciences.

I would like to express my sincere thanks to my committee members, Professor Jochen Stutz and Professor Laurent Pilon, for their insightful comments and strong help in my research.

I also want to thank all my collaborators, particularly Professor Ping Yang, Professor Renyi Zhang, Dr. Joshua P. Schwarz, and Dr. L. Ruby Leung, for their creative comments, stimulating discussions, and substantial contributions to my work. Special thanks to Dr. Yoshi Takano for his tremendous help in my research. I also want to extend my appreciation to my fellow group members, Dr. Ling Qi, Dr. Bin Zhao, Dr. Mei Gao, Dr. Yuhao Mao, Dr. Hsien-Liang Tseng, Dr. Yu Gu, and Dr. Run Liu, for all the helpful discussions, and to my fellow colleagues, Yue Wang, Xin An, Dr. Yang Cao, Dr. Xuan Ji, Dr. Qianli Ma, Chao Yue, Wu Sun, and Xiaobi Kuang, for all the help. I would like to thank them for their company in the past few years and for sharing all my happiness and sorrows.

My great thanks also go to my dear friends, Bo Wang, Ruyi Huang, Jinxing Li, Mengjie Wu, Han Gu, Song Xu, Yi Liu, Baoni Shi, and Yuting Guan, for enormously enriching my life and for bringing me the kind of love, happiness, and friendship that will last forever with no doubt.

Last but not least, I would like to give my special thanks to my family, particularly my parents, who have been with me through all my good times and bad. I would not be here without their endless love, wholehearted support, and all the sacrifice they had made for me.

<h1 align="center">Vita</h1>

2008–2012	B.S. in Environmental Sciences and B.S. in Applied Mathematics, Peking Univeristy, China
2012–2013	M.S. in Atmospheric Sciences, University of California, Los Angeles, USA
2012–present	Graduate Student Researcher, University of California, Los Angeles, USA
Jan.–Jun. 2016	Teaching Assistant, University of California, Los Angeles, USA

<h2 align="center">Publications</h2>

1. **He, C.**, Takano, Y., and Liou, K. N. (2017), Close packing effects on clean and dirty snow albedo and associated climatic implications, Geophys. Res. Lett., 44, doi: 10.1002/2017GL072916.

2. **He, C.**, Y. Takano, K. N. Liou, P. Yang, Q. B. Li, and D. W. Mackowski (2016): Intercomparison of the GOS approach, superposition T-matrix method, and laboratory measurements for black carbon optical properties during aging, J. Quant. Spectrosc. Radiat. Transf., 184, 287–296, doi:10.1016/j.jqsrt.2016.08.004.

3. **He, C.**, Li, Q., Liou, K.-N., Qi, L., Tao, S., and Schwarz, J. P. (2016): Microphysics-based black carbon aging in a global CTM: constraints from HIPPO observations and impli-

cations for global black carbon budget, Atmos. Chem. Phys., 16, 3077-3098, doi:10.5194/acp-16-3077-2016.

4. **He, C.**, Liou, K.-N., Takano, Y., Zhang, R., Zamora, M. L., Yang, P., Li, Q., and Leung, L. R. (2015): Variation of the radiative properties during black carbon aging: theoretical and experimental intercomparison, Atmos. Chem. Phys., 15, 11967-11980, doi:10.5194/acp-15-11967-2015.

5. **He, C.**, Q. Li, K.-N. Liou, Y. Takano, Y. Gu, L. Qi, Y. Mao, and L. R. Leung (2014): Black carbon radiative forcing over the Tibetan Plateau, Geophys. Res. Lett., 41, 7806–7813, doi:10.1002/2014GL062191.

6. **He, C.**, Q.B. Li, K.N. Liou, J. Zhang, L. Qi, Y. Mao, M. Gao, Z. Lu, D. G. Streets, Q. Zhang, M. M. Sarin, and K. Ram (2014): A global 3-D CTM evaluation of black carbon in the Tibetan Plateau, Atmos. Chem. Phys., 14, 7091-7112, doi:10.5194/acp-14-7091-2014.

7. **He, C.**, Liu,J., Carlton,A.G., Fan,S., Horowitz,L.W., LevyII,H., and Tao,S. (2013): Evaluation of factors controlling global secondary organic aerosol production from cloud processes, Atmos. Chem. Phys., 13, 1913-1926, doi:10.5194/acp-13-1913-2013.

8. **He, C.** and T.-M. Fu (2013): Air-Sea Exchange of Volatile Organic Compounds: A New Model with Microlayer Effects, Atmos. Oceanic Sci. Lett., 6, 97–102.

CHAPTER 1

Overview

Black carbon (BC) is the most important light-absorbing aerosol formed during incomplete combustion, with major emissions from fossil fuel and biofuel combustion and open biomass burning. Atmospheric BC warms the atmosphere and cools down the surface by strongly absorbing solar radiation in the visible and near infrared (i.e., direct radiative effect), influences cloud formation by acting as cloud condensation nuclei (CCN) (i.e., indirect radiative effect), and accelerates snow and ice melting by reducing snow and ice albedo (i.e., snow albedo effect). BC is now considered as the second most important human emission in terms of its global climate forcing in the present-day atmosphere (*Bond et al.*, 2013). The regional warming effect of BC can be even stronger, particularly over snow-covered regions (*Jacobson*, 2004; *Flanner et al.*, 2007). Ample evidence has shown the rapid glacier retreat over the Tibetan Plateau associated with BC deposition on snow (*Ming et al.*, 2008). It has also been illustrated that the radiative forcing from ever-increasing deposition of BC in snow was an important driver of the abrupt retreat of Alpine glaciers from the mid-19th century (*Painter et al.*, 2013).

The Tibetan Plateau, considered to be the third pole of the world, holds the largest snow and ice mass outside the Arctic and Antarctic. The Tibetan glaciers provide the primary source of fresh water supply for drinking and agricultural irrigation for more than one billion people in Asia. Changes of snow cover in the Plateau also affect heat flux and water exchange between the surface and the atmosphere, and further disturb the formation of the Asian monsoon (*Lau and Kim*, 2006).

Observations have shown significant warming in the Tibetan Plateau in the past decades (*Dahe et al.*, 2006). *Ramanathan et al.* (2007) pointed out that the increasing amount of BC transported to the Himalayas accounts for half of the observed warming in the region. Recent studies reaffirmed a strong BC-induced regional warming over the Plateau that results in more than 1% decrease of snow/ice cover (*Menon et al.*, 2010), 2–5% reduction of snow albedo (*Yasunari et al.*, 2010), and an increase of runoff in early spring (*Qian et al.*, 2011). Surrounded by the world's two largest BC source regions, South and East Asia, the Tibetan Plateau has received an increasing BC deposition from 1951 to 2000, particularly after 1990 (*Ming et al.*, 2008). *Kaspari et al.* (2011) found that BC concentrations in snow over Mt. Everest during 1975–2000 have increased approximately threefold compared to 1860–1975. Recent studies have shown that the amount of BC transported to the Plateau has increased by 41% from 1996 to 2010, with South and East Asia accounting for 67% and for 17% on an annual basis (*Lu et al.*, 2012). The modeling study by *Kopacz et al.* (2011) suggested that long-range transport from Middle East, Europe, and Northern Africa also contributes to the BC deposition over the Plateau.

However, the climatic effects of BC over the Tibetan Plateau are not well understood, with large uncertainties in the estimates of BC radiative forcing. Using a chemical transport model (CTM), *Kopacz et al.* (2011) estimated that BC direct radiative forcing (DRF) at the top of the atmosphere (TOA) was 0.2–1.7 W m^{-2} at five Tibetan glacial sites and that BC snow albedo forcing was 4–16 W m^{-2} at the same sites. *Wang et al.* (2014a), using the same CTM with updates, derived a substantially smaller BC TOA DRF ($<$0.5 W m^{-2}) across much of the Plateau. *Flanner et al.* (2009) estimated an annual BC snow albedo forcing of 1.3 W m^{-2} over the Plateau and 10–20 W m^{-2} in spring in parts of the Plateau. *Qian et al.* (2011) found a springtime BC snow albedo forcing of 14–18 W m^{-2} in the western Plateau. Accurate assessment of BC-related radiative forcing in the Tibetan Plateau critically depends on reliable model simulations of BC emissions, aging process, transport, vertical distribution, wet and dry deposition and interaction with surface snow over the Plateau. Therefore, it

is imperative to understand and quantify BC-radiation and BC-snow-radiation interactions and to improve current model simulations of BC including its evolution in the atmosphere, so that we can get better estimates of the climatic effects of BC over the Tibetan Plateau.

In Chapter 2, we systematically evaluate the BC simulations over the Tibetan Plateau by a global 3-D chemical transport model (CTM) (GEOS-Chem), using in situ measurements of BC in surface air, BC in snow, and BC absorption aerosol optical depth (AAOD). To our knowledge, this is the first attempt to assess BC simulations in this region by using all these three types of available measurements. We also delineate the effects of three key factors on the simulation, including Asian anthropogenic emissions, BC aging process, and model resolution. This work improves our understanding on model uncertainty/bias in BC simulations and pointed to imperative needs for more extensive BC measurements in the Tibetan Plateau.

In Chapter 3, we develop a theoretical BC aging-optics model to account for three typical evolution stages, namely, freshly emitted aggregates, coated BC by soluble material, and BC particles undergoing further hygroscopic growth. The geometric-optics surface-wave (GOS) approach is employed to compute the BC single-scattering properties at each aging stage, which are subsequently compared with laboratory measurements. Theoretical calculations are generally consistent with measurements in optical cross sections for both fresh BC aggregates and coated BC particles with different sizes. Substantial variations occurring in absorption and scattering during aging, depending on coating morphology and aging stages. This work suggests that an accurate estimate of BC radiative effects requires the incorporation of a dynamic BC aging process that accounts for realistic coating structures in climate models.

In Chapter 4, we perform a comprehensive intercomparison of the GOS approach, the widely-used superposition T-matrix method, and laboratory measurements for optical properties of fresh and aged BC particles with complex structures. Results show a good agreement between the two methods for various BC sizes and structures, which also generally capture

laboratory measurements. This work provides the foundation for downstream application of the GOS approach in radiative transfer and climate studies.

In Chapter 5, we develop and examine a microphysics-based BC aerosol aging scheme that accounts for condensation, coagulation, and heterogeneous chemical oxidation processes in a global 3-D chemical transport model by interpreting the BC measurements from the HIAPER Pole-to-Pole Observations (HIPPO, 2009–2011) using the model. Compared with a widely-used fixed aging scheme with an e-folding time of 1.2 days, the microphysical scheme significantly reduces model-observation discrepancies by about a factor of 3, particularly in the middle and upper troposphere as well as the tropics. This BC aging scheme can be easily applied to other global models.

In Chapter 6, we develop a new snow albedo model for widely-observed close-packed snow grains internally mixed with BC and demonstrate that albedo simulations match closer to observations by accounting for snow grain packing. Close packing enhances BC-induced snow albedo reduction and associated surface radiative forcing by up to 15% (20%) for fresh (old) snow, with larger enhancements for stronger structure packing. The results suggest that BC-snow albedo forcing and snow albedo feedback are underestimated in previous studies, making snow close packing consideration a necessity in climate modeling and analysis.

In Chapter 7, we estimate the snow albedo forcing and direct radiative forcing (DRF) of BC in the Tibetan Plateau using a global chemical transport model in conjunction with a stochastic snow model and a radiative transfer model. This, for the first time, accounts for realistic non-spherical snow grain shape and stochastic multiple inclusions of BC within snow in assessing BC-snow interactions. The annual mean BC snow albedo forcing over snow-covered Plateau regions is a factor of three larger than the value over global land snowpack. The annual BC DRF at the top of the atmosphere has an uncertainty of -70% – +85% in the Plateau. The BC forcings are attributed to emissions from different regions.

In Chapter 8, a final summary of all the aforementioned work has been presented. The future work will focus on developing a physically-based parameterization for BC-snow inter-

action based on a stochastic snow model for application in climate models. The parameterization will be further implemented into a widely-used land surface model coupled with a regional climate-chemistry model to assess hydro-climatic effects of BC deposition over the Tibetan Plateau with interactive feedbacks.

CHAPTER 2

A global 3-D CTM evaluation of black carbon in the Tibetan Plateau

Abstract

We systematically evaluate the black carbon (BC) simulations for 2006 over the Tibetan Plateau by a global 3-D chemical transport model (CTM) (GEOS-Chem) driven by GEOS-5 assimilated meteorological fields, using in situ measurements of BC in surface air, BC in snow, and BC absorption aerosol optical depth (AAOD). Using improved anthropogenic BC emission inventories for Asia that account for rapid technology renewal and energy consumption growth (*Zhang et al.*, 2009; *Lu et al.*, 2011) and improved global biomass burning emission inventories that account for small fires (*Van der Werf et al.*, 2010; *Randerson et al.*, 2012), we find that model results of both BC in surface air and in snow are statistically in good agreement with observations (biases <15%) away from urban centers. Model results capture the seasonal variations of the surface BC concentrations at rural sites in the Indo-Gangetic

Plain, but the observed elevated values in winter are absent. Modeled surface BC concentrations are within a factor of two of the observations at remote sites. Part of the discrepancy is explained by the deficiencies of the meteorological fields over the complex Tibetan terrain. We find that BC concentrations in snow computed from modeled BC deposition and GEOS-5 precipitation are spatiotemporally consistent with observations ($r = 0.85$). The computed BC concentrations in snow are a factor of 2–4 higher than the observations at several Himalayan sites because of excessive BC deposition. The BC concentrations in snow are biased low by a factor of two in the central Plateau, which we attribute to the absence of snow aging in the CTM and strong local emissions unaccounted for in the emission inventories. Modeled BC AAOD is more than a factor of two lower than observations at most sites, particularly to the northwest of the Plateau and along the southern slopes of the Himalayas in winter and spring, which is attributable in large part to underestimated emissions and the assumption of external mixing of BC aerosols in the model. We find that assuming a 50% increase of BC absorption associated with internal mixing reduces the bias in modeled BC AAOD by 57% in the Indo-Gangetic Plain and the northeastern Plateau and to the northeast of the Plateau, and by 16% along the southern slopes of the Himalayas and to the northwest of the Plateau. Both surface BC concentration and AAOD are strongly sensitive to anthropogenic emissions (from China and India), while BC concentration in snow is especially responsive to the treatment of BC aerosol aging. We find that a finer model resolution ($0.5° \times 0.667°$ nested over Asia) reduces the bias in modeled surface BC concentration from 15% to 2%. The large range and non-homogeneity of discrepancies between model results and observations of BC across the Tibetan Plateau undoubtedly undermine current assessments of the climatic and hydrological impact of BC in the region thus warrant imperative needs for more extensive measurements of BC, including its concentration in surface air and snow, AAOD, vertical profile and deposition.

2.1 Introduction

Black carbon (BC) is the most important light-absorbing aerosol formed during incomplete combustion (*Bond et al.*, 2013), with major sources from fossil fuel and biofuel combustion and open biomass burning (*Bond et al.*, 2004). BC warms the atmosphere by strongly absorbing solar radiation in the visible and the near infrared (*Ramanathan and Carmichael*, 2008), influences cloud formation as cloud condensation nuclei (*Jacobson*, 2006), and accelerates snow and ice melting by significantly reducing snow and ice albedo (i.e., the snow-albedo effect) (*Hansen and Nazarenko*, 2004; *Flanner et al.*, 2007). With an estimated global climate forcing of $+1.1$ W m^{-2}, BC is now considered the second most important human emission in terms of its climate forcing in the present-day atmosphere after carbon dioxide (*Ramanathan and Carmichael*, 2008; *Bond et al.*, 2013). The regional warming effect of BC can be even stronger, particularly over snow-covered regions (*Jacobson*, 2004; *Flanner et al.*, 2007, 2009). There is ample evidence that BC aerosols deposited on Tibetan glaciers have been a significant contributing factor to observed rapid glacier retreat in the region (e.g. *Xu et al.*, 2009). It has also been proposed that the radiative forcing from ever-increasing deposition of BC in snow was an important cause for the retreat of Alpine glaciers from the last little ice age through the mid-19th century (*Painter et al.*, 2013).

The Tibetan Plateau is the highest plateau in the world with the largest snow and ice mass outside the polar regions (*Xu et al.*, 2009). The Tibetan glaciers and the associated snowmelt are the primary source of fresh water supply for drinking, agricultural irrigation, and hydropower for more than one billion people in Asia (*Immerzeel et al.*, 2010). The Plateau also plays a critical role in regulating the Asian hydrological cycle. Changes of snow cover affect heat flux and water exchange between the surface and the atmosphere, and further disturb the formation of the Asian monsoon (*Lau and Kim*, 2006).

Observations have shown remarkable warming and accelerated glacier retreat in the Tibetan Plateau in the past decades (*Dahe et al.*, 2006; *Prasad et al.*, 2009). *Ramanathan*

et al. (2005, 2007) argued that the ever-increasing amount of BC transported to the Himalayas accounts for half of the observed warming in the region, comparable to the warming attributable to greenhouse gases (*Barnett et al.*, 2005). Recent studies reaffirmed a strong BC-induced regional warming over the Plateau that results in more than 1% decrease of snow/ice cover (*Lau et al.*, 2010; *Menon et al.*, 2010), 2–5% reduction of snow albedo (*Yasunari et al.*, 2010), and an increase of runoff in early spring (*Qian et al.*, 2011). Surrounded by the world's two largest BC source regions, South and East Asia (*Lamarque et al.*, 2010), the Plateau has received an increasing BC deposition from 1951 to 2000, particularly after 1990 (*Ming et al.*, 2008). Recent studies have shown that the amount of BC transported to the Plateau has increased by 41% from 1996 to 2010, with South and East Asia accounting for 67% and for 17% on an annual basis (*Lu et al.*, 2012). The modeling study by *Kopacz et al.* (2011) suggested that long-range transport from Middle East, Europe, and Northern Africa also contributes to the BC deposition over the Plateau.

The climatic effects of BC over the Tibetan Plateau are not well understood, with large uncertainties in the estimates of BC radiative forcing (e.g., *Flanner et al.*, 2007; *Kopacz et al.*, 2011; *Ming et al.*, 2013). Accurate assessment of BC-related radiative forcing in the Tibetan Plateau critically depends on reliable model simulations of BC emissions, transport and subsequent deposition, and vertical distribution over the Plateau. Previous modeling studies have found invariably large discrepancies with observations. For example, the simulations of surface BC at several sites in the southern slope of the Himalayas are biased low by more than a factor of two, particularly in winter and spring in regional, multi-scale and global models (*Nair et al.*, 2012; *Moorthy et al.*, 2013). *Fu et al.* (2012) showed that a global chemical transport model (CTM) simulated surface BC concentrations are more than 50% lower than observations in China in general and across the Tibetan Plateau in particular. A global CTM study (*Kopacz et al.*, 2011) and a global climate model (GCM) study (*Qian et al.*, 2011) both showed large differences between modeled and observed BC concentration in snow over the Plateau. *Sato et al.* (2003) and *Bond et al.* (2013) pointed out large underestimates of

BC absorption aerosol optical depth (AAOD) in previous models compared with Aerosol Robotic Network (AERONET) retrievals.

In this study, we seek to understand the capability of a global 3-dimentional CTM (GEOS-Chem) in simulating BC in the Tibetan Plateau and the associated discrepancies between model results and observations. The GEOS-Chem model has been widely used in previous studies to understand BC emissions, transport and deposition in the Plateau (*Kopacz et al.*, 2011), in China (*Fu et al.*, 2012), over Asia (*Park et al.*, 2005), in the Arctic (*Wang et al.*, 2011) and globally (*Wang et al.*, 2014a). To our knowledge, this is the first attempt to systematically evaluate a global simulation of BC in the Tibetan Plateau using all three types of available in situ measurements: BC in surface air, BC in snow, and BC AAOD. We further delineate the effects of anthropogenic BC emissions from China and India, BC aging process and model resolution on the simulation. Potential factors driving model versus observation discrepancies are also examined, which gives implications for improving the estimate of BC climatic effects. Observations and model description are presented in Sect. 2.2. Simulations of surface BC, BC in snow and BC AAOD are discussed in Sect. 2.3. Sensitivity and uncertainty analyses are in Sects. 2.4, 2.5, and 2.6. Finally, summary and conclusions are given in Sect. 2.7.

2.2   Method

2.2.1   Observations

For the sake of clarity, we define here the Tibetan Plateau roughly as the region in 28°N–40°N latitudes and 75°E–105°E longitudes. We also define several sub-regions of the Plateau and adjacent regions (Fig. 2.1): the central Plateau (30°N–36°N, 82°E–95°E), the northwestern Plateau (36°N–40°N, 75°E–85°E), the northeastern Plateau (34°N–40°N, 95°E–105°E), the southeastern Plateau (28°N–34°N, 95°E–105°E), to the north of the Plateau (40°N–50°N, 85°E–95°E), to the northwest of the Plateau (40°N–50°N, 70°E–85°E), to the northeast

of the Plateau (40°N–50°N, 95°E–105°E), and the Himalayas. There are rather limited measurements of BC in the Tibetan Plateau. Figure 2.1 shows sites with measurements of BC surface concentration, concentration in snow, and AAOD in the region

2.2.1.1 BC surface concentration

There are 13 sites with monthly or seasonal measurements of surface BC concentration (Table 2.1 and Fig. 2.1). Observations are available for 2006 at nine of the sites. Four sites provide observations for 1999–2000, 2004–2005, or 2008–2009. We distinguish these sites as urban, rural, or remote sites based upon annual mean surface BC concentration, following *Zhang et al.* (2008b). The concentration is typically higher than 5 μg m^{-3} at urban sites (within urban centers or near strong local residential and vehicular emissions), in the range of 2–5 μg m^{-3} at rural sites, and less than 2 μg m^{-3} at more remote, pristine sites.

Ganguly et al. (2009a) retrieved surface BC concentration at Gandhi College (25.9°N, 84.1°E, 158 m a.s.l.) by combining aerosol optical properties from AERONET measurements and aerosol extinction profiles from Cloud-Aerosol Lidar with Orthogonal Polarization (CALIOP) observations. The retrieval is rather sensitive to errors in the aerosol single scattering albedo, size distribution and vertical profiles derived from the observations (*Ganguly et al.*, 2009b). Measurements at Delhi (28.6°N, 77.2°E, 260 m a.s.l.), Digrugarh (27.3°N, 94.6°E, 111 m a.s.l.), Kharagpur (22.5°N, 87.5°E, 22 m a.s.l.) and Nepal Climate Observatory at Pyramid (NCOP, 28.0°N, 86.8°E, 5079 m a.s.l.) used Aethalometer (*Beegum et al.*, 2009; *Pathak et al.*, 2010) or Multi-angle Absorption Photometer (*Bonasoni et al.*, 2010; *Nair et al.*, 2012). The uncertainties of these measurements stem mainly from the interference from other components in the aerosol samples (*Bond et al.*, 1999; *Petzold and Schönlinner*, 2004) and the shadowing effects under high filter loads (*Weingartner et al.*, 2003). BC concentrations at the other sites were derived from measurements of the Thermal Optical Reflectance or Thermal Optical Transmittance (*Carrico et al.*, 2003; *Qu et al.*, 2008; *Zhang et al.*, 2008b; *Ming et al.*, 2010; *Ram et al.*, 2010a,b). These measurements are strongly in-

11

fluenced by the temperature chosen to separate BC and organic carbon (OC) (*Schmid et al.*, 2001; *Chow et al.*, 2004).

2.2.1.2 BC concentration in snow

There are 16 sites with monthly or seasonal measurements of BC concentration in snow during 1999–2007 and two with annual measurements (*Xu et al.*, 2006, 2009; *Ming et al.*, 2009a,b, 2012, 2013). These sites are at high-elevation (>3500 m a.s.l.), remote locations in the Himalayas and other parts of the Plateau (Table 2.2 and Fig. 2.1). The snow and ice samples taken from these sites were heated and filtered through fiber filters in the laboratory. Thermal techniques (*Cachier and Pertuisot*, 1994; *Chow et al.*, 2004) were then used to isolate BC from other constituents (especially OC) in the filters, followed by analysis using carbon analyzers including heating-gas chromatography (*Xu et al.*, 2006), optical carbon analysis (*Chow et al.*, 2004) and coulometric titration-based analysis (*Cachier and Pertuisot*, 1994). The accuracy of the heating-gas chromatography system is dominated by the variability of the blank loads of pre-cleaned filters (*Xu et al.*, 2006). The coulometric titration-based analysis measures the acidification of the solution by carbon dioxide produced from BC combustion in the system (*Ming et al.*, 2009a), where the pH value of the solution may be interfered by other ions.

2.2.1.3 AERONET AAOD

There are 14 AERONET sites with AAOD retrievals in the Tibetan Plateau and adjacent regions (Table 2.3 and Fig. 2.1). These sites are mostly in the Indo-Gangetic Plain, in northern India and along the southern slope of the Himalayas. Following *Bond et al.* (2013), we infer BC AAOD from monthly averaged AOD data from AERONET (Version 2.0 Level 2.0 products) for 2006–2012. The monthly means are derived for months when there are five or more days with AOD observations. The measurements provide sun and sky radiance observations in the mid-visible range (*Dubovik et al.*, 2000), which allows for inference of

aerosol column absorption from retrievals of AOD and single scattering albedo (SSA) via $AAOD = AOD \times (1 - SSA)$. As pointed out by *Bond et al.* (2013), the removal of SSA data at low AOD values from the AERONET data (for data quality assurance) likely introduces a positive bias in the AAOD retrieval. Both BC aerosols and dust particles contribute to the absorption. The absorption by fine-mode aerosols is primarily from BC while the absorption by larger particles (diameter >1 μm) is principally from dust. Dust AAOD is estimated from the super-micron part of aerosol size distribution provided by the AERONET retrieval method and a refractive index of $1.55 - 0.0015i$ (*Bond et al.*, 2013). BC AAOD is then the difference between the total and dust AAOD. This process attributes all fine-mode aerosol absorption to BC. Because of the contributions from OC and fine dust particles to fine-mode AAOD, the inferred BC AAOD is likely biased high. *Bond et al.* (2013) estimated that the uncertainty from the impact of dust and OC on the fine-mode AAOD could be as large as 40–50%. The limited AERONET sampling in this region is another source of uncertainty (*Bond et al.*, 2013).

2.2.2   Model description and simulations

The GEOS-Chem model is driven by assimilated meteorology from the Goddard Earth Observing System (GEOS) of the NASA Global Modeling and Assimilation Office (GMAO). We use here GEOS-Chem version 9-01-03 (available at http://geos-chem.org), driven by GEOS-5 data assimilation system (DAS) meteorological fields. The meteorological fields have a native horizontal resolution of 0.5° × 0.667°, 72 vertical layers, and a temporal resolution of 6 hours (3 hours for surface variables and mixing depths). The spatial resolution is degraded to 2° × 2.5° in the horizontal and 47 layers in the vertical (from the surface to 0.01 hPa) for computational expediency. The lowest model levels are centered at approximately 60, 200, 300, 450, 600, 700, 850, 1000, 1150, 1300, 1450, 1600, 1800 m a.s.l.

Tracer advection is computed every 15 minutes with a flux-form semi-Lagrangian method (*Lin and Rood*, 1996). Tracer moist convection is computed using GEOS convective, entrain-

ment, and detrainment mass fluxes as described by *Allen et al.* (1996a,b). The deep convection in GEOS-5 is parameterized using the relaxed Arakawa-Schubert scheme (*Arakawa and Schubert*, 1974; *Moorthi and Suarez*, 1992), and the shallow convection treatment follows *Hack et al.* (1994). *Park et al.* (2003, 2006) first described GEOS-Chem simulation of carbonaceous aerosols.

2.2.2.1 BC emissions

The global anthropogenic BC emissions are from *Bond et al.* (2007), with an annual emission of 4.4 TgC for the year 2000. Anthropogenic BC emissions in Asia, chiefly in China and India, have increased significantly since 2000 (*Granier et al.*, 2011). *Zhang et al.* (2009) developed an Asian anthropogenic BC emissions (for China and India and the rest of Asia) for 2006 for the Intercontinental Chemical Transport Experiment-B (INTEX-B) field campaign (*Singh et al.*, 2009), with considerable updates to a previous inventory developed by *Streets et al.* (2003). They employed a dynamic methodology that accounts for rapid technology renewal and updated the fuel consumption data. *Fu et al.* (2012) pointed out that *Zhang et al.* (2009) underestimates anthropogenic BC emissions in China by a factor of 1.6 compared with the top-down estimates. *Lu et al.* (2011) further updated the activity rates, technology penetration data and emission factors in China and India, and reported anthropogenic BC emissions only in these two countries for 1996–2010. Table 2.4 is a summary of the two inventories. Anthropogenic BC emissions in India are lower in the *Zhang et al.* (2009) inventory (hereinafter the INTEX-B inventory) than in the *Lu et al.* (2011) inventory (hereinafter the LU inventory) by a factor of two, while emissions in China are 10% higher in the INTEX-B inventory than in the LU inventory (Table 2.4). The higher emissions in India in the LU inventory are primarily a result of the updated biofuel emission factors and the new method used to estimate biofuel consumptions. The biofuel emissions, which are dominated by residential burning, account for more than 50% of total BC emissions in India (*Lu et al.*, 2011). There are large uncertainties in both inventories. *Lu et al.* (2011) used

a Monte Carlo method to show that the 95% uncertainty ranges of BC emissions are from -43% to 93% for China and from -41% to 87% for India. The uncertainties in the INTEX-B inventory are $\pm208\%$ for China and $\pm360\%$ for India (*Zhang et al.*, 2009). A recent study by *Qin and Xie* (2012) showed slightly (5–10%) lower total anthropogenic BC emissions in China than those from *Lu et al.* (2011) for 2006 but a factor of 2 higher emissions in the northeastern and northwestern China. *Kurokawa et al.* (2013) further updated BC emissions in Asia and found 10% lower anthropogenic BC emissions for China and 30% lower for India compared with those from *Lu et al.* (2011), yet with a similar spatial distribution. *Wang et al.* (2014b) developed a new global BC emission inventory, where anthropogenic BC emissions are 20% higher in China and 30% lower in India than those from *Lu et al.* (2011). They found that the use of the new inventory reduces model biases of surface BC concentrations in Asia by 15–20%. However, the abovementioned three latest inventories are still associated with large uncertainties (95% confidence intervals), which are more than 100% for anthropogenic BC emissions in China and India (*Qin and Xie*, 2012; *Kurokawa et al.*, 2013; *Wang et al.*, 2014b).

Global biomass burning emissions are from the Global Fire Emissions Database version 3 (GFEDv3) (*Van der Werf et al.*, 2010). *Kaiser et al.* (2012) showed that GFEDv3 underestimates carbon emissions by a factor of 2–4 globally because of undetected small fires. *Randerson et al.* (2012) reported an updated GFEDv3 inventory that accounts for small fire emissions. Small fires increase carbon emissions by 50% in Southeast Asia and Equatorial Asia (*Randerson et al.*, 2012). We use the GFEDv3 emissions with a monthly temporal resolution in the present study. The uncertainty of the GFEDv3 emissions is at least 20% globally and higher in boreal regions and Equatorial Asia (*Van der Werf et al.*, 2010). The major uncertainty lies in insufficient data on burned area, fuel load and emission factor (*Van der Werf et al.*, 2010; *Randerson et al.*, 2012).

2.2.2.2 BC deposition

Simulation of aerosol dry and wet deposition follows *Liu et al.* (2001). Dry deposition of aerosols uses a resistance-in-series model (*Walcek et al.*, 1986) dependent on local surface type and meteorological conditions. There have since been many updates. A standard resistance-in-series scheme (*Wesely*, 1989) has been implemented in the non-snow/non-ice regions (*Wang et al.*, 1998) with a constant aerosol dry deposition velocityof 0.03 cm s^{-1} prescribed over snow and ice (*Wang et al.*, 2011). This velocity is within the range (0.01–0.07 cm s^{-1}) employed in *Liu et al.* (2011) to improve the BC simulation in the Geophysical Fluid Dynamics Laboratory (GFDL) Atmospheric Model version 3 (AM3) global model (*Donner et al.*, 2011). We found that dry deposition accounts for 20% of the total BC deposition over the Tibetan Plateau in winter and 10% in summer.

Liu et al. (2001) described the wet scavenging scheme for aerosols in the GEOS-Chem. *Wang et al.* (2011) implemented in the model a new below-cloud scavenging parameterization for individual aerosol mode, which distinguishes between the removal by snow and by rain drops for aerosol washout. They also applied different in-cloud scavenging schemes to cold and to warm clouds, and with an improved areal fraction of a model grid box that experiences precipitation. These changes are included in the GEOS-Chem version used for the present study.

The GEOS-Chem model does not directly predict BC (or any aerosols for that matter) in snow at the surface in the absence of a land-surface model that explicitly treats snow including its aging. As an approximation, we estimate BC concentration in snow in the model as the ratio of total BC deposition to total precipitation, following *Kopacz et al.* (2011) and *Wang et al.* (2011). Although the use of total precipitation here is reasonable considering the low temperature typical over the Tibetan Plateau (*Wu and Liu*, 2004), it introduces uncertainties to the calculation of snow BC concentration. *Bonasoni et al.* (2010) found that precipitation can be partly in the form of rain even at altitudes of 5 km in the Himalayas. Thus, the use of total precipitation may overestimate both snow precipitation

16

and BC removed by snow. Besides, rain also results in the melting of snowpack (*Marks et al.*, 2001), which further affects BC concentration in snow. Additional uncertainties exist in the GEOS-5 precipitation fields because of the coarse model resolution and the complex topography in the Plateau (see Sect. 2.3.2). *Ménégoz et al.* (2013) showed that using a higher resolution model ($0.2° × 0.2°$) improves the simulation of the spatial variability of precipitation in the Himalayas, but the bias in total precipitation remains high. The uncertainty in precipitation is thus propagated to the BC concentration in snow computed from model results. Our calculation of BC concentration in snow assumes a well mixing of BC and snow. However, BC content is not uniform throughout a snow column. Thus, an ideal comparison of modeled and observed BC concentrations in snow should be for the same depth of a snow column. We also neglect the aging of surface snow and the internal mixing of snow and BC, which conceivably contribute to the underestimate of BC concentration in snow computed here. This may be an especially important issue for comparisons in the central Plateau and to the north of the Plateau, where snowmelt has been suggested to strongly increase BC concentration in snow (*Zhou et al.*, 2007; *Ming et al.*, 2013).

2.2.2.3 BC aging

Freshly emitted BC is mostly (80%) hydrophobic (*Cooke et al.*, 1999). Hydrophobic BC becomes hydrophilic typically on the timescale of a few days (*McMeeking et al.*, 2011), because of coating by soluble materials like sulfate and organic matter (*Friedman et al.*, 2009; *Khalizov et al.*, 2009a). The internal mixing of BC and other aerosol constituents significantly changes the morphology, hygroscopicity and optical properties of BC particles (*Zhang et al.*, 2008a). This further influences BC absorption efficiency (*Bond et al.*, 2006) and lifetime against deposition (*Mikhailov et al.*, 2001). However, the aging process is not explicitly simulated in the GEOS-Chem, where an e-folding time of 1.15 days for the conversion of hydrophobic to hydrophilic BC is simply assumed (*Park et al.*, 2005; *Kopacz et al.*, 2011; *Wang et al.*, 2011). *Liu et al.* (2011) proposed a condensation-coagulation parameterization

17

for BC aging where the conversion time is not uniform but varies. Specifically, the conversion is assumed to be primarily a result of sulfuric acid deposition (condensation) onto BC particles and the mass deposition rate is proportional to the concentration of gaseous sulfuric acid and to the BC particle surface area. Gaseous atmospheric sulfuric acid is a product of sulfur dioxide oxidation by the hydroxyl radical (OH). Consequently, its steady-state concentration is linearly linked to OH concentration. Thus, in the absence of nucleation, which is a slow process when there exists plenty of primary particles as found in urban and biomass burning plumes (*Seinfeld and Pandis*, 2006), the BC aging rate can be parameterized as a linear function of OH concentration, where the coefficient of OH concentration controls a fast aging process (i.e. condensation) and the constant term governs a slow aging process (e.g. coagulation). *Huang et al.* (2013) further combined the *Liu et al.* (2011) parameterization with a chemical oxidation aging mechanism from chamber study results (*Pöschl et al.*, 2001) in GEOS-Chem. They found that the chemical aging effects on surface BC concentrations are strongest in the tropical regions but negligible over the Tibetan Plateau.

2.2.2.4   Model simulations

For the present study, we conducted four GEOS-Chem simulations for 2006 (Table 2.5). Detailed discussions and justifications for these model experiments are provided below where appropriate. Model results are sampled at the corresponding locations of the measurement sites. Model results presented here are monthly averages. As pointed out in previous studies (*Fairlie et al.*, 2007; *Mao et al.*, 2011), comparing localized observations with model results that are representative of a much larger area is inherently problematic. The mountainous sites and the complex terrain in the Tibetan Plateau further complicate the comparison. In Experiment A, we replace the *Bond et al.* (2007) emissions in China and India with the LU inventory and use the INTEX-B inventory for the rest of Asia. This is our standard simulation and the results are used for all model evaluations presented here unless stated otherwise. We also provide the model results from Experiment A but instead using the

lower and upper bounds of anthropogenic BC emissions from China and India estimated by *Lu et al.* (2011). We find that wet deposition accounts for 83% of the global annual BC deposition, consistent with the previous results of 78.6±17% from the Aerosol inter-Comparison project (AeroCom) multi-model study (*Textor et al.*, 2006). The tropospheric lifetime of BC against deposition is 5.5 days, at the lower end of the range (5–11 days) reported by *Koch et al.* (2009). The difference between Experiments B and A is that we replace the *Bond et al.* (2007) emissions in China and India with the INTEX-B inventory in Experiment B. By contrasting model results from these two experiments, we aim to assess the sensitivity of BC in the Tibetan Plateau to changes in the anthropogenic emissions from India and China, the two largest source regions of BC to the Plateau (*Kopacz et al.*, 2011; *Lu et al.*, 2012), as will be discussed in further details in Sect. 2.4. Both Experiments A and B use an e-folding time of 1.15 days for BC aging. Experiment C applies the *Liu et al.* (2011) parameterization for BC aging instead. We used monthly mean OH concentrations with diurnal variations in the parameterization, which is derived from the offline GEOS-chem simulation with the same spatial resolution as BC simulations. The resulting e-folding time is 2.5 days on average globally and 2 days in Asia. The longer e-folding time results in longer atmospheric lifetime, larger deposition and higher hydrophobic fraction of BC over the Tibetan Plateau (not shown). We discuss further in Sect. 2.5 the differing results between Experiments C and A, which allow us to appraise the effect of a variable BC aging time on BC in the Plateau. In Experiment D, we replace the model resolution of 2° × 2.5° used in Experiment A with a finer resolution of 0.5° × 0.667° nested over Asia (11°S–55°N, 70°E–150°E). The differences between the results from Experiments D and A will be discussed in Sect. 2.6 for the purpose of evaluating the impact of model resolution on BC in the Plateau. In all model experiments, we use a BC mass absorption cross section (MAC) of 7 m^2 g^{-1} from observations (*Clarke et al.*, 2004) for calculating modeled BC AAOD. We note that BC MAC is associated with large uncertainties, which varies from 3 to 25 m^2 g^{-1} depending on atmospheric conditions (*Bond and Bergstrom*, 2006).

2.3 Results and discussions

2.3.1 BC in surface air

Figure 2.2 shows surface BC concentrations at Kharagpur (22.5°N, 87.5°E, 28 m a.s.l.), Gandhi College (25.9°N, 84.1°E, 158 m a.s.l.) and Kanpur (26.4°N, 80.3°E, 142 m a.s.l.), three rural sites. Model results reproduce the observed BC concentrations with the exception of winter, when the model underestimates the concentrations by 50%. The high wintertime concentrations are primarily because of emissions from agricultural waste and wood fuel burning that is dominant over the Indo-Gangetic Plain during winter (*Ram et al.*, 2010b). Model results using the upper bound of BC emissions capture the observed high concentrations in winter (Fig. 2.2). The wintertime low biases in the model therefore clearly call for enhanced emission estimates. *Moorthy et al.* (2013) found that modeled surface BC concentrations in this region are underestimated by more than a factor of two during winter when the planetary boundary layer (PBL) is convectively stable, while model underestimates are smaller in summer when the PBL is unstable. They suggested that the overestimate of wintertime PBL height in chemical transport models is an important contributor to model underestimates of surface pollutant concentrations. *Lin and McElroy* (2010) pointed out that the assumption of full PBL mixing (instantaneous vertical mixing throughout the mixing depth) in the GEOS-Chem tends to overestimate vertical mixing under a stable PBL condition. They proposed and implemented in GEOS-Chem a non-local PBL mixing scheme (*Holtslag and Boville*, 1993; *Lin et al.*, 2008), where the mixing states are determined by static instability. They used a local K-theory scheme (*Louis*, 1979) for a stable PBL and added a "non-local" term for an unstable PBL to account for the PBL-wide mixing triggered by large eddies. Our results show that the non-local boundary layer mixing increases surface BC concentrations by up to 25% in winter and spring, a significant improvement. *Nair et al.* (2012) showed that the non-local boundary layer mixing still tends to overestimate the vertical mixing during winter in the Indo-Gangetic Plain.

Model results are within ±50% of the observations at two remote sites, Zhuzhang (28.0°N, 99.7°E, 3583 m a.s.l., Fig. 2.2) and NCOS (30.8°N, 91.0°E, 4730 m a.s.l., Fig. 2.2), where observations are available for only fall and winter. Model results are lower than the observations at NCOP (28.0°N, 86.8°E, 5079 m a.s.l.) and Nagarkot (27.7°N, 85.5°E, 2150 m a.s.l.) by a factor of two in spring. Using the upper bound of BC emissions captures the springtime high concentrations at Nagarkot but not at NCOP (Fig. 2.2). The two sites are influenced by emissions from nearby Nepal valleys transported by the mountain-valley wind (*Carrico et al.*, 2003; *Bonasoni et al.*, 2010). In contrast, model results capture the relatively high concentrations in winter and spring observed at Manora Peak (29.4°N, 79.5°E, 1950 m a.s.l.) and Langtang (28.1°N, 85.6°E, 3920 m a.s.l.), but overestimate the summertime concentrations by a factor of two. Using the lower bound of BC emissions is still not able to capture the observed low values in summer (Fig. 2.2). Part of the discrepancies is explained by the inherent difficulty in simulating the meteorological fields over the complex Himalayan terrain. *Chen et al.* (2009) showed that the terrain effects and meteorological features in the Tibetan Plateau are not entirely reproduced by the GEOS-5 meteorological fields. Such difficulty is not unique to the Himalaya region. *Emery et al.* (2012) also showed that the transport of chemical species is not well simulated over the complex terrain in the western U.S. using GEOS-Chem driven by GEOS-5 meteorological fields 2° × 2.5°.

Surface concentrations of BC at Lhasa and Delhi, two urban sites (see Table 2.1), are strongly affected by emissions from city traffic and industries (*Zhang et al.*, 2008b; *Beegum et al.*, 2009). The BC concentrations at Dibragarh are highly impacted by the emissions from the oil wells upwind and vehicular emissions from national highways nearby (*Pathak et al.*, 2010). The concentrations at Dunhuang, a well-known tourist attraction and archaeological site, likely reflect vehicular emissions associated with tourist traffic including tour buses. All four sites are characterized by strong local emissions. Model results reproduce the seasonal trends at these urban sites (sites that are near urban centers or heavily influenced by local emissions), but are low by an order of magnitude (Fig. 2.3). Using the upper bound of BC

emissions results in doubling BC concentrations (Table 2.1), which by itself still cannot fully explain the model versus observation discrepancies. We exclude these four urban sites from analysis hereinafter.

There is a small negative bias of -0.3 μg m^{-3} in model simulated surface BC concentrations (Fig. 2.4, left column), and the difference between model results and the observations is statistically insignificant. We note that the residual errors at very low BC concentrations may not be particularly meaningful. Overall, model results reproduce the spatiotemporal variation of surface BC concentration throughout the Tibetan Plateau ($r = 0.9$, root-mean-square-error RMSE = 1.3 μg m^{-3}) with the exception of peak values (Fig. 2.4).

2.3.2 BC in snow

BC deposition and precipitation together determine BC concentration in snow, which we approximate as the ratio of total BC deposition to total precipitation (see Sect. 2.2.2.2). Figure 2.5 shows GEOS-Chem simulated annual mean BC deposition and GEOS-5 precipitation over Asia. The largest BC deposition over the Tibetan Plateau is in the Himalayas and the southeastern Plateau (Fig. 2.5), reflecting the proximity of strong BC sources in northern India and southwestern China (*Lu et al.*, 2012) and the intense precipitation in the region (Fig. 2.5). The northern Plateau is heavily influenced by BC transported in the westerlies (*Kopacz et al.*, 2011; *Lu et al.*, 2012), but the lack of strong precipitation results in considerably smaller BC deposition (Fig. 2.5).

Table 2.2 shows BC concentrations in snow at 18 sites across the Plateau. The concentrations are 30% lower during the monsoon season (June–September) than during the non-monsoon seasons (October–May), both in the observations and in the model. Here the monsoon and non-monsoon seasons are defined following *Xu et al.* (2009). The lowest BC concentrations in snow (minimum of 4.3 μg kg^{-1}) are in the northern slope of the Himalayas, while the highest values (maximum of 141 μg kg^{-1}) are to the north of the Plateau. Such spatial variation largely reflects the varying elevations of the sites. *Ming et al.* (2009a, 2013)

have shown that observed BC concentration in snow over the Tibetan Plateau is inversely correlated with the elevation of a site, with lower concentrations at higher elevations. Our model results capture this spatial variation, but deviate from the observed concentrations by more than a factor of two at several sites in the Himalayas and the central Plateau (Table 2.2).

Model results overestimate BC concentrations in snow during the monsoon season by a factor of 2–4 at three Himalayan sites, Zuoqiupu (29.2°N, 96.9°E, 5500 m a.s.l.), East Rongbuk (28.0°N, 87.0°E, 6500 m a.s.l.) and Namunani (30.4°N, 81.3°E, 5900 m a.s.l.) (Fig. 2.6). Model results using the lower bound of BC emissions still overestimate the concentrations at these three sites (Table 2.2). Wet scavenging accounts for more than 80% of the BC deposition over the Tibetan Plateau during the monsoon season in the model. The large overestimate implies either excessive wet deposition or inadequate precipitation or both in the Himalayas, given that BC concentration in snow is approximated here as the ratio of BC deposition to precipitation (see Sect. 2.2.2.2). Figure 2.7 shows the monthly precipitation over different parts of the Tibetan Plateau from the Global Precipitation Climatology Project (GPCP, *Huffman et al.*, 2001), the NOAA Climate Prediction Center (CPC) Merged Analysis of Precipitation (CMAP, *Xie and Arkin*, 1997), the University of East Anglia Climate Research Unit (CRU, *Harris et al.*, 2014) and GEOS-5. GPCP precipitation is generally consistent with that from CMAP in most parts of the Plateau except the southeastern Plateau, where it is stronger by more than a factor of two. CRU precipitation tends to be much stronger than those from GPCP and CMAP during the monsoon season, particularly in the southeastern Plateau and the Himalayas (Fig. 2.7). Previous studies have shown that the monsoon precipitation in the Himalayas is too weak in both GPCP and CMAP data (*Kitoh and Kusunoki*, 2008; *Voisin et al.*, 2008) yet too strong in the CRU data (*Zhao and Fu*, 2006; *Xie et al.*, 2007). The scarcity of observational sites and the complex terrain of the Himalayas are two of the principle reasons for large uncertainties in different precipitation datasets and apparent inconsistencies among them (*Ma et al.*, 2009; *Andermann et al.*, 2011). Figure 2.7

shows that GEOS-5 precipitation is stronger than GPCP and CMAP data by a factor of two in the Himalayas during the monsoon season. To probe the sensitivity of BC deposition and our calculated BC concentration in snow in the Himalayas to precipitation, we conducted a GEOS-Chem simulation where we reduced GEOS-5 precipitation in the region by 20% during the monsoon season. The resulting BC wet deposition is only slightly lower (up to 5%), rather insensitive to changes in presumably already intense precipitation during the monsoon season in the region. This lack of strong sensitivity reflects an already efficient wet scavenging of BC in the intense monsoon precipitation. The resulting BC concentrations in snow are higher by 18% on average in the region, because the reduced precipitation tends to concentrate BC in snow. Therefore, model overestimates of BC concentration in snow in the region are less likely resulting from excessive monsoon precipitation but more likely from excessive BC deposition. This is likely a result of overlong BC lifetime due to insufficient wet removal. *Wang et al.* (2014a) compared GEOS-Chem simulated atmospheric BC concentrations with the HIAPER Pole-to-Pole Observations (HIPPO) aircraft measurements and concluded that wet scavenging in the model is too weak. This is in part because of the underestimated scavenging efficiency of BC in the model. In addition, the relatively long BC aging time used in the model is also potentially contributing to the weak wet scavenging. Recent observations suggest that the e-folding time of about one day, for the hydrophobic-to-hydrophilic conversion of BC, typically used in global models is too long (*Akagi et al.*, 2012). The uncertainties in wet scavenging in the model reduce the accuracy in the estimates of snow BC concentrations. Excessive BC deposition can in part result from too strong PBL mixing in the source regions and consequently excessive BC being transported into the free troposphere. Our model results show that the non-local boundary layer mixing (*Lin and McElroy*, 2010) reduces BC wet deposition by up to 5% on average in the Himalayas during the monsoon season.

Figure 2.6 shows that our calculated BC concentrations in snow are lower than observations by a factor of two across the central Plateau. Model results using the upper bound of

BC emissions are able to reproduce the high BC concentrations in snow at La'nong but miss those high values at the other sites (Table 2.2). *Ming et al.* (2009a) pointed out that this region is predominantly influenced by biofuel burning (residential cooking and heating) and biomass burning from religious activities. These local emissions are largely unaccounted for in current emission inventories (*Wang et al.*, 2012a). In addition, it is likely that the lack of consideration of snow aging also lowers the BC concentration in snow computed here (*Xu et al.*, 2006). We choose to exclude Meikuang and Zhadang from the comparison here on account of local emissions from coal-containing rock strata at the former (*Xu et al.*, 2006) and strong snow melting at the latter (*Zhou et al.*, 2007). GEOS-5 precipitation in the central Plateau is in general agreement with those from CMAP and CRU during the non-monsoon season and that from GPCP during the monsoon season (Fig. 2.7).

Model results are consistent with observations at the elevated sites in the northwestern and northeastern Plateau and to the north of the Plateau (Fig. 2.6), where free tropospheric BC is primarily northern mid-latitude pollution transported by the westerlies (*Kopacz et al.*, 2011; *Lu et al.*, 2012). Regional emissions from western and central China also contribute to BC deposition in these regions (*Lu et al.*, 2012). Although precipitation in these regions is weaker in GEOS-5 than in GPCP and CMAP (Fig. 2.7), previous studies have shown that GPCP and CMAP precipitation is likely too strong there (*Voisin et al.*, 2008; *Ma et al.*, 2009).

Overall model results of BC concentration in snow have a small negative bias but a large RMSE (Fig. 2.4, middle column), the latter results from the large discrepancies in the Himalayas and the central Plateau. Model results are statistically in good agreement with observations and reproduce the observed spatiotemporal variation ($r = 0.85$).

2.3.3 BC AAOD

Modeled BC AAOD is consistently lower than AERONET retrievals at most sites on both a monthly (Fig. 2.4, right column) and an annual basis (Table 2.3). The annual mean

modeled BC AAOD over the Tibetan Plateau is 0.002 (Fig. 2.8), considerably lower than the observations. Model results somewhat capture the observed spatial and seasonal trends ($r = 0.53$), but to varying degrees underestimate the magnitudes (Fig. 2.9). Forty percent of the data points are too low by more than a factor of two in the model, particularly in the Himalayas and to the northwest of the Plateau during winter and spring when emissions are larger (relative to emissions during the rest of the year). Most AERONET measurements in and around the Plateau are after 2006, whereas our model results are for 2006. BC emissions in India have increased by 3.3% yr[-1] since 2006 (*Lu et al.*, 2011). Therefore, the large low bias in part reflects the abovementioned temporal (hence emissions) mismatch. Using the upper bound of BC emissions reduces the model versus observations discrepancies at six sites (Table 2.3), but model results are still lower by a factor of two than the observed high AAODs at the other sites. We also note that there are large uncertainties in the AERONET AAOD retrieval (*Bond et al.*, 2013), and that BC AAOD data is only scarcely available in the Plateau and adjacent regions.

Another equally important factor contributing to the large discrepancy is the assumption of external mixing of BC in the model, which leads to a weaker BC absorption (*Jacobson*, 2001). Previous studies have found that BC absorption is enhanced by 50% because of internal mixing (*Bond and Bergstrom*, 2006). We find that a 50% increase of BC absorption (using a MAC of 11 m^2 g^{-1} in our calculation) would reduce the model bias by 57% in the Indo-Gangetic Plain and the northeastern Plateau and to the northeast of the Plateau, and by 16% along the southern slopes of the Himalayas and to the northwest of the Plateau (Fig. 2.9, right panel). There is evidence that the enhancement of BC absorption due to internal mixing may be considerably smaller than previously thought (*Cappa et al.*, 2012). It is clear that the large discrepancy (more than a factor of two) in the Himalayas and to the northwest of the Plateau cannot be fully explained by the lack of BC internal mixing consideration (and the associated larger absorption) in the model. *Bond et al.* (2013) pointed out that current models significantly underestimate BC AAOD, particularly in South and

Southeast Asia, primarily because of the absence of internal mixing and underestimated emissions. They recommended scaling up modeled BC AAOD to AERONET observations in order to accurately estimate BC radiative effects.

Therefore, although surface BC concentration is relatively well captured by model results (see Sect. 2.3.1), more measurements of vertical profiles over the Tibetan Plateau are imperative for evaluating column quantities such as BC AAOD.

2.4   Sensitivity to BC emissions

Figure 2.2 shows that model simulated surface BC concentrations are considerably lower in Experiment B (using the INTEX-B inventory) relative to Experiment A (using the LU inventory) at rural sites. The difference in surface BC concentration is more than 30% at rural sites and 10–20% at remote sites, decreasing with distance from the source region. Such varying difference in surface BC concentration largely reflects the spatially non-uniform differences between the two emission inventories. The difference in BC concentration in snow between the two sets of results is less than 20%. The relatively smaller difference is because the sites with measurements of BC concentration in snow are invariably remote high-elevation sites, further away from the source regions. BC concentrations in snow are higher over the northwestern and northeastern Plateau and to the north of the Plateau but lower in the Himalayas and the central Plateau in Experiment B than in A. This is because of the lower BC emissions in the central Plateau and India and the higher emissions in northwestern and central China in the INTEX-B than in the LU inventories. BC AAOD values are higher (<15%) to the northeast and northwest of the Plateau and lower (10–60%) in the Indo-Gangetic Plain in Experiment B than in A. Therefore, both surface BC concentration and AAOD along the southern slope of the Himalayas are strongly sensitive to Indian emissions, while the high-altitude remote sites are less affected by the emission changes in the source regions. Overall, Experiment B results show larger negative bias and root mean square error

(RMSE) (Table 2.6) and lower Taylor score (Fig. 2.10) relative to Experiment A. As such, our results suggest that the INTEX-B inventory considerably underestimates anthropogenic BC emissions in India, which is also implied by some latest estimates of BC emissions in Asia (*Kurokawa et al.*, 2013; *Wang et al.*, 2014a).

2.5   Sensitivity to BC aging parameterization

Compared with model results from the standard simulation (Experiment A, Table 2.5), the use of *Liu et al.* (2011) parameterization for BC aging in the model (Experiment C, Table 2.5) results in increased surface BC concentrations, BC concentrations in snow, and BC AAOD, because of the longer BC atmospheric lifetime against wet scavenging (see Sect. 2.2.2.3). The increase in surface BC concentration is 1% on average (maximum 3%) at rural sites and 10% on average (maximum 30%) at remote sites (Fig. 2.2). This is consistent with the results from *Huang et al.* (2013), where the use of *Liu et al.* (2011) parameterization only changes GEOS-Chem simulated surface BC concentrations by less than 0.01 μg m^{-3} in the Tibetan Plateau. *Liu et al.* (2011) showed that their aging parameterization significantly improves seasonal variations of modeled surface BC concentrations in the Arctic. This is different from the present study, where the aging parameterization has a minor impact on the seasonality of both surface BC concentrations and AAOD (Fig. 2.2 and Table 2.6). The increase in BC AAOD is 10% on average (maximum 30%) at most AERONET sites but leads to lower spatiotemporal correlations with observations (Table 2.6). The aging parameterization has a much stronger impact on modeled BC concentration in snow than on surface BC concentration and BC AAOD. The increase in BC concentration in snow is more than 30% at a number of sites in the Himalayas and the central Plateau (Table 2.2). Compared with the standard simulation (Experiment A), the use of the *Liu et al.* (2011) parameterization results in an overestimate of BC concentration in snow relative to observations, which increases the absolute bias by a factor of two (Table 2.6) and decreases the Taylor score (Fig. 2.10). This suggests that the *Liu et al.* (2011) aging parameterization

may result in too long conversion times of BC (from hydrophobic to hydrophilic) hence too long atmospheric lifetimes.

2.6 Sensitivity to model resolution

Compared with model results from the standard simulation (Experiment A, Table 2.5), the use of a finer model resolution ($0.5° \times 0.667°$) nested over Asia (Experiment D, Table 2.5) reduces the bias in modeled surface BC concentrations from 15% to 2% but increases the RMSE (Table 2.6). *Wang et al.* (2014b) found that replacing a coarse-resolution model ($1.27° \times 2.5°$) with a finer-resolution one ($0.51° \times 0.66°$) reduces the bias of surface BC simulation in Asia by 30%. Figure 2.2 shows that the nested model simulation slightly improves seasonal variations of surface BC concentrations at several remote sites, whereas it does not improve those at urban sites both in magnitude and in temporal variation (Fig. 2.3). This is similar to the results in *Fu et al.* (2012), where the GEOS-Chem nested model underestimates surface BC concentrations by an order of magnitude at Dunhuang and Lhasa sites, even using the enhanced BC emissions from top-down estimates. Compared with the standard simulation, the nested model simulation increases the absolute bias by 57% in modeled snow BC concentration and by 5% in modeled BC AAOD (Table 2.6). The nested model results also show a lower spatiotemporal correlation with observations of snow BC concentration and BC AAOD (Fig. 2.10). Our results suggest that the finer model resolution alone cannot explain model versus observation discrepancies on the simulation of snow BC concentration and BC AAOD in the Tibetan Plateau.

2.7 Summary and conclusions

This study sought to understand the capability of GEOS-Chem in simulating BC over the Tibetan Plateau and the potential factors driving model versus observation discrepancies. We used GEOS-Chem version 9-01-03 driven by GEOS-5 assimilated meteorological fields

and systematically evaluated the model simulations against in situ measurements of BC in surface air, BC in snow, and BC AAOD for 2006. We also examined the effects of anthropogenic BC emissions from China and India, BC aging process and model resolution on BC simulations.

Model results captured the seasonal variation of surface BC concentrations at rural sites, but the observed wintertime high values were absent in the model, which calls for improved emission estimates particularly in the Indo-Gangetic Plain. The use of non-local PBL mixing scheme reduced part of the discrepancy between observed and modeled surface BC concentrations in winter. Modeled surface BC concentrations at remote sites were within a factor of two of the observations. Part of the discrepancy is explained by the inherent difficulty in simulating the meteorological fields over the complex Himalayan terrain. Surface BC concentrations at urban sites are significantly underestimated by model results.

Modeled BC concentrations in snow were spatiotemporally consistent with observations ($r = 0.85$). The highest snow BC concentrations were seen north of the Plateau (40°N–50°N), while the lowest values were found in the northern slope of the Himalayas. However, model results were a factor of 2–4 higher than the observations at three Himalayan sites during the monsoon, primarily because of the excessive BC deposition resulted from overlong BC lifetime. Model results underestimated snow BC concentration by a factor of two in the central Plateau, due to the lack of snow aging in the CTM and the strong local emissions unaccounted for in the emission inventories. Model results are consistent with the observations at the elevated sites in the northwestern and northeastern Plateau and to the north of the Plateau. Model results of both BC in snow and in surface air showed no statistically significant difference with observations with biases less than 15%.

Modeled BC AAOD is consistently biased low at most AERONET sites over the Plateau, especially to the northwest of the Plateau and in the Himalayas in winter and spring. The large model versus observation discrepancies were mainly because of underestimated emissions and the assumption of external mixing of BC in the model. This suggests that modeled

BC AAOD should be scaled to AERONET observations in order to accurately estimate BC climatic effects. More measurements of vertical profiles over the Tibetan Plateau are imperative for evaluating modeled column quantities such as BC AAOD.

Sensitivity simulations showed that both surface BC concentration and BC AAOD along the southern slope of the Himalayas were strongly sensitive to Indian emissions, while the elevated remote sites were less affected by the change of emissions in source regions. The BC aging parameterization from *Liu et al.* (2011) resulted in a large increase of BC concentration in snow, but only had a minor impact on surface BC concentration and AAOD. The use of a finer model resolution nested over Asia reduced the bias in modeled surface BC concentration from 15% to 2%, but increased the bias in modeled snow BC concentration and BC AAOD by 57% and 5%, respectively. More quantitative analyses are required to investigate the uncertainties in different model processes of BC simulations.

Therefore, accurate model simulations of BC in surface air, BC in snow and BC AAOD over the Tibetan Plateau require improvements in BC emission inventories particularly for China and India, model meteorological fields over the complex Himalayan terrain, PBL mixing scheme particularly under a stable PBL condition, model representation of atmospheric BC aging process including the conversion of hydrophobic to hydrophilic BC and the enhancement of BC absorption resulted from internal mixing, model parameterization of BC wet scavenging, and model simulation of snow processes such as snow aging, snow melting and BC transfer among different snow layers.

Faculty scheme (No. DST/INSPIRE Faculty Award/2012; IFA-AES-02). This study also used the data collected within the SHARE Project thanks to contributions from the Italian National Research Council and the Italian Ministry of Foreign Affairs. This study was funded by NASA grants NNX09AF07G and NNX08AF64G from the Atmospheric Chemistry Modeling and Analysis Program (ACMAP).

2.8 Tables and figures

Table 2.1: Observed and simulated surface BC concentrations over the Tibetan Plateau.

Region	Site	Lat. (°N)	Lon. (°E)	Elev. (m)	Time	Freq.	Technique[a]	Surface BC ($\mu g\ m^{-3}$)				
								Obs.[b]	Exp.A[c]	Exp.B[d]	Exp.C[e]	Exp. D[f]
Urban	Delhi	28.6	77.2	260	2006	monthly	Aethalometer	13.5[1]	2.6 (1.6-4.7)	1.7	2.6	2.6
	Dibrugarh	27.3	94.6	111	2008-2009	monthly	Aethalometer	8.9[2]	0.8 (0.5-1.5)	0.5	0.9	1.6
	Lhasa	29.7	91.1	3663	2006	monthly	TOR	3.7[3]	0.08 (0.05-0.14)	0.07	0.09	0.05
	Dunhuang	40.2	94.7	1139	2006	monthly	TOR	4.1[3]	0.1 (0.08-0.24)	0.2	0.1	0.3
Rural	Kharagpur	22.5	87.5	28	2006	monthly	Aethalometer	5.5[4]	4.2 (2.5-8.4)	2.4	4.2	6.1
	Kanpur	26.4	80.3	142	2006	monthly	TOT	3.7[5]	3.1 (1.0-5.8)	2.2	3.1	2.8
	Gandhi College	25.9	84.1	158	2006	monthly	Retrieval	4.8[6]	4.6 (2.9-8.5)	3.2	4.6	5.0
Remote	Nagarkot	27.7	85.5	2150	1999-2000	seasonal	TOT	1.0[7]	0.8 (0.5-1.3)	0.7	0.8	0.7
	NCOP	28.0	86.8	5079	2006	monthly	MAAP	0.2[8]	0.07 (0.05-0.13)	0.07	0.08	0.07
	Manora Peak	29.4	79.5	1950	2006	monthly	TOT	1.1[9]	1.3 (0.9-2.2)	1.2	1.3	1.2
	NCOS	30.8	91.0	4730	2006	monthly	TOR	0.1[10]	0.08 (0.05-0.15)	0.07	0.09	0.04
	Langtang	28.1	85.6	3920	1999-2000	seasonal	TOT	0.4[7]	0.4 (0.2-0.7)	0.4	0.4	0.5
	Zhuzhang	28.0	99.7	3583	2004-2005	monthly	TOR	0.3[11]	0.3 (0.2-0.5)	0.3	0.4	0.3

[a]Thermal Optical Reflectance (TOR), Thermal Optical Transmittance (TOT), Multi-Angle Absorption Photometer (MAAP)
[b]Values are multi-month averages. References: [1]Beegum et al. (2009), [2]Pathak et al. (2010), [3]Zhang et al. (2008), [4]Nair et al. (2012), [5]Ram et al. (2010b), [6]Ganguly et al. (2009b), [7]Carrico et al. (2003), [8]Bonasoni et al. (2010), [9]Ram et al. (2010a), [10]Ming et al. (2010), [11]Qu et al. (2008).
[c]Values from Experiment A (Table 2.5) for 2006. See text for details. Values in parentheses are from the same Experiment but using instead the upper and lower bounds of anthropogenic BC emissions in China and India.
[d]Values from Experiment B (Table 2.5) for 2006. See text for details.
[e]Values from Experiment C (Table 2.5) for 2006. See text for details.
[f]Values from Experiment D (Table 2.5) for 2006. See text for details.

Table 2.2: Observed and simulated BC concentrations in snow over the Tibetan Plateau.

Region	Site	Lat. (°N)	Lon. (°E)	Elev. (km)	Time	BC in snow (µg kg^{-1})				
						Obs.[a]	Exp.A[b]	Exp.B[c]	Exp.C[d]	Exp.D[e]
The Himalayas	Zuoqiupu	29.21	96.92	5.50	monsoon 2006	7.9[2]	22.5 (13.6-43.0)	18.4	25.5	24.6
		29.21	96.92	5.60	non-monsoon 2006	15.9[2]	21.2 (13.6-36.9)	18.3	31.9	53.9
	Qiangyong	28.83	90.25	5.40	summer 2001	43.1[1]	66.1 (42.2-122.8)	49.7	63.7	18.3
	Noijin Kangsang	29.04	90.20	5.95	annual 2005	30.6[2]	39.5 (21.1-60.8)	34.6	52.3	22.5
	East Rongbuk	28.02	86.96	6.50	monsoon 2001	35.0[3]	26.4 (16.8-48.9)	22.7	29.2	22.4
		28.02	86.96	6.50	non-monsoon 2001	21.0[3]	32.8 (21.6-55.6)	31.1	59.4	42.7
		28.02	86.96	6.50	summer 2002	20.3[4]	26.5 (16.8-49.3)	22.8	28.9	23.0
		28.02	86.96	6.50	Oct. 2004	18.0[4]	20.5 (13.6-35.6)	20.8	26.0	25.4
		28.02	86.96	6.50	Sept. 2006	9.0[7]	26.0 (16.7-47.6)	22.4	30.0	20.6
		28.02	86.96	6.52	May 2007	41.8[6]	27.1 (16.9-41.7)	24.7	29.7	45.2
	Kangwure	28.47	85.82	6.00	summer 2001	21.8[1]	26.5 (16.8-49.3)	22.8	28.9	18.0
	Namunani	30.45	81.27	5.90	summer 2004	4.3[1]	24.8 (15.8-45.2)	21.2	26.6	19.6
Northwestern Tibetan Plateau	Mt. Muztagh	38.28	75.02	6.35	summer 2001	37.2[1]	31.0 (23.3-52.8)	36.6	31.9	32.9
		38.28	75.10	6.30	1999	26.6[1]	33.0 (26.6-48.6)	36.4	45.8	42.1
Northeastern Tibetan Plateau	Laohugou #12	39.43	96.56	5.05	Oct. 2005	35.0[4]	54.4 (34.9-97.2)	60.0	60.3	65.0
	Qiyi	39.23	97.06	4.85	Jul. 2005	22.0[4]	25.7 (18.5-67.0)	30.3	27.4	48.9
	July1 glacier	39.23	97.75	4.60	summer 2001	52.6[1]	59.2 (32.8-122.8)	68.8	61.0	106.2
Central Tibetan Plateau	Meikuang	35.67	94.18	5.20	summer 2001	446[1]	24.4 (15.4-47.0)	24.8	27.2	32.9
		35.67	94.18	5.20	Nov. 2005	81.0[5]	40.9 (18.8-50.0)	43.3	50.5	38.6
	Tanggula	33.11	92.09	5.80	2003	53.1[2]	16.1 (10.4-28.6)	14.5	25.6	12.0
	Dongkemadi	33.10	92.08	5.60	summer 2001	18.2[1]	19.6 (12.2-36.8)	17.7	22.1	15.0
		33.10	92.08	5.60	year 2005	36.0[7]	15.8 (10.2-28.1)	14.2	23.7	11.8
	La'nong	30.42	90.57	5.85	Jun. 2005	67.0[4]	39.1 (25.8-72.9)	35.9	37.8	22.9
	Zhadang	30.47	90.50	5.80	Jul. 2006	87.4[4]	27.9 (17.0-53.4)	21.7	30.3	19.3
North of the Plateau	Haxilegen River	43.73	84.46	3.76	Oct. 2006	46.9[4]	36.1 (34.1-45.2)	37.9	36.7	71.4
	Urumqi Riverhead	43.10	86.82	4.05	Nov. 2006	141[5]	131.9 (71.8-270.4)	155.2	118.4	127.9
	Miao'ergou #3	43.06	94.32	4.51	Aug. 2005	111[4]	98.8 (59.3-158.2)	113.2	103.7	113.8

[a]References: [1]Xu et al. (2006), [2]Xu et al. (2009), [3]Ming et al. (2008), [4]Ming et al. (2009a), [5]Ming et al. (2009b), [6]Ming et al. (2012), [7]Ming et al. (2013).
[b]Values from Experiment A (Table 2.5) for 2006. See text for details. Values in parentheses are from the same Experiment but using instead the upper and lower bounds of anthropogenic BC emissions in China and India.
[c]Values from Experiment B (Table 2.5) for 2006. See text for details.
[d]Values from Experiment C (Table 2.5) for 2006. See text for details.
[e]Values from Experiment D (Table 2.5) for 2006. See text for details.

Table 2.3: Observed and simulated annual mean BC AAOD at AERONET sites over the Tibetan Plateau.

Region	Site	Lat. (°N)	Lon. (°E)	Alt. (m)	Time	BC AAOD		
						Obs.[a]	Model[b]	Ratio[c]
The Indo-Gangetic Plain	Lahore	31.54	74.33	270	2007~2012	0.0434	0.0162 (0.0125-0.0239)	2.7
	Kanpur	26.51	80.23	123	2006~2012	0.0426	0.0221 (0.0071-0.0413)	1.9
	Gandhi College	25.87	84.13	60	2006~2012	0.0443	0.0282 (0.0179-0.0517)	1.6
	Gual_Pahari	28.43	77.15	384	2008~2010	0.0511	0.0222 (0.0147-0.0382)	2.3
	Jaipur	26.91	75.81	450	2009~2012	0.0202	0.0168 (0.0110-0.0296)	1.2
The Himalayas	Jomsom	28.78	83.71	2803	2012	0.0231	0.0136 (0.0092-0.0228)	1.7
	Pantnagar	29.05	79.52	241	2008~2009	0.0507	0.0114 (0.0079-0.0193)	4.4
	Nainital	29.36	79.46	1939	2008~2010	0.0204	0.0125 (0.0086-0.0212)	1.6
	Pokhara	28.15	83.97	807	2010~2012	0.0524	0.0056 (0.0037-0.0097)	9.4
	Kathmandu Univ.	27.60	85.54	1510	2009~2010	0.0406	0.0057 (0.0038-0.0099)	7.1
Northeastern Tibetan Plateau	SACOL	35.95	104.14	1965	2007~2011	0.0163	0.0100 (0.0056-0.0204)	1.6
Northeast of the Tibetan Plateau	Dalanzadgad	43.58	104.42	1470	2006, 2012	0.0038	0.0025 (0.0020-0.0041)	1.5
Northwest of the Tibetan Plateau	Issyk-Kul	42.62	76.98	1650	2008~2010	0.0196	0.0020 (0.0017-0.0029)	9.8
	Dushanbe	38.55	68.86	821	2011~2012	0.0131	0.0030 (0.0027-0.0035)	4.4

[a]AERONET retrieved BC AAOD (Bond et al., 2013). Values are multi-year averages.
[b]Values from Experiment A (Table 2.5) for 2006. See text for details. Values in parentheses are from the same Experiment but using instead the upper and lower bounds of anthropogenic BC emissions in China and India.
[c]The ratio of AERONET retrieved to GEOS-Chem modeled BC AAOD.

Table 2.4: Anthropogenic BC emissions in China and India in 2006.

Emissions (Gg yr⁻¹)	China		India	
	Lu et al. (2011)	Zhang et al. (2009)	Lu et al. (2011)	Zhang et al. (2009)
Industry	509	575	201	47
Power plants	15	36	1	8
Residential	971	1022	608	268
Transportation	178	205	75	80
Total	1673 (954-3229*)	1838 (884-3823)	885 (522-1655)	404 (112-1454)

[*]Uncertainties (in parentheses).

Table 2.5: GEOS-Chem simulations of BC.

Model experiment		A	B	C	D
Resolution		2°×2.5°	2°×2.5°	2°×2.5°	0.5°×0.667° (Asia) 2°×2.5° (Global)
Anthropogenic emissions	China & India	Lu et al. (2011)	Zhang et al. (2009)	Lu et al. (2011)	Lu et al. (2011)
	Rest of Asia	Zhang et al. (2009)			
	Rest of world	Bond et al. (2007)			
Biomass burning emissions		GFEDv3 (van der Werf et al., 2010), with updates fromRanderson et al. (2012)			
BC aging (hydrophobic to hydrophilic)		e-folding time 1.15 days	e-folding time 1.15 days	Liu et al. (2011)	e-folding time 1.15 days
Deposition	Dry deposition	Wesely (1989) as implemented by Wang et al. (1998)			
	Wet deposition	Liu et al. (2001) with updates from Wang et al. (2011)			

Table 2.6: Error statistics of GEOS-Chem simulations of BC in the Tibetan Plateau for 2006.

Statistical quantities[*]	BC in surface air				BC in snow				BC AAOD			
	Model experiments (see Table 5)											
	A	B	C	D	A	B	C	D	A	B	C	D
Mean Error	-0.29	-0.82	-0.26	-0.03	-1.23	-0.75	3.39	1.94	-0.019	-0.023	-0.020	-0.020
Mean Absolute Error	0.59	0.93	0.59	0.74	13.39	12.74	16.09	19.67	0.020	0.023	0.020	0.021
Fractional Gross Error	0.39	0.46	0.39	0.46	0.43	0.40	0.48	0.58	0.78	0.93	0.80	0.77
Root Mean Square Error (RMSE)	1.34	1.95	1.33	1.33	16.73	16.65	18.67	24.54	0.026	0.029	0.027	0.027
Bias-corrected RMSE	1.31	1.77	1.30	1.33	16.69	16.63	18.36	24.46	0.017	0.018	0.018	0.019
Correlation coefficient (p-value < 0.001)	0.90	0.87	0.90	0.87	0.85	0.86	0.81	0.70	0.53	0.46	0.45	0.37

[*]Units for mean error, mean absolute error, RMSE and bias-corrected RMSE are $\mu g\ m^{-3}$ for BC in surface air and $\mu g\ kg^{-1}$ for BC in snow.
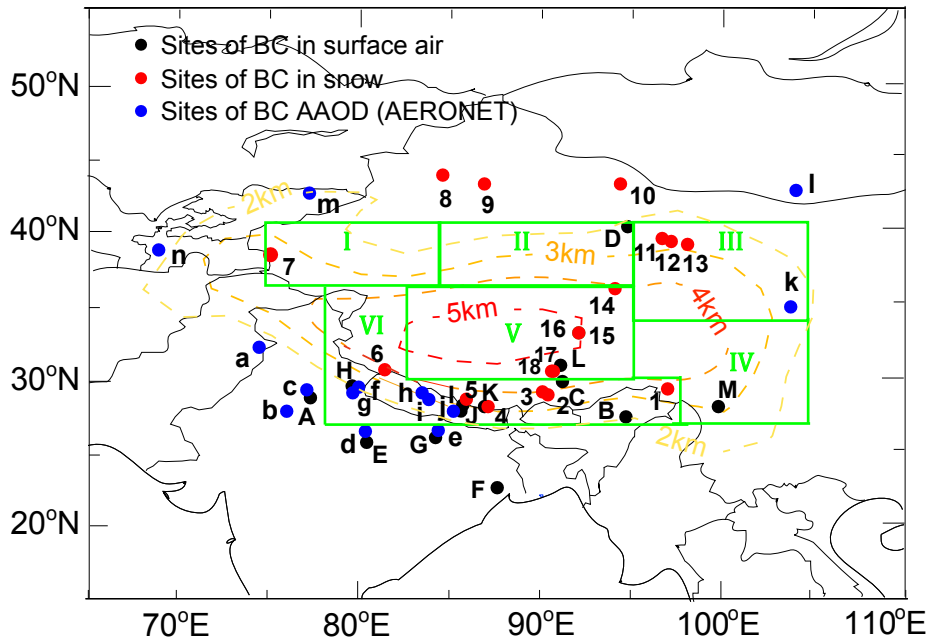
Figure 2.1: BC measurements at sites in and around the Tibetan Plateau (see also Tables 2.1 – 2.3). Black circles are surface measurements: Delhi (A), Dibragarh (B), Lhasa (C), Dunhuang (D), Kanpur (E), Kharagpur (F), Gandhi College (G), Manora Peak (H), Langtang (I), Nagarkot (J), Nepal Climate Observatory at Pyramid (NCOP, K), Nam Co Observational Station (NCOS, L), Zhuzhang (M). Red circles are measurements of BC in snow: Zuoqiupu (1), Qiangyong (2), Noijin Kangsang (3), East Rongbuk (4), Kangwure (5), Namunani (6), Mt. Muztagh (7), Haxilegen Riverhead (8), Urumqi Riverhead (9), Miao'ergou No.3 (10), Laohugou No. 12 (11), Qiyi (12), July 1 glacier (13), Meikuang (14), Tanggula (15), Dongkemadi (16), La'nong (17), Zhadang (18). Blue circles are BC AAOD measurements: Lahore (a), Jaipur (b), Gual'Pahari (c), Kanpur (d), Gandi college (e), Nainital (f), Pantnagar (g), Jomsom (h), Pokhara (i), Kathmandu University (j), SACOL (k), Dalanzadgad (l), Issyk-Kul (m), Dushanbe (n). The rectangles are the six sub-regions: the northwestern Plateau (I), the northern Plateau (II), the northeastern Plateau (III), the southeastern Plateau (IV), the central Plateau (V), and the Himalayas (VI). Topography is also shown (dashed colored contours).

37
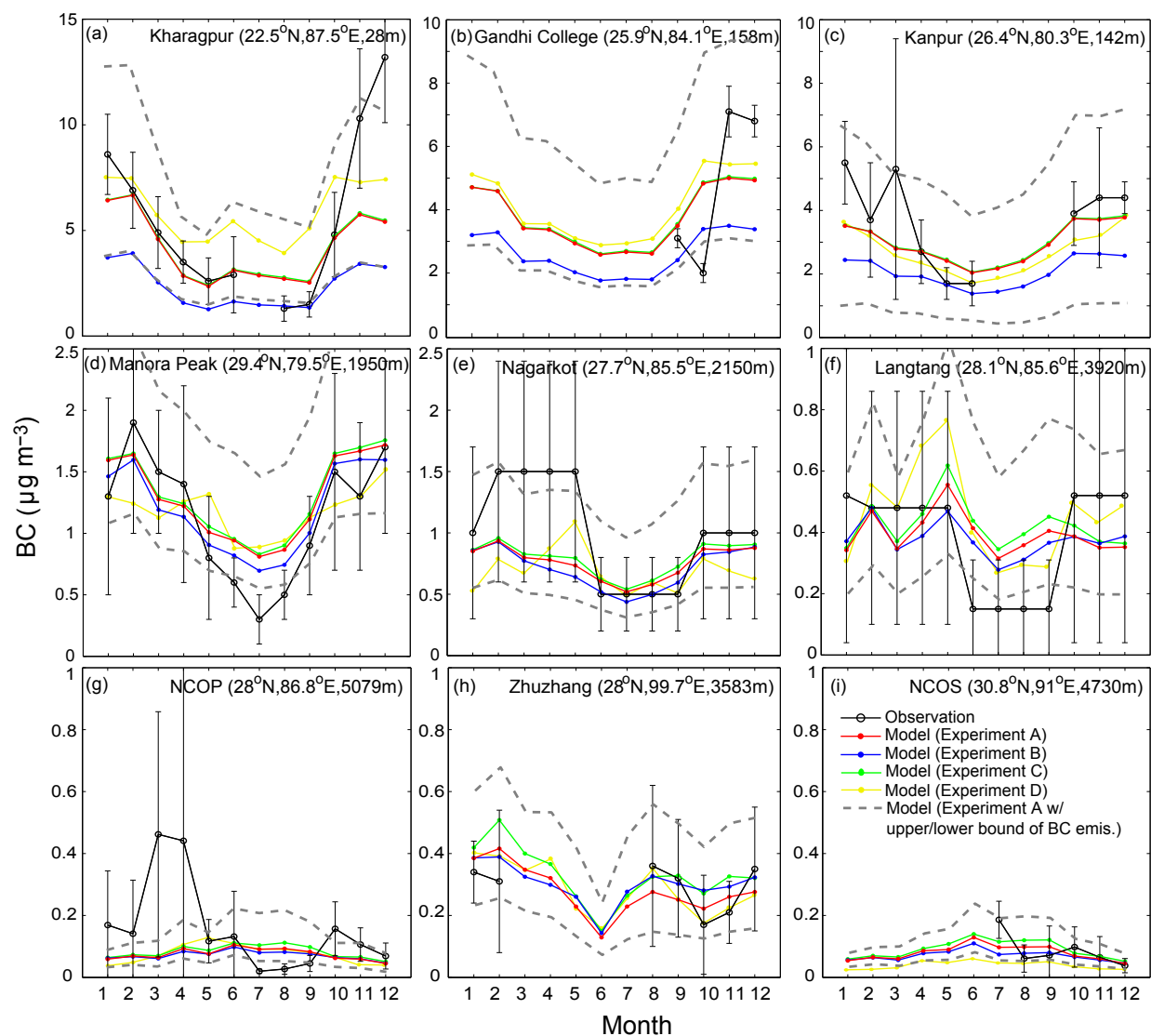
Figure 2.2: Observed (black curve) and GEOS-Chem simulated (colored curves: red - Experiment A; blue - Experiment B; green - Experiment C; yellow - Experiment D; grey dashed curves - Experiment A using upper/lower bounds of anthropogenic BC emissions in China and India) monthly mean surface BC concentration (μg m^{-3}) at three rural sites (a–c) and six remote sites (d–i) over the Tibetan Plateau in 2006 (see Table 2.1 and Figure 2.1). Only seasonal mean observations are available at sites e and f. Also shown are standard deviations for observations (error bars). See text for details.
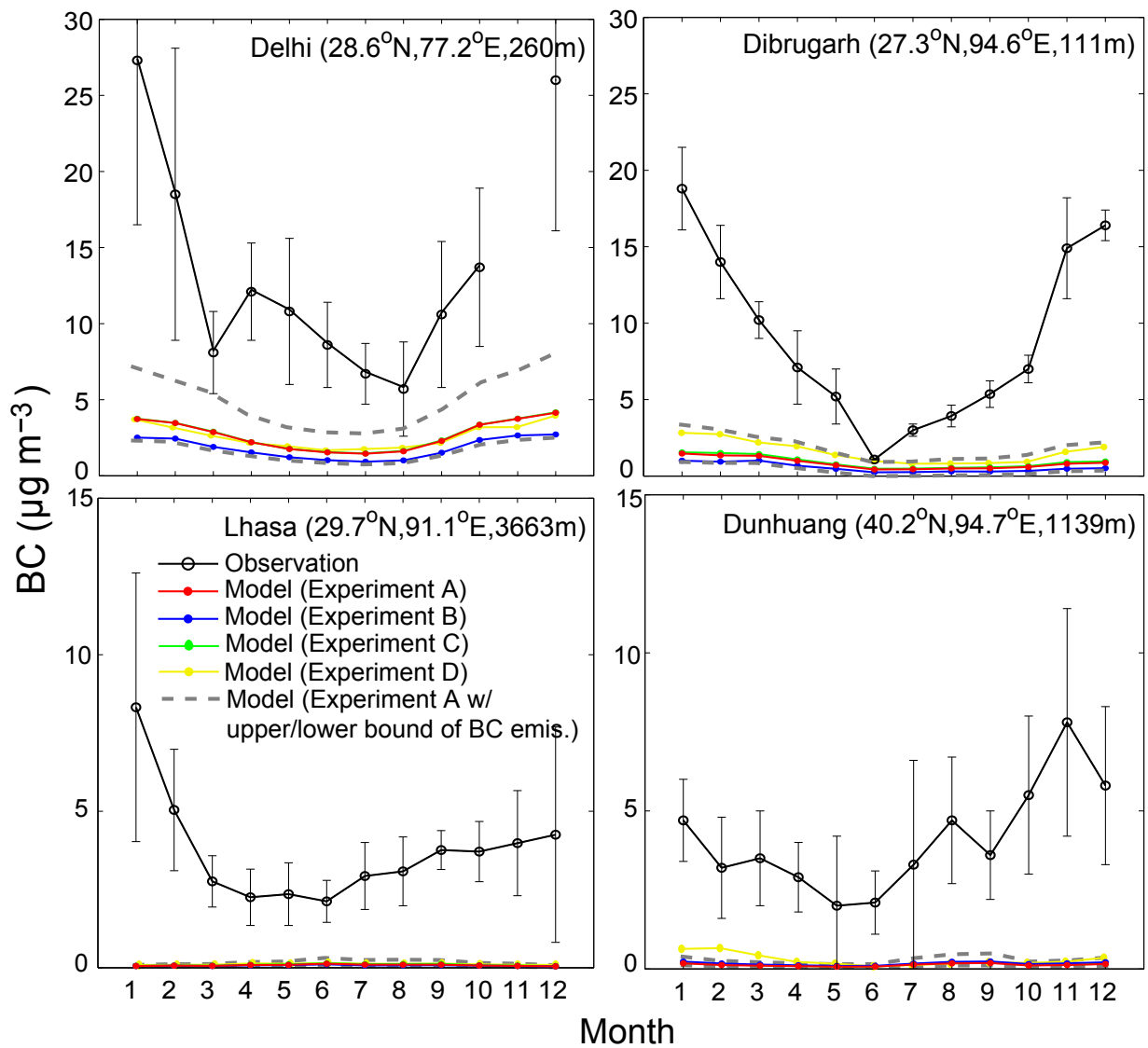
Figure 2.3: Same as Figure 2.2, but for four urban sites (see Table 2.1 and Figure 2.1).
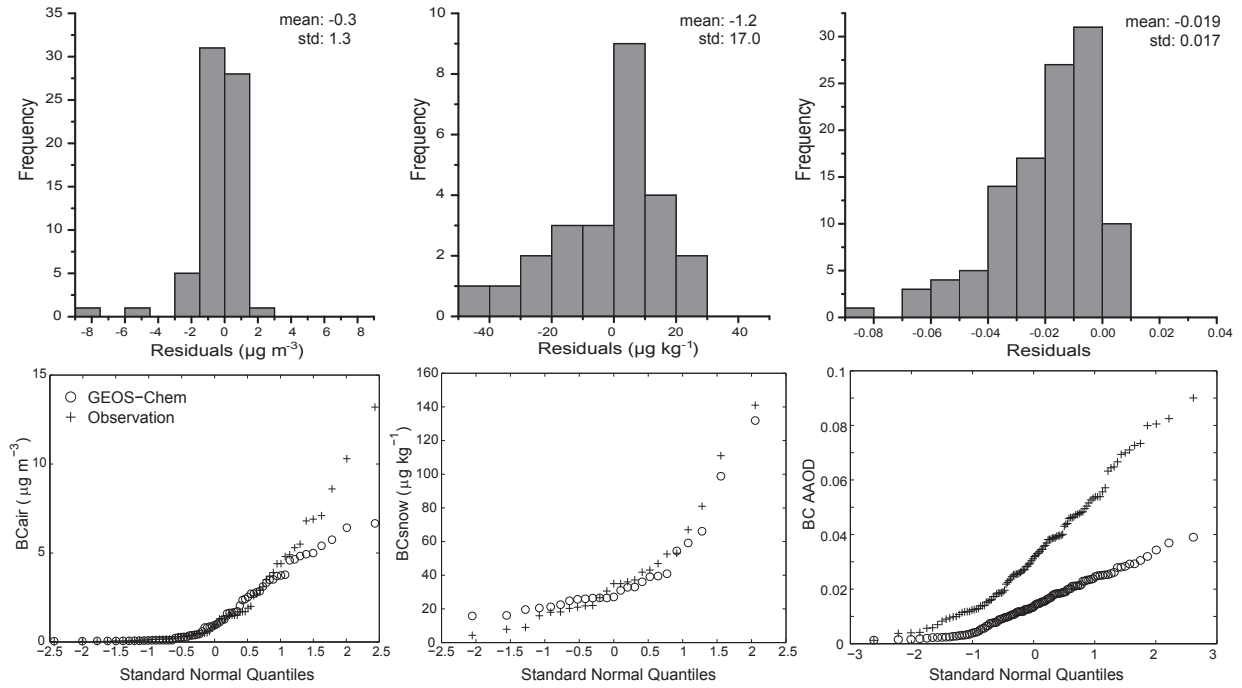
Figure 2.4: Frequency histogram of residual errors (model - observation) (top row) and cumulative probability distributions (bottom row) for surface BC (left column), BC in snow (middle column), and BC AAOD (right column) at sites in and around the Tibetan Plateau (see Tables 2.1 – 2.3 and Fig. 2.1). Also shown are the mean and standard deviation of residual errors. Values are for 2006 unless stated otherwise. See text for details.
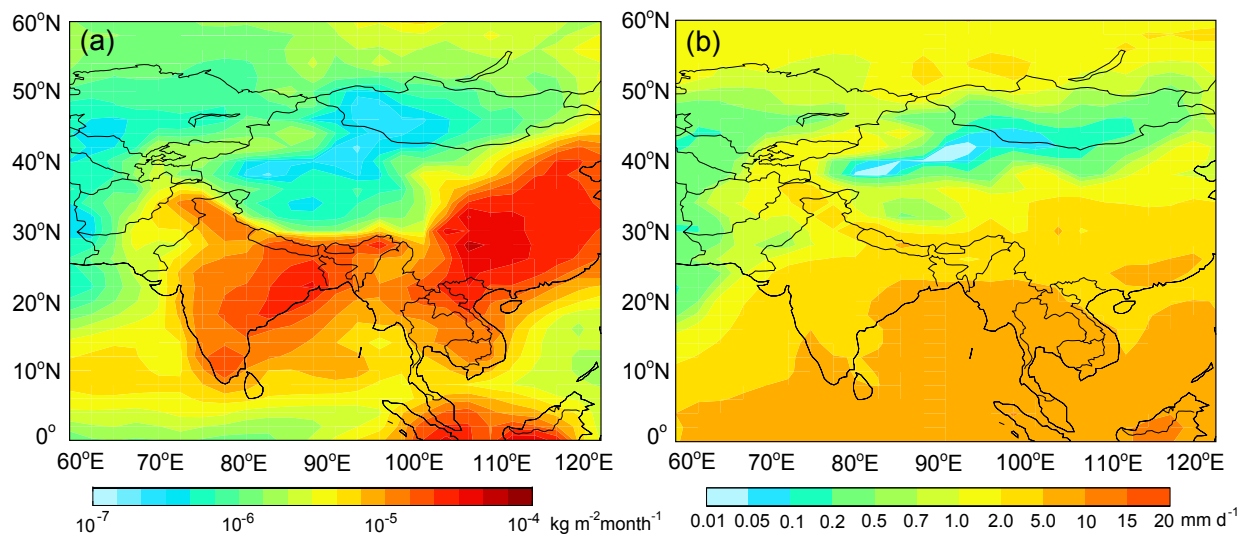
Figure 2.5: (a) GEOS-Chem simulated annual mean total BC deposition (kg m^{-2} month^{-1}) over Asia and (b) GEOS-5 annual mean total precipitation (mm day^{-1}) over Asia. Values are for 2006.
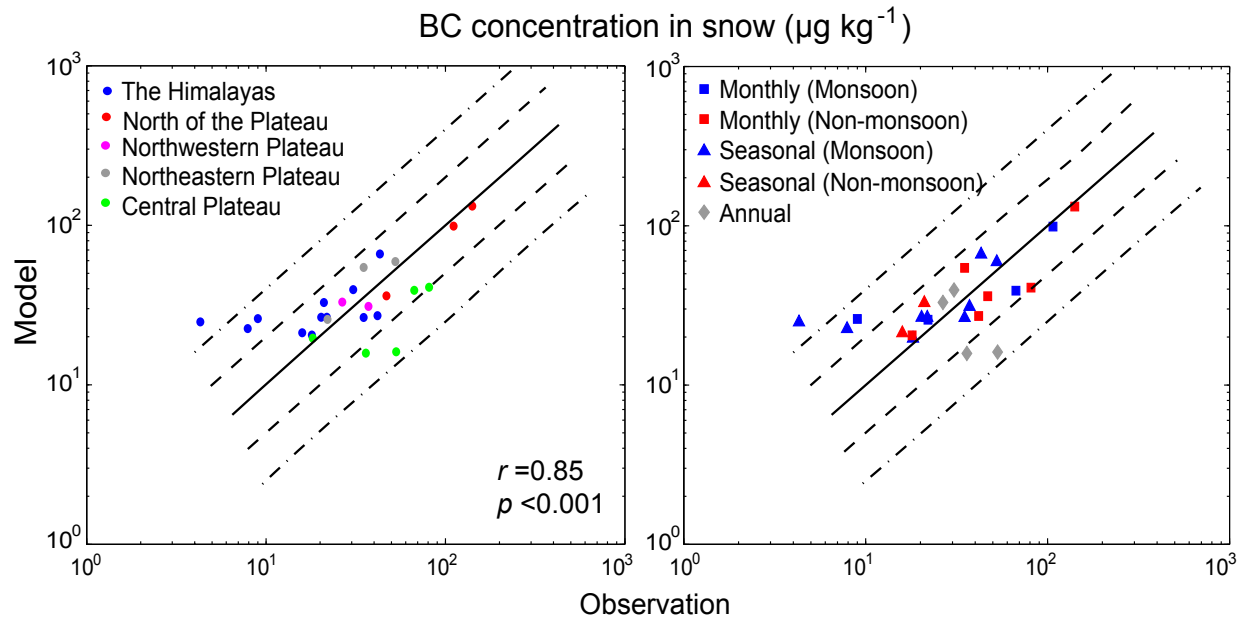
Figure 2.6: Observed and GEOS-Chem simulated monthly or seasonal mean BC concentration in snow (μg kg^{-1}) at sites over the Tibetan Plateau (see Table 2.2 and Fig. 2.1). Left panel: sub-regions of the Tibetan Plateau are color-coded. Right panel: different temporal resolutions are symbol-coded: monthly - square; seasonal - triangle; annual - diamond, with blue for monsoon season and red for non-monsoon season. Solid lines are 1:1 ratio lines; dashed lines are 1:2 (or 2:1) ratio lines; dashed-dotted lines are 1:4 (or 4:1) ratio lines. Also shown are the correlation coefficient (r) and p-value. Values are for 2006 unless stated otherwise. See text for details.
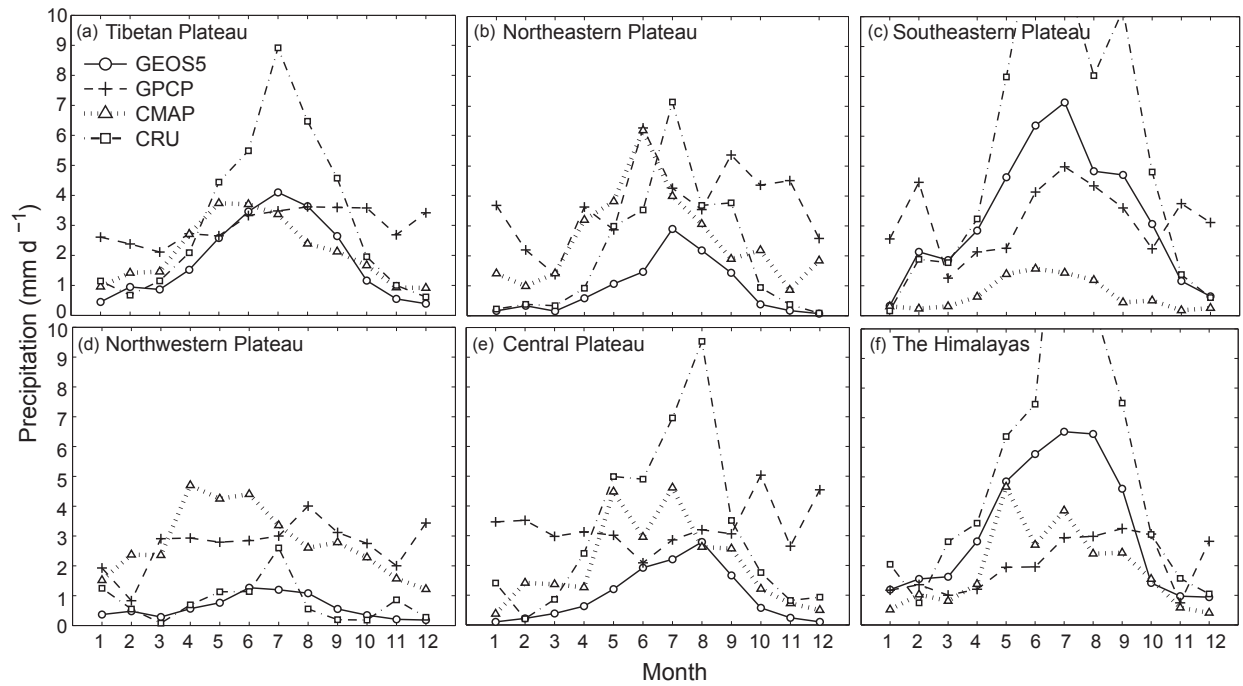
Figure 2.7: Monthly mean precipitation (mm d^{-1}) in 2006, averaged over different parts of the Tibetan Plateau (see Fig. 2.1). Data is from the Goddard Earth Observing System Model version 5 data assimilation system (GEOS-5 DAS), Global Precipitation Climatology Project (GPCP), NOAA Climate Prediction Center (CPC) Merged Analysis of Precipitation (CMAP), and Climate Research Unit (CRU) of University of East Anglia.

43
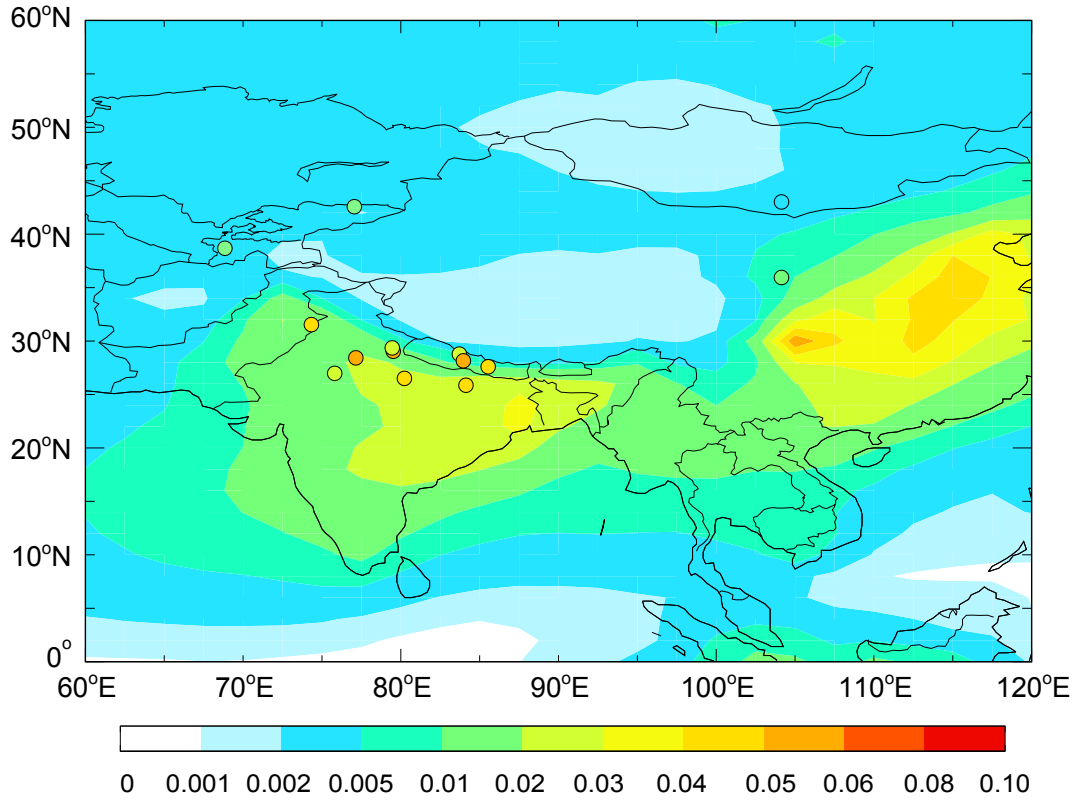
Figure 2.8: GEOS-Chem simulated annual mean BC AAOD (color contours) for 2006. Colored circles are values retrieved from AERONET observations (see Table 2.3).
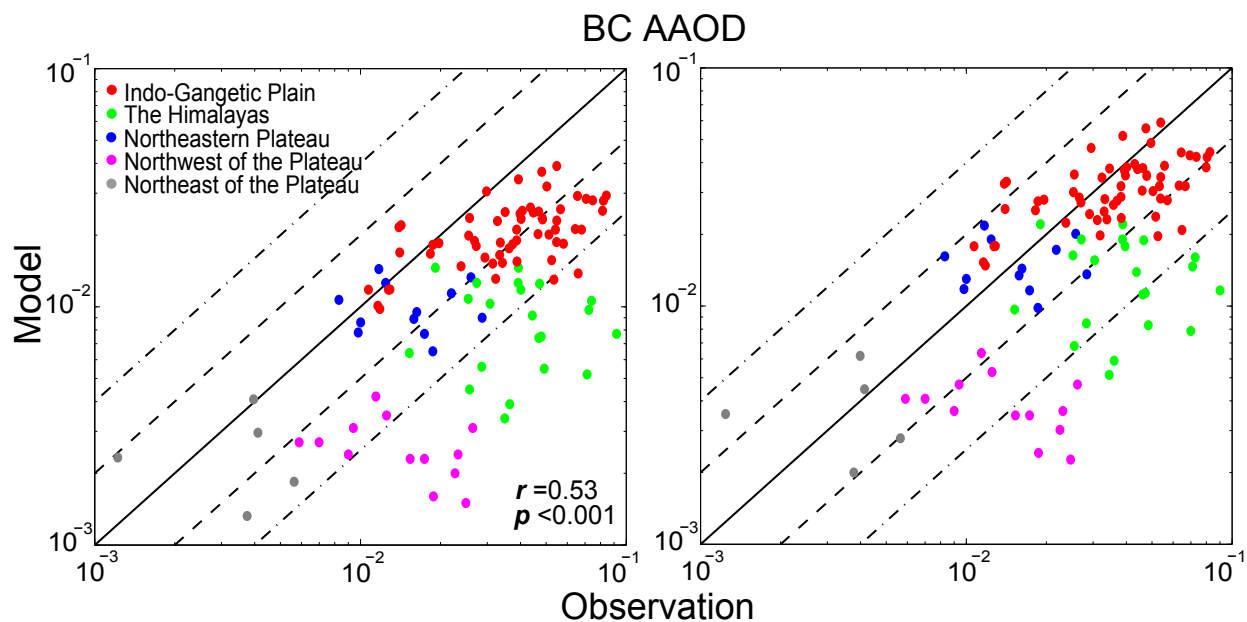
Figure 2.9: Observed and GEOS-Chem simulated monthly mean BC AAOD at AERONET sites over the Tibetan Plateau (see Table 2.3 and Fig. 2.1). Left panel: assuming external mixing of BC. Right panel: assuming a 50% increase of BC absorption associated with internal mixing. Regions are color-coded: Indo-Gangetic Plain (red), the Himalayas (green), the northeastern Plateau (blue), Northeast of the Plateau (grey), Northwest of the Plateau (magenta). Solid lines are 1:1 ratio lines; dashed lines are 1:2 (or 2:1) ratio lines; dashed-dotted lines are 1:4 (or 4:1) ratio lines. Also shown are the correlation coefficient (r) and p-value. Values are for 2006 unless stated otherwise. See text for details.
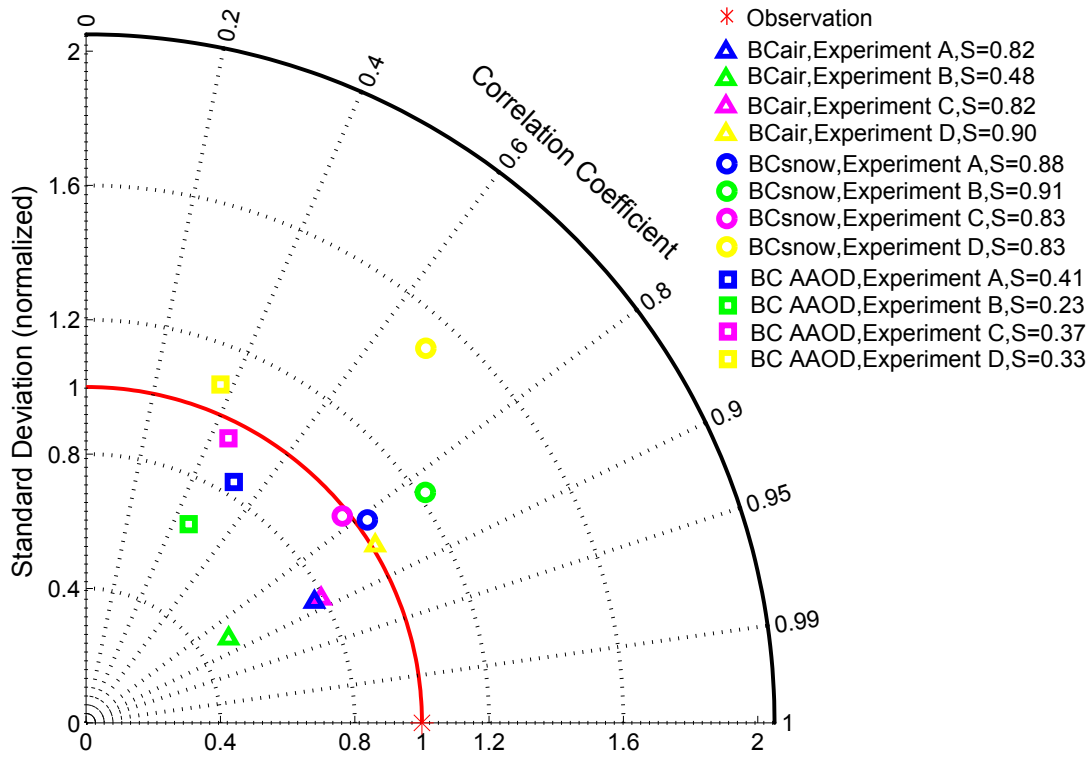
Figure 2.10: Taylor diagram of GEOS-Chem simulated versus observed BC concentration in surface air (BC_{air}) and in snow (BC_{snow}), and BC AAOD at sites over the Tibetan Plateau (see Tables 2.1 – 2.3 and Fig. 2.1). Red asterisk is the observation. Triangles, circles and squares, respectively, indicate modeled BC_{air}, BC_{snow}, and BC AAOD from Experiments A (blue), B (green), C (magenta) and D (yellow). See Table 2.5 and text for more details on the model experiments. Also shown are the Taylor scores (S). Values are for 2006 unless stated otherwise. See text for details.

CHAPTER 3

Variation of the radiative properties during black carbon aging: theoretical and experimental intercomparison

Abstract

A theoretical black carbon (BC) aging model is developed to account for three typical evolution stages, namely, freshly emitted aggregates, coated BC by soluble material, and BC particles undergoing further hygroscopic growth. The geometric-optics surface-wave (GOS) approach is employed to compute the BC single-scattering properties at each aging stage, which are subsequently compared with laboratory measurements. Theoretical calculations are consistent with measurements in extinction and absorption cross sections for fresh BC aggregates with different BC sizes (i.e., mobility diameters of 155, 245, and 320 nm), with differences of ≤25%. The measured optical cross sections for coated BC by sulfuric acid

and for those undergoing further hygroscopic growth are generally captured (differences <30%) by theoretical calculations using a concentric core-shell structure, with overestimates in extinction and absorption for the smallest BC size and underestimates in scattering for the largest BC size. We find that the absorption and scattering cross sections of fresh BC aggregates vary by 20–40% and 50–65%, respectively, due to the use of upper $(1.95 – 0.79i)$ and lower $(1.75 – 0.63i)$ bounds of BC refractive index, while the variations are <20% in absorption and <50% in scattering in the case of coated BC particles. Sensitivity analyses on the BC morphology show that the optical properties of fresh BC aggregates are more sensitive to fractal dimension than primary spherule size. The absorption and scattering cross sections of coated BC particles vary by more than a factor of two due to different coating structures. We find an increase of 20–250% in absorption and a factor of 3–15 in scattering during aging, significantly depending on coating morphology and aging stages. This study suggests that an accurate estimate of BC radiative effects requires the incorporation of a dynamic BC aging process that accounts for realistic coating structures in climate models.

3.1   Introduction

Black carbon (BC) has been identified as the second most important anthropogenic global warming agent in the atmosphere by virtue of its strong absorption of solar radiation and its role as cloud condensation nuclei (CCN) in cloud formation (*Ramanathan and Carmichael*, 2008; *Bond et al.*, 2013; *Wang et al.*, 2013; *Jacobson*, 2014). The BC climatic effects are significantly influenced by BC aging process in the atmosphere, which transforms BC from an external to internal mixing state (*Schwarz et al.*, 2008; *China et al.*, 2013) and increases its hygroscopicity (*Zhang et al.*, 2008a; *Popovicheva et al.*, 2010) and light absorption (*Jacobson*, 2001; *Shiraiwa et al.*, 2010; *Qiu et al.*, 2012; *Scarnato et al.*, 2013).

Freshly emitted BC particles are mostly hydrophobic and externally mixed with other aerosol constituents (*Zuberi et al.*, 2005; *Zhang et al.*, 2008a). BC agglomerates shortly after

emission to form irregular aggregates because of multi-phase processes (*Zhang et al.*, 2008a; *Pagels et al.*, 2009; *Xue et al.*, 2009). Early studies have found that BC particles age in the atmosphere through condensation and coagulation processes (e.g., *Heintzenberg and Covert*, 1984; *Heintzenberg*, 1989). Recent studies confirmed that BC becomes coated by water-soluble material during atmospheric aging, including condensation of sulfate, nitrate, and organics (*Moteki et al.*, 2007; *Shiraiwa et al.*, 2007), coagulation with preexisting aerosols (*Johnson et al.*, 2005; *Kondo et al.*, 2011), and heterogeneous reactions with gaseous oxidants (*Zuberi et al.*, 2005; *Khalizov et al.*, 2010; *Zhang et al.*, 2011). At the same time, BC aggregates also exhibit considerable restructuring and compaction (*Weingartner et al.*, 1997; *Saathoff et al.*, 2003; *Zhang et al.*, 2008a), which significantly alters BC morphology (*Adachi and Buseck*, 2013; *China et al.*, 2015). Aged BC particles experience hygroscopic growth and activate efficiently as CCN (*Zuberi et al.*, 2005; *Zhang et al.*, 2008a). The hygroscopic growth of BC particles depends on its initial size, condensed soluble material mass, surface chemical property, and ambient relative humidity (RH) (*Zhang et al.*, 2008a; *Khalizov et al.*, 2009b; *Popovicheva et al.*, 2010).

A number of laboratory experiments have been conducted to investigate the effects of atmospheric aging on BC radiative properties. *Gangl et al.* (2008) showed that internal BC-wax mixture amplifies BC absorption coefficient by 10–90%, depending on the amount of coating. *Shiraiwa et al.* (2010) found that BC absorption enhancement due to organic coating varies significantly for various BC sizes and coating thickness, with up to a factor of 2 enhancement for thick coatings. Under different experimental conditions, relatively small increases (∼30%) in BC absorption have also been observed for BC coated by sulfuric acid (*Zhang et al.*, 2008a) and some organics (*Saathoff et al.*, 2003). Furthermore, *Xue et al.* (2009) and *Qiu et al.* (2012) showed a less than 20% increase in BC absorption for organic coating, which depends on organic species and coating thickness. Thus, the resulting large variation among different experimental studies indicates that the aging effects on BC radiative properties strongly depend on coating material and thickness as well as BC particle size.

It is clear, therefore, that experimental details are critically important in making meaningful and appropriate comparisons among various experimental studies involving BC absorption enhancement associated with coating. Field measurements have also revealed substantial variation in BC optical properties during atmospheric aging. *Bond and Bergstrom* (2006) showed that observed BC mass absorption cross sections (MAC) vary by more than a factor of two (mostly 5–13 m^2 g^{-1}) under different atmospheric conditions. Based on direct measurements at a suburban site in Japan, *Naoe et al.* (2009) showed that coating increases BC absorption by a factor of 1.1–1.4 with a larger increase for thicker coatings. *Knox et al.* (2009) found an absorption enhancement of up to 45% due to BC coating based on measurements in downtown Toronto. Similar increases in absorption have also been directly observed for the internal mixing of biomass-burning BC (*Lack et al.*, 2012). However, *Cappa et al.* (2012) reported that the observed BC absorption increased only by 6% due to internal mixing based on direct in situ measurements over California. This suggests that coating effects on BC absorption are rather complex in reality, which depends on different coating material, mass, and structure influenced by emission sources and atmospheric processes.

Adachi et al. (2010) found that many BC particles embedded within host material are chainlike aggregates locating in off-center positions, based on transmission electron microscope (TEM) observations for samples collected from Mexico City. Using the discrete dipole approximation (DDA) method developed by *Draine and Flatau* (1994), *Adachi et al.* (2010) showed that a more realistic BC coating morphology results in 20–40% less absorption at visible wavelengths than a concentric core-shell shape. Based on ground-based measurements during the California Research at the Nexus of Air Quality and Climate Change (CalNex) campaign, *Adachi and Buseck* (2013) further observed that many BC particles are only attached to host material instead of fully embedded within them, leading to only a slight increase in BC absorption. They concluded that the complex mixing structure of BC particles could explain a smaller absorption amplification by BC coating determined from observations than the results computed from an idealized core-shell model. *China et al.*

(2013, 2015) classified the observed irregular BC coating shapes into four types: embedded (heavily coated), thinly coated, partly coated, and partially encapsulated. These complex coating structures substantially affect BC optical properties (e.g., *Videen et al.*, 1994; *Liu and Mishchenko*, 2007; *Kahnert et al.*, 2013), which is one of the most important uncertainty sources in evaluating BC direct radiative forcing (DRF) (*Bond et al.*, 2013). Thus, a reliable estimate of BC DRF requires a quantitative understanding of the evolution of BC radiative properties under the influence of various morphology during atmospheric aging.

In this study, we have developed a theoretical BC aging model based on the current understanding of BC aging process, which accounts for three major stages, namely, freshly emitted aggregates, coated BC by soluble material, and BC particles undergoing further hygroscopic growth. We apply the geometric-optics surface-wave (GOS) approach to compute light absorption and scattering of BC particles at each aging stage. The theoretical calculations are compared with laboratory measurements, followed by a systematic evaluation of uncertainties associated with BC morphology and refractive index. Finally, we discuss the implication of model results for BC radiative effect assessment.

3.2 Methods

3.2.1 A theoretical BC aging model

Based on the current knowledge of BC atmospheric aging, we have developed a theoretical model accounting for three major BC aging stages, as depicted in Fig. 3.1. Stage I represents freshly emitted BC aggregates that are externally mixed with other particles. Stage II represents BC particles coated by water-soluble aerosol constituents through condensation, coagulation, and/or heterogeneous oxidations. Stage III represents BC particles coated by both soluble material and water through hygroscopic growth. In this study, six typical BC coating structures (Fig. 3.1) have been considered for Stages II and III to approximately represent observations in the real atmosphere or laboratory, including embedded

51

(i.e., concentric core-cell, off-center core-shell, and closed-cell), partially encapsulated, and partly coated (i.e., open-cell and externally attached) structures following the classification presented in *China et al.* (2013, 2015). The concentric and off-center core-shell structures (*Martins et al.*, 1998; *Sedlacek et al.*, 2012) are a result of considerable collapse of BC aggregates into more compact and spherical clusters when fully engulfed in coating material (*Zhang et al.*, 2008a). The closed-cell structure is an example where coating material not only covers the outer layers of BC aggregates but also fills the internal voids among primary spherules (*Strawa et al.*, 1999). The partially encapsulated structure is formed when only a part of BC aggregate merges inside coating material (*China et al.*, 2015). The open-cell and externally attached structures are produced by coating material sticking to a part of BC aggregates' surface (*Stratmann et al.*, 2010; *China et al.*, 2015). We wish to note that the six coating structures used in this study, including closed-cell and open-cell structures, are theoretical models and as such, they may not completely capture detailed BC coating structures from aircraft and ground-based observations. Further hygroscopic growth of BC particles after Stage III could lead to the formation of cloud droplets, a subject beyond the scope of the present study.

3.2.2 Laboratory measurements

The physical and radiative properties of BC particles during aging after exposure to sulfuric acid (H_2SO_4) under various RH conditions (5–80%) have been measured in the laboratory by *Zhang et al.* (2008a) and *Khalizov et al.* (2009a). BC aggregates were generated by incomplete combustion of propane in a laminar diffusion burner (*Santoro et al.*, 1983) and sampled by a pinhole diluter (*Kasper et al.*, 1997). A tandem differential mobility analyzer (TDMA) system was used to produce singly-charged mobility-classified BC particles, followed by a coating chamber with controlled RH and H2SO4 vapor concentrations at room temperatures (299±1 K). The BC mass and size growth due to H_2SO_4 and water vapor (H_2O) condensation during aging were measured by an aerosol particle mass (APM) analyzer and

TDMA, respectively. The effective density and fractal dimension (D_f) of BC particles were derived from the measured BC mobility diameter (D_{BC}) and mass (see Eqs. 1 and 2 in *Zhang et al.* (2008a)). The compaction and restructuring of BC aggregates were captured by a TEM (see Fig. 1 in *Zhang et al.* (2008a)). BC extinction and scattering cross sections were measured at 532-nm wavelength by a cavity ring-down spectrometer (CRDS) and an integrating nephelometer, respectively. The absorption cross section was determined from the resulting difference between extinction and scattering cross sections. *Khalizov et al.* (2009a) showed that uncertainty in measured optical cross sections of coated BC particles is within 10%, which primarily represents uncertainty in relative humidity, particle size, number density, and instrument calibration. This uncertainty, however, does not include the contribution from multiply charged particles. For freshly emitted BC aggregates, measured scattering cross sections involve relatively large uncertainties. More details in laboratory experiments have been presented in *Zhang et al.* (2008a) and *Khalizov et al.* (2009a). Three experimental cases with initial D_{BC} of 155, 245, and 320 nm were used in this study (see Table 3.1). In each case, BC particles exposed to H_2SO_4 vapor (1.4×10^{10} molecules cm^{-3}) at 5% and 80% RH were used to represent coated BC at Stages II and III (see Sect. 3.2.1), respectively.

3.2.3 Geometric-optics surface-wave (GOS) approach

We employed the GOS approach developed by *Liou et al.* (2011, 2014), which explicitly treats fractal aggregates and various coating structures, to compute absorption and scattering properties of BC particles at three aging stages. In the GOS approach, a stochastic procedure developed by *Liou et al.* (2011) is applied to simulate homogeneous aggregates and coated particles with different shapes in a 3-D coordinate system. In this study, we have extended the original stochastic process to generate more complex coating morphology, including the partially encapsulated and externally attached structures. Once the particle shape and composition are determined by the stochastic procedure, the reflection and refraction of particles are computed with the hit-and-miss Monte Carlo photon tracing technique.

The extinction and absorption cross sections are derived following a ray-by-ray integration approach (*Yang and Liou*, 1997). Diffraction by randomly oriented nonspherical particles is computed on the basis of Babinet's principle (*Born and Wolf*, 1980) and photon-number weighted geometric cross sections. The GOS approach accounts for the interaction of incident waves at grazing angles near the particle edge and propagating along the particle surface into shadow regions, referred to as the surface wave, using the formulation developed by *Nussenzveig and Wiscombe* (1980) for spheres as the basis for physical adjustments and application to nonspherical particles (*Liou et al.*, 2010, 2011). The concept of the GOS approach is graphically displayed in Fig. 3.2 and it is designed for computations of absorption and extinction cross sections and asymmetry factors in line with experimental results.

Liou et al. (2010, 2011) and *Takano et al.* (2013) demonstrated that the single-scattering properties of aerosols with different sizes and shapes determined from the GOS approach compare reasonably well (differences <20%) with those determined from the Finite Difference Time Domain (FDTD) method (*Yang and Liou*, 1996) and DDA (*Draine and Flatau*, 1994) for column and plate ice crystals, the superposition T-matrix method (*Mackowski and Mishchenko*, 1996) for fractal aggregates, and the Lorenz-Mie model (*Toon and Ackerman*, 1981) for a concentric core-shell shape. Moreover, compared with other numerical methods, the GOS approach can be applied to a wider range of particle sizes, shapes, and coating morphology with a high computational efficiency, including very large particles (e.g., ~100–1000 μm snowflakes) and complex multiple inclusions of aerosols within irregular snow grains (*Liou et al.*, 2014; *He et al.*, 2014a), in which the FDTD, DDA, and T-matrix methods have not been able to apply. As stated previously, the GOS approach has been developed specifically for optical cross sections (i.e., extinction, absorption, and scattering) and the asymmetry factor. Also, due to the approximation in the use of geometric photon tracing, the GOS approach has limitation and uncertainty for application to size parameters much smaller than 1.0. To supplement GOS, we have developed the Rayleigh-Gan-Debye (RGD) approximation coupled with GOS for very small particles, which has been cross-validated

with the superposition T-matrix method (*Takano et al.*, 2013). *Takano et al.* (2013) showed that the coupled GOS-RGD and superposition T-matrix results are both close to the observed specific absorption of BC aggregates for the range of size parameter considered in the present study. The coupled GOS-RGD approach can be applied to size parameters covering 0.1 to 1000. In the present study, the coupled GOS-RGD approach is used for fresh BC aggregates (Stage I), while the GOS approach without RGD coupling is used for coated BC particles (Stages II and III).

3.2.4 Theoretical calculations

We used BC physical properties measured from laboratory experiments (see Sect. 3.2.2) as input to theoretical calculations (see Table 3.1). In standard calculations, the freshly emitted BC aggregates (Stage I) were assumed to be comprised of primary spherules with a diameter of 15 nm (D_p) measured from the experiments and were constructed by the GOS stochastic procedure to reproduce the measured mass and fractal dimension (= 2.1) of BC aggregates. The BC mass was the product of measured BC effective densities and mobility volumes. The mass of H_2SO_4 coating on BC at Stage II was derived from the observed relationship between condensed H_2SO_4 mass and particle diameter at 5% RH. The mass of H_2O condensed on H_2SO_4-coated BC at Stage III was derived from the measured hygroscopic mass growth ratio of H_2SO_4-coated BC at 80% RH. In standard calculations, we used a concentric core-shell structure for coated BC particles at Stages II and III, because of the strong particle compaction during aging based on laboratory observations (*Zhang et al.*, 2008a). Thus, BC core size and coating thickness were computed from the mass of BC and H_2SO_4/H_2O coating. The refractive index (RI) of H_2SO_4-H_2O coating at Stage III was derived as the volume-weighted RI of H_2SO_4 and H_2O. We used a BC RI of $1.95 - 0.79i$ (upper bound) recommended by *Bond and Bergstrom* (2006) and a BC density of 1.77 g cm^{-3} suggested by *Zhang et al.* (2008a). Under the preceding conditions, computations of BC optical properties at 532-nm wavelength were carried out for comparison with laboratory measurements. The

comparison between GOS and experimental results in this study provides an additional dimension of validation/cross-check of the GOS approach.

In addition, we conducted four sensitivity calculations for Stage I and six sensitivity calculations for Stages II and III to quantify uncertainties associated with BC RI and morphology (see Table 3.1). In the first sensitivity calculation for each aging stage, a lower bound of BC RI of $1.75 - 0.63i$ recommended by *Bond and Bergstrom* (2006) was used. For other three sensitivity tests on morphology effects at Stage I, we increased BC fractal dimension from 2.1 to 2.5 and primary spherules diameter from 15 to 20 nm without changing BC mass, and replaced BC aggregates with a single volume-equivalent sphere, respectively. We then applied five types of BC coating structures, including off-center core-shell, closed-cell, open-cell, partially encapsulated, and externally attached structures (see Fig. 3.1 and Sect. 3.2.1), and conducted five additional sensitivity calculations for both Stages II and III. Specifically, the off-center core-shell structure assumes a spherical BC core internally tangent to the particle surface with the same size as the concentric core-shell structure used in standard calculations. The closed-cell structure assumes that all primary spherules have the same concentric core-shell shape with a BC core diameter of 15 nm. The open-cell structure also assumes a diameter of 15 nm for all primary spherules, which are either pure BC or pure coating material. Both closed- and open-cell structures were constructed to have the same fractal dimension as measured in the experiments. The partially encapsulated structure assumes that a random part of BC aggregates is inside a spherical coating particle, while the externally attached structure assumes that a single spherical coating particle is randomly sticking to a part of BC aggregate's surface. BC primary spherules in both structures have diameters of 15 nm. We note that assuming a cluster of spheres for the above-mentioned coating structures may not be sufficiently realistic and that nonspherical morphology models without restrictions to composite of spheres appear to be more plausible (*Adachi et al.*, 2010), a challenging subject to be investigated in future work.

3.3 Results and discussions

3.3.1 Fresh BC aggregates (Stage I)

Figure 3.3 shows the extinction, absorption, and scattering cross sections (at 532 nm) of fresh BC aggregates at Stage I based on laboratory measurements and theoretical calculations using different BC RI and morphology. For comparison with experimental measurements, theoretical results with BC RI of $1.95 - 0.79i$ (i.e., standard calculations) are used unless stated otherwise. The calculated extinction cross sections are consistent (differences $\leq 20\%$) with measurements for fresh BC aggregates at Stage I with different sizes (i.e., $D_{BC} = 155$, 245, and 320 nm). However, theoretical calculations tend to overestimate and underestimate extinction for the smallest and largest BC aggregates, respectively. The discrepancies between theoretical and measured BC absorption cross sections at Stage I increase from 7% (overestimate) to -15% (underestimate) as BC size becomes larger (Fig. 3.3). Although the calculated scattering cross sections at Stage I are consistently overestimated for different BC sizes compared with measurements, the absolute discrepancies are small. This overestimate is partly because of the uncertainty associated with extinction and absorption calculations for small particles, where theoretical results overestimate (underestimate) extinction cross sections more (less) than absorption cross sections for D_{BC} of 155 nm (D_{BC} of 245 and 320 nm). The scattering measurements also contribute to the discrepancy in view of the fact that the integrating nephelometer misses light scattering signals at near-forward directions (*Anderson and Ogren*, 1998). We note that the calculated SSA (~ 0.16) of BC aggregates at Stage I is within the range of 0.15–0.3 measured for BC from different combustion sources (*Bond and Bergstrom*, 2006), while the experimentally measured SSA is smaller than 0.10 due to the relatively open and loosely connected BC aggregate structures (*Khalizov et al.*, 2009a).

Sensitivity calculations show that using a BC RI of $1.75 - 0.63i$ narrows the gap between calculated and measured scattering cross sections of fresh BC aggregates by up to a factor of

two (Fig. 3.3). Because of using the BC RIs of $1.95 - 0.79i$ (upper bound) and $1.75 - 0.63i$ (lower bound), the extinction and absorption cross sections of fresh BC aggregates can vary by 25–40% and 20–30%, respectively, while the scattering cross section ranges from 50% to 65% with a higher sensitivity for larger BC sizes. Based on the T-matrix calculations using BC RI of $2 - 1i$ and $1.75 - 0.5i$, *Liu et al.* (2008) showed variation of 50–70% in BC absorption and scattering cross sections depending on aggregate structures, which is comparable to the results derived in this study. *Scarnato et al.* (2015) also found a strong dependence of BC absorption on BC RI for uncoated aggregates using the DDA method.

Figure 3.4 shows the extinction, absorption, and scattering cross sections for different aggregate morphology normalized by BC aggregate cross sections determined from standard calculations (i.e., fractal aggregates with a D_f of 2.1 and D_p of 15 nm; see Sect. 2.4) at Stage I. We found that a 20% increase in D_f (i.e., more compact structure) decreases BC absorption and scattering cross sections by 20–50%, with greater reductions for larger BC sizes. Using the DDA method, *Scarnato et al.* (2013) also found a smaller BC absorption for more compact structures. *Liu et al.* (2008) applied a T-matrix calculation to show that as D_f increases from 1.5 to 3, the absorption of BC aggregates either decreases monotonically or decreases until D_f reaching a certain value and then increases, depending on BC RI, size and the number of primary spherules. This is because the amount of BC directly exposed to the incident light becomes smaller as D_f increases, while the growing interaction among primary spherules could increase light absorption (*Liu et al.*, 2008). The present calculations illustrated that BC absorption and scattering are weakly dependent on the size of primary BC spherules. An increase in the spherule diameter from 15 to 20 nm results in less than 10% variation in BC extinction, absorption, and scattering cross sections (Fig. 3.4), which is consistent with the T-matrix results presented by *Liu and Mishchenko* (2007) who concluded that the monomer size has a rather weak effect on BC scattering and absorption, if fractal dimension is fixed. Nevertheless, the effect of monomer size on BC optical properties could vary significantly depending on BC aggregate shape, size, the number of primary

spherules, and BC RI (*Liu et al.*, 2008; *Kahnert et al.*, 2014). Assuming a volume-equivalent BC sphere instead of fractal aggregates results in 5–25% weaker absorption and extinction and up to 65% smaller scattering cross sections for different BC sizes, compared with BC aggregates in standard calculations. The stronger absorption and scattering from aggregate structures is due primarily to the interaction between neighboring primary spherules of BC aggregates (*Fuller*, 1995). The present calculated increase (5–20%) in absorption from sphere to aggregate structures is slightly smaller than the value (∼30%) reported by *Bond and Bergstrom* (2006), because of different numbers and sizes of primary spherules, aggregate shapes, and fractal dimensions employed in calculations (*Iskander et al.*, 1991; *Liu et al.*, 2008; *Kahnert et al.*, 2014). Using the T-matrix method, *Kahnert and Devasthale* (2011) showed a two times higher radiative forcing of BC aggregates than the volume-equivalent sphere counterparts.

3.3.2 Coated BC particles (Stages II and III)

The extinction, absorption, and scattering cross sections (at 532 nm) of coated BC particles at aging Stages II and III determined from laboratory measurements and theoretical calculations are depicted in Fig. 3.3. Theoretical results with the BC RI of $1.95 - 0.79i$ are used for comparison with experimental measurements unless stated otherwise. The calculated optical cross sections (i.e., extinction, absorption, and scattering) of coated BC at Stages II and III are in general agreements (differences ≤30%) with laboratory measurements, because of the observed efficient structure compaction during aging in laboratory experiments (*Zhang et al.*, 2008a). However, theoretical calculations tend to overestimate extinction and absorption for D_{BC} of 155 and 245 nm at both Stages II and III, while the extinction and absorption for the largest particle (D_{BC} of 320 nm) is underestimated at Stage II. The calculated scattering cross sections are overestimated for the smallest BC size (D_{BC} of 155 nm) at Stage II, but tend to be underestimated for larger BC sizes at Stage III, particularly for D_{BC} of 320 nm. The present sensitivity calculations show that the discrepancy in scattering for D_{BC} of

320 nm at Stage III cannot be explained by uncertainties associated with BC RI or coating morphology (Fig. 3.3), which, however, could be attributed to uncertainty associated with the coating mass of H_2SO_4 and H_2O. We assumed only H_2O condensation during BC hygroscopic growth from Stage II to III in the calculation of coating mass, which may not be accurate considering that H_2SO_4 condenses on BC surface simultaneously along with H_2O. A sensitivity calculation shows that replacing H_2O by H_2SO_4 in the coating material reduces scattering discrepancy to 10% for D_{BC} of 320 nm at Stage III, since H_2SO_4 is more reflective than H_2O, but increases overestimate in BC absorption from 17% to 25%.

Theoretical calculations show that using BC RI of $1.75 - 0.63i$ decreases extinction and absorption cross sections of coated BC particles by 10–17% at Stage II and by 5–15% at Stage III for different BC sizes, which, however, is smaller compared with the decrease for fresh BC aggregates (20–40%). The scattering cross sections of coated BC particles decrease by up to 50% due to the use of smaller BC RI for different BC sizes and aging stages.

Figures 3.5 and 3.6 show the extinction, absorption, and scattering cross sections for different coated BC structures normalized by cross sections of the concentric core-shell structure determined from standard calculations. The off-center core-shell structure has little impacts on BC optical properties at Stage II (Fig. 3.5) with differences of less than 10% compared with the concentric core-shell structure, primarily because of the thin coating layer. As the coating thickness increases after hygroscopic growth, the off-center core-shell structure results in a 5–30% decrease in extinction, absorption, and scattering cross sections at Stage III (Fig. 3.6). This finding is consistent with the result presented by *Adachi et al.* (2010) using the DDA method, where they found up to 30% reductions in BC absorption depending on the position of BC core inside coating material. A recent T-matrix study (*Mishchenko et al.*, 2014) also showed that the absorption of BC-water mixture tends to decrease as a BC particle moves from the droplet center to the boundary.

Compared with the concentric core-shell structure, the closed-cell structure tends to have stronger absorption and weaker scattering for D_{BC} of 245 and 320 nm at Stages II and III,

while the reverse is true for the open-cell structure (Figs. 3.5 and 3.6). This is in line with the conclusion presented in *Liou et al.* (2011) that closed-cell aggregates have larger absorption and smaller SSA than their open-cell counterparts. The closed-cell structure has a larger surface area for interaction of the incident light with each primary spherule that acts as a coated core-shell unit, leading to a stronger lensing effect and thus stronger absorption compared with the concentric core-shell structure. However, the open-cell structure lacks a closed coating structure to produce efficient lensing effects. The coating spherules sticking to pure BC spherules in the open-cell structure increase the interaction between the incident light and non-absorbing coating material, resulting in a stronger scattering.

The extinction and absorption cross sections of partially encapsulated and externally attached structures are consistently lower than those of the concentric core-shell structure by 30–80% for different BC sizes (Figs. 3.5 and 3.6). This is because the relatively open coating structure leads to inefficient lensing effect for partially encapsulated and externally attached structures, in which a part of BC aggregates is shielded from interaction with incident photons that are backscattered by the attached non-absorbing coating material. *Adachi et al.* (2010) showed that the concentric core-shell structure has a 20–30% stronger absorption than BC aggregates that are fully embedded within host sulfate. Thus, the partially encapsulated structure with only a part of BC aggregates embedded inside coating material in the present study could further decrease the absorption and lead to much smaller absorption values than a concentric core-shell structure. *Kahnert et al.* (2013) found that the difference in BC absorption between concentric core-shell and encapsulated structures strongly depends on particle size, BC volume fraction, and wavelength, based on the DDA calculation. Interestingly, we found that the absorption of partially encapsulated structure is 10–40% weaker than that of externally attached structure with larger differences for thicker coating, while their scattering cross sections are similar (differences ≤5%). The preceding analysis demonstrates that coating structures exert a significant impact on BC optical properties. Thus, in order to produce reliable and accurate estimates of BC radiative forcing in climate

61

models, the development of a realistic BC coating morphology parameterization appears to be essential, which, however, could be a challenging task in view of limited observations available at the present time.

3.3.3 Evolution of BC absorption and scattering

Figure 3.7 shows the enhancement in absorption and scattering during BC aging from freshly emitted aggregates (Stage I) to BC coated by H_2SO_4 (Stage II) and by H_2SO_4-H_2O (Stage III) for different BC coating structures and sizes. The measured BC absorption increases by 10–45% due to coating, while the concentric core-shell model results in a 20–65% absorption increase depending on BC sizes and aging stages. This implies that assuming a concentric core-shell shape could overestimate BC radiative forcing. *Adachi et al.* (2010) found that using a more realistic BC coating morphology from field measurements leads to about 20% less BC DRF than using a concentric core-shell shape.

Moreover, coated BC particles with closed-cell structures enhance absorption by 50–100% for Stage II and more than 100% after hygroscopic growth (Fig. 3.7). In contrast, the open-cell structures produce less than 10% increase in absorption during aging for D_{BC} of 245 and 320 nm, while the enhancement tends to be stronger for smaller BC size (D_{BC} = 155 nm). Surprisingly, we found that the partially encapsulated and externally attached BC structures have a weaker absorption than fresh BC aggregates, probably because that the two structures in the absence of fully embedded shape have no efficient lensing effect and that the non-absorbing coating material blocks the photons coming from behind BC aggregates and produces a shadowing effect (*Liu and Mishchenko*, 2007). This shadowing effect could also explain the decreasing BC absorption for partially encapsulated, externally attached, and open-cell structures when coating material increases during Stages II to III. *Adachi and Buseck* (2013) and *Scarnato et al.* (2013) found that BC particles attached to or partially immersed in host material, instead of fully embedded within them, do not show noticeable increases in BC absorption relative to uncoated aggregates based on DDA

calculations. *Bond et al.* (2006) recommended a 50% increase in BC absorption to account for the averaged coating effect during atmospheric aging. However, in light of the preceding analysis, the morphology, composition and amount of coating play significant roles in altering the BC optical properties during aging. It appears that a fixed enhancement factor may not represent the realistic increase in BC absorption due to complex coating, particularly over regions with highly heterogeneous aging conditions.

Compared with absorption enhancement, BC coating results in a much larger increase in scattering, with a greater enhancement for a larger amount of coating material (Fig. 3.7). The measured scattering cross sections from laboratory experiments for different BC sizes increase by a factor of 5–6 from Stage I to II and a factor of 11–13 from Stage I to III. Theoretical calculations show that the increase in scattering from Stage I to II varies from a factor of 3 to 8 for D_{BC} of 245 and 320 nm depending on coating morphology, while both the magnitude and variation of enhancement are much larger for D_{BC} of 155 nm ranging from a factor of 6 to 15. After hygroscopic growth (Stage III), BC scattering further increases by 20–200% for different coating structures relative to that at Stage II. *Cheng et al.* (2009) observed that the increase in BC scattering, due to both the increased amount of coating and the transition of uncoated to coated BC, can reach up to a factor of 8–10 within several hours' aging at a polluted site in northeastern China, which is comparable to laboratory measurements and theoretical calculations presented above.

3.4 Atmospheric implications

Our theoretical calculations have shown that BC absorption and scattering are highly sensitive to coating morphology and the amount of coating at different aging stages. This suggests that the change of BC coating states (e.g., coating thickness, morphology, and composition) during aging process in the real atmosphere could substantially affect BC radiative properties and thus its climatic effects. *Metcalf et al.* (2012) observed that the mean BC coating

thickness increases from ∼95 nm over urban areas within boundary layers to ∼150 nm in its downwind regions and ∼190 nm in the free troposphere, with a factor of two higher number fractions of thickly coated BC in the free troposphere and downwind regions than near the source. Such large variations in BC coating thickness and number fraction of thickly coated BC during aging have also been observed over the tropics from the ground to high altitudes (*Schwarz et al.*, 2008), implying a strong dependence of BC coating state on aging condition and timescale that BC particles have experienced. Furthermore, atmospheric observations also suggest large variability in the composition of coating materials (*Moteki et al.*, 2007; *Metcalf et al.*, 2012) and coating morphology (*China et al.*, 2013, 2015) during BC aging under different atmospheric conditions. Thus, better characterizations of BC coating mass, composition, and morphology during aging are critically important to accurately estimate BC radiative effects.

However, many global models tend to use fixed BC optical properties or simplified core-shell models for the computation of BC radiative effects (*Bond et al.*, 2013), which may not be representative and sufficiently accurate in view of various BC coating states in the real atmosphere. This study suggests that a reliable estimate of BC radiative effects in climate models would require the representation of a dynamic BC aging process with realistic coating structures, especially for regional analysis with highly heterogeneous atmospheric conditions.

3.5   Conclusions

We developed a theoretical model that accounts for three typical BC aging stages, including freshly emitted aggregates, coated BC by soluble material, and coated BC particles after further hygroscopic growth. The GOS approach was used to compute BC absorption and scattering at each aging stage, which was coupled with a stochastic procedure to construct different BC structures. The theoretical calculations were compared with laboratory measurements, followed by a systematic analysis on uncertainties associated with BC RI and

morphology. Finally, we discussed atmospheric implications of our results in the assessment of BC radiative effects.

Theoretical calculations yielded consistent extinction (sum of absorption and scattering) cross sections for fresh BC aggregates at Stage I, with differences of less than 20% compared with measurements. Theoretical calculations underestimated BC absorption by up to 25%, while overestimated BC scattering for different sizes, because of uncertainties associated with both theoretical calculations for small particles and scattering measurements in laboratory experiments. Sensitivity calculations showed that variation of the extinction and absorption cross sections of fresh BC aggregates is 20–40% due to the use of upper and lower bounds of BC RIs, while variation of the scattering cross section ranges from 50% to 65% with a higher sensitivity for larger BC sizes. We also found that the optical cross sections of BC aggregates are sensitive to D_f, but insensitive to the size of primary spherules. Using volume-equivalent spheres instead of aggregates decreased the BC absorption at Stage I.

The measured extinction, absorption, and scattering cross sections of coated BC were generally captured (differences ≤30%) by theoretical calculations using a concentric core-shell structure for Stages II and III. However, theoretical calculations tend to overestimate extinction and absorption for D_{BC} of 155 and 245 nm at Stages II and III, while the scattering tends to be underestimated for larger BC sizes at Stage III, particularly for D_{BC} of 320 nm due partly to the uncertainty associated with H_2SO_4-H_2O coating mass. Sensitivity analyses showed that the effects of BC RI on extinction and absorption for coated BC were much smaller than that for fresh BC aggregates. The off-center core-shell structure resulted in up to 30% less absorption and scattering cross sections than the concentric core-shell structure. The open-cell structure tended to have weaker absorption and stronger scattering than the concentric core-shell structure, while the reverse is true for the closed-cell structure. Compared with the concentric core-shell structure, the partially encapsulated and externally attached structures had substantially smaller absorption and scattering cross sections due to the lack of efficient lensing effects.

Theoretical calculations showed that using a concentric core-shell structure overestimated the measured enhancement in BC absorption by up to 30% during aging. The closed-cell structure led to a factor of two higher increases in BC absorption than measured values, while the open-cell structure did not show a noticeable increase in absorption for D_{BC} of 245 and 320 nm during aging. The partially encapsulated and externally attached coating structures had a weaker absorption than fresh BC aggregates, likely produced by the shadowing effect from non-absorbing coating material as well as the lack of efficient lensing effect. The increase in BC scattering during aging was much stronger than absorption, ranging from a factor of 3 to 24 depending on BC size, morphology, and aging stage. Thus, the present analysis showed that BC optical properties are highly sensitive to BC morphology and coating mass at different aging stages.

Our theoretical calculations suggested that the evolution of BC coating states (e.g., coating thickness, morphology, and composition) during aging in the real atmosphere could exert significant impacts on BC radiative properties and thus its climatic effects, particularly over regions with high heterogeneity. Therefore, to accurately estimate BC radiative effects requires the incorporation of a dynamic BC aging process accounting for realistic coating structures in climate models.

3.6 Tables and figures

Table 3.1: BC physical properties used in theoretical calculations[a]

Aging Stage[b]	Pure BC		Coating material		Standard calculation	Sensitivity calculation
	Mobility diameter (nm)	Mass $(10^{-16}g)$	Species	Mass $(10^{-16}g)$		
I	155	5.13	--	--	BC aggregates with a fractal dimension of 2.1, BC refractive index of $1.95 - 0.79i$, and 164/416/651 primary spherules with diameters of 15 nm for three experimental cases, respectively	(1) BC refractive index of $1.75 - 0.63i$; (2) Fractal dimension of 2.5; (3) Primary spherule diameter of 20 nm; (4) Single volume-equivalent BC sphere
	245	13.0				
	320	20.3				
II	155	5.13	Sulfuric acid (H_2SO_4)	3.67	Concentric core-shell coating structures with BC refractive index of $1.95 - 0.79i$	(1) BC refractive index of $1.75 - 0.63i$; (2) Off-center core-shell structure; (3) Closed-cell structure; (4) Open-cell structure (5) Partially encapsulated structure (6) Externally attached structure
	245	13.0		11.0		
	320	20.3		17.9		
III	155	5.13	Sulfuric acid and water $(H_2SO_4\text{-}H_2O)$	7.59	Concentric core-shell coating structures with BC refractive index of $1.95 - 0.79i$	(1) BC refractive index of $1.75 - 0.63i$; (2) Off-center core-shell structure; (3) Closed-cell structure; (4) Open-cell structure (5) Partially encapsulated structure (6) Externally attached structure
	245	13.0		20.7		
	320	20.3		33.6		

[a]Particle properties are derived from measurements in laboratory experiments (Zhang et al., 2008) with initial BC mobility diameters of 155, 245 and 320 nm. See text for details.
[b] See Fig. 3.1 and text for details.
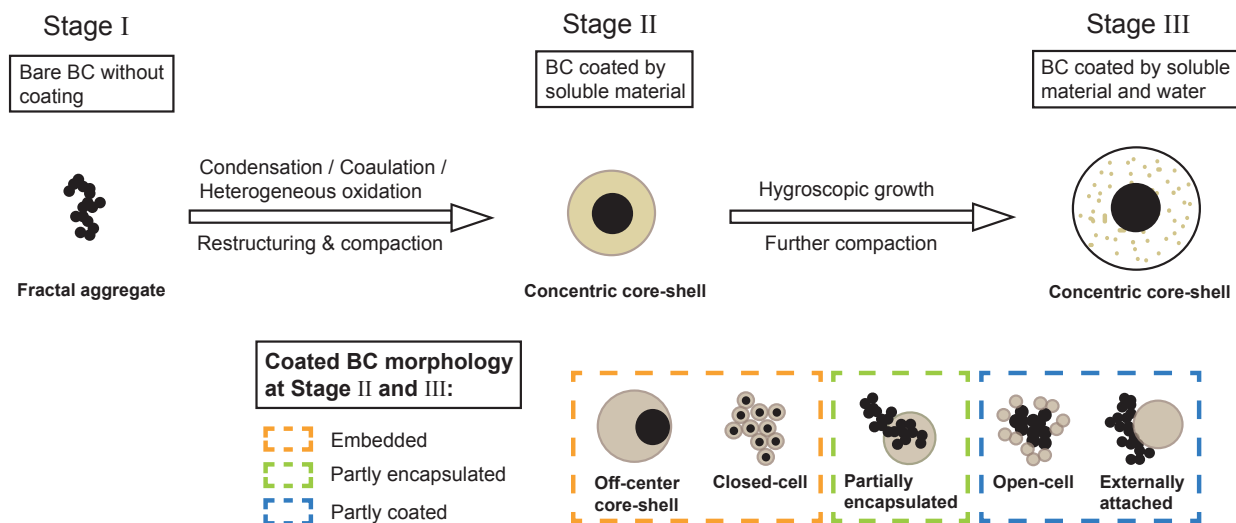
Figure 3.1: A theoretical model that accounts for three BC aging stages and the associated BC structures, including freshly emitted aggregates (Stage I), coated BC by soluble material (Stage II), and those after further hygroscopic growth (Stage III). Six typical structures for coated BC at Stages II and III are considered based on atmospheric observations, including embedded (i.e., concentric core-shell, off-center core-shell, and closed-cell), partially encapsulated, and partly coated (i.e., open-cell and externally attached) structures. See text for details.

Surface wave

Refracted photons

Incident photons

Reflected photons

Coated BC aggregates

Diffracted wave
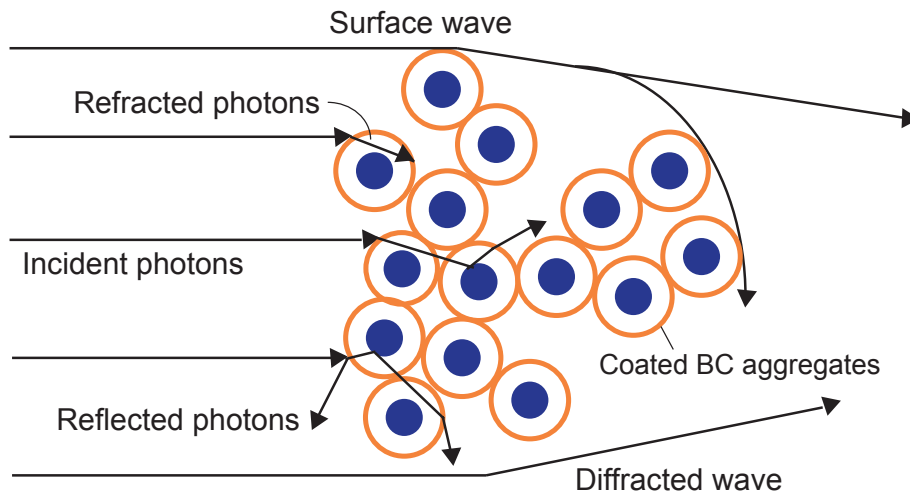
Figure 3.2: A graphical description of the geometric-optics surface-wave (GOS) approach for light scattering and absorption by coated BC aggregates. The GOS components include the hit-and-miss Monte Carlo photon tracing associated with internal and external refractions and reflections, diffraction following Babinet's principle for randomly oriented irregular particles, and surface waves traveling along the particle edges and propagating into shadow regions. See text for details.
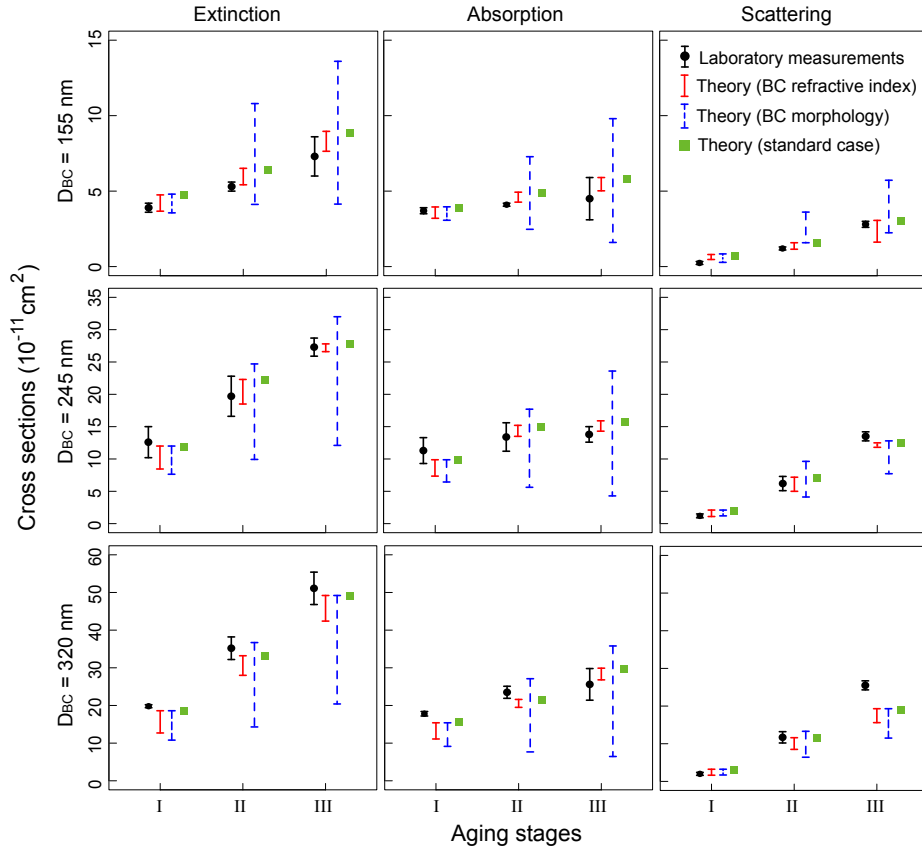
Figure 3.3: Laboratory measurements and theoretical calculations of BC extinction (left column), absorption (middle column), and scattering (right column) cross sections (at 532 nm) at three aging stages for BC with initial mobility diameters (D_{BC}) of 155 nm (top row), 245 nm (middle row), and 320 nm (bottom row). Black circles represent mean values from measurements and black error bars indicate experimental uncertainties reported by *Zhang et al.* (2008a) and *Khalizov et al.* (2009a). Green squares indicate results from the standard theoretical calculations (see Table 3.1 for details). Red error bars indicate the range of theoretical calculations using BC refractive index of 1.95 – 0.79i (upper bound) and 1.75 – 0.63i (lower bound). Blue error bars represent the upper and lower bounds of sensitivity calculations using different BC morphology with refractive index of 1.95 – 0.79i (see also Fig. 3.1 and Table 3.1).

70
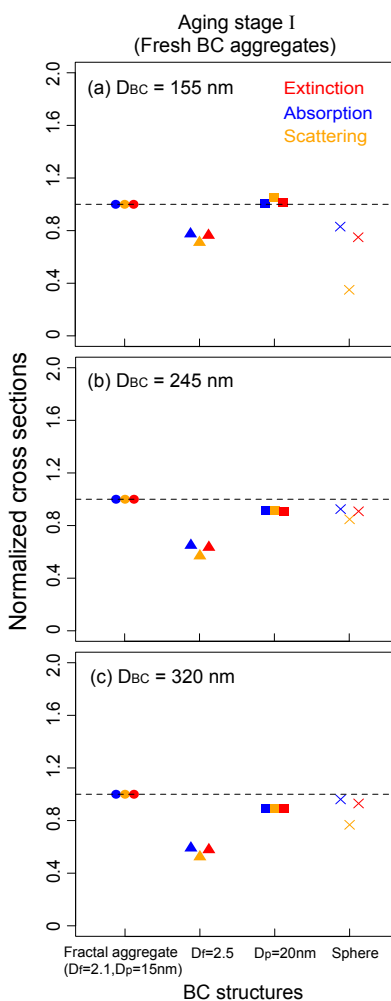
Figure 3.4: Extinction (red), absorption (blue), and scattering (orange) cross sections (at 532 nm) for different BC morphology normalized by BC aggregate cross sections determined from standard calculations at aging Stage I for initial BC mobility diameters (D_{BC}) of 155 nm (top), 245 nm (middle), and 320 nm (bottom). Results for four BC structures are shown, including BC aggregates in standard calculations (circles) with a fractal dimension (D_f) of 2.1 and a primary spherule diameter (D_p) of 15 nm, BC aggregates with D_f of 2.5 (triangles; versus 2.1 in standard calculations), BC aggregates with a D_p of 20 nm (squares; versus 15 nm in standard calculations), and a single mass-equivalent BC sphere (crosses; versus fractal aggregate in standard calculations). Dashed horizontal lines indicate a value of 1.

71
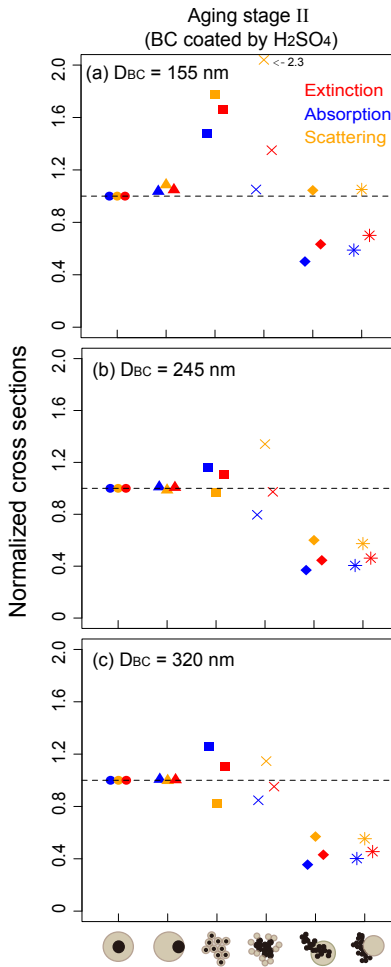
Figure 3.5: Extinction (red), absorption (blue), and scattering (orange) cross sections (at 532 nm) for different coating morphology normalized by cross sections of concentric core-shell structures determined from standard calculations at aging Stage II (BC coated by sulfuric acid (H_2SO_4)) for initial BC mobility diameters (D_{BC}) of 155 nm (top), 245 nm (middle), and 320 nm (bottom). Six BC coating structures are considered, including concentric core-shell (circles), off-center core-shell (triangles), closed-cell (squares), open-cell (crosses), partly encapsulated (diamonds), and externally attached (asterisks) structures (see also Fig. 3.1). Dashed horizontal lines indicate a value of 1.
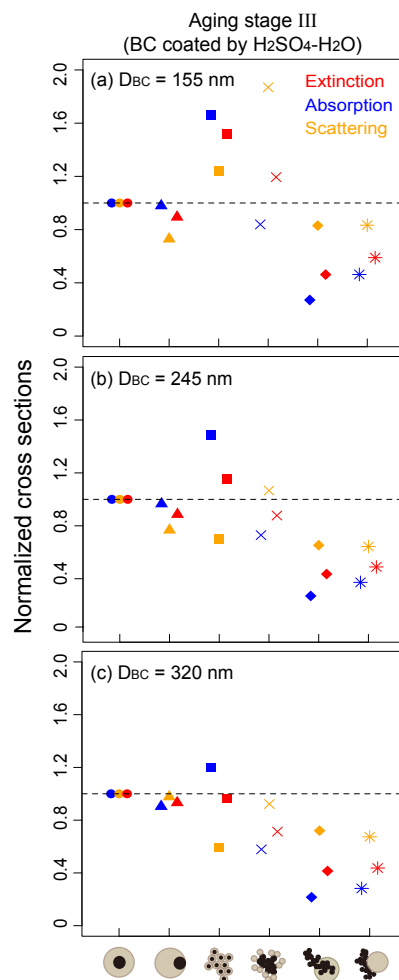
Figure 3.6: Same as Figure 3.5, but for aging stage III where BC particles are coated by both sulfuric acid and water (H_2SO_4-H_2O).
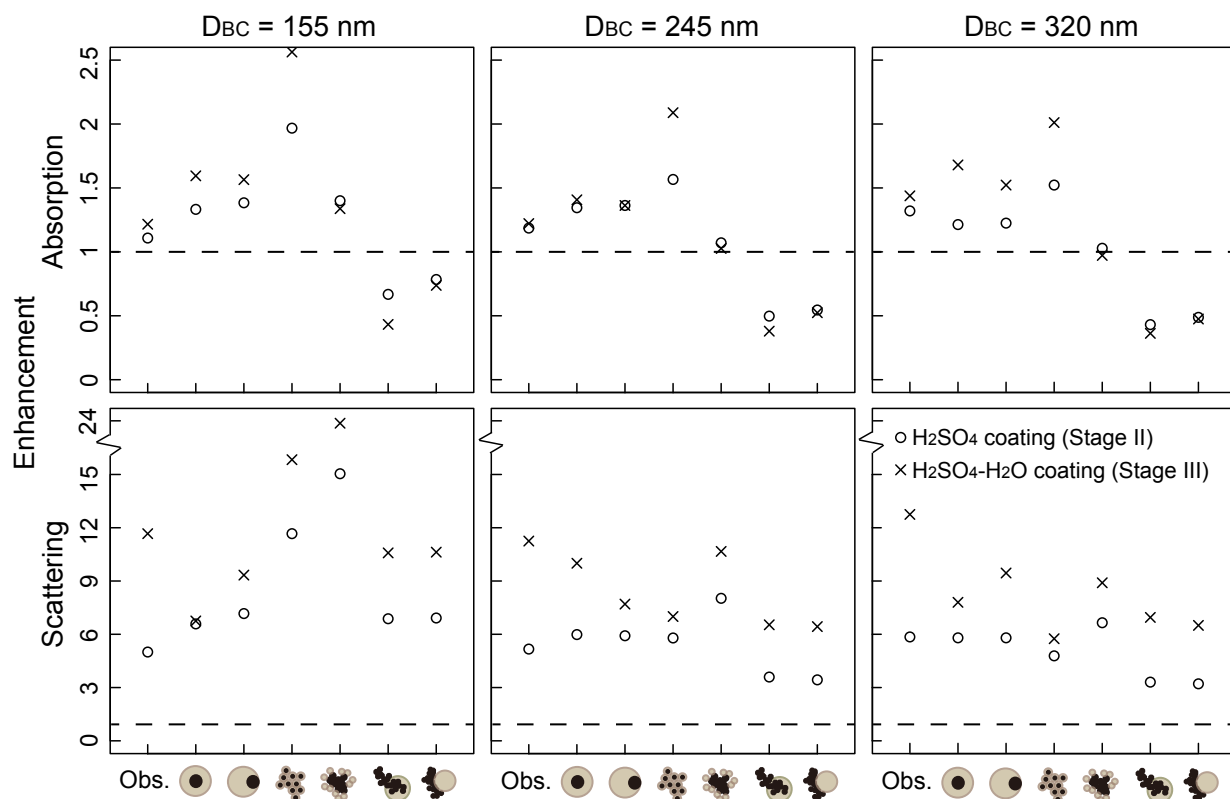
Figure 3.7: Enhancement in BC absorption (top) and scattering (bottom) during aging from freshly emitted aggregates at Stage I to BC coated by sulfuric acid (H_2SO_4) at Stage II (circles) and by both sulfuric acid and water (H_2SO_4-H_2O) at Stage III (crosses) for initial BC mobility sizes (D_{BC}) of 155 nm (left), 245 nm (middle), and 320 nm (right). The enhancements for different BC coating morphology are shown, including concentric core-shell, off-center core-shell, closed-cell, open-cell, partly encapsulated, and externally attached structures (see also Fig. 3.1). The reference case for enhancement calculation is the fresh BC aggregate measured in laboratory experiments, which is used for all six BC coating morphology cases. Thus, the enhancement is computed as the ratio of calculated absorption/scattering cross sections of coated BC particles to observed values of fresh BC aggregates. Also shown is the measured enhancement from laboratory experiments (Obs.). Horizontal dashed lines indicate a value of 1.0.

CHAPTER 4

Intercomparison of the GOS approach, superposition T-matrix method, and laboratory measurements for black carbon optical properties during aging

Abstract

We perform a comprehensive intercomparison of the geometric-optics surface-wave (GOS) approach, the superposition T-matrix method, and laboratory measurements for optical properties of fresh and coated/aged black carbon (BC) particles with complex structures. GOS and T-matrix calculations capture the measured optical (i.e., extinction, absorption, and scattering) cross sections of fresh BC aggregates, with 5–20% differences depending on particle size. We find that the T-matrix results tend to be lower than the measurements, due to uncertainty in theoretical approximations of realistic BC structures, particle property measurements, and numerical computations in the method. On the contrary, the GOS

results are higher than the measurements (hence the T-matrix results) for BC radii <100 nm, because of computational uncertainty for small particles, while the discrepancy substantially reduces to 10% for radii >100 nm. We find good agreement (differences <5%) between the two methods in asymmetry factors for various BC sizes and aggregating structures. For aged BC particles coated with sulfuric acid, GOS and T-matrix results closely match laboratory measurements of optical cross sections. Sensitivity calculations show that differences between the two methods in optical cross sections vary with coating structures for radii <100 nm, while differences decrease to ∼10% for radii >100 nm. We find small deviations (≤10%) in asymmetry factors computed from the two methods for most BC coating structures and sizes, but several complex structures have 10–30% differences. This study provides the foundation for downstream application of the GOS approach in radiative transfer and climate studies

4.1   Introduction

Black carbon (BC) is the most important light-absorbing aerosol in the current atmosphere because of its strong positive climate forcing from direct radiative and snow albedo effects (*Ramanathan and Carmichael*, 2008; *Bond et al.*, 2013). Both effects are significantly affected by BC optical properties during atmospheric aging (*Bond et al.*, 2013; *He et al.*, 2015), which transforms BC from freshly emitted hydrophobic aggregates to hydrophilic particles coated with soluble materials (*Schwarz et al.*, 2008; *Zhang et al.*, 2008a; *He et al.*, 2016a). Observations have shown that BC particles experience considerable variations in optical properties via aging, due to complex changes in particle morphology (*Adachi et al.*, 2010; *Adachi and Buseck*, 2013; *China et al.*, 2015). Thus, a reliable estimate of BC climatic effects requires accurate computations of optical properties for BC particles with complex structures during aging.

A number of theoretical approaches have been developed and are widely used to compute particle single-scattering properties, including the Lorenz-Mie (LM) method for homo-

76

geneous spheres or concentric core-shell structures (*Toon and Ackerman*, 1981), the Finite Difference Time Domain (FDTD) method for nonspherical particles (*Yang and Liou*, 1996), the Rayleigh-Debye-Gans (RDG) approximation for homogeneous fractal aggregates (*Dobbins and Megaridis*, 1991), the Discrete Dipole Approximation (DDA) (*Draine and Flatau*, 1994) and the superposition T-matrix method (*Mackowski and Mishchenko*, 1996) for inhomogeneous and irregular shapes. Particularly, the superposition T-matrix method has increasing popularity due to its ability to deal with various aggregating structures with high accuracy (*Mackowski*, 2014). For example, *Liu and Mishchenko* (2007) and *Liu et al.* (2008) used the superposition T-matrix method to compute radiative properties of BC aggregates with different compactness and sizes. *Kahnert and Devasthale* (2011) quantified the morphological effects of fresh BC aggregates on optical properties based on the T-matrix calculation. *Mishchenko et al.* (2014) applied the T-matrix method to study optical properties of BC-cloud mixtures.

Recently, *Liou et al.* (2010, 2011) developed a geometric-optics surface-wave (GOS) approach to compute particle light absorption and scattering by explicitly resolving complex particle structures. They found that optical cross sections, single scattering albedos, and asymmetry factors of particles calculated from the GOS method are consistent (differences < 20%) with those derived from the LM method for concentric core-shell particles (*Liou et al.*, 2010), the DDA and FDTD methods for plate and column ice crystals (*Liou et al.*, 2011), and the superposition T-matrix method for fresh BC aggregates (*Takano et al.*, 2013). Compared with the aforementioned methods, the GOS approach can be applied to a wider range of particle sizes and mixing structures with high computational efficiency. *Liou et al.* (2014) and *He et al.* (2014a) applied the GOS approach to deal with multiple internal mixing of BC with nonspherical snow grains (up to 1000 μm), where the T-matrix and DDA methods currently are unsuitable. However, comprehensive evaluation and validation of the GOS approach for small and complex coated BC particles have not been performed.

He et al. (2015) compared optical cross sections of BC aggregates from GOS calcula-

tions and laboratory measurements, and found that GOS results generally captured the measurements. In this study, as an extension of their work, we perform a comprehensive intercomparison of the GOS approach, the superposition T-matrix method, and laboratory measurements for optical properties of fresh and coated BC particles with complex structures during aging. We describe the theoretical calculations and laboratory experiments in Section 4.2. We compare and discuss the GOS, T-matrix, and experimental results in Section 4.3. Finally, we present conclusions in Section 4.4.

4.2 Methods

4.2.1 Geometric-optics surface-wave (GOS) approach

The GOS approach (*Liou et al.*, 2011, 2014; *He et al.*, 2014a, 2015), accounting for geometric reflection and refraction, diffraction, and surface wave components (Fig. 4.1), is designed only to compute particle optical cross sections and asymmetry factors for application to radiative transfer and climate modeling. It does not compute the full Mueller matrix. The GOS approach computes particle optical properties by explicitly simulating various aggregating and coating structures. The irregular particle shapes are constructed by a stochastic procedure (*Liou et al.*, 2011) in a 3-D coordinate system. Once the shape and composition of a particle are defined from the stochastic process, the geometric reflection and refraction are carried out using hit-and-miss Monte Carlo photon tracing. Following a ray-by-ray integration approach (*Yang and Liou*, 1997), the extinction and absorption cross sections for a single particle are computed by

$$C_{ext} = \frac{2\pi}{k^2} Re[S_{11}(\hat{e}_0) + S_{22}(\hat{e}_0)] \tag{4.1}$$

$$C_{abs} = \frac{1}{2} \sum_{\gamma} \sum_{p=1}^{\infty} exp(-2k \sum_{j=1}^{p-1} m_{i,j} d_j)[1 - exp(-2km_{i,p}d_p)](t_1^2 r_1^{p-1} + t_2^2 r_2^{p-1}) \tag{4.2}$$

78

where C_{ext} and C_{abs} are the extinction and absorption cross sections, respectively. In Eq. (4.1), k is the wavenumber, Re denotes the real part, S_{11} and S_{22} are two diagonal elements of the scattering amplitude matrix in the forward direction, and $\hat{e}_0$ denotes the incident direction. In Eq. (4.2), the subscript index p ($= 1, 2, ...$) indicates the internal localized ray, γ represents all incident rays impinging onto the sphere, $m_{i,j(or\ p)}$ represents the imaginary part of the refractive index for an inhomogeneous sphere, $d_{j(or\ p)}$ is a vector distance between two points, and $t_j^2 r_j^{p-1}$ ($j = 1, 2$) indicates the cumulative product of Fresnel coefficients.

Subsequently, an effective geometric cross section (i.e., photon-number weighted shadow area on a plane perpendicular to the incident light) is used to compute the extinction and absorption efficiency for a group of randomly oriented aggregates (*Liou et al.*, 2011). Diffraction by randomly oriented particles with irregular shape is computed using the Babinet's principle and the effective geometric cross section (*Liou et al.*, 2011). Based on the geometric-optics components (reflection, refraction, and diffraction; hereinafter GO), we define a radiation pressure efficiency for nonspherical particles (*Liou et al.*, 2011) as

$$Q_{pr}(GO) = Q_{ext}(GO) - g(GO)[Q_{ext}(GO) - Q_{abs}(GO)] \tag{4.3}$$

where Q_{pr}, Q_{ext}, and Q_{abs}, respectively, are the efficiency factors for radiation pressure (pr), extinction (ext), and absorption (abs), and $g(GO)$ is the geometric-optics asymmetry factor.

The surface-wave component of GOS accounts for the interaction of incident waves at grazing angles near the particle edge and propagating along the particle surface into shadow regions. Following the complex-angular-momentum (CAM) formulation developed by *Nussenzveig and Wiscombe* (1980), *Liou et al.* (2010) showed that a linear combination of the geometric optics component (i.e., GO) and the surface-wave adjustment (hereinafter GOS) leads to a solution that matches the exact LM theory so that

$$Q_w(GOS) = Q_w(GO) + f\triangle Q_w \sim Q_w(LM), w = ext,\ abs,\ pr \tag{4.4}$$

where $\triangle Q_w$ is the surface-wave adjustment and f is a correction factor for nonsphericity of

scattering particles (*Liou et al.*, 2011), given by

$$f = c(\frac{r_v}{r_a})^3 \tag{4.5}$$

where r_v and r_a are, respectively, volume and area equivalent radii of aggregates, and c (≤ 1) is an adjustment factor for aggregation. Thus, $f = 1$ for spheres ($r_v = r_a$) and $f \approx 0$ for elongated particles ($r_v \ll r_a$). For large particles (size parameters $> \sim 50$), the geometric optics component dominates.

Based on Eqs. (4.3) and (4.4), the GOS asymmetry factor $g(GOS)$ is computed by

$$g(GOS) = \frac{[1 - \frac{Q_{pr}(GOS)}{Q_{ext}(GOS)}]}{\omega(GOS)} \tag{4.6}$$

where ω is the single scattering albedo. Because the CAM theory for surface-wave formulation cannot be applied to the $g(GOS)$ calculation for small inhomogeneous particles (*Nussenzveig and Wiscombe*, 1980), we use the improved geometric-optics method (*Yang and Liou*, 1996) and the ray-by-ray integration method (*Yang and Liou*, 1997) to compute $g(GOS)$ for inhomogeneously coated BC aggregates in this study. Considering the relatively large uncertainty in the Monte Carlo photon tracing for small particles, we further couple GOS with the RGD approximation to improve the computational accuracy of $g(GOS)$ for fresh BC aggregates with size parameter <1, which has shown consistent results with the T-matrix calculation (*Takano et al.*, 2013). A comprehensive description of the GOS approach and its application is provided in *Liou and Yang* (2016).

4.2.2   Superposition T-matrix method

The superposition T-matrix method (*Mackowski and Mishchenko*, 1996, 2011) has recently been extended to calculate the scattering properties of multiple sphere domains with the removal of external configuration constraints (*Mackowski*, 2014). It solves Maxwell's equations for fractal aggregates, where the scattering and extinction cross sections are given by

$$C_{sca} = \frac{\pi}{k^2} \sum_{n=1}^{L} \sum_{m=-n}^{n} \sum_{p=1}^{2} |a_{mnp}^0|^2 \tag{4.7}$$

$$C_{ext} = \frac{\pi}{k^2} \sum_{n=1}^{L} \sum_{m=-n}^{n} \sum_{p=1}^{2} a_{mnp}^0 f_{mnp}^0 \tag{4.8}$$

where f_{mnp}^0 and a_{mnp}^0, respectively, are incident and scattered field coefficients expressed in

$$\mathbf{E}_{inc}(\mathbf{r}) = \sum_{n=1}^{L} \sum_{m=-n}^{n} \sum_{p=1}^{2} f_{mnp}^0 \mathbf{N}_{mnp}^{(1)}(k\mathbf{r}) \tag{4.9}$$

$$\mathbf{E}_{sca}(\mathbf{r}) = \sum_{n=1}^{L_0} \sum_{m=-n}^{n} \sum_{p=1}^{2} a_{mnp}^0 \mathbf{N}_{mnp}^{(3)}(k\mathbf{r}) \tag{4.10}$$

where $\mathbf{N}_{mnp}^{(1)}$ and $\mathbf{N}_{mnp}^{(3)}$ are vector spherical wave functions (VSWFs) with degree m, order n, and mode p. $\mathbf{E}_{inc}(\mathbf{r})$ and $\mathbf{E}_{sca}(\mathbf{r})$ are incident and scattered fields, respectively. The asymmetry factor (g) defined as

$$g = \frac{1}{2} \int_0^{\pi} P(\theta) sin\theta cos\theta d\theta \tag{4.11}$$

is computed after the scattering matrix is numerically solved by the T-matrix method (*Liu and Mishchenko*, 2007). $P(\theta)$ in Eq. (4.11) is the phase function (i.e., the first element of the scattering matrix). More details about the superposition T-matrix theory and formulation are provided in *Mackowski* (2014). In this study, we use the Multi-Sphere T-Matrix (MSTM) version 3 program developed by *Mackowski* (2014) (available at www.eng.auburn.edu/users/dmckwski/scatcodes).

4.2.3   Laboratory experiments

He et al. (2015) compared GOS calculations with laboratory experiments for various aggregating structures of BC particles during aging. Extending their work, we apply both the GOS and superposition T-matrix methods to their experimental cases, where the experimental results are used as a reference for comparison of the two methods. The laboratory

experiments measure optical cross sections at 532 nm wavelength for freshly emitted BC aggregates and aged BC particles coated with sulfuric acid through condensation of sulfuric acid vapor. Uncertainty in the measurement of optical cross sections is primarily from particle size, relative humidity, number density, and instrument calibration. The experiments also measure the density, mass, size, and fractal dimension of BC aggregates and coating materials, which are used as input for theoretical calculations by the GOS and T-matrix methods (see Section 4.2.4). Details about laboratory experiments are provided in *He et al.* (2015). We investigate three experimental cases, where the volume-equivalent radii are 41, 56, and 65 nm for fresh BC aggregates, and 49, 69, and 80 nm for coated BC particles with coating thicknesses of 8, 13, and 15 nm, respectively.

4.2.4 Theoretical computations

We apply the GOS and superposition T-matrix methods to compute optical cross sections and asymmetry factors of fresh and coated/aged BC particles at 532 nm wavelength for comparison with experimental measurements (see Section 4.2.3). For fresh BC aggregates (Fig. 4.1), the standard computation case includes BC volume-equivalent radii of 41, 56, 65, and 137 nm, where the first three values are in line with the experiments and the last one represents a mean observed value near combustion sources in the atmosphere (*Bond et al.*, 2006). In the standard calculation, we use the measured primary spherule radius (r_{ps}) of 7.5 nm and fractal dimension (D_f) of 2.1 for BC aggregates. We use $1.95 - 0.79i$ for BC refractive index as recommended by (*Bond and Bergstrom*, 2006). To investigate morphological effects, we increase the fractal dimension to 2.5 and the primary spherule radius to 10 nm, respectively, in two sensitivity calculations. We use $1.75 - 0.63i$ as the lower bound of BC refractive index (*Bond and Bergstrom*, 2006) in a third sensitivity calculation to investigate the effect of refractive index.

For coated BC particles after aging, the pure BC component has the same volume-equivalent radii (i.e., 41, 56, 65, and 137 nm) as the fresh BC aggregates, while the coating

82

thicknesses (sulfuric acid) are 8, 13, 15, and 27 nm, respectively, in the concentric core-shell structure shown in Fig. 4.1. The first three coating thicknesses are derived from the experimental measurements (*He et al.*, 2015), while the last one is set to have the same core-shell ratio as the experimental case. The amounts of BC and coating material in each case are fixed for all the particle structures considered in this study. We use $1.95 - 0.79i$ and $1.52 - 0i$ for the refractive indices of pure BC and sulfuric acid (coating), respectively. We conduct computations for six typical coated BC structures (Fig. 4.1), including concentric core-shell, off-center core-shell, open-cell, closed-cell, partially encapsulated, and externally attached structures based on atmospheric observations (*China et al.*, 2015; *He et al.*, 2015). We note that these structures are a simplification of coated BC particles in the real atmosphere and hence may not capture all observed particle features. More realistic structures such as nonspherical coating shells will be investigated in future work. The BC particle structures are constructed by the stochastic procedure developed by *Liou et al.* (2011) with a single realization for each structure, which may introduce some uncertainty. We apply the GOS and T-matrix methods to the same realization of each structure. Detailed descriptions of particle construction are provided in *He et al.* (2015).

4.3   Results and discussions

4.3.1   Fresh BC aggregates

Figures 4.2 and 4.3 show the extinction and absorption cross sections of fresh BC aggregates computed from the GOS and superposition T-matrix methods and measured from laboratory experiments. The scattering cross sections (not shown) are the differences between extinction and absorption cross sections. The standard GOS and T-matrix calculations capture the measured BC optical cross sections, with differences of 5–20% depending on BC size (Figs. 4.2 and 4.3). However, the GOS results tend to be higher than the measurements, while the T-matrix results tend to be lower. The differences between the T-matrix and

experimental results are likely caused by uncertainty associated with theoretical approximation of the complex BC structures produced by the experiments and the application of a single realization for each aggregate (*Skorupski et al.*, 2013; *Wu et al.*, 2015a,b, 2016). Using different realizations of each structure, we found only small ($<5\%$) variations in optical cross sections and asymmetry factors. In addition, measurement uncertainties in particle fractal dimension and primary spherule radius could lead to the theory-measurement discrepancy. We found that increasing the fractal dimension or primary spherule radius reduces the difference between the T-matrix and experimental results in BC optical cross sections (Figs. 4.2 and 4.3). The uncertainty involved in BC refractive index, measured optical cross sections, and numerical computations may also contribute to the discrepancy between the T-matrix results and measurements.

BC extinction, absorption, and scattering cross sections computed from the GOS approach are consistently higher than the T-matrix method for BC size (i.e., volume-equivalent radius) less than 100 nm (Figs. 4.2 and 4.3). This is because of uncertainty in the Monte Carlo photon tracing and the ray-by-ray integration for small particles. Increasing the BC radius to 137 nm reduces the difference in optical cross sections to 10%. We note that most BC particles observed in the real atmosphere are larger than 100 nm (*Bond et al.*, 2006; *Schwarz et al.*, 2008). Considering the performance of the Monte Carlo photon tracing depends on the number of rays used, we doubled the photon number and found only small ($<5\%$) changes in optical cross sections, suggesting a sufficient photon number in the current computations.

Similar to the T-matrix calculations, the GOS results show a 20% decrease in extinction and absorption cross sections and 30% in scattering cross sections by using the lower bound of BC refractive index ($1.75 - 0.63i$). *Liu et al.* (2008) found 50–70% differences in BC absorption and scattering cross sections by using $2 - i$ and $1.75 - 0.5i$ for refractive index, which depends on aggregate structures. By increasing the fractal dimension (from 2.1 to 2.5), we found that BC absorption cross sections computed from the GOS method decrease

by 5–15% with larger reductions for larger sizes (Fig. 4.3), while the T-matrix results show a rather small (<3%) change in absorption. *Scarnato et al.* (2013) showed that more compact structures (i.e., larger fractal dimension) lead to weaker BC absorption by using the DDA method. This is because of fewer BC primary spherules directly exposed to incident rays for aggregates with a larger fractal dimension (*Liu et al.*, 2008). Both GOS and T-matrix calculations show less than 5% changes in BC extinction and absorption cross sections by increasing the primary spherule radius (Fig. 4.3). This is consistent with the conclusion from *Liu and Mishchenko* (2007) that BC scattering and absorption are weakly affected by primary spherule size.

Figure 4.4 shows the asymmetry factor of fresh BC aggregates computed from the GOS and T-matrix methods. The GOS results closely match (differences <5%) the T-matrix calculations for different BC sizes in both standard and sensitivity cases. The two methods show negligible (<1%) changes in asymmetry factors when using a smaller BC refractive index. We found a 5–15% reduction in asymmetry factors for a larger primary spherule radius (r_{ps} = 10 nm) but a much stronger reduction (40–50%) for a larger fractal dimension (D_f = 2.5) for BC radii smaller than 100 nm. *Liu et al.* (2008) also showed that the asymmetry factor of BC aggregates decreases substantially with an increasing fractal dimension from 2 to 3.

4.3.2 Coated/aged BC particles

Figures 4.5 and 4.6 show the extinction and absorption cross sections of coated/aged BC particles computed from the GOS and superposition T-matrix methods and measured from laboratory experiments. Both GOS and T-matrix results are consistent with measurements in optical cross sections for the concentric core-shell structure, with differences of 5–20% depending on BC size. This is consistent with the observed efficient structure compaction during BC aging in the experiments (*He et al.*, 2015). For the concentric core-shell, off-center core-shell, and partially encapsulated structures, the GOS calculations show a good

agreement with the T-matrix results in BC optical cross sections, while the GOS calculations are consistently higher than the T-matrix results for closed-cell, open-cell, and externally attached structures with radii smaller than 100 nm. The discrepancy is larger for smaller BC sizes, due to the uncertainty in the GOS calculation for small particles. As the particle radius increases to larger than 100 nm, the discrepancy between the two methods in optical cross sections reduces to less than 15% for all six coating structures.

We found that the off-center core-shell structure only leads to less than 5% change in BC optical cross sections computed from the GOS and T-matrix methods (Figs. 4.5 and 4.6), due to the small coating thickness. *He et al.* (2015) found up to 30% decrease in BC optical cross sections for the off-center core-shell structure with a thick coating layer. Similar reductions in absorption caused by the off-center position of BC cores are also found by *Adachi et al.* (2010) using the DDA method. The GOS and T-matrix results both show a substantial decrease in extinction, absorption, and scattering cross sections for the partially encapsulated structure with radii smaller than 100 nm but a slight increase for radii larger than 100 nm, relative to the concentric core-shell structure. *Kahnert et al.* (2013) pointed out that the effect of encapsulated structures on BC absorption and scattering are strongly dependent on particle size. The GOS method shows an enhancement of 40–70% in BC absorption for the closed-cell structure with radius smaller than 100 nm compared with the concentric core-shell structure, whereas the T-matrix method shows a 40% decrease in this case (Fig. 4.6). We note that BC absorption for the closed-cell structure, which depends on particle size and refractive index, could vary from lower to higher than that of the concentric core-shell structure. For the open-cell and externally attached structures with radii smaller than 100 nm, the T-matrix calculations lead to about 40% reduction in BC absorption relative to the concentric core-shell structure. This is likely because the two coating structures are relatively loose and open, which cannot produce effective lensing effects to enhance BC absorption (*He et al.*, 2015), as well as due to the shadowing effect from non-absorbing coating material attached outside pure BC spherules (*Liu and Mishchenko*, 2007). However, the GOS approach shows a slight

increase ($\leq 15\%$) in BC absorption by the open-cell and externally attached structures, as a result of the overestimate produced by GOS calculations for small particles with complex structures.

Figure 4.7 shows the asymmetry factor of coated BC structures computed from the GOS and T-matrix methods. The T-matrix calculations show a negligible change in asymmetry factors of the off-center core-shell structure compared to the concentric core-shell structure, while the closed-cell structure results in a 10–40% increase. We found that the asymmetry factors computed from the T-matrix method for the open-cell, partially encapsulated, and externally attached structures are lower than the concentric core-shell structure with the smallest radius (i.e., 49 nm), but increase quickly to be higher than that of the concentric core-shell structure as BC size becomes larger. The GOS results generally capture the T-matrix results, but the consistency between the two methods varies across different structures and sizes. The two methods show negligible differences ($\leq 5\%$) for concentric core-shell, off-center core-shell, and open-cell structures with all four particle sizes. The GOS calculations also agree with the T-matrix results for the externally attached structures with differences $\leq 10\%$. The discrepancies between the GOS and T-matrix methods are less than 10% for the closed-cell structure with radii of 49, 69, and 164 nm but reach up to 25% for a radius of 80 nm. The differences in the partially encapsulated structure also vary with size, where the GOS results show 10–30% overestimates for radii smaller than 100 nm and 15% underestimates for radii larger than 100 nm, compared with the T-matrix calculations. This is probably because of the approximation in GOS computations of asymmetry factors by the improved geometric-optics and ray-by-ray integration methods.

In addition, we compared the computational efficiency of the GOS and superposition T-matrix methods. The T-matrix calculation is usually fast for particles with size parameter less than 10, particularly when considering that orientation-averaging is done analytically. For simple particle shapes, the T-matrix method shows similar computational time as the GOS approach. However, when particles have rather complex structures such as coated BC

aggregates in this study, the T-matrix calculation requires much more time than the GOS calculation. For example, for open-cell and closed-cell coating structures with radii of 164 nm, the GOS computation time is ~1 minute, whereas the T-matrix computation requires 1–2 hours.

4.4   Conclusions

We have performed a comprehensive intercomparison of the GOS and superposition T-matrix calculations with laboratory measurements for optical properties of fresh and coated/aged BC particles with complex structures. The GOS and T-matrix results both captured the measured optical (extinction, absorption, and scattering) cross sections of fresh BC aggregates, with differences of 5–30% depending on size. However, the T-matrix calculations tended to be lower than the measurements, due to uncertainty associated with theoretical approximations of realistic BC structures, measurements of particle properties, and numerical computations in the method. In contrast, the GOS calculations were consistently higher than the measurements (hence the T-matrix results) for BC radius smaller than 100 nm, due to computational uncertainty for small particles. The discrepancy reduced to 10% as the particle size increased to larger than 100 nm. The asymmetry factor computed from the GOS approach showed a good agreement (differences <5%) with the T-matrix results for various BC sizes and aggregating structures. Both the GOS and T-matrix results showed a 20–30% decrease in optical cross sections of fresh BC aggregates by using the lower bound of BC refractive index and less than 5% changes by increasing the primary spherule radius, while the two methods differed to some extent in the sensitivity of BC absorption to fractal dimension.

For coated/aged BC particles, the GOS and T-matrix results were consistent with laboratory measurements in optical cross sections for the concentric core-shell structure, because of the observed efficient structure compaction during BC aging. The GOS calculations showed

a good agreement in optical cross sections with the T-matrix results for the concentric core-shell, off-center core-shell, and partially encapsulated structures, but were higher than the T-matrix results for the closed-cell, open-cell, and externally attached structures with radii smaller than 100 nm. The discrepancy decreased significantly for BC radii larger than 100 nm. The GOS results captured (differences $\leq 10\%$) the T-matrix calculations of asymmetry factors for different coating structures and sizes, except for a few particle sizes of the closed-cell and partially encapsulated structures. We found that the sensitivity of optical cross sections and asymmetry factors to BC coating strongly depends on particle structures and sizes, where the GOS results deviated to some extent from the T-matrix calculations. This is likely due to uncertainty in GOS calculations for small particles with complex structures. This study provided the foundation to further apply the GOS approach to radiative transfer and climate studies in future work.

4.5   Tables and figures
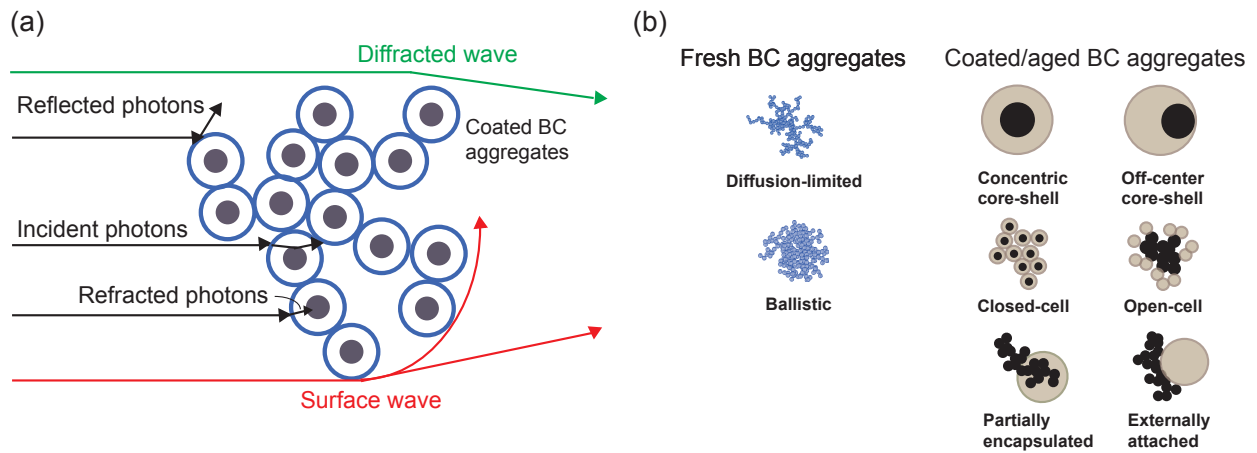
Figure 4.1: (a) A graphical demonstration of the geometric-optics surface-wave (GOS) method for light scattering and absorption by BC aggregates, including reflection, refraction, diffraction, and surface-wave components. (b) Typical structures of fresh and coated BC particles used in this study to approximate atmospheric observations (modified from *He et al.* (2015) and *Liou et al.* (2011)).
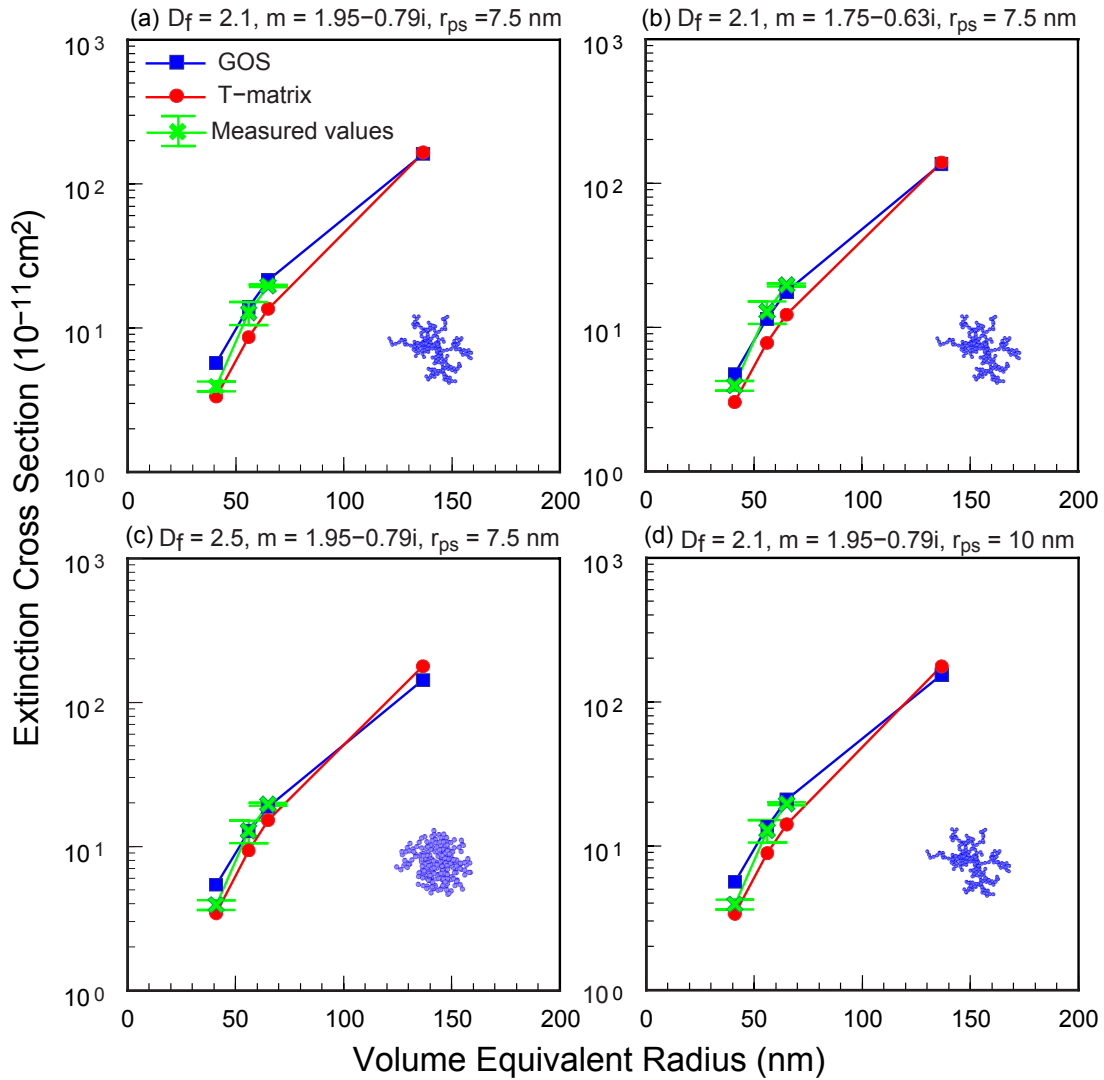
Figure 4.2: Extinction cross sections (at 532 nm) of fresh BC aggregates computed from the GOS (blue) and superposition T-matrix (red) methods and measured from laboratory experiments (green). One standard case (a) and three sensitivity cases (b–d) are shown with different fractal dimensions (D_f), BC refractive index (m), and radius of primary spherule (r_{ps}). Note that the measured values shown as a reference are the same in all four panels.
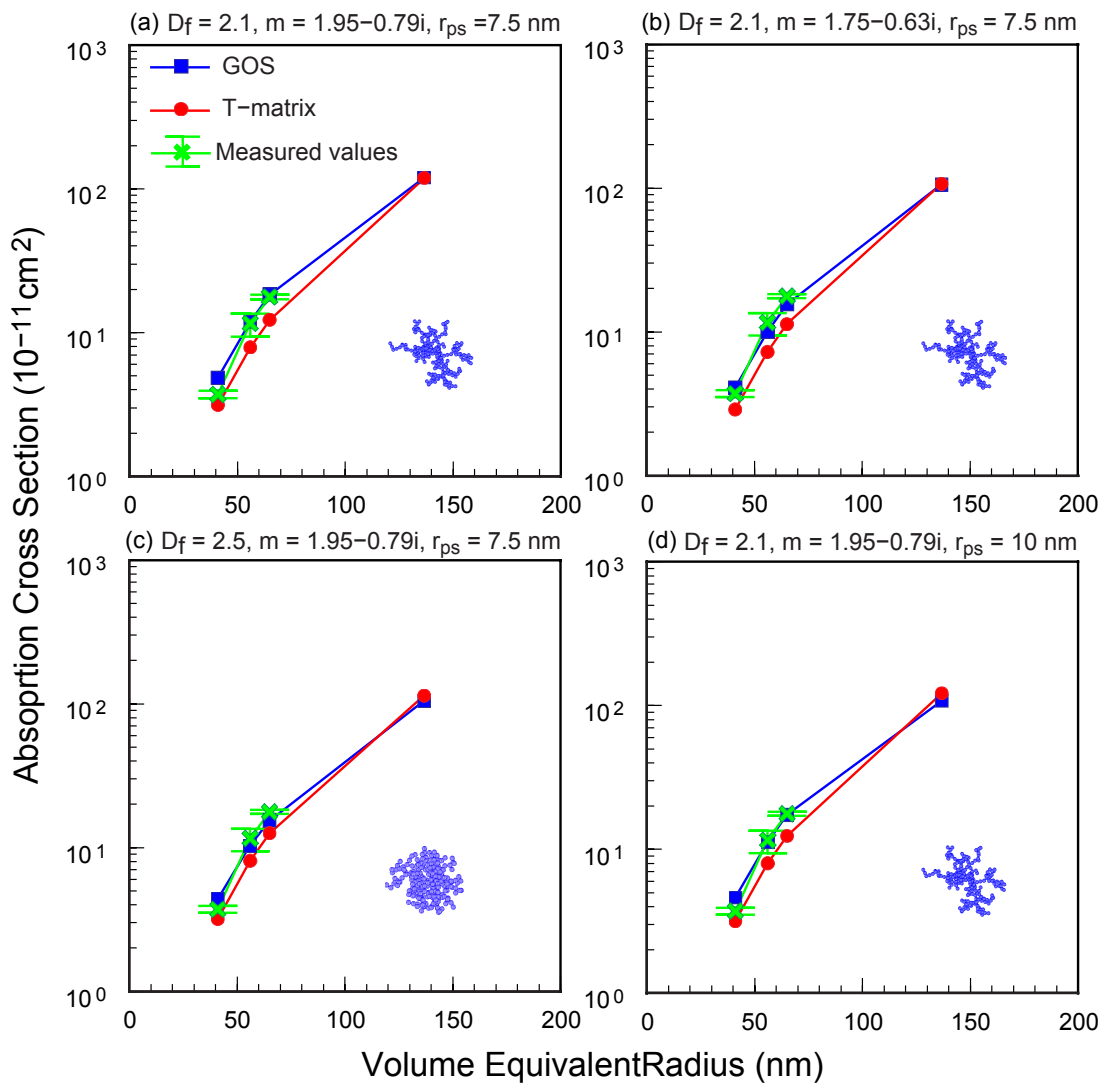
Figure 4.3: Same as Figure 4.2, but for absorption cross sections.
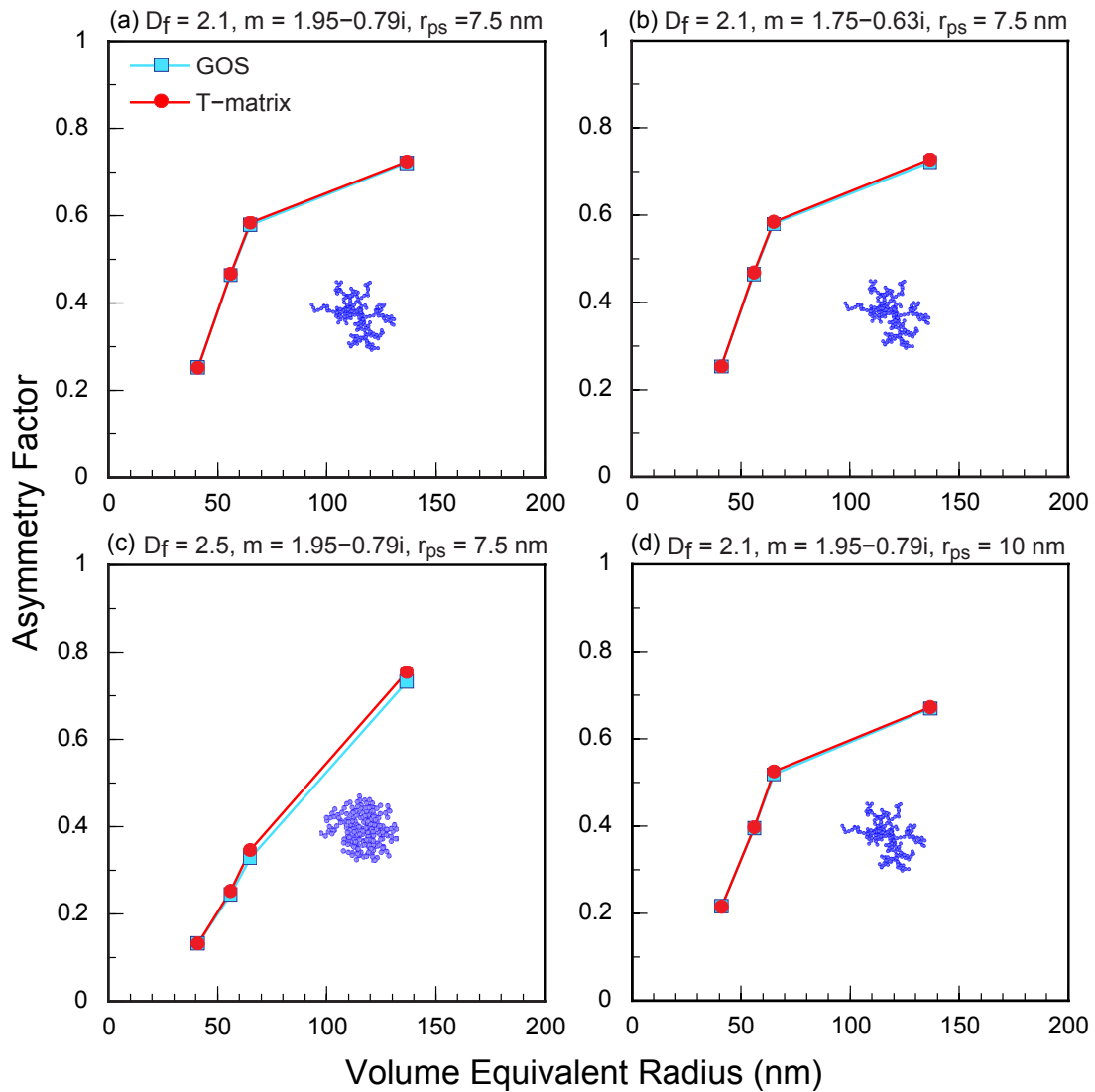
Figure 4.4: Same as Figure 4.2, but for asymmetry factors. Note that asymmetry factors are not measured in laboratory experiments.
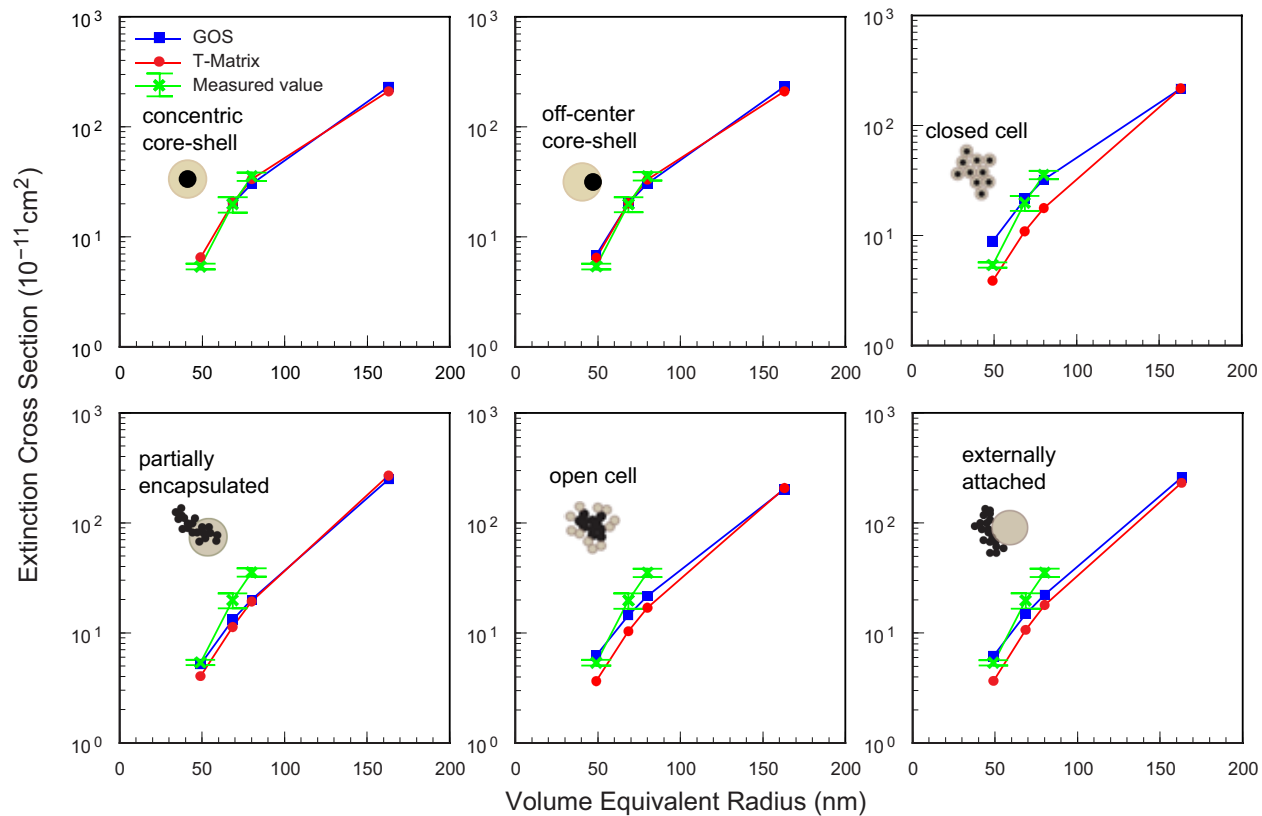
Figure 4.5: Extinction cross sections (at 532 nm) of coated BC particles with six typical structures computed from the GOS (blue) and superposition T-matrix (red) methods and measured from laboratory experiments (green). Note that the measured values shown as a reference are the same in all panels.

Figure 4.6: Same as Figure 4.5, but for absorption cross sections.

Figure 4.7: Same as Figure 4.5, but for asymmetry factors. Note that asymmetry factors are not measured in laboratory experiments.

CHAPTER 5

Microphysics-based black carbon aging in a global CTM: constraints from HIPPO observations and implications for global black carbon budget

Abstract

We develop and examine a microphysics-based black carbon (BC) aerosol aging scheme that accounts for condensation, coagulation, and heterogeneous chemical oxidation processes in a global 3-D chemical transport model (GEOS-Chem) by interpreting the BC measurements from the HIAPER Pole-to-Pole Observations (HIPPO, 2009–2011) using the model. We convert aerosol mass in the model to number concentration by assuming lognormal aerosol size distributions and compute the microphysical BC aging rate (excluding chemical oxidation aging) explicitly from the condensation of soluble materials onto hydrophobic BC and the coagulation between hydrophobic BC and preexisting soluble particles. The chem-

ical oxidation aging is tested in the sensitivity simulation. The microphysical aging rate is about 4 times higher in the lower troposphere over source regions than that from a fixed aging scheme with an e-folding time of 1.2 days. The higher aging rate reflects the large emissions of sulfate-nitrate and secondary organic aerosol precursors hence faster BC aging through condensation and coagulation. In contrast, the microphysical aging is more than fivefold slower than the fixed aging in remote regions, where condensation and coagulation are weak. Globally BC microphysical aging is dominated by condensation, while coagulation contribution is largest over East China, India, and Central Africa. The fixed aging scheme results in an overestimate of HIPPO BC throughout the troposphere by a factor of 6 on average. The microphysical scheme reduces this discrepancy by about a factor of 3, particularly in the middle and upper troposphere. It also leads to a threefold reduction in model bias in the latitudinal BC column burden averaged along the HIPPO flight tracks, with largest improvements in the tropics. The resulting global annual mean BC lifetime is 4.2 days and BC burden is 0.25 mg m^{-2}, with 7.3% of the burden at high altitudes (above 5 km). Wet scavenging accounts for 80.3% of global BC deposition. We find that in source regions the microphysical aging rate is insensitive to aerosol size distribution, condensation threshold, and chemical oxidation aging, while it is the opposite in remote regions, where the aging rate is orders of magnitude smaller. As a result, global BC burden and lifetime show little sensitivity (<5% change) to these three factors.

5.1 Introduction

Black carbon (BC) aerosol is one of the most important contributors to current global and regional warming (*Bond et al.*, 2013). BC directly absorbs solar radiation, leading to significant atmospheric warming (*Ramanathan and Carmichael*, 2008). It also acts as cloud condensation nuclei (CCN), affecting cloud formation and distribution (*Jacobson*, 2014). Additionally, BC reduces snow albedo after deposition on snow, resulting in accelerated snow melting (*Painter et al.*, 2013; *Liou et al.*, 2014). The assessment by *Bond et al.* (2013)

pointed out that current estimates of BC climatic effects involve large uncertainties. One of the critical uncertainty sources is BC atmospheric aging through the physical and chemical transformation of BC from hydrophobic to hydrophilic particles.

BC is emitted mostly as hydrophobic particles externally mixed with other aerosol constituents (*Zhang et al.*, 2008a). Recent studies showed that BC can also be frequently mixed with organics even at emission under specific conditions (*Willis et al.*, 2016). Hydrophobic BC becomes hydrophilic due to increasing internal mixing with water-soluble materials through condensation (*Moteki et al.*, 2007), coagulation (*Johnson et al.*, 2005), and heterogeneous oxidation (*Khalizov et al.*, 2010) during atmospheric aging. Hereinafter we refer to these internal mixtures generically as "coatings" without making any specific reference to mixing morphology. Coating enhances BC absorption and scattering capacities (*Bond et al.*, 2006), which depends on coating properties and particle morphology (*Scarnato et al.*, 2013; *He et al.*, 2015). Coated BC particles typically have a higher hygroscopicity (*Zhang et al.*, 2008a) and hence more efficient wet scavenging, which further affects BC atmospheric lifetime (*Zhang et al.*, 2015). Thus, BC aging is expected to play a critical role in affecting both BC optical properties and global distribution.

In global chemical transport models (CTMs), BC aging is typically parameterized by a fixed e-folding time of 1–2 days for the hydrophobic-to-hydrophilic BC conversion (e.g., *Chung and Seinfeld*, 2002; *Koch et al.*, 2009; *Wang et al.*, 2011, 2014a). However, *Koch et al.* (2009) and *Schwarz et al.* (2013) showed that most global models significantly deviate from observed global BC distributions. It is likely that the prescription of uniform BC aging timescales may be partially contributing to such biases. In this vein, *Shen et al.* (2014) optimized the fixed e-folding aging time of BC by fitting a global CTM results to HIPPO observations. They suggested that anthropogenic BC from East Asia ages much faster than one day, while the aging of biomass burning BC from Southeast Asia is much slower. Using another global CTM constrained by HIPPO observations, *Zhang et al.* (2015) pointed out that the optimized e-folding aging time following *Shen et al.* (2014) varies significantly for

BC emitted from different source regions, with less than half a day for BC emitted from the tropics and mid-latitudes and ∼1 week for BC emitted from high latitudes. Thus, a uniform BC aging time is likely not representative and can conceivably lead to large uncertainties.

In addition, field measurements have shown that a fixed e-folding time of 1–2 days underestimates the BC aging rate in polluted areas and is unrepresentative under complex atmospheric conditions. For example, *Johnson et al.* (2005) found that ambient BC particles that underwent aging for less than a few hours were heavily coated in Mexico City, primarily with ammonium sulfate. *Schwarz et al.* (2008) showed that 60–80% of BC particles are coated in fresh emissions from biomass burning sources. *Moffet and Prather* (2009) observed a BC aging time of ∼3 hours in Mexico City under photochemically active conditions. *Akagi et al.* (2012) showed that the fraction of coated BC particles produced from a chaparral fire in California increased up to ∼85% over a 4-hour period. Therefore, it is imperative to better capture BC aging rate under different atmospheric conditions in order to accurately estimate BC spatiotemporal distribution and consequently its radiative effects.

To that end, several global models have treated BC aging with size-resolved aerosol microphysics (e.g., *Jacobson*, 2010; *Aquila et al.*, 2011). Many global models still rely on relatively simple parameterizations for BC aging (e.g., *Riemer et al.*, 2004; *Liu et al.*, 2011; *Oshima and Koike*, 2013) in part for computational efficiency consideration. For example, *Riemer et al.* (2004) developed a BC aging parameterization in which aging rate was a function of total number concentration of secondary inorganic particles and internally mixed BC particles, representing the effects of condensation and coagulation processes. *Liu et al.* (2011) proposed another parameterization in which BC aging rate was a linear function of hydroxyl radical (OH) concentration (i.e., a fast-aging term representing condensation of sulfuric acid) with a constant slow-aging term (e.g., coagulation). *Croft et al.* (2005) and *Huang et al.* (2013) further employed these two parameterizations in a global model to estimate aging effects on BC budget and lifetime. However, there are limitations in these simplified aging parameterizations. The *Riemer et al.* (2004) parameterization was designed

specifically for domains dominated by fossil fuel emissions, which may not be suitable for application to a global scale. The *Liu et al.* (2011) formulation neglected the dependencies of BC aging on different condensable materials and their precursors (e.g., SO_2). Furthermore, under complex atmospheric conditions, these parameterizations likely introduce large uncertainties by lumping microphysical details of BC aging into a few parameters. Incorporating explicit microphysical representations of the BC aging process in global models may partially rectify and reduce the uncertainties.

In this study, we develop a "hybrid" microphysics-based BC aging scheme that accounts for condensation and coagulation processes in the GEOS-Chem global 3-D CTM. GEOS-Chem has been widely used to simulate BC in source regions (*Li et al.*, 2016), continental outflows (*Park et al.*, 2005), remote mountainous regions (*He et al.*, 2014b), the Arctic (*Wang et al.*, 2011), and remote oceans (*Wang et al.*, 2014a). Presently GEOS-Chem employs a fixed e-folding time of 1.2 days for the BC aging (*Park et al.*, 2003). We convert aerosol mass in the model to number concentration by assuming lognormal aerosol size distributions and explicitly compute the microphysical BC aging rate from the condensation of soluble materials onto hydrophobic BC and the coagulation between hydrophobic BC and preexisting hydrophilic particles. The "hybrid" microphysical aging scheme thus not only takes account of the microphysical aging processes but also avoids the use of full-fledged dynamic aerosol microphysics thereby retains the computational efficiency of the fixed e-folding time aging scheme. The "hybrid" microphysical aging scheme can be similarly applied in other CTMs. We systematically examine BC simulations using the aging scheme by comparison with the HIAPER Pole-to-Pole Observations (HIPPO) of BC during 2009–2011. We further analyze the effects of the aging scheme on global BC lifetime and budget. Finally, we quantify the uncertainties associated with key parameters in the aging scheme and the effects of chemical oxidation on BC aging.

5.2 Methods

5.2.1 Observations

We use the HIPPO aircraft measurements (*Wofsy*, 2011) of BC in this study. HIPPO (http://hippo.ornl.gov/) provides unique constraints on BC distributions from the surface up to $\sim$14 km across the Pacific from 67°S to 85°N latitudes. There were five deployments during 2009–2011 (Fig. 5.1, HIPPO 1: January 8–30, 2009; HIPPO 2: October 30 – November 22, 2009; HIPPO 3: March 24 – April 16, 2010; HIPPO 4: June 14 – July 11, 2011; HIPPO 5: August 9 – September 9, 2011). The refractory BC (rBC) mass concentration was measured by a single-particle soot photometer (SP2) that detects individual particles (*Schwarz et al.*, 2010, 2013). SP2 measures rBC in a mass range corresponding to volume-equivalent diameter range of about 90–550 nm assuming 1.8 g cc^{-1} void free density. This range contains about 90% of the total BC mass in the accumulation mode. The observed rBC concentration was scaled upwards by 10% to account for BC particles undetected by SP2 (*Schwarz et al.*, 2010) in this mode. rBC is experimentally equivalent to elemental carbon at the 15% level (*Kondo et al.*, 2011), and hence is equivalent to BC in the model. The effective detection limit (2σ level) is 0.01 ng kg^{-1} (0.1 ng kg^{-1}) for 15-minute (1-minute) sampling at low altitudes and increase to 0.05 ng kg^{-1} (0.5 ng kg^{-1}) at the higher altitudes (*Schwarz et al.*, 2013). The SP2 measurement of rBC mass is insensitive to non-BC mass and not influenced by other absorbing particles such as dust or non-absorbing species including salt and sulfate. *Schwarz et al.* (2013) determined a total systematic uncertainty of 30% associated with rBC mass concentration measured with the SP2. *Schwarz et al.* (2010, 2013) provided details of the BC measurement during HIPPO. We average the BC observations that are located within each model grid and over the model transport time step (15 minutes), thus ensuring a consistent spatiotemporal resolution for direct comparison with the model results.

5.2.2 Model description and simulations

In this study, we use the GEOS-Chem model (version 9-01-03) driven by assimilated meteorological fields from the Goddard Earth Observing System (GEOS-5) of the NASA Global Modeling and Assimilating Office (GMAO). GEOS-5 meteorological fields have a 6-hour temporal resolution (3 hours for surface variables and mixing depths), a native horizontal resolution of $0.50° \times 0.667°$, and 72 vertical layers (from the surface to 0.01 hPa). The spatial resolution is degraded to $2° \times 2.5°$ horizontally and 47 layers vertically for computational efficiency. GEOS-Chem includes a fully coupled treatment of tropospheric O_3-NO_x-VOC chemistry, sulfate-nitrate-ammonia and carbonaceous aerosols. *Park et al.* (2003) presented the first GEOS-Chem simulation of carbonaceous aerosols including BC and organic carbon (OC). The model also accounts for other aerosols including secondary organic aerosol (SOA), dust, and sea salt. GEOS-Chem uses a bulk aerosol scheme that separately tracks mass concentrations of different aerosol species (i.e., externally mixed). The model resolves hydrophobic and hydrophilic BC and OC, fine-mode (0.01–0.5 μm) and coarse-mode (0.5–8.0 μm) sea salt, dust in four size bins (0.1–1.0, 1.0–1.8, 1.8–3.0, and 3.0–6.0 μm), and five types of lumped SOA formed from different precursors. Aerosol and gas phase simulations are coupled through formation of sulfate, nitrate, and SOA, heterogeneous chemistry, and aerosol effects on photolysis rates. Details on the GEOS-Chem aerosol simulations are provided, respectively, by *Park et al.* (2003) for BC and OC, *Park et al.* (2004) for sulfate-nitrate-ammonia, *Liao et al.* (2007) for SOA, *Fairlie et al.* (2007) for dust, and *Alexander et al.* (2005) for sea salt.

5.2.2.1 A microphysics-based BC aging scheme

We assume that 80% of freshly emitted BC particles are hydrophobic (*Cooke et al.*, 1999; *Park et al.*, 2003). Recent observations (e.g., *Johnson et al.*, 2005; *Willis et al.*, 2016) showed that BC particles can be often coated with organics at emissions, suggesting that the hydrophobic fraction of freshly emitted BC particles depends on the amount and type

of coated organics. Thus, the assumed fresh hydrophobic BC fraction in this study could involve uncertainty, which requires further investigation. Presently BC aging process is not explicitly represented in GEOS-Chem. Instead, a fixed e-folding time (τ) of 1.2 days is assumed for the hydrophobic-to-hydrophilic BC conversion in the forms (*Park et al.*, 2003):

$$(\frac{dm_{BCPO}}{dt}) = -\frac{m_{BCPO}}{\tau} \tag{5.1}$$

$$(\frac{dm_{BCPI}}{dt}) = -(\frac{dm_{BCPO}}{dt}) \tag{5.2}$$

where m_{BCPO} and m_{BCPI} are the mass concentration of hydrophobic (BCPO) and hydrophilic BC (BCPI), respectively. In this study, we develop a microphysics-based BC aging scheme in the model by explicitly accounting for both condensation and coagulation processes. This microphysical aging scheme can be similarly applied in other CTMs. Additionally, we incorporate an experiment-based parameterization for BC aging through heterogeneous chemical oxidation (*Pöschl et al.*, 2001) for comparison and contrast.

Condensation

The condensation rate of a gaseous species (A) onto an individual particle can be expressed as follows (*Seinfeld and Pandis*, 2006):

$$J_{A,p} = 4\pi f(K_n, \alpha) R_p D_{f_A}(c_\infty - c_s) \tag{5.3}$$

$$f(K_n, \alpha) = \frac{1 + K_n}{1 + \frac{2K_n(1+K_n)}{\alpha}} \tag{5.4}$$

where $J_{A,p}$ is the condensation rate (mol s^{-1}) of A onto a particle, R_p represents the particle radius (m), D_{f_A} is the gas-phase diffusivity (m^2 s^{-1}) of A, c_∞ and c_s are gas-phase concentrations (mol m^{-3}) of A far from the particle and at the particle surface, respectively. K_n is the Knudsen number (i.e., ratio of air mean free path to particle radius), α is the accommodation coefficient (= 1 in this study), and $f(K_n, \alpha)$ is the correction factor for non-continuum

effects and imperfect surface accommodation based on the mathematical expression from *Dahneke* (1983). The mass of A condensing onto BCPO in a model grid per unit time, k_A, can be calculated by the product of the total available mass of A for condensing onto all pre-existing aerosols and the fraction of condensed mass partitioned to BCPO, which depends on condensation rate (J) and particle number concentration (N) as follows:

$$k_A = \frac{J_{A,BCPO,tot}}{\sum_{p_i=1}^{p_i=7} J_{A,p_i,tot}} M_{A,cond} = \frac{\int_0^\infty n_{BCPO}(R_{BCPO}) f_{BCPO}(K_n,\alpha) R_{BCPO} dR_{BCPO}}{\sum_{p_i=1}^{p_i=7} \int_0^\infty n_{p_i}(R_{p_i}) f_{p_i}(K_n,\alpha) R_{p_i} dR_{p_i}} M_{A,cond}$$

(5.5)

where p_i ($i = 1$–7) represents seven types of pre-existing aerosols (i.e., BCPO, BCPI, hydrophobic OC, hydrophilic OC, sulfate, fine-mode and coarse-mode sea salt) available for condensation, $J_{A,p_i,tot}$ is the condensation rate of A onto particle p_i, $M_{A,cond}$ is the total condensed mass of A in a model grid per unit time, R_{p_i} and n_{p_i} ($= \frac{dN_{p_i}}{dR_{p_i}}$) are the radius and number concentration distribution function of pre-existing particles, respectively. We account for condensation of gaseous sulfuric acid (H_2SO_4), nitric acid (HNO_3), ammonia (NH_3), and SOA onto pre-existing BC, OC, sulfate (SO_4^{2-}, NO_3^-, and NH_4^+), and sea salt aerosols. We do not include the condensation of soluble materials on dust particles, which may introduce some uncertainty.

GEOS-Chem tracks only aerosol mass concentration rather than number concentration that is required in Eq. (5.5). We convert aerosol mass concentration (m_{p_i}) to number concentration (N_{p_i}), assuming lognormal distributions for different aerosols following *Croft et al.* (2005) in the form:

$$N_{p_i} = \frac{m_{p_i}}{\rho_{p_i}} \left(\frac{\pi}{6} D_{p_i}^3 exp(\frac{9}{2} ln^2 \sigma_{p_i}) \right)^{-1}$$

(5.6)

where ρ_{p_i} is the particle density (1.8 g cm^{-3} for BC and OC, 1.7 g cm^{-3} for sulfate, and 2.2 g cm^{-3} for sea salt), D_{p_i} and σ_{p_i} are the geometric mean diameter and standard deviation of number size distribution, respectively. Following *Dentener et al.* (2006) and *Yu and Luo* (2009), we assume $D_p = 60$ nm and $\sigma_p = 1.8$ for BCPO and hydrophobic OC, and $D_p = 150$ nm and $\sigma_p = 1.8$ for BCPI and hydrophilic OC (Table 5.1). We use size distributions

from the Global Aerosol Dataset (GADS) (*Koepke et al.*, 1997) for sulfate ($D_p = 150$ nm, $\sigma_p = 1.6$), fine sea salt ($D_p = 200$ nm, $\sigma_p = 1.5$), and coarse sea salt ($D_p = 800$ nm, $\sigma_p = 1.8$). In order to analytically compute the integral in Eq. (5.5), we have assumed a constant correction factor $f(K_n, \alpha)$ for each type of aerosols with different sizes, which may introduce uncertainty in the computation. Under this assumption and using a lognormal aerosol size distribution, the integral can now be computed by following the mathematical identity:

$$\int_0^\infty n_{p_i}(R_{p_i}) R_{p_i} dR_{p_i} = N_{p_i} \frac{D_{p_i}}{2} exp(\frac{1}{2} ln^2 \sigma_{p_i}) \tag{5.7}$$

The hydrophobic-to-hydrophilic BC conversion rate (kg m^{-3} s^{-1}) due to condensation can be written as

$$(\frac{dm_{BCPO}}{dt})_{cond} = -\frac{F_{BCPO \to BCPI} m_{BCPO}}{\triangle t} \tag{5.8}$$

$$F_{BCPO \to BCPI} = \frac{\sum_{A_i=1}^{A_i=4} k_{A_i} \triangle t}{\beta M_{BCPO}} \tag{5.9}$$

where $F_{BCPO \to BCPI}$ represents the fraction of BCPO becoming BCPI through condensation of four types of soluble species A_i ($i = 1$–4, i.e., H_2SO_4, HNO_3, NH_3, and SOA) in a model time step ($\triangle t$). This implicitly assumes that different secondary aerosol species have the same hygroscopicity. We note that some SOA species could be less hygroscopic than ammonia sulfate (*Prenni et al.*, 2007). m_{BCPO} is BCPO mass concentration (kg m^{-3}), M_{BCPO} is the total BCPO mass (kg) in a model grid, and β is the condensation threshold (i.e., the mass fraction of condensed soluble materials on BCPO required for the hydrophobic-to-hydrophilic conversion). Following *Riemer et al.* (2004), we set $\beta = 5\%$ in the standard simulation based on hygroscopic growth behavior of aerosols (*Weingartner et al.*, 1997). After the hydrophobic-to-hydrophilic BC conversion, we lump the mass of secondary aerosol material coated on BC with those not mixed with BC in order to be compatible with the bulk aerosol scheme in GEOS-Chem, where the mass concentrations of different aerosol species are separately tracked. The lumping, instead of treating coating materials and hydrophilic BC together, only introduces small uncertainty, considering that the size distribution of

hydrophilic BC is similar to that of SOA and sulfate in this study (see Table 5.1). Further sensitivity analysis also show minor effects of the hydrophilic aerosol size distribution on global BC concentration and lifetime (see Sect. 5.4.3). The use of global uniform particle size distributions and β value can conceivably introduce large uncertainties. To quantify the uncertainties, we conduct additional model simulations by varying the size distribution and β value (see Table 5.1 and Sect. 5.4).

Coagulation

The coagulation rate ($J_{BCPO,X}$, m^{-3} s^{-1}) between BCPO and hydrophilic particles (X) can be expressed by (*Seinfeld and Pandis*, 2006)

$$J_{BCPO,X} = \gamma K_{BCPO,X} N_{BCPO} N_X \tag{5.10}$$

$$K_{BCPO,X} = 4\pi (R_{BCPO} + R_X)(D_{f_{BCPO}} + D_{f_X}) \tag{5.11}$$

where N_{BCPO} and N_X are number concentrations (m^{-3}) of BCPO and particle X computed from Eq. (5.6), $K_{BCPO,X}$ is the coagulation coefficient (m^3 s^{-1}) that depends on particle radius (R_{BCPO} and R_X) and Brownian diffusivities ($D_{f_{BCPO}}$ and D_{f_X}), and γ (from 0.014 for 0.001 μm particles to 1.0 for 1 μm particles) is a correction factor that accounts for kinetic effects of small particles. We use geometric mean radii for R_{BCPO} and R_X, which could introduce uncertainty for particle sizes largely deviating from the mean value. We note that the resulting uncertainty in BC concentration and lifetime is likely small, because model results show that coagulation only makes a small contribution to the total BC aging rate over the globe (see Sect. 5.3.1) and the global BC distribution is insensitive to aerosol size distribution in this study (see Sects. 5.4.2 and 5.4.3). The hydrophobic-to-hydrophilic BC conversion rate through coagulation can be written in the form:

$$(\frac{dN_{BCPO}}{dt})_{coag} = -\sum_{p_j=1}^{p_j=6} \gamma_{p_j} K_{BCPO,p_j} N_{p_j} N_{BCPO} \tag{5.12}$$

where p_j ($j = 1$–6) represents six types of hydrophilic particles, including sulfate-nitrate-ammonia, BCPI, hydrophilic OC, SOA, fine-mode and coarse-mode sea salt. We assume that BCPO is converted to BCPI upon coagulating with these hydrophilic aerosols. The resulting BCPO mass change per unit time (kg m^{-3} s^{-1}) is given by:

$$\left(\frac{dm_{BCPO}}{dt}\right)_{coag} = \frac{\pi}{6}\rho_{BCPO}D_{BCPO}^3 exp(\frac{9}{2}ln^2\sigma_{BCPO})\left(\frac{dN_{BCPO}}{dt}\right)_{coag} \tag{5.13}$$

Chemical oxidation

To account for the BC aging through ozone oxidation on the BC surface, we follow an experiment-based parameterization by *Pöschl et al.* (2001). The same parameterization has been used in previous studies (*Croft et al.*, 2005; *Huang et al.*, 2013). The chemical hydrophobic-to-hydrophilic BC conversion rate (kg m^{-3} s^{-1}) can be expressed by

$$\left(\frac{dm_{BCPO}}{dt}\right)_{chem} = -k_{chem}m_{BCPO} \tag{5.14}$$

where k_{chem} is the reaction rate coefficient (s^{-1}) given by

$$k_{chem} = \frac{\lambda K_\infty K_{O_3}[O_3]}{1 + K_{O_3}[O_3] + K_{H_2O}[H_2O]} \tag{5.15}$$

where K_∞ (= 0.015 s^{-1}) is the pseudo-first-order decay rate coefficient in the presence of high ozone concentrations, K_{O_3} (= 2.8×10^{-13} cm^3) and K_{H_2O} (= 2.1×10^{-17} cm^3) are the adsorption rate coefficients of O$_3$ and H$_2$O, which are a function of available adsorption sites residence time, and sticking coefficients of O$_3$ and H$_2$O on BC surface. λ (= 0.01) is the physical shielding factor that accounts for the fact that the oxidized coating material is not distributed homogenously over the BC particle surface (*Croft et al.*, 2005). [O$_3$] and [H$_2$O] are atmospheric concentrations (molec cm^{-3}) of O$_3$ and H$_2$O, respectively.

Recent experimental studies also confirmed that BC can be aged through heterogeneous chemical oxidation by O$_3$ (*Decesari et al.*, 2002; *Zuberi et al.*, 2005) and NO$_2$ (*Khalizov et al.*, 2010), which results in the formation of soluble organic compounds on BC particle surface.

However, none of these recent studies have given explicit quantitative parameterizations for BC chemical aging, which can be applied in modeling studies. Moreover, experimental results presented in these studies vary substantially, suggesting that BC chemical aging process could involve large uncertainty. For this reason, the parameterization scheme developed by *Pöschl et al.* (2001) should be used with caution.

Total BC aging rate

We assume a linear combination of the condensation, coagulation, and chemical oxidation processes, following *Croft et al.* (2005) and *Huang et al.* (2013). The total BC aging rate can thus be expressed in the forms:

$$(\frac{dm_{BCPO}}{dt})_{mic} = (\frac{dm_{BCPO}}{dt})_{cond} + (\frac{dm_{BCPO}}{dt})_{coag} \tag{5.16}$$

$$(\frac{dm_{BCPO}}{dt})_{mic+chem} = (\frac{dm_{BCPO}}{dt})_{mic} + (\frac{dm_{BCPO}}{dt})_{chem} \tag{5.17}$$

where the subscripts *mic* and *chem* represent microphysical and chemical aging, respectively. Such linear combination may overestimate BC aging rate, because these processes likely compete with each other rather than occur independently (*Croft et al.*, 2005). However, no observational evidence is currently available to quantify interactions among these processes.

5.2.2.2 BC emissions

We use a global anthropogenic BC emission inventory developed by *Wang et al.* (2014b) (hereinafter the PKU-BC inventory), with an annual emission of 8.5 TgC for 2008. PKU-BC incorporates a recent global high-resolution ($0.1° \times 0.1°$) fuel combustion dataset (*Wang et al.*, 2013) that covers 64 types of combustion based on local or national fuel statistics. The dataset significantly improves the spatial resolution of emission distribution for large countries. In addition, the inventory uses updated BC emission factors based on up-to-date measurements, particularly for developing countries (*Wang et al.*, 2012a,b). The use of

local and subnational fuel data and updated emission factors results in 70% higher global anthropogenic BC emissions than previous bottom-up inventories (4.9 ± 0.4 TgC) (*Dentener et al.*, 2006; *Bond et al.*, 2007; *Lamarque et al.*, 2010; *Granier et al.*, 2011) yet still 20% lower than top-down estimates (*Bond et al.*, 2013). The PKU-BC emissions are 58% higher than the global anthropogenic emissions used in our previous studies (*He et al.*, 2014b,a). *Wang et al.* (2014b) found that using PKU-BC reduces the bias in modeled surface BC concentrations by up to 25% in Asia, Africa, and Europe. However, *Bond et al.* (2013) pointed out that current anthropogenic BC emission estimates are associated with large uncertainties (more than a factor of 2 across different inventories). Based on a Monte Carlo estimation, *Wang et al.* (2014b) showed an uncertainty range (interquartile) of -40% to +70% for global annual anthropogenic BC emissions in PKU-BC, where errors in emission factors dominate the overall uncertainty.

We use the Global Fire Emissions Database version 3 (GFED3) (*Van der Werf et al.*, 2010) for global biomass burning emissions, which now includes small fire emissions (*Randerson et al.*, 2012). Carbon emissions in GFED3 increase by 35% globally when small fires are included. In this study, the GFED3 emissions with a 3-hour temporal resolution are used. The uncertainty in GFED3 is $\geq$20% globally and highest in boreal regions and Equatorial Asia, primarily because of insufficient data on fuel load, emission factor, and burned area (*Van der Werf et al.*, 2010; *Randerson et al.*, 2012).

5.2.2.3 BC deposition

Aerosol dry deposition follows a standard resistance-in-series scheme (*Wesely*, 1989), which depends on local surface type and meteorological conditions, as implemented by *Wang et al.* (1998). *Wang et al.* (2011) further updated aerosol dry deposition velocity over snow- and ice-covered regions for improved BC simulations in GEOS-Chem. They applied a constant value of 0.03 cm s^{-1}, within the range (0.01–0.07 cm s^{-1}) employed in previous studies (*Liu et al.*, 2011). In the GEOS-Chem simulations presented here, dry deposition accounts for

~20% of global BC deposition, consistent with the results (17–23%) from previous studies using GEOS-Chem (*He et al.*, 2014b; *Wang et al.*, 2014a) and that (21.4±17%) from the AeroCom multi-model study (*Textor et al.*, 2006).

Liu et al. (2001) first described aerosol wet scavenging in GEOS-Chem. *Wang et al.* (2011) updated in the model the below-cloud scavenging parameterization for fine and coarse aerosol modes by distinguishing between aerosol removals by snow and by rain. Different in-cloud scavenging schemes have also been applied to cold and warm clouds, with an improved areal fraction of model grids that experience precipitation (*Wang et al.*, 2011). Following *Wang et al.* (2014a), we further update in-cloud scavenging of water-soluble aerosols by accounting for homogeneous and heterogeneous freezing nucleation in cold clouds.

5.2.2.4 Model simulations

To investigate the effects of the microphysics-based BC aging scheme, we first conduct two GEOS-Chem BC simulations with the fixed aging (e-folding time of 1.2 days) scheme (FIX, Table 5.1; see also Eq. (5.1)) and the standard microphysics-based scheme (MP$_{\text{STD}}$, Table 5.1; see also Eq. (5.16)). In addition, we conduct 11 sensitivity simulations for the microphysics-based scheme to quantify the effects of chemical oxidation on BC aging and the uncertainty associated with aerosol size distribution and condensation threshold in the microphysics-based scheme. Specifically, we combine the standard microphysics-based scheme with the *Pöschl et al.* (2001) parameterization for chemical oxidation to examine the effects of chemical oxidation on BC aging (MP$_{\text{chem}}$, Table 5.1; see also Eq. (5.17)). We use geometric mean diameters of 30 nm and 90 nm for BCPO number size distribution as lower and upper bounds (D$_{\text{BCPO}}$30 and D$_{\text{BCPO}}$90, Table 5.1), following *Bond et al.* (2006), instead of 60 nm in the standard simulation (i.e., MP$_{\text{STD}}$). We use geometric standard deviations of 1.4 and 2.0 for BCPO number size distribution as lower and upper bounds (SD$_{\text{BCPO}}$1.4 and SD$_{\text{BCPO}}$2.0, Table 5.1), following *Bond et al.* (2006), instead of 1.8 in the standard simulation. We vary the geometric mean diameters and standard deviations of all hydrophilic particles'

number size distribution in the standard simulations by $\pm 50\%$ (D_{PI}+50% and D_{PI}-50%, Table 5.1) and ± 0.2 (SD_{PI}+0.2 and SD_{PI}-0.2, Table 5.1). We vary the condensation threshold (β in Eq. (5.9)) from 5% in the standard simulation to 2.5% (BETA2.5, Table 5.1) and to 10% (BETA10, Table 5.1). Model results used for comparison with HIPPO observations are sampled along the HIPPO flight tracks.

5.3   Results and discussions

5.3.1   BC aging rate

Figure 5.2 shows model simulated surface-layer and zonal distributions of annual mean aging rate with the fixed (r_{fix}, calculated by Eq. 5.1) and microphysics-based (r_{mic}, calculated by Eq. 5.16) aging schemes. The maximum rates are in the surface layer over major BC source regions such as Eastern China, India, Europe, eastern United States, and tropical Africa, ranging from less than 100 ngC m^{-3} h^{-1} for the fixed scheme (Fig. 5.2) to 100–500 ngC m^{-3} h^{-1} for the microphysics-based scheme (Fig. 5.2). r_{mic} is 2–6 times higher than r_{fix} throughout the year over both continents and oceanic areas with heavy marine traffic. This is primarily because of the strong anthropogenic emissions of SO_2, NO_X, and NH_3 in major continents and along shipping corridors in the Northern Hemisphere (*Park et al.*, 2004) and biomass burning emissions of SOA precursors in tropical continents (*Guenther*, 2006). These emissions lead to fast BC aging through both condensation of soluble materials (i.e., H_2SO_4-HNO_3-NH_3 and SOA) and coagulation with hydrophilic particles.

Figure 5.3 shows the probability density function (PDF) of simulated annual mean BC e-folding aging time (τ in Eq. 5.1) over the globe. The first PDF peak around $\tau = 8$ h represents the fast aging near source regions, while the second bump corresponds to $\tau = $ ~1 day, which reflects the aging over rural areas and in the middle troposphere. The third small bump is around $\tau = 100$ h, mainly representing the very slow aging in remote regions (e.g., Polar regions and the upper troposphere). The microphysics-based scheme results in

an e-folding BC aging time of 0.6–2 hours in summer and 1–3 hours in winter when averaged within the boundary layer over major anthropogenic source regions including Eastern China, eastern United States, and Europe. These are much faster than the timescale of 1–2 days typically assumed in many global models (*Chung and Seinfeld*, 2002; *Koch et al.*, 2009; *He et al.*, 2014b). Such fast aging for anthropogenic BC has been reported in previous studies. For example, *Riemer et al.* (2004) used a size-resolved aerosol model to show an e-folding BC aging time of about 2 hours during the day from 250 to 1500 m above source (urban) regions for both summer and winter. *Jacobson* (2010) also reported a ~3-hour e-folding aging time for fossil-fuel BC based on a global size-resolved aerosol model. *Shen et al.* (2014) found that the e-folding aging timescale of anthropogenic BC from East Asia is several hours, based on constraints from the HIPPO observations. In addition, *Akagi et al.* (2012) observed that about 20% of BC ages within one hour after emission in a biomass-burning plume over California in November 2009, whereas our microphysics-based scheme shows a mean BC aging rate of 24% h^{-1} within the same region and time period. *Moteki et al.* (2007) measured a BC aging rate of 2.3% h^{-1} downwind of an urban area in Japan in March 2004. Though not a direct comparison, our microphysics-based scheme results in a BC aging rate of 10% h^{-1} averaged over the same region for March 2009.

r_{mic} decreases by several orders of magnitude with increasing altitude and from continents to remote oceans and the polar regions (Fig. 5.2). r_{fix} is a factor of 1.5–4 lower than r_{mic} below 900 hPa in the tropics and middle latitudes, but more than 5 times higher in the polar regions, remote oceans, and above 800 hPa throughout the year. The annual mean r_{mic} is 50% higher than r_{fix} in the middle to lower troposphere but more than fivefold lower in the middle to upper troposphere (Table 5.2). Because the aging rates in remote regions are vanishingly small, the difference in global BC distribution between the two aging schemes is thus dominated by the difference in the significantly larger aging rates over the source regions (see Sect. 5.3.3).

Figure 5.4 shows that condensation dominates (>70%) BC aging globally, particularly

113

in the middle to upper troposphere (500–200 hPa) and in the southern high latitudes. In contrast, the contribution from coagulation is <15% throughout much of the globe, with the exception of about 30% over Eastern China, India, and central Africa, where relatively abundant hydrophilic aerosols are available. This is primarily because hydrophilic aerosols are substantially removed by wet scavenging during the transport to remote regions, thus reducing the coagulation between hydrophobic BC and hydrophilic particles. The H_2SO_4-HNO_3-NH_3 condensation dominates (>70%) the total condensation in the northern low and middle latitudes throughout the troposphere and in the southern middle latitudes below 800 hPa. This is largely explained by strong anthropogenic emissions of SO_2 and NO_x in the Northern Hemisphere (*Park et al.*, 2004) and global oceanic emissions of dimethylsulfide (DMS) (*Lana et al.*, 2011). The SOA condensation, however, contributes to more than 80% of the total condensation over tropical continents dominated by biomass burning emissions and the southern extratropics above 700 hPa, where rather limited sulfuric acid is produced.

5.3.2 Model evaluation with HIPPO observations

Figure 5.5 shows the PDF of observed and simulated BC concentrations during the HIPPO measurements. Model results from the fixed aging scheme significantly overestimate BC concentrations, with a PDF peak at about 15 ng kg^{-1} (corresponding to BC in the northern extratropics) that is an order of magnitude higher than the observations. The microphysics-based aging scheme substantially reduces the discrepancy between modeled and observed PDFs, particularly at BC concentrations of <1 ng kg^{-1} and 10–50 ng kg^{-1}. The remaining model bias at extremely low BC concentrations (<0.1 ng kg^{-1}), corresponding to regions remote from combustion influence and highly influenced by tropical convection, likely reflects the inefficient BC wet scavenging in the model (*Wang et al.*, 2014a). Statistical analysis shows that compared with the fixed aging scheme, the microphysics-based aging scheme reduces the percentages of modeled BC concentrations that are more than a factor of 10 and 4 higher/lower than the observations from 28% to 16% and from 53% to 37%, respectively,

with a better model-observation correlation as well (Fig. 5.6). The median BC concentration (6.6 ng kg^{-1}) from the fixed aging scheme is biased high by a factor of four compared with the observations (1.6 ng kg^{-1}), while the microphysics-based median concentration (3.5 ng kg^{-1}) reduces the bias by a factor of two.

Figure 5.7 shows the median vertical profiles of BC concentration in different latitude bands from HIPPO observations and model simulations. The median in the northern extra-tropics (20°–90°N) is 5–10 ng kg^{-1} near the surface and decreases to <1 ng kg^{-1} above 200 hPa, while the concentration is a factor of 2–10 lower in tropical regions and Southern Hemisphere throughout the troposphere. This is because of strong BC emissions in the Northern Hemisphere and strong wet scavenging of BC during transport to the tropics and Southern Hemisphere, particularly by tropical deep convection (*Wang et al.*, 2014a). Model results using the fixed aging scheme generally capture the spatiotemporal pattern of BC median vertical profiles in the northern extratropics, but overestimate the magnitude by a factor of ~5 on average (Fig. 5.7). The largest model-observation absolute discrepancies (>20 ng kg^{-1}) are at 900–400 hPa during non-winter seasons. The microphysics-based aging scheme reduces that discrepancy by 2–3 times across different altitudes in the northern extratrop-ics, particularly at 900–300 hPa (Fig. 5.7). This is a result of the faster BC aging from the microphysics-based scheme over source regions in the Northern Hemisphere (Fig. 5.2), which increases the amount of hydrophilic BC removed by wet scavenging during the transport to the free troposphere.

In the tropics (20°S–20°N), the median BC concentration is generally less than 1 ng kg^{-1}, with small variations across different altitudes and seasons (Fig. 5.7). Model results using the microphysics-based aging scheme reproduce the observed BC vertical distributions in different seasons with discrepancies of <0.5 ng kg^{-1}, except for a 50% underestimate in the lower troposphere (Fig. 5.7). This could be due to the overestimate in GEOS-5 precipitation fields over the tropics (*Molod et al.*, 2012). Compared with the microphysics-based aging scheme, model results from the fixed aging scheme overestimate BC concentration by more

than fivefold above 800 hPa in the tropics, particularly in summer and fall. This is primarily because of the slow BC aging over tropical source regions in the fixed aging scheme, resulting in insufficient BC wet removal and thus excessive BC transported to the free troposphere.

In the Southern Hemisphere (20°–70°S), the microphysics-based aging scheme improves the modeled median BC vertical profiles by a factor of 2–4 throughout all altitudes and seasons (Fig. 5.7) with the largest improvement at 600–200 hPa, compared with the fixed aging scheme. However, the microphysics-based model results still overestimate the BC concentration above 300 hPa by about 3 times in the Southern Hemisphere, probably due to inefficient in-cloud scavenging of BC in the model for ice clouds or mixed-phase clouds at such high altitudes. However, we note that the ability of BC to be ice nuclei is largely uncertain. For example, *Cozic et al.* (2008) suggested that BC particles can act as efficient ice nuclei based on observations in mixed-phase clouds, whereas *Friedman et al.* (2011) showed that BC particles are unlikely to serve as ice nuclei efficiently in cold clouds based on laboratory experiments.

Figure 5.8 shows the observed and model simulated latitudinal and seasonal BC column burden averaged along the HIPPO flight tracks. The lowest burden is in the tropics due to strong wet scavenging by deep convection. It is two orders of magnitude lower than that in the extratropical Northern Hemisphere. The burden in the Southern Hemisphere is minimum in spring because of the wet season in the southern low latitudes (*Wang and Ding*, 2008), while the burden in the Northern Hemisphere is maximum during the same period when the impact of Asian outflow on the Pacific peaks (*Schwarz et al.*, 2013). Model results using the fixed aging scheme capture the latitudinal and seasonal trend for the observations, but significantly overestimate the magnitude with a mean positive bias of 194%, particularly in the Northern Hemisphere during summer and fall, as a result of the model overestimate of BC vertical profiles in the Northern Hemisphere (Fig. 5.7). The microphysics-based aging scheme reduces the model overestimate at most latitudes throughout the year, with a mean positive bias of 60% and a correlation coefficient (r) of 0.85 with observations. The largest

improvement from the microphysics-based scheme is in the tropics (Fig. 5.8), except in January.

Therefore, the microphysics-based aging scheme substantially improves BC simulations pole-to-pole over the Pacific during HIPPO, both spatially and temporally, compared with the fixed aging scheme. The remaining model-observation discrepancy, particularly in the northern extratropics and the upper troposphere, is likely a result of the uncertainty associated with BC emissions, wet scavenging, and model meteorological fields (*Molod et al.*, 2012; *Bond et al.*, 2013; *Wang et al.*, 2014a). We note that it is important to quantify the contribution of these factors to the model-observation discrepancies, which will be investigated in our future study. Additionally, the spatiotemporal variability of the observed BC concentration is significantly large within each altitude and latitude band (Fig. 5.7), suggesting a strong dependence of BC vertical profile on sampling location and time during the HIPPO aircraft measurements.

5.3.3 Global BC distribution and budget

Figure 5.9 shows the annual mean global BC column burden from model results using the fixed and microphysics-based BC aging schemes. Both schemes result in a similar spatial distribution of BC burden, with highest values over source regions and lowest values in the southern hemispheric oceans. However, BC burden from the microphysics-based scheme is much smaller than that from the fixed scheme globally, with the major difference over source regions throughout the year. This is because the maximum enhancement of BC aging rate from the microphysics-based scheme is over source regions (Fig. 5.2), where there is a 20–60% increase of the hydrophilic BC fraction in total BC particles relative to the fixed aging scheme. The faster hydrophobic-to-hydrophilic conversion leads to a stronger BC wet removal for the microphysics-based aging scheme. As a result, the global annual mean BC load is 0.24 mg m^{-2} in the microphysics-based scheme, consistent with the result (0.23±0.07 mg m^{-2}) from the AeroCom multi-model study (*Schulz et al.*, 2006). It is also comparable

to the value (0.25 mg m^{-2}) reported by *Jacobson* (2010), which accounted for size-resolved aerosol microphysical processes. *Bond et al.* (2013) reported a much higher BC load (0.55 mg m^{-2}) based on top-down estimated BC emissions that are 70% larger than the emissions used in this study. The resulting global BC lifetime of 4.2 days from the microphysics-based scheme is within the range (3.2–9.9 days) from previous studies (Table 5.2).

Figure 5.9 also shows model simulated annual zonal mean BC concentration. The concentration decreases substantially from the surface in the northern middle latitudes to high altitudes and the polar regions, varying by three orders of magnitude. The concentration from the microphysics-based aging scheme is smaller than that from the fixed aging scheme at different latitudes and altitudes, with the largest difference (>400 ng m^{-3}) in the northern middle latitudes. Although the microphysical aging rate is much lower than the rate from the fixed aging scheme in the middle and upper troposphere and the polar regions (Fig. 5.2), the faster microphysical aging over source regions dominates the aging effects on global BC distribution, resulting in a substantial reduction of BC concentration globally. As a result, the fraction of global BC load above 5 km is 7.3% for the microphysics-based scheme, which is close to the lower bound of the range (6.1–40%) from previous studies (e.g., *Schulz et al.*, 2006; *He et al.*, 2014a; *Wang et al.*, 2014a). The relatively low BC load at high altitudes in the microphysics-based scheme has a significant implication for global BC radiative effects. *Samset et al.* (2013) showed that more than 40% of global BC direct radiative forcing is contributed by BC particles above 5 km, whereas this estimate has large uncertainties across various models. BC particles at high altitudes could also affect the formation and distribution of cirrus clouds and thus BC indirect radiative effects (e.g., *Liu et al.*, 2009).

5.4 Uncertainty analysis

5.4.1 Heterogeneous chemical oxidation

Figure 5.10 shows the annual mean contribution of chemical oxidation to the total BC aging rate. The contribution is 10–30% below 900 hPa over most regions at 60°S–60°N latitudes, particularly at low latitudes and over source regions, due partly to the strong condensation-coagulation in these areas. Additionally, the relatively high humidity and low ozone concentration also contribute to less efficient chemical oxidation aging in the lower troposphere and the tropics, compared with the middle troposphere and the polar regions (Fig. 5.10). There is efficient chemical oxidation aging over the Arctic and Antarctic in the middle troposphere, where water vapor is scarce and relatively abundant ozone is available. This is consistent with the conclusion from *Huang et al.* (2013), which used the same chemical oxidation scheme and showed the lowest chemical aging rate over the tropics at lower altitudes and faster aging at higher altitudes including the polar regions.

Compared with the standard microphysics-based aging scheme (MP$_{\text{STD}}$), incorporating chemical oxidation (MP$_{\text{chem}}$) slightly ($<$5%) increases the total BC aging rate at 60°S–60°N latitudes in the lower troposphere but more than halves the aging rate over the polar regions (Figs. 5.11 and 5.12). This is because faster BC aging over non-polar regions reduces the amount of hydrophobic BC transported to remote areas. However, the absolute aging rate over the polar regions is several orders of magnitude smaller than that in non-polar regions. Chemical oxidation aging thus has a vanishingly small ($<$0.5%) impact on the global annual mean BC aging rate (Table 5.2). It leads to only a small ($<$1%) reduction in BC column burden and zonal mean concentration globally (Figs. 5.13 and 5.14) as well as global BC lifetime (Table 5.2). *Croft et al.* (2005) showed a comparably small ($\sim$5%) decrease in global BC burden and lifetime when the chemical oxidation process is included, while *Huang et al.* (2013) found a $\sim$10% decrease in BC burden and lifetime with the incorporation of chemical oxidation aging.

5.4.2 Size distribution of hydrophobic BC

Reducing the geometric mean diameter of hydrophobic BC from 60 to 30 nm (D_{BCPO}30) and the standard deviation from 1.8 to 1.4 (SD_{BCPO}1.4) increases hydrophobic BC number concentration. As a result, more hydrophobic BC particles are available for condensation-coagulation aging, leading to a 5–50% increase of condensation-induced aging rate within 60°S–60°N below 900 hPa. The enhancement of aging rate is stronger for SD_{BCPO}1.4 than for D_{BCPO}30, suggesting that the condensation-induced aging is more sensitive to the change in geometric standard deviation than geometric mean diameter. Interestingly, the largest enhancement for both simulations is over the oceans, while only less than 10% increase occurs in the source regions. This is probably because the BC aging rate over the oceans is much smaller than that over the source regions (Fig. 5.2), making it more sensitive to the change in the size distribution of hydrophobic BC.

D_{BCPO}30 increases the coagulation-induced aging rate by up to a factor of 2 within 60°S–60°N near the surface, particularly in source regions, whereas SD_{BCPO}1.4 only increases the coagulation-induced surface-layer aging rate along shipping corridors over the oceans, with up to 50% decrease in the rest of non-polar regions. In the middle to upper troposphere and the polar regions, both D_{BCPO}30 and SD_{BCPO}1.4 result in a more than 50% decrease in coagulation-induced and condensation-induced BC aging rates, because of the reduction in the amount of hydrophobic BC transported to remote regions. The change in total BC aging rate shows a very similar spatial pattern with that of condensation (Figs. 5.11 and 5.12), due to the dominant role of condensation-induced aging globally. However, because of the rather low BC aging rate over the oceans and at high altitudes relative to that over source regions, the impact of hydrophobic BC size distribution on global BC distribution is dominated by the change of aging rate in source regions for both D_{BCPO}30 and SD_{BCPO}1.4, which results in less than 5% reductions in BC column burden and zonal mean concentration globally, except a 10–20% reduction in the tropics at 600–200 hPa (Figs. 5.13 and 5.14). The resulting global annual mean BC load and lifetime show negligible (<1%) increases (Table

5.2).

Increasing the geometric mean diameter of hydrophobic BC from 60 to 90 nm ($D_{BCPO}90$) and the standard deviation from 1.8 to 2.0 ($SD_{BCPO}2.0$) decreases hydrophobic BC number concentration. Both simulations exhibit opposite patterns of the change in BC aging rate compared with those from $D_{BCPO}30$ and $SD_{BCPO}1.4$, because of lower hydrophobic BC number concentrations in the former two. Nevertheless, similar to $D_{BCPO}30$ and $SD_{BCPO}1.4$, $D_{BCPO}90$ and $SD_{BCPO}2.0$ also result in less than 10% change in global BC column burden and zonal mean concentration. We note that the observationally constrained accumulation mode BC mass size distributions for HIPPO have a geometric mean diameter of about 180 nm (*Schwarz et al.*, 2010), which is the upper bound value used in this study for the geometric mean diameter of mass size distribution (60–180 nm) converted from that of number size distribution (30–90 nm).

5.4.3 Size distribution of hydrophilic aerosols

Increasing the geometric mean diameters of all hydrophilic aerosols by 50% ($D_{PI}+50\%$) and the standard deviations by 0.2 ($SD_{PI}+0.2$) reduces the number concentration of hydrophilic particles. This results in an enhanced condensation-induced aging rate due to fewer hydrophilic particles competing for condensed soluble materials, but a reduced coagulation-induced aging rate due to fewer hydrophilic particles available for coagulating with hydrophobic BC. Both simulations show up to 50% increase in the annual mean condensation-induced BC aging rate at 60°S–60°N below 900 hPa, particularly over the oceans where BC aging rate is relatively small. The faster aging through condensation in the lower troposphere reduces the amount of hydrophobic BC transported to higher altitudes and the polar regions, resulting in more than 50% slower condensation-induced aging in remote regions. In contrast, the coagulation-induced aging rate decreases globally, by 20–50% at 60°S–60°N near the surface and more than 50% in elsewhere. The change of total BC aging rate follows the spatial pattern of the condensation-induced aging rate (Figs. 5.11 and 5.12). The global annual mean

BC aging rate is slightly higher ($\sim$1.5%) in both D_{PI}+50 and SD_{PI}+0.2. Figures 5.11 and 5.12 show that increasing geometric mean diameters and standard deviations of hydrophilic particles only reduces global BC column burden and zonal mean concentration by less than 10% and BC lifetime by less than 1% (Table 5.2).

Decreasing the geometric mean diameters of hydrophilic aerosols by 50% (D_{PI}-50%) and the standard deviations by 0.2 (SD_{PI}-0.2) increases the number concentration of hydrophilic particles, resulting in an opposite spatial pattern of the change in BC aging rate than that from D_{PI}+50% and SD_{PI}+0.2. Both condensation-induced and coagulation-induced aging rates are more sensitive to the decrease of geometric mean diameters (D_{PI}-50%) than geometric standard deviations (SD_{PI}-0.2) globally. The resulting BC concentration change is less than 10% over much of the globe, with a <2% increase in global BC load and lifetime (Table 5.2).

5.4.4 Condensation threshold

The condensation-induced BC aging rate is critically dependent on the condensation threshold β (see Eq. (5.9)), which represents the mass fraction of condensed soluble materials on hydrophobic BC required for hydrophobic-to-hydrophilic BC conversion. Reducing β by a factor of 2 (BETA2.5) increases the condensation-induced aging rate by 5–10% near source regions and by up to 50% over remote oceans at 60°S–60°N, while the condensation-induced aging rate decreases by 20–50% in the middle and upper troposphere and more than 80% over the polar regions, because of the reduced amount of hydrophobic BC transported to remote areas. The change in total BC aging rate follows the pattern of the change in condensation-induced aging rate, with major increases at 60°S–60°N below 900 hPa (Figs. 5.11 and 5.12). This results in a decrease (<20%) of BC concentration globally, particularly in the tropics at 600–200 hPa (Figs. 5.13 and 5.14). In contrast, doubling β (BETA10) shows the opposite spatial pattern of the change in BC aging rate compared with BETA2.5, where the aging rate decreases by up to 20% in the non-polar regions below 900 hPa but increases by up to

more than twofold at high altitudes and polar regions. The resulting global BC load and lifetime, however, change by less than 2% for both BETA10 and BETA2.5 (Table 5.2).

There is strong spatial heterogeneity in the sensitivity of microphysical BC aging to aerosol size distribution, condensation threshold, and chemical oxidation, with little sensitivity over the source regions but rather large sensitivity in remote regions. However, the BC aging rate in remote areas is several orders of magnitude smaller than that over source regions. As a result, the global BC column burden and zonal mean concentration are only slightly affected by the change in the above-mentioned factors, with less than 5% change over much of the globe (Figs. 5.13 and 5.14). Very small changes are also seen in global BC lifetime (Table 5.2). Nevertheless, using a uniform aerosol size distribution and condensation threshold may not be realistic or representative, particularly on a regional scale with complex atmospheric conditions. The two-/three-moment aerosol scheme (*Li et al.*, 2008), which predicts aerosol size distribution from simulated aerosol mass, number, and/or surface area depending on atmospheric conditions, could be a potential improvement to represent and understand BC aging, interaction with cloud, and deposition compared with the microphysical scheme developed in this study.

5.5 Conclusions

We have developed and examined a microphysics-based BC aging scheme that explicitly accounts for condensation and coagulation processes in GEOS-Chem global CTM. We analyzed the difference in BC aging rate between the microphysics-based scheme and a fixed aging scheme with an e-folding time of 1.2 days, followed by a systematic evaluation of BC simulations using HIPPO observations from 2009 to 2011. We further analyzed the effects of the microphysics-based aging scheme on global BC distribution and lifetime. Finally, we quantified the uncertainty associated with aerosol size distribution and condensation threshold in the microphysics-based aging scheme and the impact of heterogeneous chemical oxidation

on BC aging.

In the microphysics-based BC aging scheme, we converted aerosol mass to number concentration by assuming lognormal aerosol size distributions. We computed the condensation-induced aging rate from the condensation of soluble materials onto hydrophobic BC, which converted hydrophobic to hydrophilic BC when the condensed mass reached the condensation threshold (β in Eq. (5.9)). We computed the coagulation-induced aging rate from the coagulation between hydrophobic BC and hydrophilic particles, assuming a hydrophobic-to-hydrophilic BC conversion upon coagulating. This microphysics-based scheme thus incorporated an explicit microphysical representation of BC aging and retained the computational efficiency of the fixed aging scheme. The microphysical aging scheme can also be applied in other CTMs.

The microphysical aging rate was a factor of 2–6 higher than that from the fixed aging scheme in the lower troposphere over such source regions as East China, India, Europe, United States, tropical continents, and marine shipping corridors, because of strong emissions of sulfate-nitrate and SOA precursors, which resulted in faster BC aging through condensation and coagulation. The microphysical aging rate is more than fivefold lower than that from the fixed aging scheme in remote regions, where condensation and coagulation are rather weak. We found that condensation dominated (>70%) BC aging globally, particularly in the Southern Hemisphere and above 5 km, while the largest coagulation contribution ($\sim$30%) was over East China, India, and Central Africa, primarily because the hydrophilic aerosols required for coagulation were substantially removed by wet scavenging during transport to remote regions.

Compared with the fixed aging scheme, the microphysical scheme substantially reduced the discrepancy between modeled and observed probability density functions of BC concentrations during HIPPO, particularly at BC concentrations of <1 ng kg^{-1} and 10–50 ng kg^{-1}. Model results using the fixed aging scheme overestimated BC median vertical profiles in the northern extratropics by about 5 times on average, while the microphysical scheme

improved the modeled BC vertical profiles by a factor of 2–3 throughout the troposphere, particularly at 900–300 hPa. Model results using the microphysical aging scheme reproduced the observed BC vertical distribution in the tropics. In the Southern Hemisphere, the microphysical aging scheme reduced the model bias in BC vertical profiles by a factor of 2–4, with largest improvements at 600–200 hPa, compared with the fixed aging scheme. The model bias in latitudinal BC column burden along the HIPPO flight tracks was reduced from +194% for the fixed aging scheme to +60% for the microphysics-based scheme, with largest improvements in the tropics. The remaining model-observation discrepancy for the microphysics-based simulation was likely due to the uncertainty associated with BC emissions, wet scavenging, and meteorological fields in the model. We note that it is also very important to evaluate BC simulations from other perspectives in addition to atmospheric concentration, such as aerosol optical depth, a subject requiring further investigation.

We found that the faster BC aging over the source regions from the microphysics-based scheme dominated the aging effects on global BC distribution, resulting in a much lower BC column burden and zonal mean concentration globally, compared with the fixed aging scheme. The global annual mean BC lifetime was 4.2 days in the microphysics-based scheme, where wet scavenging accounts for 80.3% of global BC deposition. The resulting global BC burden was 0.25 mg m^{-2}, with 7.3% of the burden above 5 km. The relatively low BC load at high altitudes had important implications on the estimate of global BC radiative effects.

Furthermore, we found that BC aging rate was insensitive ($<10\%$ change) to aerosol size distribution, condensation threshold, and chemical oxidation over source regions, while it was the opposite (more than twofold change) in the polar regions and at high altitudes. However, the BC aging rate in remote regions was orders of magnitude lower than that in source regions. Thus, the global BC burden and lifetime showed little sensitivity ($<5\%$ change) to the above-mentioned three factors. Nevertheless, assuming global uniform aerosol size distribution and condensation threshold may not be representative or accurate, particularly for regions with complex atmospheric conditions. Further improvements require the

incorporation of a dynamic size-resolved microphysical aging scheme.

5.6   Tables and figures

Figure 5.1: HIPPO aircraft flight tracks in January 2009 (black), October – November 2009 (blue), March – April 2010 (pink), June – July 2011 (red), and August – September 2011 (green).

Table 5.1: Key aging parameters used in GEOS-Chem simulations of BC.

Simulations		Hydrophobic[a]		Hydrophilic[a]		Condensation threshold (β)[b]
		D_p (nm)	σ_p	D_p (nm)	σ_p	
Fixed aging (FIX)		e-folding BC aging time $\tau_{\text{fix}} = 1.2$ days				
Standard Microphysics-based (MP$_{\text{STD}}$)[c]		$D_{BC} = 60$ $D_{OC} = 60$	$\sigma_{BC} = 1.8$ $\sigma_{OC} = 1.8$	$D_{BC} = 150$ $D_{OC} = 150$ $D_{sulf} = 150$ $D_{fss} = 200$ $D_{css} = 800$	$\sigma_{BC} = 1.8$ $\sigma_{OC} = 1.8$ $\sigma_{sulf} = 1.6$ $\sigma_{fss} = 1.5$ $\sigma_{css} = 1.8$	5% of hydrophobic BC mass
Sensitivity simulations	D$_{\text{BCPO}}$30	Hydrophobic $D_{BC} = 30$ nm[d]				
	D$_{\text{BCPO}}$90	Hydrophobic $D_{BC} = 90$ nm[d]				
	SD$_{\text{BCPO}}$1.4	Hydrophobic $\sigma_{BC} = 1.4$[d]				
	SD$_{\text{BCPO}}$2.0	Hydrophobic $\sigma_{BC} = 2.0$[d]				
	D$_{\text{PI}}$+50%	All hydrophilic particles D_p increased by 50%				
	D$_{\text{PI}}$-50%	All hydrophilic particles D_p decreased by 50%				
	SD$_{\text{PI}}$+0.2	All hydrophilic particles σ_p increased by 0.2				
	SD$_{\text{PI}}$-0.2	All hydrophilic particles σ_p decreased by 0.2				
	BETA2.5	$\beta = 2.5\%$				
	BETA10	$\beta = 10\%$				
	MP$_{\text{chem}}$	Standard microphysics-based scheme with chemical oxidation parameterization from Poschl et al. (2001)				

[a]D_p and σ_p are geometric mean diameter and geometric standard deviation for particle number size distribution, respectively.

[b]Condensation threshold (β in Eq. (7)) represents the mass fraction of condensed soluble materials on hydrophobic BC required for hydrophobic-to-hydrophilic BC conversion. A value of 5% is used in the standard microphysics-based scheme following Riemer et al. (2004).

[c]Geometric mean diameters (D_p)and standard deviations (σ_p) are followling Dentener et al. (2006) and Yu and Luo (2009) for hydrophobic and hydrophilic BC and OC, and the Global Aerosol Dataset (GADS) (Koepke et al., 1997) for sulfate-nitrate-ammonia ("sulf"), fine-mode sea salt ("fss"), and coarse-mode sea salt ("css"). SOA is treated as hydrophilic OC.

[d]Lower and upper bounds of geometric mean diameters (30 nm and 90 nm) and standard deviations (1.4 and 2.0) for hydrophobic BC are following Bond et al. (2006).

Table 5.2: GEOS-Chem simulated global annual mean BC budget.

References		BC aging rate (ngC m^{-3} h^{-1})			Emissions (Tg yr^{-1})[c]	Lifetime (day)	Loading (mg m^{-2})	Loading above 5 km (%)	Wet deposition (%)	Hydrophilic fraction (%)
		< 5 km	> 5 km	mean						
This study	FIX	0.378	0.005	0.221		13.7	0.795	26.2	78.9	85.8
	MP$_{STD}$	0.560		0.324		4.21	0.244	7.32	80.3	98.8
	MP$_{chem}$	0.561		0.325		4.21	0.244	7.31	80.3	98.9
	D$_{BCPO}$30	0.570		0.330		4.18	0.242	7.16	80.2	99.3
	D$_{BCPO}$90	0.551		0.319		4.25	0.246	7.53	80.3	98.1
	SD$_{BCPO}$1.4	0.571		0.331		4.18	0.242	7.14	80.2	99.4
	SD$_{BCPO}$2.0	0.550	< 0.001	0.319	10.8	4.25	0.246	7.55	80.3	98.1
	D$_{PI}$+50%	0.568		0.329		4.19	0.243	7.19	80.3	99.2
	D$_{PI}$-50%	0.548		0.317		4.27	0.247	7.68	80.2	97.8
	SD$_{PI}$+0.2	0.567		0.328		4.19	0.243	7.20	80.3	99.2
	SD$_{PI}$-0.2	0.552		0.320		4.24	0.246	7.50	80.3	98.2
	BETA2.5	0.569		0.330		4.19	0.242	7.17	80.3	99.3
	BETA10	0.547		0.317		4.27	0.247	7.65	80.2	97.7
He et al. (2014a, b)	Fixed aging (τ = 1.2 days)				8.1	6.6	0.29	18	83	-
Q. Q. Wang et al. (2014)	Fixed aging (τ = 1.2 days)				6.5	4.2	0.15	8.7	77	-
Bond et al. (2013)[a]	Model ensemble mean				17	6.1	0.55	-	-	-
Jacobson (2012)	Aging microphysics				9.3	3.2	0.18	-	94	-
Chung et al. (2012)	Fixed aging				6.3	5.5	0.19	-	-	-
Jacobson (2010)	Aging microphysics				4.7	9.9	0.25	-	92	-
Schulz et al. (2006)[b]	Model ensemble mean				6.3	6.8±1.8	0.23±0.07	21±11	-	-

[a]Based on AeroCom Phase I simulations after scaling to match AERONET BC absorption optical depth (AAOD).
[b]Mean and standard deviations for eight models from AeroCom Phase I simulations. All AeroCom models use the same emissions.
[c]Global total BC emissions including anthropogenic and biomass burning sources.
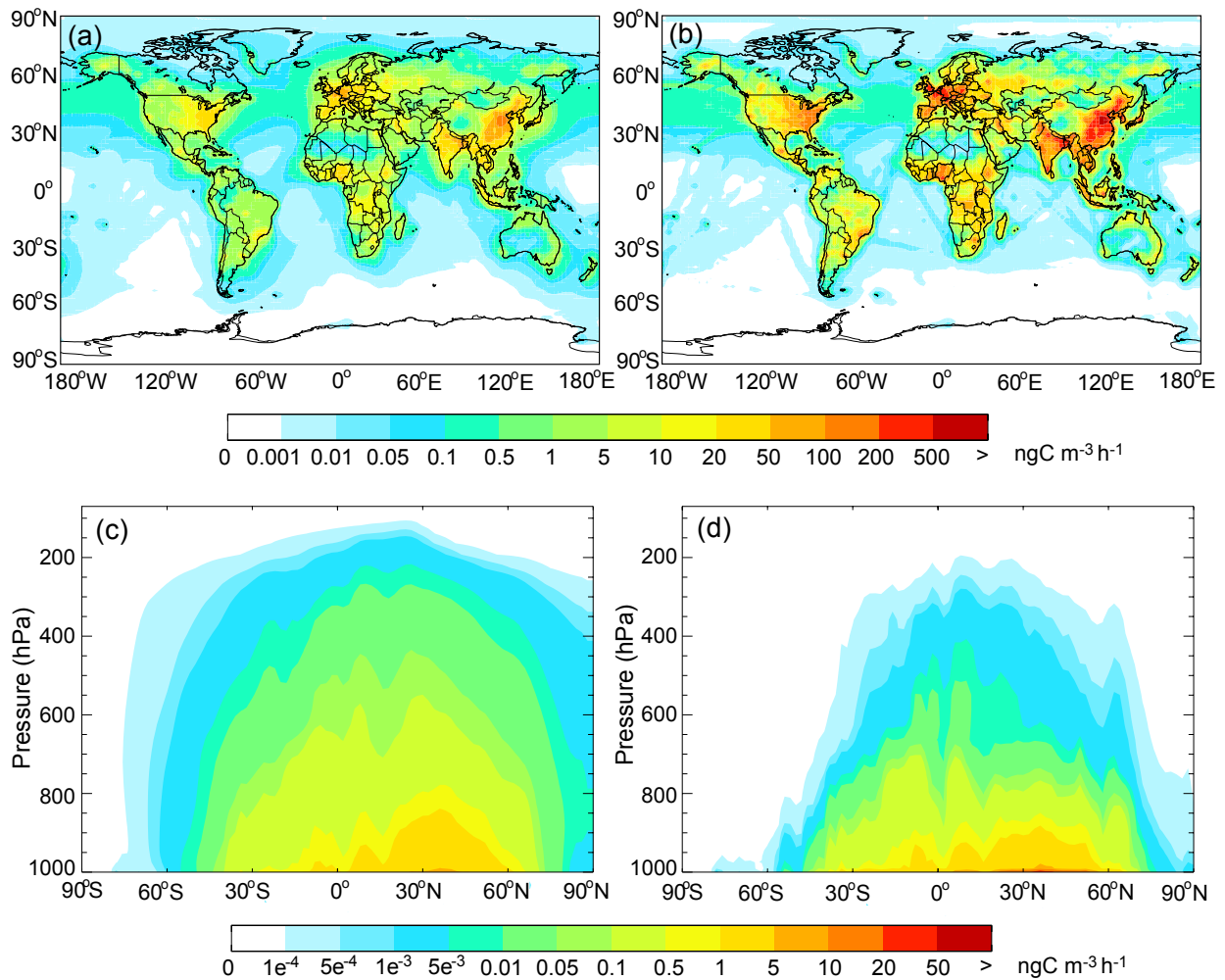
Figure 5.2: GEOS-Chem simulated annual mean BC aging rates (ngC m^{-3} h^{-1}) in the surface layer (top panels) and averaged zonally (lower panels) from a fixed BC aging scheme (left panels) and a microphysics-based aging scheme (right panels). See text for details. Model results are for 2009.
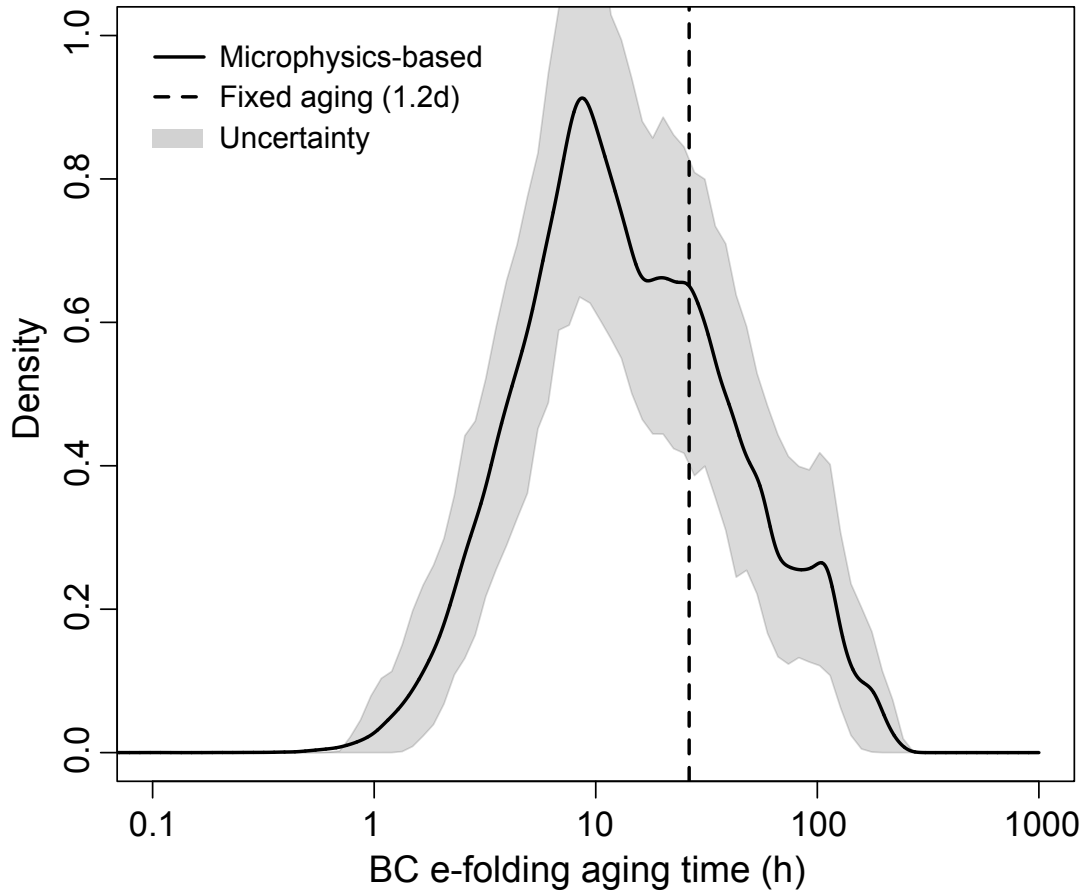
Figure 5.3: Probability density function of simulated annual mean BC e-folding aging time (h) over the globe for a microphysics-based scheme (solid line) and a fixed aging scheme (dashed line). Also shown is 95% uncertainty range (in grey) of the microphysics-based aging time estimated from a Monte Carlo method.
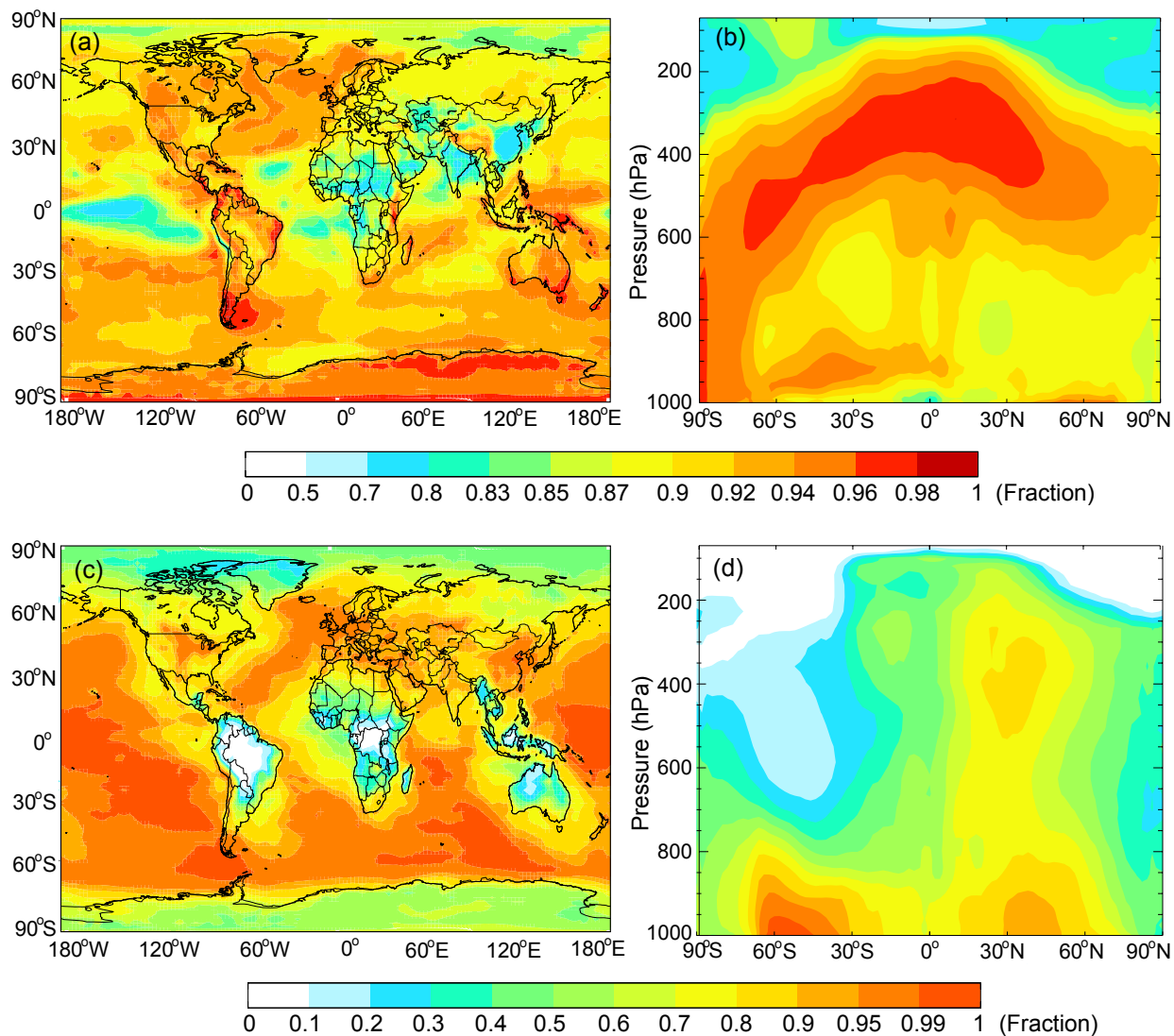
Figure 5.4: GEOS-Chem simulated annual mean contribution of condensation to total BC aging rate (sum of condensation and coagulation) averaged within 0–1 km above the surface (top left) and zonally (top right) and annual mean contribution of H_2SO_4-HNO_3-NH_3 condensation to the BC aging rate through total condensation (sum of H_2SO_4-HNO_3-NH_3 and SOA condensation) averaged within 0–1 km above the surface (lower left) and zonally (lower right). Model results are for 2009.
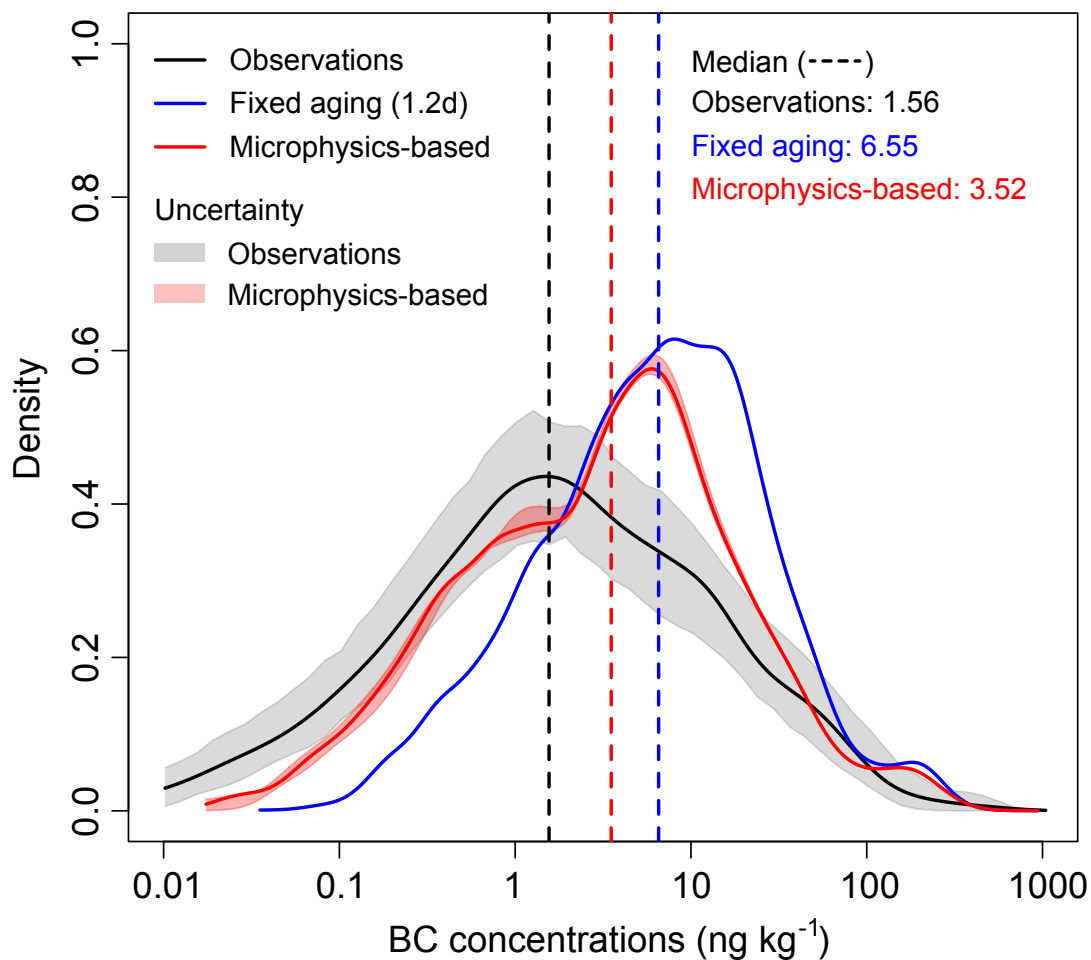
Figure 5.5: Probability density functions of HIPPO observed (black) and GEOS-Chem simulated BC concentrations. Model results using a fixed BC aging (blue) and a microphysics-based aging (red) are shown. The 95% uncertainty range of the HIPPO observations, estimated from a Monte Carlo method, is shown (in grey). Also shown (in light red) is the range of model results from microphysics-based sensitivity simulations (see Table 5.1 and text for details). Dashed lines show the median of observations (1.56 ng kg^{-1}, black), fixed aging (6.55 ng kg^{-1}, blue), and microphysics-based aging (3.52 ng kg^{-1}, red). About 5% of the observed BC concentrations are below 0.01 ng kg^{-1}.
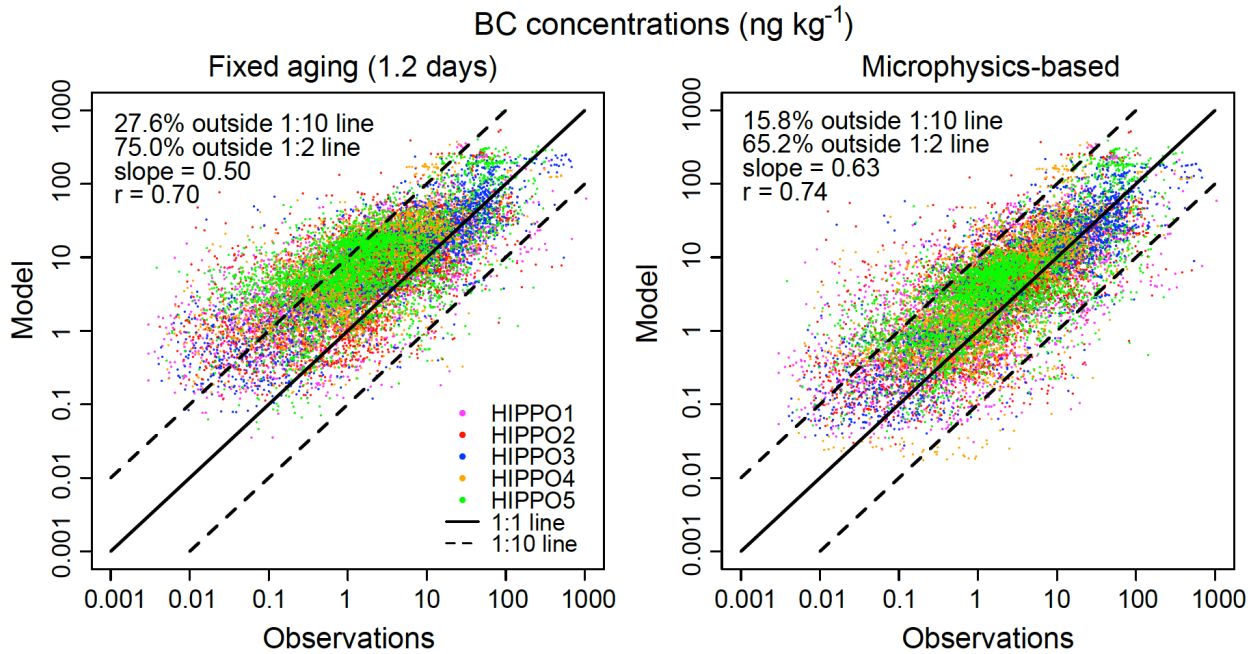
Figure 5.6: HIPPO observed and GEOS-Chem simulated BC concentrations sampled along the HIPPO flight tracks (HIPPO 1: pink, HIPPO 2: red, HIPPO 3: blue, HIPPO 4: orange, HIPPO 5: green; see Fig. 5.1), with model results using a fixed BC aging scheme (left panel) and a microphysics-based BC aging scheme (right panel). Also shown are the 1:1 and 1:10 (or 10:1) ratio lines, percentages of data points outside 1:10 (or 10:1) and 1:2 (or 2:1) ratio lines, and slopes and correlation coefficients (r) of the regression lines between model results and observations.
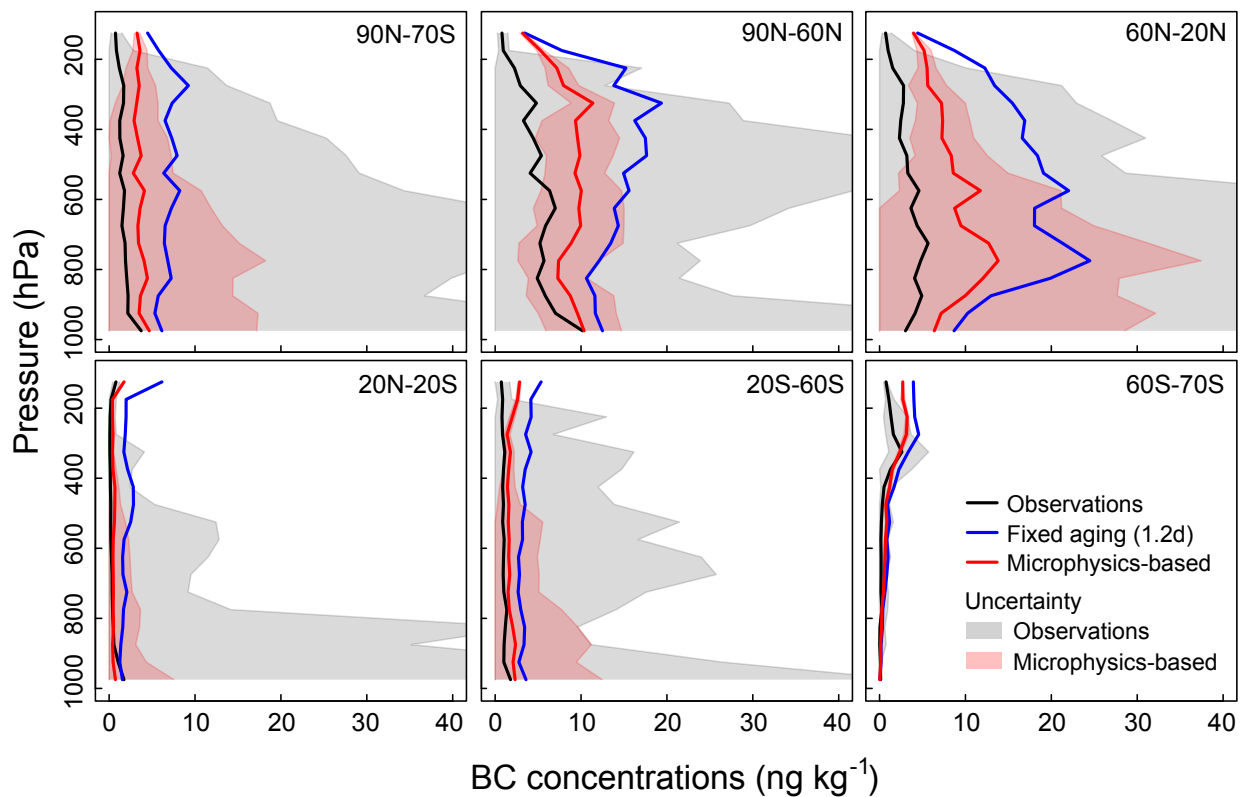
Figure 5.7: Median vertical profiles of HIPPO observed (black) and GEOS-Chem simulated BC concentrations at different latitudes. Results are averaged over 50 hPa altitude bins. Model results using a fixed BC aging (blue) and a microphysics-based aging (red) are shown. Also shown are the 1σ uncertainties of observations (grey) and model results (light red) from microphysics-based sensitivity simulations (see Table 5.1 and text for details).
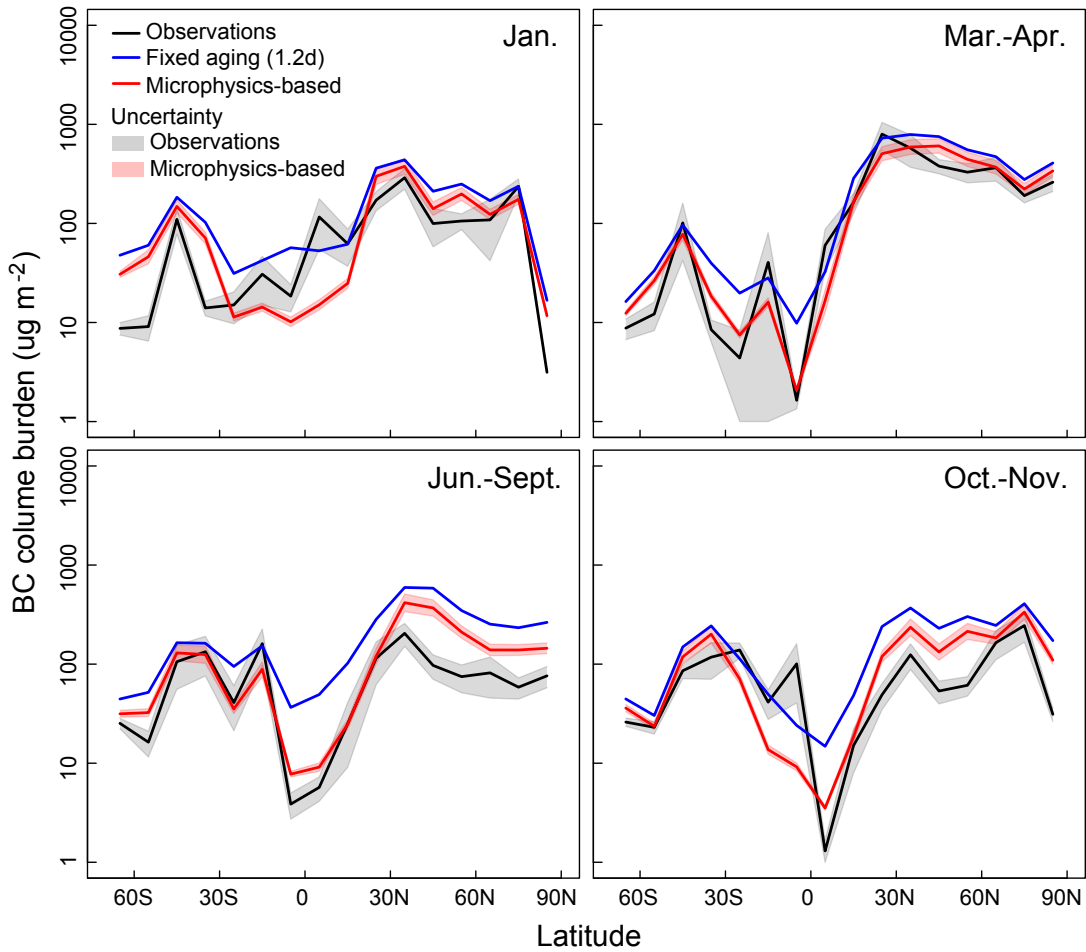
Figure 5.8: Latitudinal distributions of HIPPO observed (black) and GEOS-Chem simulated BC column burden (μg m^{-2}) in different seasons. The column burden is computed by integrating vertical profiles from the surface to 250 hPa ($\sim$10 km) in 10° latitude bins. Model results using a fixed BC aging (blue) and a microphysics-based aging (red) are shown. Also shown are the 1σ uncertainties of observations (grey) and model results (light red) from microphysics-based sensitivity simulations (see Table 5.1 and text for details).
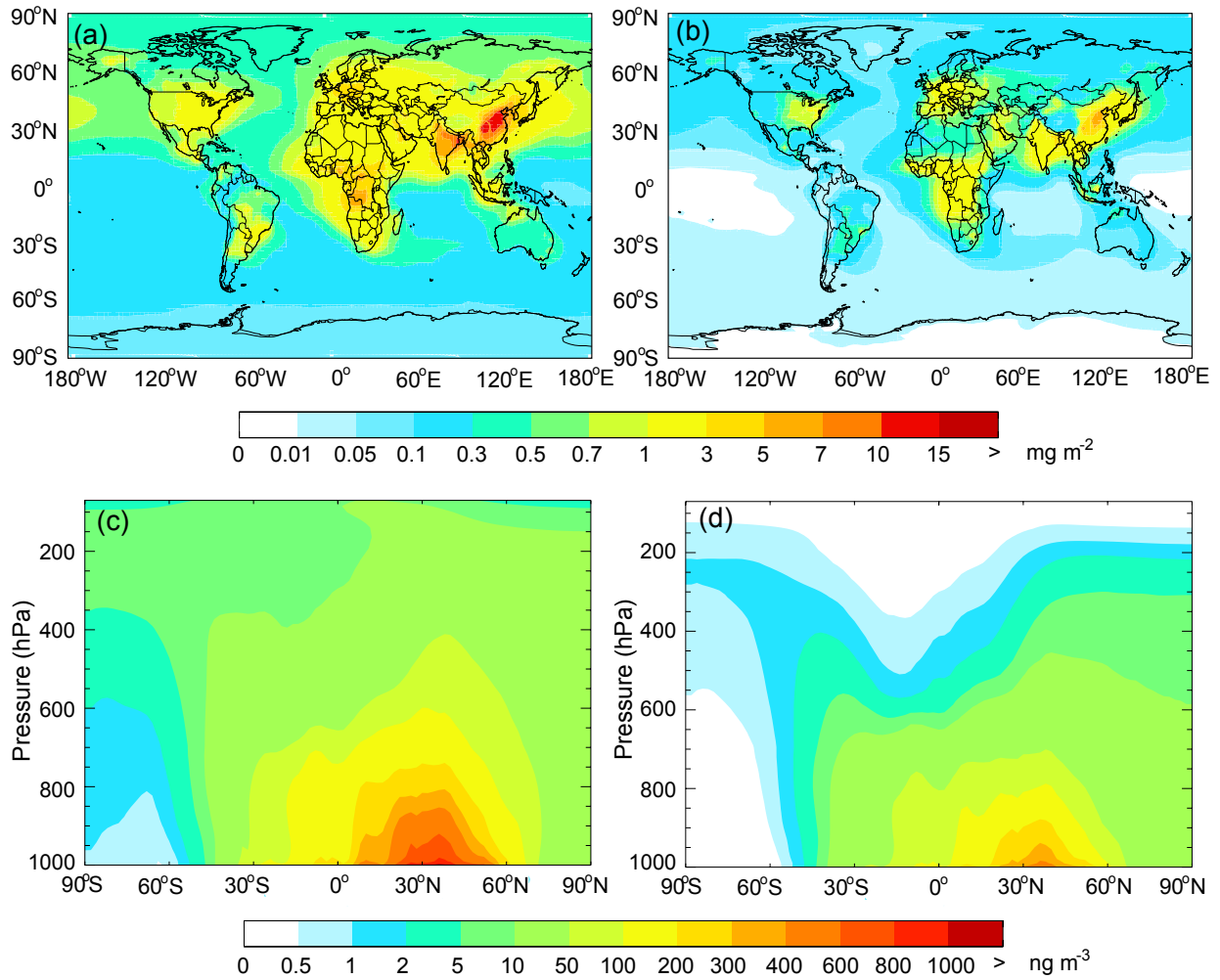
Figure 5.9: GEOS-Chem simulated annual mean BC column burden (mg m^{-2}) (top panels) and zonal mean BC concentrations (ng m^{-3}) (lower panels) using a fixed BC aging scheme (left panels) and a microphysics-based aging scheme (right panels). Model results are for 2009.
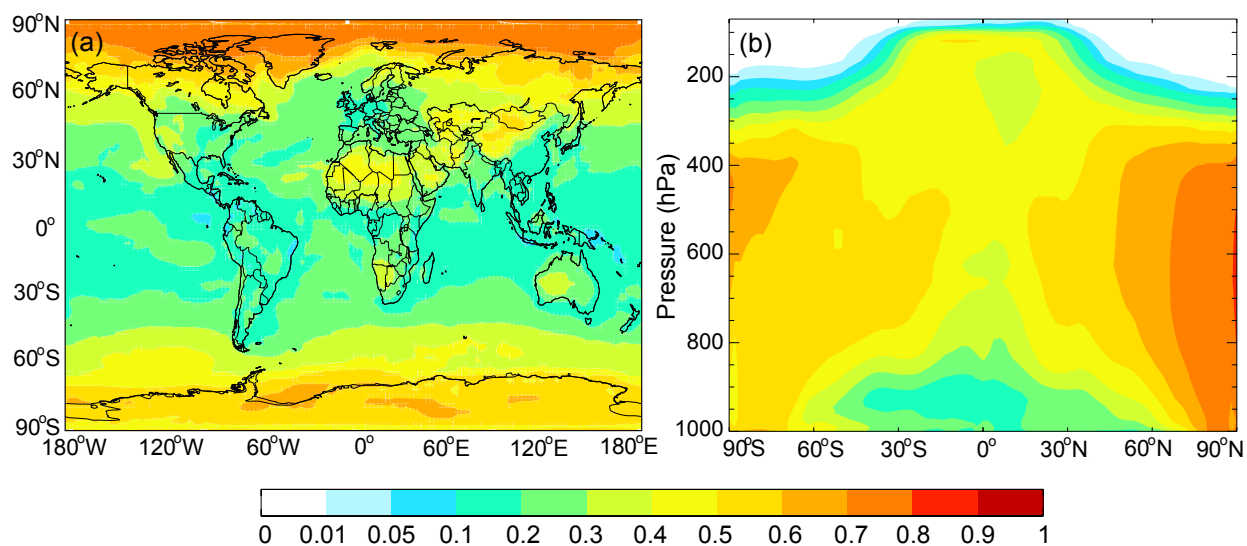
Figure 5.10: GEOS-Chem simulated annual mean contribution of chemical oxidation to the total BC aging rate (sum of condensation, coagulation, and chemical oxidation) averaged within 0–1 km above the surface (left) and zonally (right). Model results are for 2009.

138
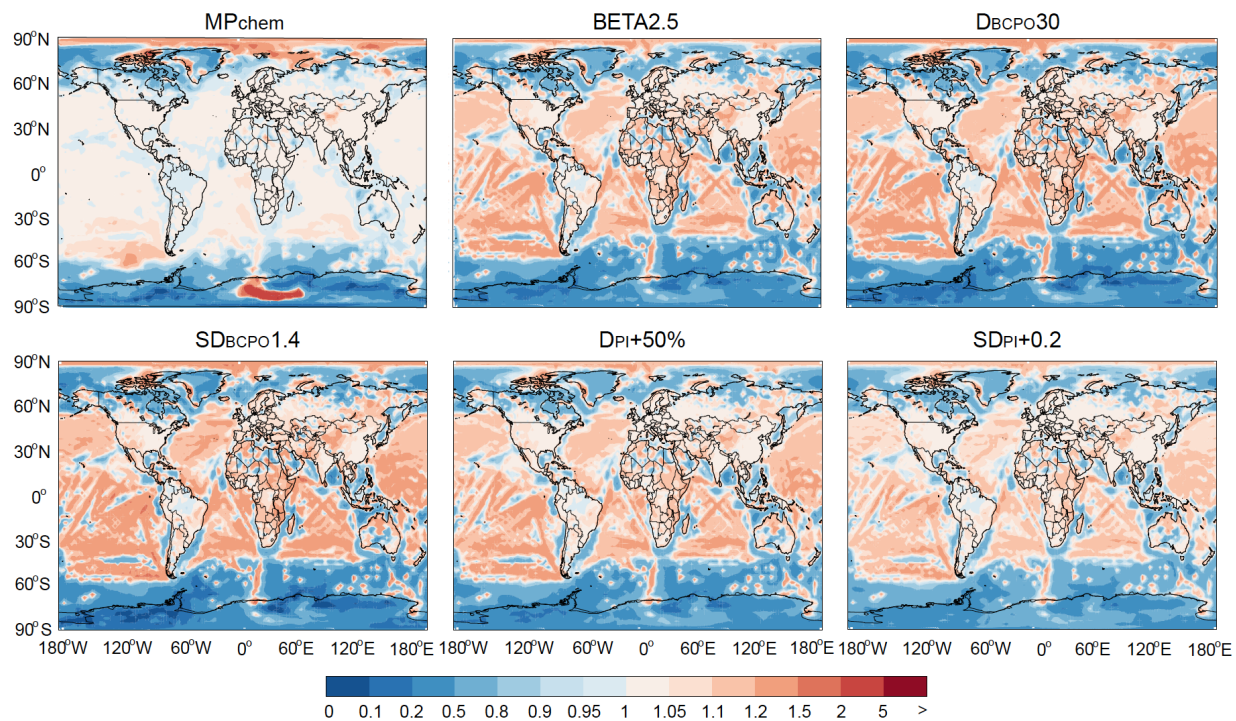
Figure 5.11: GEOS-Chem simulated ratios of annual mean BC aging rate from six microphysics-based simulations to that from the standard microphysics-based simulation in the surface layer. See Table 5.1 and text for details. Model results are for 2009.
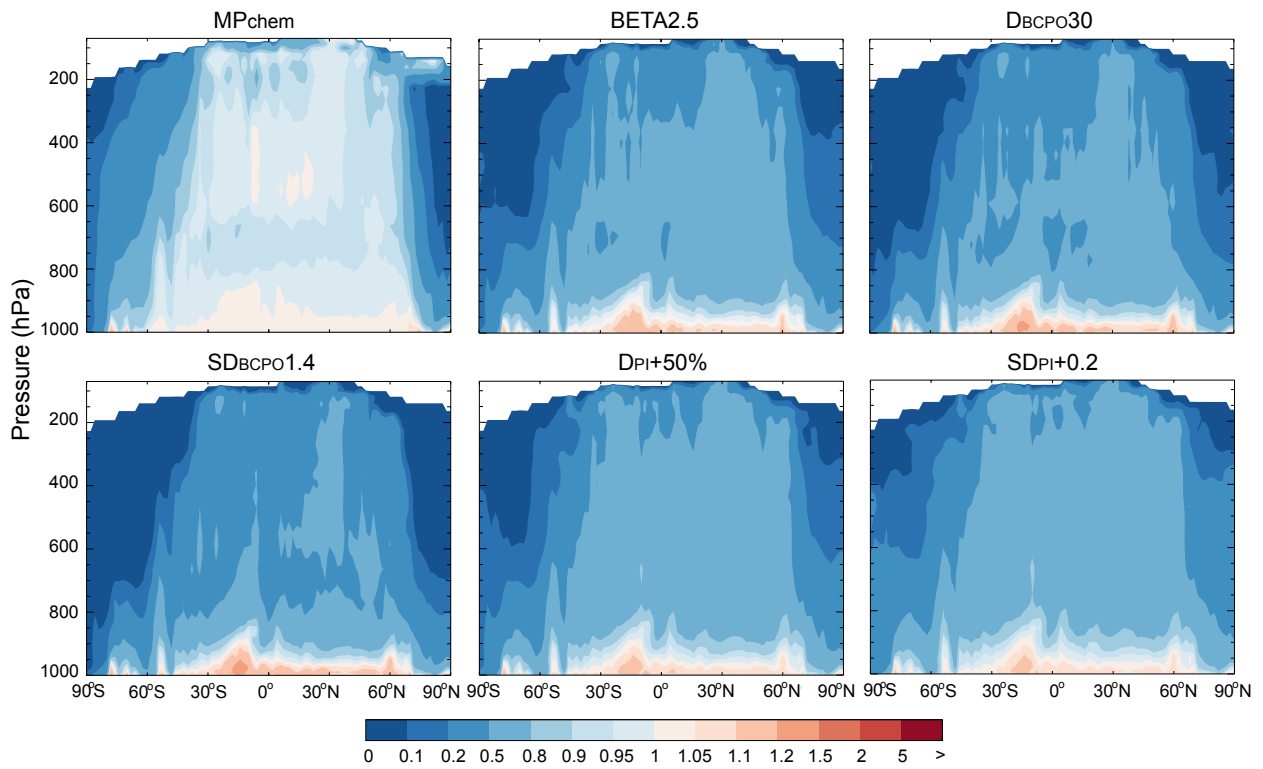
Figure 5.12: Same as Fig. 5.11, but for zonal mean BC aging rate.
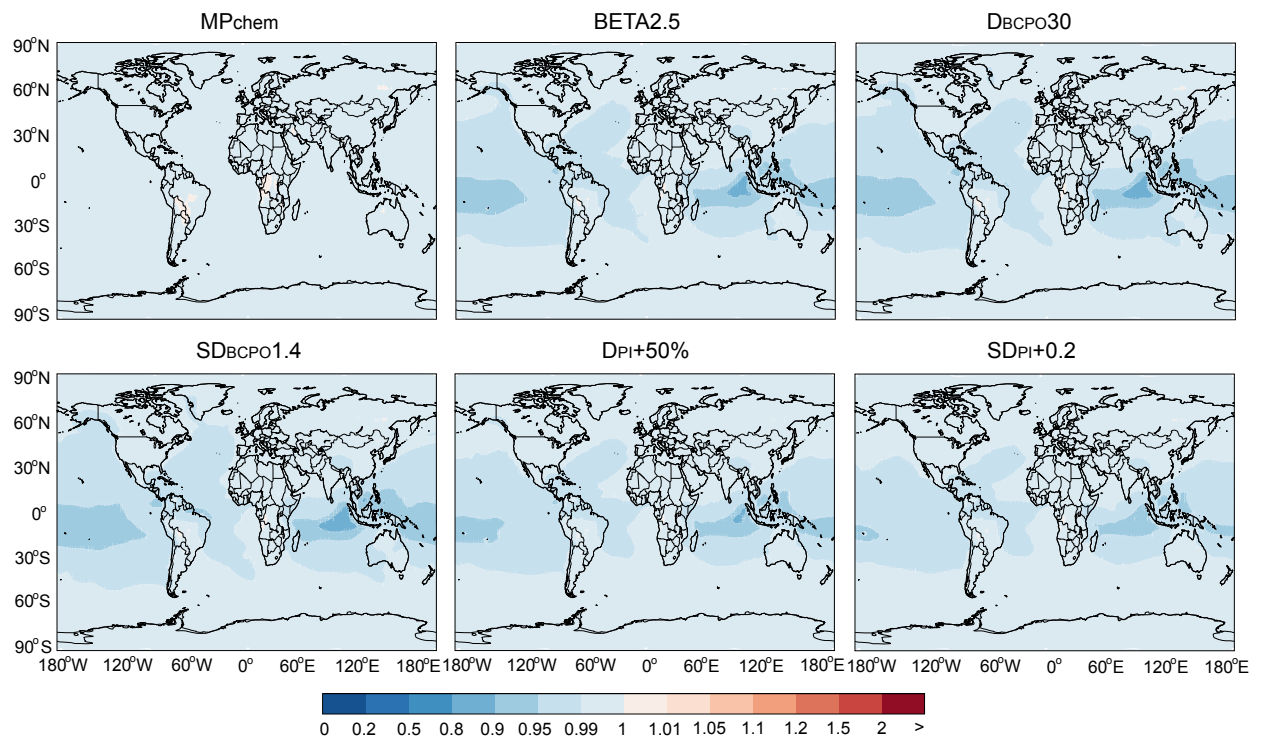
Figure 5.13: Same as Fig. 5.11, but for BC column burden.
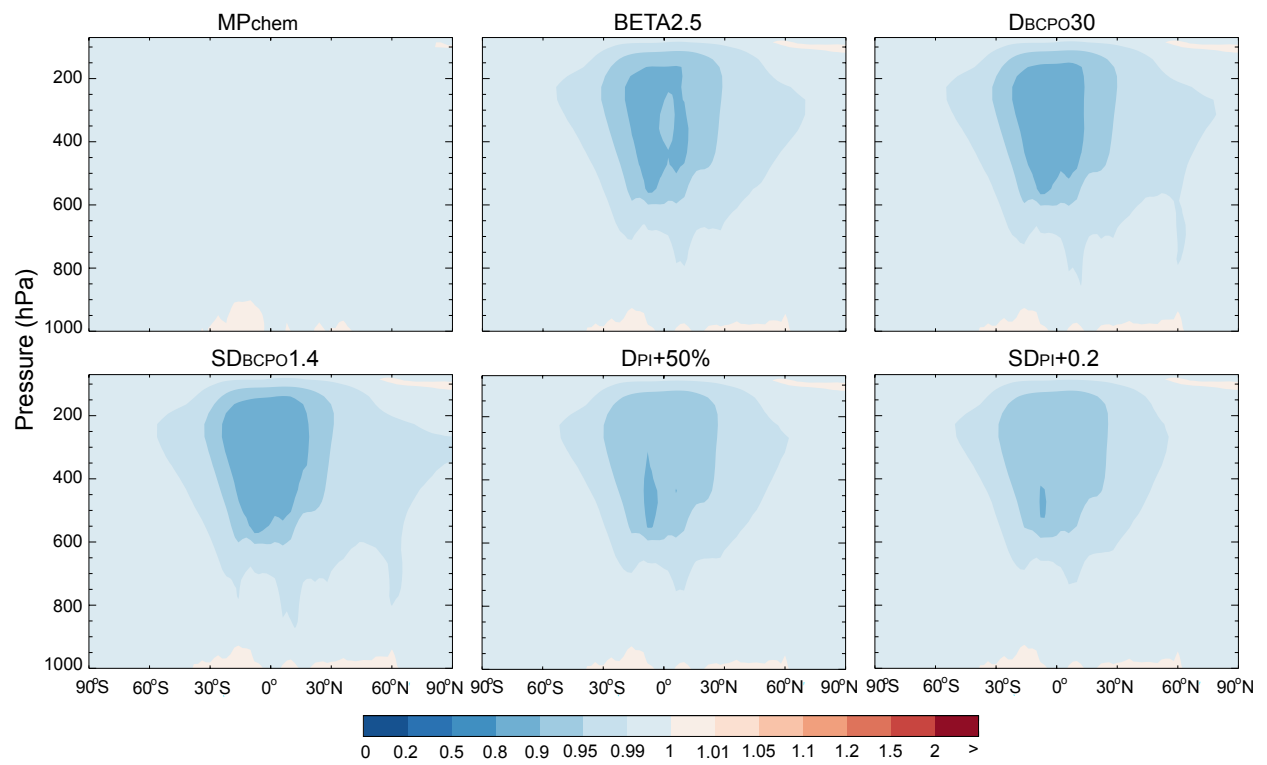
Figure 5.14: Same as Fig. 5.12, but for zonal mean BC concentrations.

CHAPTER 6

Enhanced black carbon-induced snow albedo reduction due to snow close packing

Abstract

Previous modeling of snow albedo, a key climate feedback parameter, follows the independent scattering approximation (ISA) such that snow grains are considered as a number of separate units with distances longer than wavelengths. Here, we develop a new snow albedo model for widely-observed close-packed snow grains internally mixed with black carbon (BC) and demonstrate that albedo simulations match closer to observations. Close packing results in a stronger light absorption for clean and BC-contaminated snow. Compared with ISA, close packing reduces pure snow albedos by up to $\sim$0.05, whereas it enhances BC-induced snow albedo reduction and associated surface radiative forcing by up to 15% (20%) for fresh (old) snow, with larger enhancements for stronger structure packing. Finally, our results suggest that BC-snow albedo forcing and snow albedo feedback (climate sensitivity) are underestimated in previous studies, making snow close packing consideration a necessity in climate modeling and analysis.

6.1 Introduction

Snow plays a critically important role in the Earth climate system and water cycles. It not only affects surface radiative and heat fluxes but also freshwater resources. Snow albedo feedback, the most significant positive amplification of surface temperature increase, strongly enhances warming over polar regions and high mountains (*Qu and Hall*, 2014). Observations have shown substantial albedo reductions in snowpack contaminated by aerosols (*Qian et al.*, 2015; *Lee et al.*, 2016), particularly black carbon (BC), which has the strongest light-absorbing property (*Bond et al.*, 2013). Modeling studies also indicated that BC deposition is an important contributor to snow albedo reduction and surface warming over snow-covered regions (*Qian et al.*, 2015), particularly the Tibetan Plateau (*He et al.*, 2014b,a), the Rocky Mountains (*Qian et al.*, 2009), and the Arctic (*Warren and Wiscombe*, 1985; *Qi et al.*, 2017). In addition to external factors such as impurities and solar zenith angle, internal snow properties can also influence snow albedo, including snow mass/thickness, snow grain size, grain shape, and packing structure (*Warren and Wiscombe*, 1980; *Jacobson*, 2004; *Flanner et al.*, 2007; *Jin et al.*, 2008; *Liou et al.*, 2014).

Previous snow modeling studies have used the conventional independent scattering approximation (ISA) for snow grains (*Warren and Wiscombe*, 1980; *Jacobson*, 2004; *Flanner et al.*, 2007), which assumes that light scattering and absorption of each snow grain is independent of surrounding grains so that the total intensity is the sum of intensity component for each grain. *Wiscombe and Warren* (1980) suggested that ISA is reasonable for pure snow grains in comparison to albedo measurements. However, observations showed that densely packed snow grains (i.e., close packing hereinafter) are ubiquitous (*Colbeck*, 1982), where ISA among grains may be invalid. For example, *Ishiniaru and Kuga* (1982) measured that the extinction coefficient at a visible wavelength for a dense distribution of latex-sphere suspension relative to that for sparse distribution decreases (increases) for high volume fractions when the size parameter is small (large). *Göbel et al.* (1995) observed a decrease in the scattering efficiency (visible and infrared wavelengths) of latex-sphere suspensions and TiO_2 powder

grains due to close packing effects, relative to that for ISA. *Kokhanovsky* (1998) found that the scattering efficiency and asymmetry factor of densely packed large particles such as snow grains decrease with their concentrations. Thus, in order to accurately predict and project snowpack change and its climatic impact and feedback, it is imperative to understand and assess the effect of close packing in snow albedo modeling.

Several pioneering efforts have been made to simulate snow close packing effects. Researchers in the electrical engineering field applied quasi-crystalline approximation and dense medium radiative transfer (DMRT) theory to microwave remote sensing of snowpack (e.g., *Wen et al.*, 1990). DMRT has the same structure as the conventional radiative transfer equation, but the relationship of extinction coefficient, single-scattering albedo, and phase function to optical characteristics of individual particles differs from the conventional ISA. However, their method is not applicable to large size parameters (*Tsang and Ishimaru*, 1987) such as snow albedo calculations at visible and near-infrared wavelengths under the present investigation. *Kokhanovsky and Zege* (2004) further derived a snow model to account for effects of nonsphericity of snow grains and close packing without mixing with aerosols.

In this study, we develop a new snow albedo model for close-packed snow grains internally mixed with multiple BC particles to assess the close packing effect on albedos of clean and BC-contaminated snow and associated climatic effects. We also formulate physical equations to adjust snow albedo calculations without close packing to those with close packing for application to land surface and climate models.

6.2 Methods

We extend the geometric-optics surface-wave (GOS) approach (*Liou et al.*, 2011, 2014; *Takano et al.*, 2013; *He et al.*, 2015) to compute optical properties of snow grains with close packing structures and inclusion of multiple BC particles. The GOS approach, explicitly resolving complex particle structures, accounts for geometric reflection and refraction,

diffraction, and surface wave components based on a Monte Carlo photon tracing method and a ray-by-ray integration approach. The GOS approach has been applied to a wide range of particle sizes and shapes, particularly including nonspherical snowflakes mixed with light-absorbing aerosols (*He et al.*, 2014a; *Liou et al.*, 2014). It produced consistent particle optical properties with those determined from the superposition T-matrix method and laboratory measurements for fractal aggregates with various coating structures (*He et al.*, 2016b) as well as the discrete dipole approximation and finite difference time domain methods for plate and column ice crystals (*Liou et al.*, 2011). *Liou and Yang* (2016) provided a comprehensive description of the GOS approach and its application.

Specifically, we construct a close-packed snow cube by stacking up a number of individual grain spheres ($N_s = 2^3$, 3^3, 4^3, and 5^3 in this study) with the radius of r_s as shown in Fig. 6.1, where N_s is the number of snow spheres forming a close-packed cube. We then compute an effective geometric cross sectional area (A_s) for the close-packed snow cube by using a Monte Carlo photon tracing method (*Liou et al.*, 2011). The resulting geometric shadow of the snow cube on a plane perpendicular to incident light beams is:

$$A_s(\alpha, \beta) = A\left[\frac{N_a(\alpha, \beta)}{N_t}\right] \tag{6.1}$$

where A ($= L^2$; L is the cube's maximum dimension) defines the area of a square, which is large enough to cover the geometric cross section of a snow cube. α and β are the orientation angles of a snow cube with respect to the incident light beam. N_a is the number of photons incident (scattered/absorbed) on a snow cube, depending on its orientation. N_t is the number of total photons used in the photon tracing procedure. We consider an ensemble of randomly orientated close-packed snow cubes and average their geometric cross sections over all directions. Subsequently, we compute extinction and absorption cross sections of the close-packed snow cubes by a ray-by-ray integration approach (*Liou et al.*, 2011). Diffraction is determined based on the Babinet's principle and the geometric cross section. The surface-wave component is negligible for large particles (size parameters $> \sim 50$). Following *Liou et al.* (2011, 2014), we compute single-scattering properties of close-packed snow grains, including

146

optical depth (τ), single scattering co-albedo ($1-\varpi$), and asymmetry factor (g), and perform radiative transfer computations to obtain snow albedo using the doubling/adding method (*Takano*, 1989).

Following the aforementioned procedure, we determine single-scattering properties and albedo of snow grains with ISA. We compute the geometric cross section (πr_s^2) of each snow sphere and sum up over all grains independently to obtain total cross sections ($N_{st}\pi r_s^2$, N_{st} is the total number of independent snow spheres). We further calculate the ratios (f) of the cross section (A_s) of a close-packed snow cube to that of ISA snow ($N_{st}\pi r_s^2$) with the same number of spheres ($N_{st} = N_s$). We find that $f = 0.6801$, 0.5075, 0.4029, and 0.3338 for $n = 2$, 3, 4, and 5 ($N_s = n^3$), respectively, independent of snow grain size (r_s). The f value is smaller than 1, because the close-packed snow cube prevents a part of photons from interactions with its inner part (i.e., shadowing effect), resulting in a weaker extinction than the ISA snow with the same number of spheres. We link snow optical depths for close packing (τ') to that for independent scattering (τ) by $\tau' = f\tau$, where f is referred to as optical depth adjustment factor due to close packing effects, assuming the same snow extinction efficiency ($= \sim 2$ for large particles) for close packing and ISA. We note that the present study only accounts for a small n ($n < 6$) and the results may not be generalized to cases with a large n (e.g., $n > 10$), which requires further investigations. We also note that snow close packing (changes in grain structures) can also be viewed as volume-equivalent snow spheres with different effective grain sizes. However, we assess the effect of close packing in the present study by explicitly resolving the packing structure rather than using an equivalent effective grain size.

In this study, we perform computations for both clean and BC-contaminated snow with and without close packing effects for fresh ($r_s = 100$ μm) and old ($r_s = 1000$ μm) snow. For contaminated snow, we apply a stochastic process (*Liou et al.*, 2014) to generate multiple monodisperse BC spheres with a radius of 0.1 μm randomly distributed inside each snow sphere, with BC concentrations of 100, 250, and 500 ppb in snow for moderately and highly

polluted scenarios based on observations (*Qian et al.*, 2015). We further account for BC particles coated with sulfate, which are ubiquitous in the atmosphere through aging processes (*Schwarz et al.*, 2008; *He et al.*, 2016a) and significantly alters BC optical properties (*He et al.*, 2015). We assume a core-shell structure for coated BC with a coating thickness of 20 nm to obtain a mass absorption coefficient (MAC) of $\sim$11.3 m^2 g^{-1} (*Bond et al.*, 2013). We use spectral refractive indices of snow from *Warren and Brandt* (2008), BC from *Krekov* (1993), and sulfate from *Toon et al.* (1976). For albedo calculations, we assume one-layer snow with an optical depth of 960 based on observations (*Jacobson*, 2004) for ISA cases and adjust it for close packing cases using the optical depth adjustment factor (f). One advantage of prescribing the snow optical depth is to circumvent the complexity of taking into account the effects of porous space among randomly oriented packed snow cubes and the size of packed snow aggregates on snow mass density and the consequence of optical depth calculations. The underlying surface is set to be a blackbody.

6.3   Results and discussions

6.3.1   Close packing effects on snow optical properties and albedo

Figure 6.2 shows the single scattering co-albedo, asymmetry factor, optical depth adjustment factor, and albedo for clean and BC-contaminated fresh snow with ($N_s > 1$) and without ($N_s = 1$; i.e., ISA) close packing at a wavelength of 0.55 μm. Compared to ISA, close packing leads to higher (lower) single scattering co-albedos (asymmetry factors), with a monotonic increase (decrease) with N_s, for both clean and BC-contaminated snow. The single scattering co-albedo, albeit small, increases by a factor of three with a highly-packed structure ($N_s = 5^3$) relative to that without close packing, whereas the asymmetry factor decreases by 10%. The trends are similar for clean and contaminated snow. This suggests that stronger close packing results in stronger snow absorption but weaker forward scattering. However, close packing significantly decreases snow optical depth for a constant snow water

equivalent (Fig. 6.2), where it is 50% smaller for moderate packing ($N_s = 3^3$) and 66% smaller for strong packing ($N_s = 5^3$) relative to ISA.

Close packing leads to a small (≤ 0.01) reduction in pure snow albedo at visible wavelengths (Fig. 6.2), because of the opposite effects from larger single scattering co-albedos and smaller optical depths versus weaker forward scattering. However, the albedo reduction caused by close packing is larger for BC-contaminated snow than clean snow by up to a factor of two. Moreover, BC contamination results in a snow albedo reduction by 0.05–0.08 with a concentration of 500 ppb under high pollution (Fig. 6.2), depending on BC coating and close packing (N_s). Previous measurements also showed an albedo reduction of $\sim$0.08 for the same BC concentration in snow (*Hadley and Kirchstetter*, 2012). The reduction is 40–60% smaller in the case of external mixing of BC and snow (*He et al.*, 2014a). We find that close packing enhances the BC-induced albedo reduction by up to 15% relative to ISA, with larger reductions for stronger packing, while BC coating further reduces the albedo by $\sim$20% due to a larger single scattering co-albedo compared with uncoated cases (Fig. 6.2). *He et al.* (2014a) showed a 30–50% larger snow albedo reduction caused by BC coating compared with uncoated BC aggregates, depending on concentration.

Compared with visible wavelength cases, close packing exerts much stronger effects on fresh snow albedo at a near-infrared (NIR) wavelength, where BC contamination shows negligible effects. As close packing becomes stronger (N_s increases), snow albedo reduces by 0.01–0.05, which is a factor of 3–5 larger than that at visible wavelengths. This could affect prediction of snowpack evolution and its radiative effects (*Aoki et al.*, 2011) as well as remote sensing of snow properties using NIR wavelengths (*Li et al.*, 2001).

Figure 6.3 shows that, as close packing becomes stronger, the magnitude and trend for asymmetry factors and optical depths of clean and BC-contaminated old snow at a 0.55-μm wavelength are similar to those in fresh snow cases, whereas the single scattering co-albedo of old snow is one order of magnitude higher than that of fresh snow for all packing cases. As a result, the albedo of pure old snow is lower than that of fresh snow by $\sim$0.03, consistent with

previous modeling results (*Wiscombe and Warren*, 1980). We find that close packing reduces snow albedo by up to 0.01 for pure old snow and up to 0.04 for BC-contaminated old snow, which are much larger than those for fresh snow. Moreover, moderate BC contamination (250 ppb concentration in snow) leads to reductions of 0.11 and 0.13 in old snow albedos for uncoated and coated BC under ISA, respectively (Fig. 6.3), while close packing further enhances the BC-induced albedo reduction by up to 20% for old snow. *Flanner et al.* (2007) simulated a BC-induced reduction of $\sim$0.07 in spectrally averaged (0.3–5 μm) snow albedo for the same concentration of coated BC externally mixed with old snow ($r_s = 1000$ μm) without close packing, which is approximately half of that at visible wavelengths (*Warren and Wiscombe*, 1985).

6.3.2 Quantitative albedo adjustment for close packing effects

We find that calculated snow albedos at a wavelength of 0.55 μm with and without close packing are highly correlated ($R^2 = 0.998$), which decrease with BC concentration and increase with solar zenith angle (Fig. 6.4). It turns out that the strong linear relationship is valid for different N_s values and independent of BC concentration in snow and solar zenith angle. Thus, we develop a linear regression equation to adjust modeled fresh snow albedo without close packing (A_{ncp}) to that with close packing (A_{cp}) as follows:

$$A_{cp} = 1.171 A_{ncp} - 0.178, \quad (N_s = 5^3, \ strong \ packing) \tag{6.2}$$

$$A_{cp} = 1.031 A_{ncp} - 0.035, \quad (N_s = 3^3, \ moderate \ packing) \tag{6.3}$$

These two equations quantitatively demonstrate snow albedo reduction caused by close packing, applicable to land surface and climate models.

Furthermore, we use the two equations to adjust snow albedo calculations to account for the close packing effect. Figure 6.4 shows wintertime (December to February) snow albedo during 2007–2009 at Sapporo, Hokkaido from measurements and model results with and

without close packing. We focus on wintertime to avoid effects of substantial snow melting on snow packing structures. The measured albedo and modeled albedo without close packing (but with snow impurities) are from *Aoki et al.* (2011), while model results with strong and moderate close packing are derived via adjustments from Eqs. (6.2) and (6.3), respectively. We find that, compared with observations, model results without close packing overestimate snow albedo by 0.021 (mean error, ME), with a root-mean-square-error (RMSE) of 0.030, whereas accounting for strong (moderate) close packing of fresh snow reduces the ME to 0.004 (0.015) and the RMSE to 0.024 (0.026). Albedo adjustments for close packing of old snow reduce the model-observation discrepancies more. Therefore, close packing improves snow albedo simulations, showing important implications to evaluate aerosol effects on snow albedo and snow albedo feedback (see Sect. 6.4).

6.3.3   Uncertainty analysis

We note that a number of factors could introduce uncertainty in quantifying the close packing effect. For example, this effect is significantly affected by the number (N_s) of snow spheres forming the packing snow cube (i.e., packing strength). We account for four scenarios $(N_s = 2^3, 3^3, 4^3,$ and $5^3)$ in this study, however, stronger packing with more snow spheres could occur in real snowpack. In addition, complex structure/shape of close-packed snow grains (see e.g., *Colbeck*, 1982) could be important, which are not accounted for in this study. Recent studies (*Liou et al.*, 2014; *Dang et al.*, 2016) also suggested that grain shape is critical to snow albedo modeling. Other factors, including aerosol-snow mixing state (external versus internal), aerosol composition (BC/dust/others), and aerosol size distribution in snow, likely alter the close packing effect on contaminated snow (*He et al.*, 2014a; *Liou et al.*, 2014). To the extent that the present modeling results closely match observations as illustrated in Fig. 6.4, it appears that this study has accounted for key close packing factors in snow albedo calculations.

6.4 Climate implications

We have shown that close packing, which improves snow albedo simulations (Sect. 6.3.2), can reduce modeled snow albedo by up to 0.04 compared to ISA, depending on snow grain size, impurity concentration, solar zenith angle, and packing strength (N_s). This albedo alteration due to close packing, viz-a-viz the strong positive snow albedo feedback (SAF) (*Qu and Hall*, 2014), could exert substantial impacts on surface radiative and heat flux and hence temperature and hydrological cycle. Based on an ensemble of climate models without snow close packing, *Hall and Qu* (2006) quantified the sensitivity of snow albedo change to surface air temperature change, which is a key component of SAF. They found a mean springtime sensitivity of -0.84 % K^{-1} for Northern Hemisphere (NH) continents, whereas *Fernandes et al.* (2009) showed an observed sensitivity of -1.11 % K^{-1}. *Flanner et al.* (2011) also concluded that climate models substantially underestimate albedo feedback over the NH cryosphere based on observations. The model-observation discrepancy could be reduced by close packing effects which enhance albedo reductions caused by snow aging (fresh versus old) based on our results, where surface temperature increase is a key driver of snow aging (*Flanner et al.*, 2007).

Following the observed sensitivity, we find that the snow albedo reduction induced by close packing relative to ISA could lead to an increase of up to 0.27 K in springtime surface air temperature over NH continents, and even larger for BC-contaminated snow. The surface temperature perturbation by close packing, through the strong SAF, can further affect large-scale atmospheric circulation and hydrological cycle (*Fletcher et al.*, 2009). Moreover, *Qu and Hall* (2014) found an annual mean climate sensitivity of 0.08 and 0.42 W m^{-2} K^{-1} due to SAF over the globe and NH continents, with highest sensitivities in high mountains and polar regions. However, our results suggest that the climate sensitivity via SAF has been underestimated by previous studies in view of the fact that a higher snow albedo sensitivity to surface air temperature is produced by close packing.

In addition, close packing enhances the BC-induced snow albedo reduction compared with ISA, indicating that the snow albedo effect caused by BC deposition are likely to be underestimated in previous studies. Recent studies, assuming BC-snow internal mixing but without close packing, showed an annual mean BC-induced snow albedo forcing of 0.02–0.08 W m^{-2} globally (*Flanner et al.*, 2012; *He et al.*, 2014a) and 1.5–5.0 W m^{-2} over the Tibetan Plateau (*He et al.*, 2014a). However, we find that the albedo forcing is up to 20% higher by accounting for snow close packing and that the climatic effect of BC on snow-covered regions could be much larger than previously anticipated. For these reasons, it is submitted that close packing must be incorporated in snow albedo modeling in order to improve predictions of snowpack evolution and aerosol-snow interactions.

Moreover, although ground measurements have measured BC effects on snow albedo changes (*Aoki et al.*, 2011; *Hadley and Kirchstetter*, 2012), *Warren* (2013) pointed out that signals of BC-induced albedo reductions could be difficult to detect by satellites, except over highly polluted areas, because surface albedos retrieved from satellite observations typically have errors of a few percent (e.g., *Stroeve et al.*, 2005, 2013), comparable to albedo reductions caused by BC over the majority of Northern Hemispheric snowpack based on their radiative transfer calculations. Nevertheless, the present results demonstrated that snow close packing, occurring ubiquitously in the real snowpack, could enhance the signals of BC-induced albedo reductions, which increases the detectability of BC effects on snow albedo. Furthermore, in a recent study, *Lee et al.* (2016) indicated that BC can trigger a positive snow albedo feedback and amplify initial albedo reductions, resulting in a detectable albedo change by satellite measurements in a relatively long timescale (e.g., a month).

6.5   Conclusions

We have developed a new snow albedo model for closed-packed snow grains internally mixed with BC aerosol. Compared with the widely-used ISA in previous studies, close packing

resulted in higher single scattering co-albedos but lower asymmetry factors and optical depths for both clean and BC-contaminated snow. Close packing reduced pure fresh snow albedo by up to 0.05 at NIR wavelengths, a factor of 3–5 larger than that at visible wavelengths, while it also enhanced the BC-induced snow albedo reduction and hence albedo forcing by up to 15% for fresh snow and 20% for old snow, with larger enhancements occurring in stronger structure packing. The close packing effect was stronger for larger snow grain size (old versus fresh snow). We further determined quantitative relationships to adjust snow albedo calculations for the close packing effect, resulting in a closer match between albedo simulations and observations than ISA calculations. Our results suggest that the climate sensitivity due to SAF based on ISA has been underestimated, which could affect the evaluation of regional and global hydrological cycle and surface temperature perturbations. Finally, this study highlights the necessity of accounting for snow close packing in assessing the effects of BC on snow albedo and its feedback in the BC-snow system, particularly over polar and mountain regions.

6.6   Tables and figures
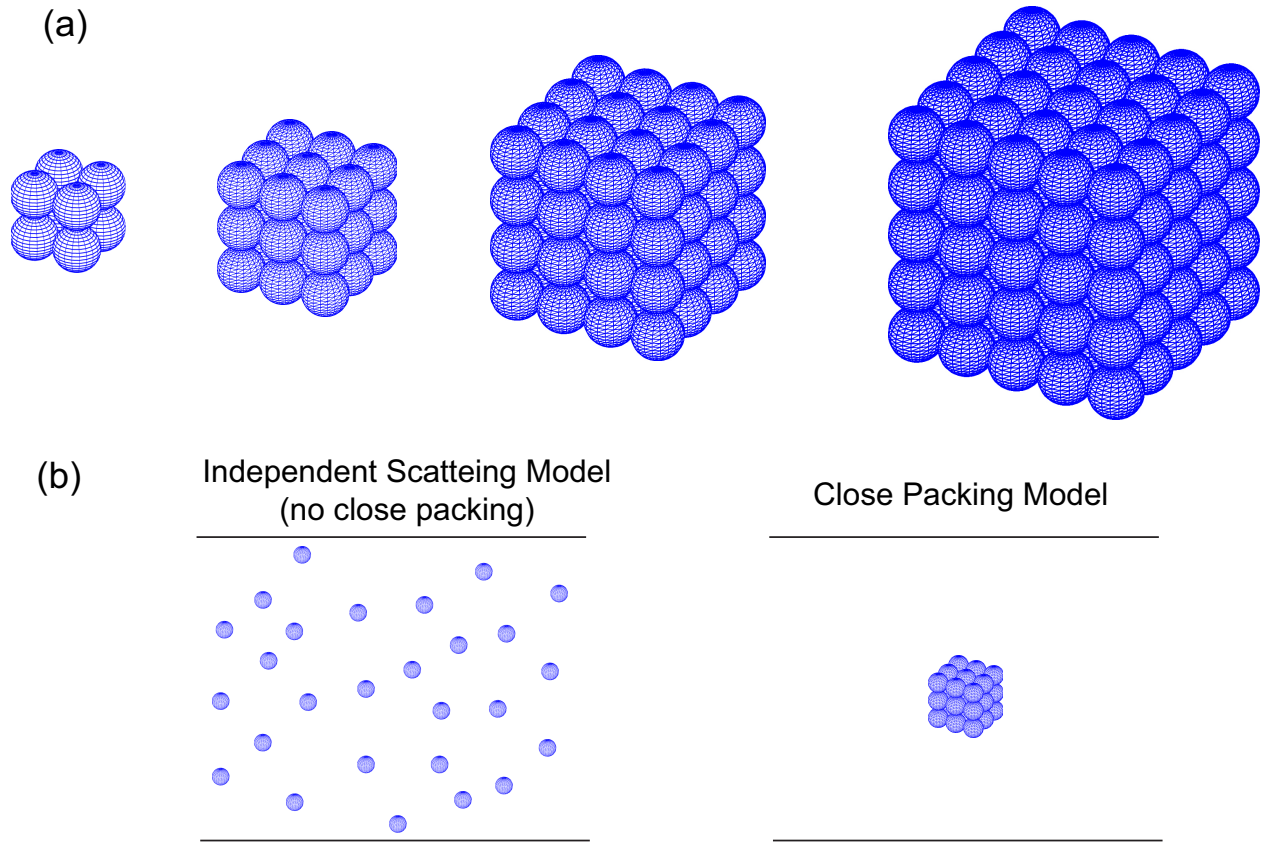
Figure 6.1: (a) Close-packed snow cubes consisting a number of snow grains/spheres ($N_s(n)$ $= 2^3, 3^3, 4^3, 5^3, ..., n^3$). These close-packed snow cubes are assumed to be randomly oriented in optical calculations. (b) A demonstration of independent scattering model ($N_s = 1$) and close packing model for the case of $n = 3$. The actual number of close-packed cubes or independent scattering spheres in a snow layer depends on snow volume and layer thickness. Each close-packed snow cube is assumed to be independent of surrounding cubes.
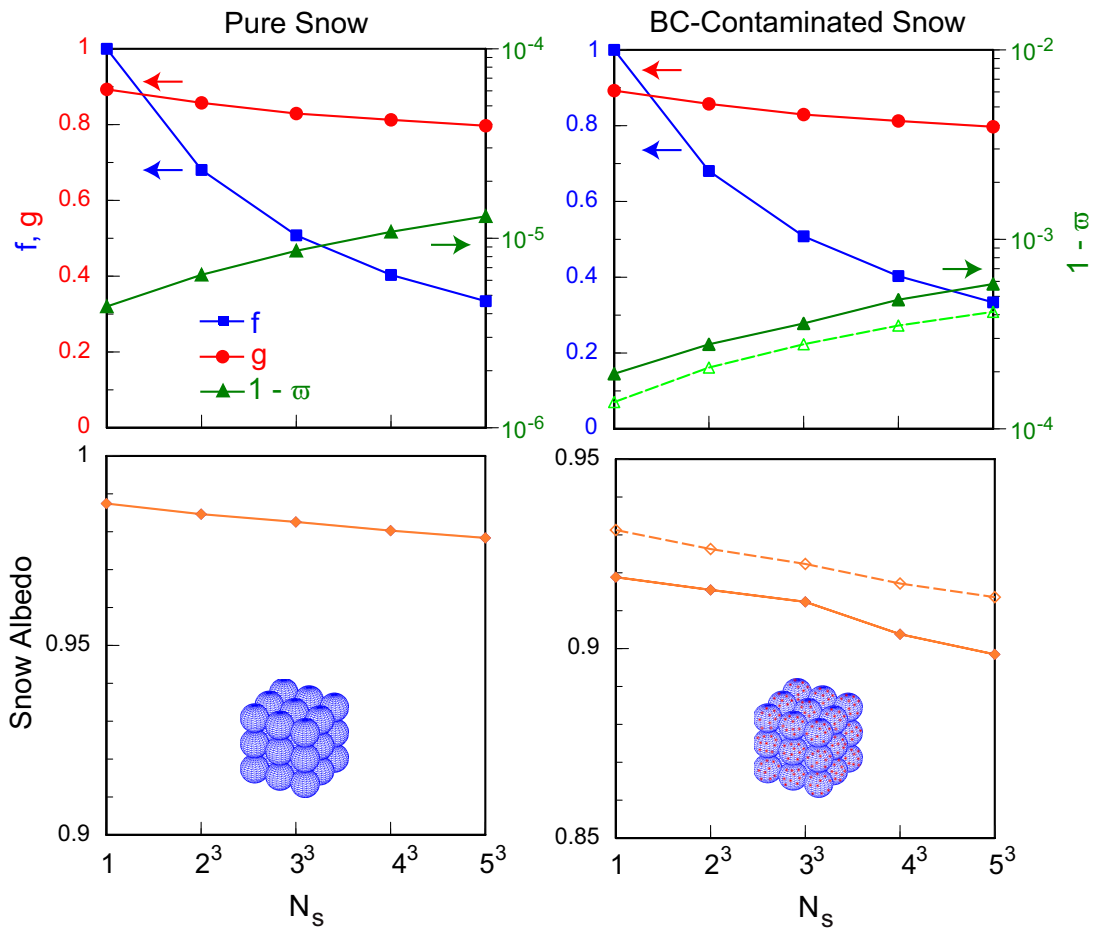
Figure 6.2: Upper panels: single-scattering co-albedo ($1 - \varpi$, green lines), asymmetry factor (g, red lines), and optical depth adjustment factor (f, blue lines) for close-packed snow cubes as a function of the number (N_s) of snow spheres forming the cube. The radius of each snow sphere is 100 μm. Results for both close packing ($N_s > 1$) and independent scattering ($N_s = 1$) snow models are shown. Lower panels: same as upper panels, but for snow albedo at a wavelength of 0.55 μm and a solar zenith angle of 60°. Results for pure snow (left panels) and BC-contaminated snow with a BC concentration of 500 ppb (right panels) are shown. For contaminated cases, snow grains contain multiple coated (solid lines) or uncoated (dashed lines) BC particles. A close-packed snow cube with $N_s = 3^3$ is shown for demonstration.
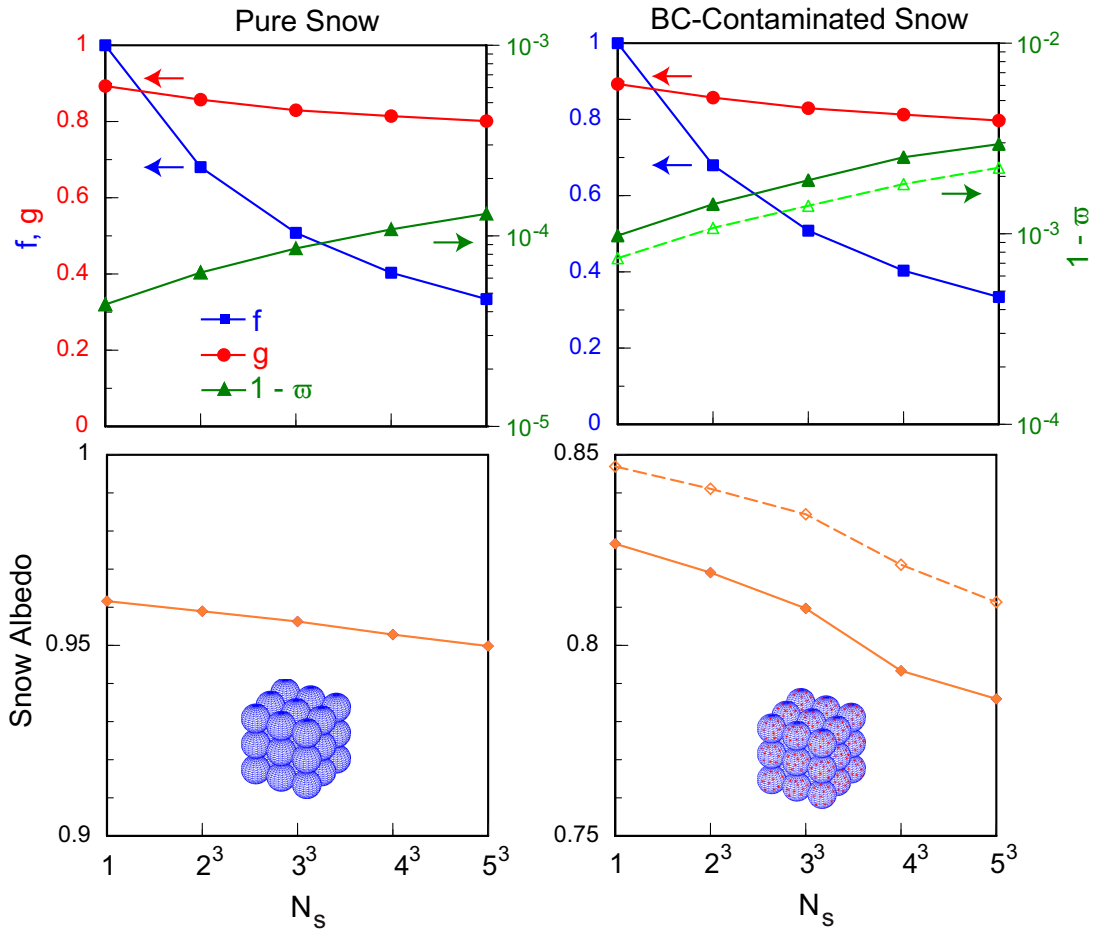
Figure 6.3: Same as Fig. 6.2, but for a radius of 1000 μm for each snow sphere and a BC concentration of 250 ppb in snow.
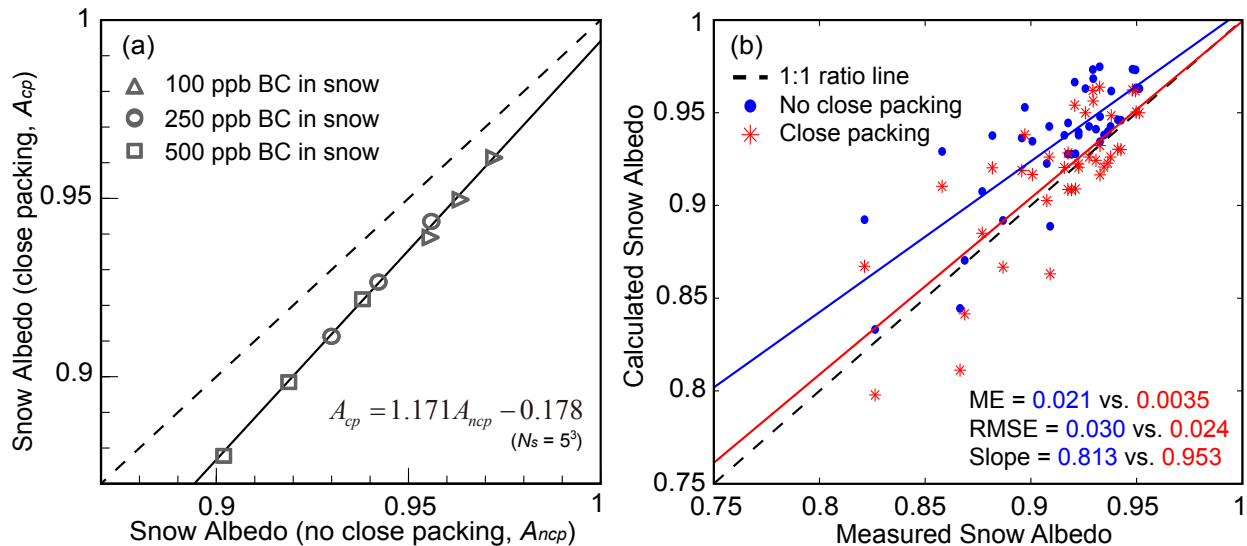
Figure 6.4: (a) Snow albedo with close packing ($N_s = 5^3$) as a function of that without close packing at a wavelength of 0.55 μm with a snow sphere radius of 100 μm and contamination by coated BC. BC concentrations in snow are 100 (triangles), 250 (circles), and 500 ppb (squares). For each BC concentration, three solar zenith angles (43°, 60°, and 74°) are used, with an increasing order in albedos. The regression line and equation between snow albedo with (A_{cp}) and without (A_{ncp}) close packing effect are also shown with $R^2 = 0.998$. (b) Wintertime (December to February) snow albedos (>0.8) during 2007 to 2009 at Sapporo, Hokkaido from measurements and snow model results without close packing (blue dots). Data are taken from *Aoki et al.* (2011). Calculated albedos with close packing (red asterisks) are derived by adjusting those without close packing with the regression equation in (a). Also shown are regression lines of data points (blue and red) as well as mean error (ME), root-mean-square-error (RMSE), and slope of regression lines of calculated results with and without close packing.

CHAPTER 7

Black carbon radiative forcing over the Tibetan Plateau

Abstract

We estimate the snow albedo forcing and direct radiative forcing (DRF) of black carbon (BC) in the Tibetan Plateau using a global chemical transport model in conjunction with a stochastic snow model and a radiative transfer model. The annual mean BC snow albedo forcing is 2.9 W m^{-2} averaged over snow-covered Plateau regions, which is a factor of three larger than the value over global land snowpack. BC-snow internal mixing increases the albedo forcing by 40–60% compared with external mixing and coated BC increases the forcing by 30–50% compared with uncoated BC aggregates, whereas Koch snowflakes reduce the forcing by 20–40% relative to spherical snow grains. The annual BC DRF at the top of the atmosphere is 2.3 W m^{-2} with uncertainties of -70% − +85% in the Plateau after scaling the modeled BC absorption optical depth to Aerosol Robotic Network observations. The BC forcings are attributed to emissions from different regions.

7.1   Introduction

Black carbon (BC) is now considered the second most important human emissions in terms of its radiative forcing in the present-day atmosphere after carbon dioxide (*Bond et al.*, 2013). BC heats the atmosphere by absorbing solar radiation (direct radiative forcing, DRF) (*Jacobson*, 2001), cools the surface by means of atmospheric scattering and absorption (*Ramanathan and Carmichael*, 2008), and reduces snow and ice albedo upon deposition on the surface (snow albedo effect) (*Warren and Wiscombe*, 1985; *Hansen and Nazarenko*, 2004). Ample evidence has pointed to significant impacts on the rapid retreat of glaciers in the Tibetan Plateau associated with BC deposited in snow (*Xu et al.*, 2009). The retreat of these glaciers and the associated changes in surface heating may adversely affect fresh water supply and hydrological cycle for much of Asia (*Menon et al.*, 2010). The snow albedo effect of BC has also been posited as an important driver of the abrupt retreat of Alpine glaciers from the mid-19th century (*Painter et al.*, 2013). Based on observations, *Flanner et al.* (2011) found that the albedo feedback from the Northern Hemisphere cryosphere is substantially stronger than the value estimated from climate models.

Large uncertainties exist in the estimate of both BC DRF and snow albedo forcing over the Tibetan Plateau. Using a chemical transport model (CTM), *Kopacz et al.* (2011) estimated that BC DRF at the top of the atmosphere (TOA) was 0.2–1.7 W m^{-2} at five Tibetan glacial sites and that BC snow albedo forcing was 4–16 W m^{-2} at the same sites. *Wang et al.* (2014a), using the same CTM with updates, derived a substantially smaller BC TOA DRF (<0.5 W m^{-2}) across much of the Plateau. *Flanner et al.* (2009) estimated an annual BC snow albedo forcing of 1.3 W m^{-2} over the Plateau and 10–20 W m^{-2} in spring in parts of the Plateau. *Qian et al.* (2011) reported a springtime BC snow albedo forcing of 14–18 W m^{-2} in the western Plateau. The preceding studies all assumed external mixing between BC and spherical snow grains. *Flanner et al.* (2012) pointed out that BC-snow internal mixing increases the albedo forcing by 40–80%. *Liou et al.* (2014) illustrated that both BC-snow mixing state and snow grain shape play critical roles in determining snow

albedo forcing.

We investigate both BC snow albedo forcing and TOA DRF over the Tibetan Plateau using an extensively evaluated global CTM (GEOS-Chem) in conjunction with a stochastic snow model and a radiative transfer model (RTM). We systematically examine the effects of BC-snow mixing states (internal versus external mixing), BC coating states (coated versus uncoated) and snow grain shapes (Koch snowflake versus sphere) on snow albedo forcing and its uncertainties. To the best of our knowledge, this is the first attempt to evaluate the effects of multiple inclusions of coated BC in nonspherical snow grains. Additionally, we quantify the relative contributions to forcing estimates from different BC source regions. Section 7.2 briefly describes the preceding models and related model simulations. We then discuss BC snow albedo forcing, DRF, and source attributions in Section 7.3. Conclusions are given in Section 7.4.

7.2   Methods

We employed the GEOS-Chem global 3-D CTM (version 9-01-03) to simulate BC distributions. GEOS-Chem is driven by the Goddard Earth Observing System (GEOS-5) meteorological fields with a spatial resolution of $2° \times 2.5°$ horizontally and 47 vertical layers, and a temporal resolution of 6 hours (3 hours for surface variables). All model results presented here are for 2006, during which substantial observations over the Tibetan Plateau are available for verification purposes. A detailed description and extensive evaluations of GEOS-Chem simulations of BC in the Plateau have been presented by *He et al.* (2014b).

We calculated the BC snow albedo forcing using a stochastic snow model (*Liou et al.*, 2014) that explicitly accounts for multiple internal mixing of BC in various types of snow grains. The nonspherical snow grains were constructed in a 3-D coordinate system with multiple BC particles stochastically distributed inside the snow grains. The light absorption and scattering by snow grains and BC were computed by the geometric-optics surface-wave

(GOS) approach developed by *Liou et al.* (2010, 2011). We have extended the original Monte Carlo photon tracing method to snow grains internally mixed with coated BC and assumed that BCs externally mixed in snowpack are in contact with snow grain surfaces, rather than in a suspended interstitial state. Thus, this approach accounted for the interaction between snow grains and BC, which differs from the conventional independent scattering assumption for external mixtures, where optical properties are computed separately for BC and snow grains and averaged using respective cross sections as weighting factors (*Warren and Wiscombe*, 1980, 1985). We have used the conventional independent scattering assumption for external mixture cases only when comparing with previous studies (see Figure 7.1).

The original surface albedo in the model was from GEOS-5 meteorological fields. For pure snow, the snow albedo was based on observations. The BC-contaminated snow albedo was determined from the adding/doubling method for radiative transfer using 20 homogeneous sub-layers with input of the single-scattering properties computed from GOS for various snow grain sizes and shapes and BC mixing conditions. The present snow model does not account for snow aging, a process that may enhance BC snow albedo forcing (*Flanner et al.*, 2012). In this study, we have assumed a constant snow grain radius of 100 μm (volume-equivalent sphere). Also, for computational expediency, we developed a parametric curve fitting to stochastic snow model results involving snow albedo reduction associated with BC in snow.

The BC concentration in snow was calculated as the ratio of GEOS-Chem simulated BC deposition flux and GEOS-5 precipitation over the snow-covered regions (*Kopacz et al.*, 2011; *He et al.*, 2014b). The snow cover was prescribed from GEOS-5 meteorological fields. Subsequently, we derived the associated surface radiative forcing by coupling snow albedo reduction with the GEOS-5 incoming solar radiation field following *Wang et al.* (2011).

We applied the Fu-Liou-Gu (FLG) RTM (*Gu et al.*, 2006, 2010) to calculate atmospheric BC DRF. The FLG RTM combines the delta-four-stream approximation for solar flux calculations with the delta-two/four-stream approximation for infrared flux calculations to assure both accuracy and efficiency. Based on absorption band locations, the solar (0–5 μm) and

162

infrared (5–50 μm) spectra are divided into 6 and 12 bands, respectively, within which the correlated k-distribution method is used to sort gaseous absorption lines. The FLG RTM is not directly coupled with the stochastic snow model such that radiative transfer through the atmosphere and snow are computed separately.

The GEOS-Chem simulated BC aerosol optical depth (AOD) and GEOS-5 meteorological fields were input to the RTM. We have shown that GEOS-Chem underestimates BC absorption AOD (AAOD) over the Tibetan Plateau and adjacent regions (*He et al.*, 2014b). Such underestimates appear to be common for current global CTMs, which vastly underestimate BC AAOD globally by several folds (*Bond et al.*, 2013). Following *Bond et al.* (2013), we determined BC DRF by scaling the modeled BC AAOD to Aerosol Robotic Network (AERONET) observations over global continents and reduce the estimated forcing by 15% to account for the incorrect BC vertical distribution. We have reported only instantaneous clear-sky shortwave BC TOA DRF, which is two orders of magnitude larger than the corresponding longwave forcing.

In addition, we assessed the uncertainty of forcing estimates using a Monte Carlo method (*Efron and Tibshirani*, 1986). This procedure generates an ensemble of random BC AAODs according to the probability distribution of the GEOS-Chem simulated BC AAOD (see Figure 4 in *He et al.* (2014b)). Correspondingly, an ensemble of BC DRF is obtained through 5000 valid RTM simulations. The same procedure was repeated for BC snow albedo forcing whereby we randomly varied the BC concentration in snow, snow grain shape, BC-snow mixing state, and BC coating state. We then analyzed resulting ensemble estimates of the BC forcing statistically, including the mean and confidence interval, and presented the 90% confidence interval as uncertainty range.

7.3   Results and discussions

7.3.1   BC snow albedo forcing

Figure 7.1 shows the comparison of snow albedo reduction in response to BC in snow between previous modeling studies and the present study under the same model assumptions. This study reproduces (differences ≤10%) snow albedo reductions from *Warren and Wiscombe* (1980), *Warren and Wiscombe* (1985), and *Flanner et al.* (2007) by using the same Lorenz-Mie (LM) approach, where external mixing of uncoated BC with spherical snow grains was assumed. The resulting small differences are primarily caused by the different methodologies used for solving radiative transfer in snow models. The results computed from the GOS approach are consistent with those computed from the LM theory (Figures 7.1). Figure 7.1 shows a much stronger snow albedo reduction presented by *Jacobson* (2004) who accounted for the internal and external mixing of coated BC with spherical snow grains simultaneously. We have used BC coated by sulfate and organics in this case, since GEOS-Chem does not simulate the coating of BC by different species dynamically, via condensation and coagulation, in the absence of microphysical processes. Our results, assuming BC coated by sulfate, are 40% lower than those presented in *Jacobson* (2004), but are in good agreement (differences <8%) with his values by assuming organic coating with a refractive index of 1.53 - 0.02i (at 550 nm). We note that the imaginary part (0.02) is at the upper end of observed values (*Chen and Bond*, 2010). Moreover, *Ming et al.* (2009a), *Yasunari et al.* (2010), and *Hadley et al.* (2010) developed empirical parameterizations of BC-induced snow albedo reductions based on linear regressions of combined results from the abovementioned four modeling studies. However, the snow albedo reductions computed by previous models under assorted assumptions vary by a factor of 2 to 5 (see Figure 7.1).

Figure 7.2 shows snow albedo reductions (at 550 nm) as a function of BC concentrations in snow computed from this study by accounting for internal/external mixing of coated/uncoated BC with Koch snowflakes. BC-snow internal mixing enhances snow albedo

164

reduction by 30–90% relative to external mixing, because (1) multiple internal reflections increase the probability of photons being absorbed within snow grains and (2) the mirror effect enables further absorption enhancement from BC particles that happen to reside near the center of snow grains. Coated BC increases snow albedo reduction by 30–70% relative to uncoated BC aggregates. The use of nonspherical Koch snowflakes leads to 20–40% lower snow albedo reductions than spherical snow grains which produce stronger forward scattering (*Liou et al.*, 2014). Thus, the use of realistic snow grain shapes could effectively offset the enhancement of snow albedo reduction from BC-snow internal mixing and BC coating. Results presented below were calculated by assuming internal mixing of coated BC with Koch snowflakes.

We calculated the spectrally averaged (0.2–5 μm, *Liou et al.* (2014)) BC-induced snow albedo reduction in the Tibetan Plateau for 2006. The resulting annual mean reduction is 1.8% over snow covered regions, with an uncertainty of 1.5–2.0%. The largest reduction is 5% in the southern Himalayas and southeastern Plateau, whereas reduction is less than 1% in the central Plateau. Observations have shown a mean annual snow albedo reduction of 0.4±0.4% during 2000–2009 in the mid-Himalayas (*Ming et al.*, 2012). That reduction results from the warming produced by many factors such as greenhouse gases and aerosol deposition. Our results show a BC-induced annual snow albedo reduction of 1–2% for 2006 in the same region.

Subsequently, we calculated the BC snow albedo forcing in the Tibetan Plateau averaged for the period November–April (Figure 7.2), during which Asian BC emissions are largest (*Lu et al.*, 2012) and snowfall is heaviest (*Pu et al.*, 2007). The resulting forcing averaged over the region is 2.7 W m^{-2}. The strongest forcing up to 5–10 W m^{-2} is in the southern Himalayas and southeastern Plateau (Figure 7.2). Our results differ from those of *Qian et al.* (2011), who showed in a modeling analysis that BC snow albedo forcing was higher in the western Plateau and much lower in the eastern Plateau. The BC snow albedo forcing at five Tibetan glacial sites (cf. *Kopacz et al.* (2011)) is more than fourfold lower in this study than

in *Kopacz et al.* (2011). 70% of the difference is because *Kopacz et al.* applied the *Ming et al.* (2009a) parameterization that produces considerably larger snow albedo reductions than the present study. Additionally, *Kopacz et al.* used an earlier version of the GEOS-Chem model that produced higher BC concentrations in snow, which explains about 30% of the difference. *Flanner et al.* (2009) showed an annual mean forcing of 1.3 W m^{-2} over the whole Plateau, 30% lower than our corresponding estimate because of the enhancement from BC-snow internal mixing employed in this study. The mean forcing, accounting for different combinations of BC-snow mixing states and BC coating states, is 2.4 W m^{-2} for Koch snowflakes annually over snow-covered Plateau regions, with an uncertainty of 1.5–3.6 W m^{-2}. Furthermore, including various snow grain shapes in the analysis, we estimate an annual mean BC snow albedo forcing of 2.9 W m^{-2}, with an uncertainty of 1.5–5.0 W m^{-2}.

We estimate a global annual mean BC snow albedo forcing of 0.05 W m^{-2}, with an uncertainty of 0.02–0.08 W m^{-2}. The uncertainty range manifests the combined impacts of snow grain shapes, BC-snow mixing states, and BC coating states. Our estimate is in the middle of the range (0.01–0.09 W m^{-2}) presented by *Bond et al.* (2013). *Flanner et al.* (2007) estimated an annual mean BC snow albedo forcing of 0.55 W m^{-2} averaged over only global land snowpack. Their value is lower than our corresponding estimate (0.86 W m^{-2}) mainly because their model did not account for BC-snow internal mixing, which increases the global BC snow albedo forcing by 40–60% compared with external mixing, within the range of 34–86% reported by *Flanner et al.* (2012).

7.3.2 BC direct radiative forcing

The annual mean BC TOA DRF before scaling the modeled BC AAOD to AERONET observations is 0.90 W m^{-2} averaged over the Plateau, with higher values in spring and summer and lower values in fall and winter. The DRF after the scaling is 2.3 W m^{-2}, with an uncertainty of 0.7–4.3 W m^{-2} without accounting for uncertainty in the AAOD scaling, which is in the range of -60% to +40% (*Bond et al.*, 2013). The strongest forcing is in

the southern Himalayas and to the east of the Plateau (Figure 7.3). The spatial pattern is consistent with those from *Sato et al.* (2003) and *Chung et al.* (2012), in which AAODs were also similarly scaled. However, the DRF at the five Tibetan glacial sites mentioned above is more than 50% higher in this study than in *Kopacz et al.* (2011), who already accounted for BC coating effects. The difference is partially because of lower BC emissions in their study. The surface dimming due to atmospheric BC is -4.7 W m^{-2} annually over the Plateau, while the annual mean atmospheric heating rate is larger than 0.2 K d^{-1} near the surface.

The global annual mean BC AAOD after scaling is 0.0041, a factor of 2.5 larger than modeled values, reflecting the absence of BC internal mixing and low BC emissions in the model. If we attribute the underestimate of modeled AAODs to the weaker BC absorption associated with external mixing, the BC mass absorption coefficient (MAC) in the model needs to be increased from 7 to 14 m^2 g^{-1} to achieve a better agreement with AERONET observations, which is at the upper end of previous estimates (8–14 m^2 g^{-1}) (*Schulz et al.*, 2006; *Jacobson*, 2010). Alternatively, a BC MAC of 11.3 m^2 g^{-1} for the mean BC mixing state from atmospheric observations (*Bond et al.*, 2006) requires increasing global BC emissions in the model from 8.1 to 10.4 Tg yr^{-1} to match AERONET observations, which is 40% lower than the global top-down estimation (*Cohen and Wang*, 2014). The global annual mean TOA DRF is 0.74 W m^{-2} using the scaled AAODs, which is 15% lower than the best estimate from *Bond et al.* (2013). We also note that the DRF is associated with large uncertainties (Figure 7.3) resulting from factors including BC mixing state and emissions used in models. Our best estimate is more than a factor of two higher than that from *Wang et al.* (2014a), primarily because of lower BC emissions and smaller absorption forcing efficiency (AFE, ratio of DRF to AAOD (*Schulz et al.*, 2006)) used in their study. Our global annual mean AFE (180 W m^{-2} AAOD^{-1}) is larger than previous estimates (97–177 W m^{-2} AAOD^{-1}) (*Jacobson*, 2010; *Chung et al.*, 2012), a direct result of the large BC loading at altitudes above 5 km in our model. This is likely a result of an overlong BC lifetime due to insufficient scavenging in the model. *Wang et al.* (2014a) suggested that BC wet scavenging in GEOS-Chem is too weak

based on comparisons with aircraft measurements over the Pacific Ocean.

7.3.3   Source attribution to BC forcings

Figure 7.4 shows the contributions of BC emissions from China, South Asia (including India and Southeast Asia) and the rest of the world to BC snow albedo forcing and TOA DRF over the Plateau. The northern Plateau (region I, Figure 7.4) is mainly influenced by the northern mid-latitude BC pollution transported by the westerlies (*Kopacz et al.*, 2011; *Lu et al.*, 2012), which accounts for half of both snow albedo forcing and DRF in the region. The anthropogenic BC emissions from South Asia (90% of its total BC emissions) dominate both BC snow albedo forcing and DRF in the central Plateau and the Himalayas (region II, Figure 7.4), reflecting the regions' proximity to large sources in India (*Lu et al.*, 2012). In the eastern Plateau (region III, Figure 7.4), anthropogenic BC emissions from China (>90% of its total BC emissions) dominate the contribution to BC DRF throughout the year (70%), which is in line with the results presented by *Kopacz et al.* (2011). However, China accounts for less than half of the snow albedo forcing in the eastern Plateau, comparable to the contribution from South Asia. This is because the fraction (70%) of hydrophilic BC upon arriving in the eastern Plateau after emitted from China is smaller than the fraction (90%) upon reaching the region after emitted from South Asia, which reflects the proximity of the eastern Plateau to large BC sources in Southwest China, leading to less efficient wet scavenging and hence lower BC concentrations in snow.

7.4   Conclusions

We have estimated both BC snow albedo forcing and TOA DRF over the Tibetan Plateau using a systematically evaluated global CTM in conjunction with a stochastic snow model and a RTM. The annual mean BC snow albedo forcing in snow-covered Plateau regions, accounting for various snow grain shapes, BC-snow mixing states and BC coating states,

is 1.5–5.0 W m^{-2}. A robust estimate of BC snow albedo forcing in the Plateau is very difficult in view of the scarcity of measurements of BC concentrations in snow that vary spatiotemporally across the Plateau and large uncertainties associated with BC-induced snow albedo reduction. The estimated snow albedo reductions differ by up to a factor of four depending on snow grain shape, BC-snow mixing state, and BC coating state. Further investigations of the important snow aging processes, including wind pumping and sintering, are necessary to understand the albedo forcing (*Flanner et al.*, 2012). The combined effects produced by snow grain shape, BC-snow mixing, BC coating, and snow aging should be simultaneously taken into account to make further advances to reduce uncertainties in BC snow albedo forcing estimates. Additionally, our best estimate of the annual mean BC TOA DRF is 2.3 W m^{-2} in the Plateau with uncertainties of -75% − +85%, which stem primarily from uncertainties associated with modeled BC AAOD. This calls for concerted measurements of BC vertical profiles, particularly in mountainous regions such as the Tibetan Plateau.

7.5   Tables and figures

Figure 7.1: Snow albedo reduction as a function of BC concentration in snow from previous studies (red): (a) *Warren and Wiscombe* (1980), (b) *Warren and Wiscombe* (1985), (c) *Flanner et al.* (2007) and (d) *Jacobson* (2004), compared with this study using the stochastic snow model with the improved geometric-optics surface-wave approach (GOS, blue) and the Lorenz-Mie approach (LM, green) under the same model assumptions, including wavelength (λ), solar zenith angle (θ_0), BC density (ρ), BC and snow grain radius (r). Results in (d) assume each snow grain including one BC particle and all remaining BCs externally mixed with snow grains. Results from this study in (d) also assume the core-shell structure for BC coated by organics/sulfate with 1-μm diameter (*Schwarz et al.*, 2013).
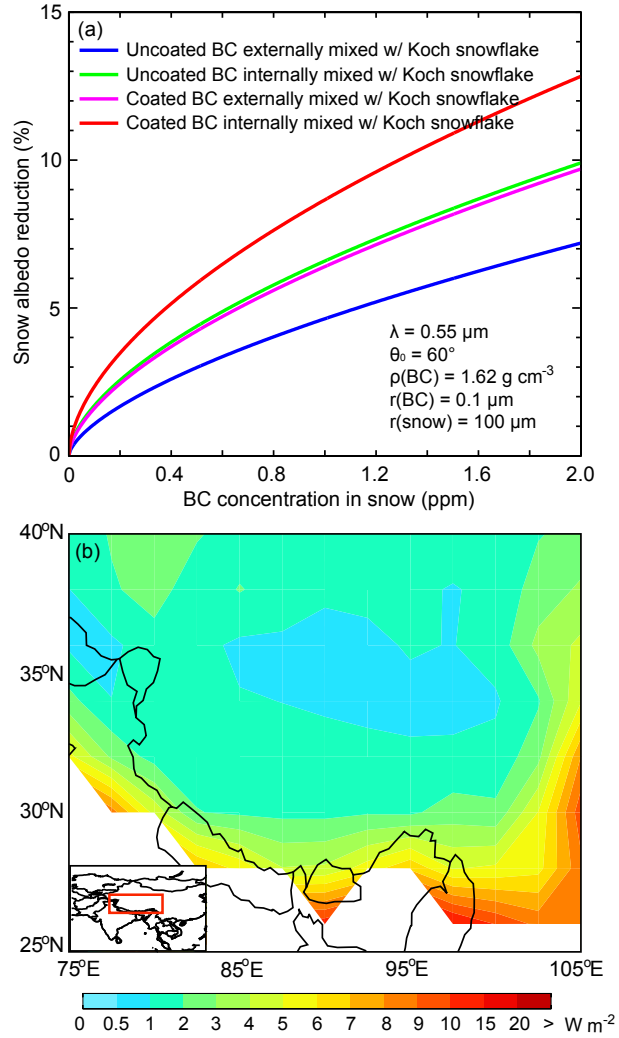
Figure 7.2: (a) Snow albedo reduction as a function of BC concentration in snow using the stochastic snow model with the improved geometric-optics surface-wave (GOS) approach for internal/external mixing of coated/uncoated BC with Koch snowflakes. Also shown are model parameters including wavelength (λ), solar zenith angle (θ_0), BC density (ρ), BC and snow grain radius (r). The snow optical depth is set to obtain the observed albedos of pure snow (*Jacobson*, 2004). The BC density is tuned to obtain a mass absorption coefficient (MAC) of pure BC of 7.5 m^2 g^{-1}. The mass of sulfate coating on BC is tuned to obtain a MAC of coated BC of 11.3 m^2 g^{-1} (*Bond et al.*, 2006). (b) Simulated BC snow albedo forcing over the Tibetan Plateau by assuming internal mixing of coated BC with Koch snowflakes. Values are averages for November–April over snow-covered regions.
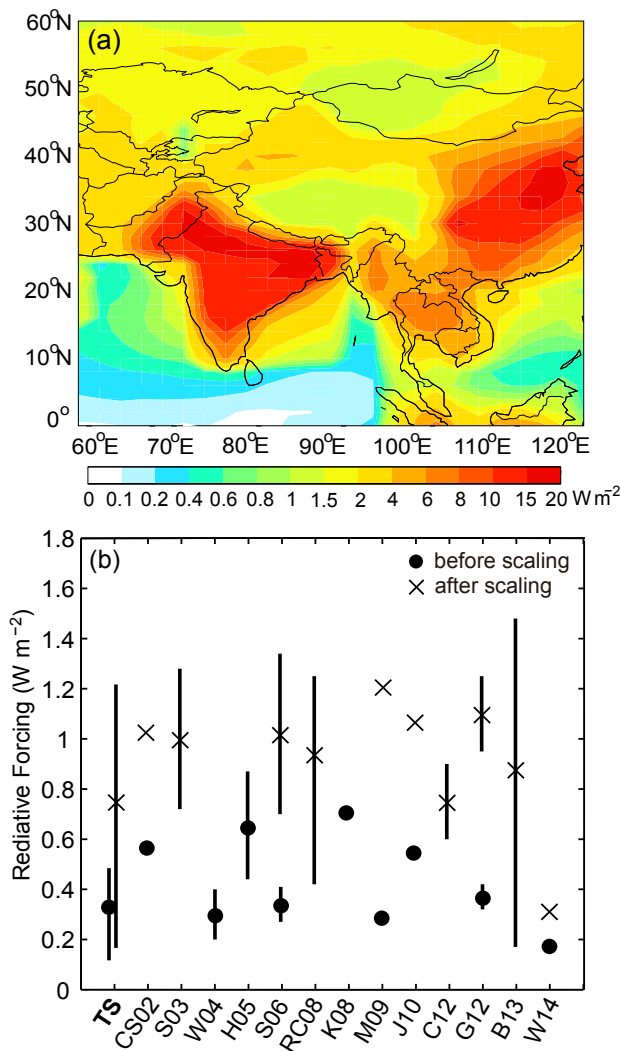
Figure 7.3: (a) Simulated annual mean BC direct radiative forcing (DRF) at the top of the atmosphere (TOA) over Asia after scaling modeled BC AAOD to AERONET observations. (b) Global annual mean BC TOA DRF before (circle) and after (cross) scaling modeled BC AAOD to AERONET observations: this study (TS); *Chung and Seinfeld* (2002) (CS02); *Sato et al.* (2003) (S03); *Wang* (2004) (W04); *Hansen et al.* (2005) (H05); *Schulz et al.* (2006) (S06); *Ramanathan and Carmichael* (2008) (RC08); *Kim et al.* (2008) (K08); *Myhre et al.* (2009) (M09); *Jacobson* (2010) (J10); *Chung et al.* (2012) (C12); *Ghan et al.* (2012) (G12); *Bond et al.* (2013) (B13); *Wang et al.* (2014a) (W14). Uncertainties (vertical bars) are shown when available.

172
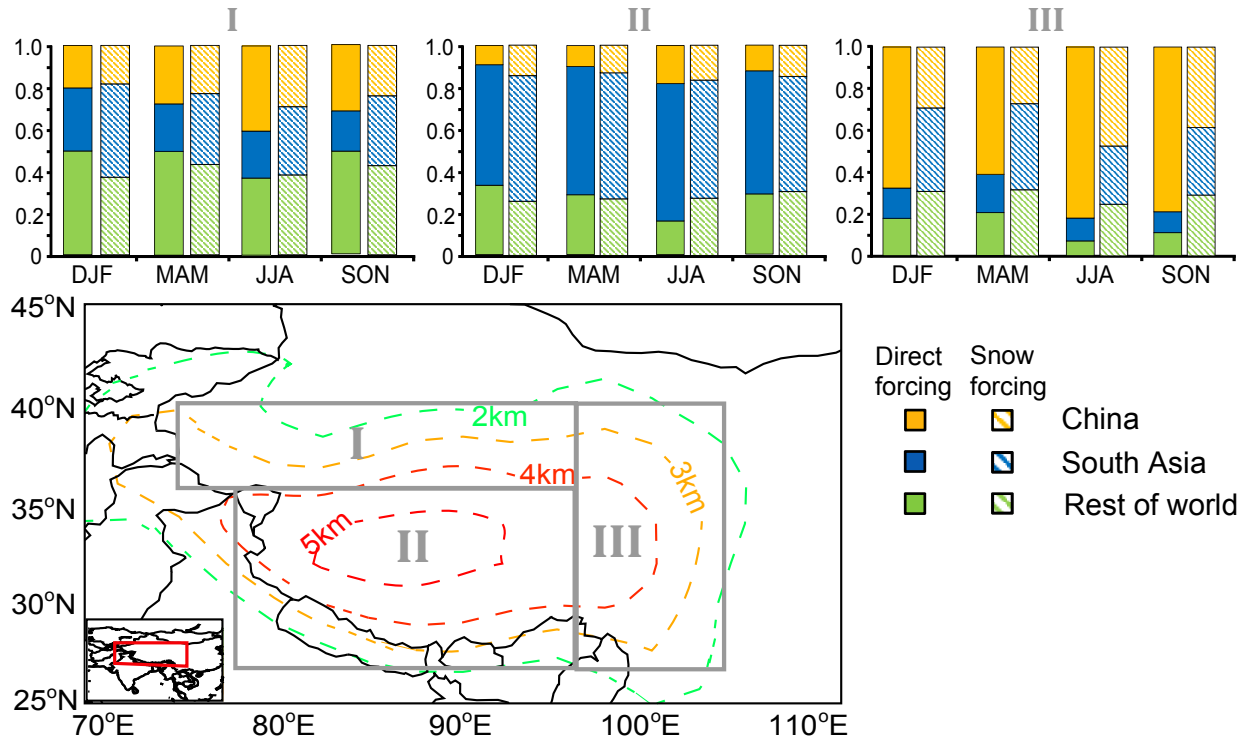
Figure 7.4: GEOS-Chem simulated seasonal contributions to BC snow albedo forcing and direct radiative forcing over the Tibetan Plateau (I – the northern Plateau, II – the Himalayas and central Plateau, III – the eastern Plateau) from BC emissions from China (orange), South Asia (blue), and the rest of the world (green). Results are for 2006. Topography is shown as colored contours.

CHAPTER 8

Final conclusions and future work

8.1 Final conclusions

BC has been identified as the second most important human emission in terms of its global climate forcing in the current atmosphere by virtue of its strong absorption of solar radiation and substantial snow albedo reduction upon deposition. The regional warming effect of BC is even stronger over snow-covered regions, such as the Tibetan Plateau, the third pole of the world. Observations have shown an increasing BC deposition in the Tibetan Plateau during the past half century, which could be an important driver of glacier retreat and snow melting in the region. Changes in snow cover and albedo in the Plateau can affect the hydrological cycle over Asia and the freshwater resource for more than one billion people in Asia. However, the climatic effects of BC over the Tibetan Plateau are not well understood, with large uncertainties in the estimates of BC radiative effects. Accurate estimates of BC climatic impacts in the Tibetan Plateau critically depends on robust model simulations of BC emissions, aging process, transport, vertical distribution, wet and dry deposition and interactions with surface snow. Therefore, it is imperative to improve current model simulations of BC evolution in the atmosphere as well as to understand and quantify BC-radiation and BC-snow-radiation interactions.

This Ph.D. study sought to understand several key BC processes from a modeling perspective, including the microphysical processes and evolution of optical properties during BC atmospheric aging, as well as resolving critical factors involved in BC-snow-radiation interactions. This could lead to a better understanding and quantification of BC direct

radiative and snow albedo effects over the Tibetan Plateau. First, we conducted a comprehensive evaluation of BC simulations over the Tibetan Plateau by a global 3-D CTM, using in situ measurements of BC in surface air, BC in snow, and BC AAOD. Using improved anthropogenic BC emission inventories for Asia that account for rapid technology renewal and energy consumption growth and improved global biomass burning emission inventories that account for small fires, we found that model results of both BC in surface air and in snow are in good agreement with observations in rural and remote regions. Modeled BC AAOD was more than a factor of two lower than observations at most sites, particularly to the northwest of the Plateau and along the southern slopes of the Himalayas in winter and spring, which was attributable primarily to underestimated emissions and the assumption of external mixing of BC aerosols in the model. Both surface BC concentration and AAOD were strongly sensitive to anthropogenic emissions from China and India, while BC concentration in snow was especially responsive to the treatment of BC aerosol aging. We found that a finer model resolution reduces the bias in modeled surface BC concentration from 15% to 2%. The large range and non-homogeneity of discrepancies between model results and observations of BC across the Tibetan Plateau suggested an imperative need for more extensive measurements of BC, including its concentration in surface air and snow, AAOD, vertical profile and deposition.

Subsequently, we developed a theoretical model that accounts for three typical BC aging stages, including freshly emitted aggregates, coated BC by soluble material, and coated BC particles after further hygroscopic growth. The GOS approach was used to compute BC absorption and scattering at each aging stage, which was coupled with a stochastic procedure to construct different BC structures. Theoretical calculations generally yielded consistent optical cross sections for both fresh BC aggregates and coated BC particles with different sizes, compared with measurements. Sensitivity analyses showed that BC optical properties are highly sensitive to BC morphology and coating mass at different aging stages. The results suggested that the evolution of BC coating states (e.g., coating thickness, morphology,

175

and composition) during aging in the real atmosphere could exert significant impacts on BC radiative properties and thus its climatic effects, particularly over regions with high heterogeneity. Therefore, accurate estimates of BC radiative effects require the incorporation of a dynamic BC aging process accounting for realistic coating structures in climate models.

Following the aforementioned work, we conducted a comprehensive intercomparison of the GOS and superposition T-matrix calculations with laboratory measurements for optical properties of fresh and aged BC particles with complex structures. The GOS and T-matrix results both captured the measured optical (extinction, absorption, and scattering) cross sections of fresh and coated BC aggregates, with differences of 5–30% depending on size. The asymmetry factor computed from the GOS approach showed a good agreement (differences <5%) with the T-matrix results for various BC sizes and aggregating structures as well as most coating structures. We found that the optical cross sections and asymmetry factors of coated BC strongly depends on particle structures and sizes (i.e., sensitivity), where the GOS results deviated to some extent from the T-matrix calculations. This is likely due to uncertainty in GOS calculations for small particles with complex structures. This study provided the foundation to further apply the GOS approach to radiative transfer and climate studies in future work.

In addition, we developed and examined a microphysics-based BC aging scheme that explicitly accounts for condensation and coagulation processes in GEOS-Chem global CTM. We analyzed the difference in BC aging rate between the microphysics-based scheme and a widely-used fixed aging scheme with an e-folding time of 1.2 days, followed by a systematic evaluation of BC simulations using HIPPO observations from 2009 to 2011. The microphysical aging rate was a factor of 2–6 higher than that from the fixed aging scheme in the lower troposphere over such source regions, because of strong emissions of sulfate-nitrate and SOA precursors, which resulted in faster BC aging through condensation and coagulation. The microphysical aging rate was more than fivefold lower than that from the fixed aging scheme in remote regions, where condensation and coagulation are rather weak. Compared with the

fixed aging scheme, the microphysical scheme reduced model-observation discrepancies by about a factor of 3, particularly in the middle and upper troposphere as well as the tropics. The faster BC aging over the source regions from the microphysics-based scheme dominated the aging effects on global BC distribution, resulting in a much lower BC column burden and zonal mean concentration globally, compared with the fixed aging scheme. BC aging rate was insensitive ($<10\%$ change) to aerosol size distribution, condensation threshold, and chemical oxidation over source regions, while it was the opposite (more than twofold change) in the polar regions and at high altitudes, where the aging rate was orders of magnitude smaller.

To understand BC-snow-radiation interactions, we developed a new snow albedo model for closed-packed snow grains internally mixed with BC aerosol. Compared with the widely-used independent scattering approximation (ISA) in previous studies, close packing resulted in higher single scattering co-albedos but lower asymmetry factors and optical depths for both clean and BC-contaminated snow. Close packing enhanced the BC-induced snow albedo reduction and hence albedo forcing by up to 15% for fresh snow and 20% for old snow, with larger enhancements occurring in stronger structure packing. We further determined quantitative relationships to adjust snow albedo calculations for the close packing effect, resulting in a closer match between albedo simulations and observations than ISA calculations. The results highlighted the necessity of accounting for snow close packing in assessing the effects of BC on snow albedo and its feedback in the BC-snow system, particularly over snow-covered regions.

Finally, we estimated both BC snow albedo forcing and TOA DRF over the Tibetan Plateau using a systematically evaluated global CTM in conjunction with a stochastic snow model and a RTM. The annual mean BC snow albedo forcing in snow-covered Plateau regions, accounting for various snow grain shapes, BC-snow mixing states and BC coating states, was 1.5–5.0 W m^{-2}, based on a Monte Carlo estimate, which differed by up to a factor of four depending on snow grain shape, BC-snow mixing state, and BC coating state. The

combined effects produced by these key factors should be simultaneously taken into account to make further advances to reduce uncertainties in BC snow albedo forcing estimates. Our best estimate of the annual mean BC TOA DRF was 2.3 W m^{-2} in the Plateau with uncertainties of -75% – +85%, which stem primarily from uncertainties associated with modeled BC AAOD. This calls for concerted measurements of BC vertical profiles, particularly in mountainous regions such as the Tibetan Plateau.

8.2   Future work

The focus of future study is to develop and incorporate parameterizations for BC-snow-radiation interactions in climate models to quantify interactive radiative and hydrological effects and feedbacks over the Tibetan Plateau. The scientific questions are: (1) To what extent do the effects of BC-snow-radiation interactions modify seasonal evolution of snowpack and surface albedo over the Tibetan Plateau? (2) What is the integrative effect of the BC-snow-radiation interactions on regional climate over the Tibetan Plateau including surface energy balance and hydrological cycle? To answer these questions, three tasks will be focused on.

First, a BC-snow parameterization will be developed based on the stochastic snow model to account for the multiple BC-snow internal mixing and nonspherical snow grain shape for application to climate models and LSMs. A number of model simulations will be conducted using various snow grain sizes and shapes, BC sizes and concentrations in snow, and BC-snow mixing states. This generates a dataset for conducting subsequent multiple non-linear regressions to parameterize spectral optical properties of BC-snow system as a function of the preceding parameters.

Second, the BC-snow parameterization will be implemented into a widely-used LSM (Noah-MP) coupled with WRF-Chem (WRF-Chem-Noah-MP) to investigate the effects of BC-induced snow albedo reduction and to improve simulations for seasonal snowpack evo-

lution. Currently, aerosol-snow interaction is completely missing in the Noah-MP model. Specifically, BC concentrations in snow will be determined by BC and snow deposition from atmospheric simulations in WRF-Chem coupled with the snowpack evolution in Noah-MP. Based on the BC concentration in snow, snow grain size and shape, and BC-snow mixing state, the spectral optical properties of BC-snow system can be obtained following the parameterization outlined above. The spectral optical properties will be used as input in subsequent radiative transfer calculations in Noah-MP to produce snow albedo for both canopy and ground.

Finally, sensitivity simulations will be conducted using WRF-Chem-Noah-MP to investigate the effects of snow grain shapes and BC-snow multiple internal mixing on BC-induced snow albedo reduction and associated surface radiative effect over the Tibetan Plateau. We will perform model simulations to examine the radiative and hydrological effects caused by BC deposition, including changes in snow albedo, snow water equivalent, surface heat flux, surface temperature, and runoff. Model simulated BC distribution in air and snow as well as meteorological variables will be compared with available in situ, aircraft, or satellite observations to evaluate model performance. Furthermore, we will carry out sensitivity simulations to pinpoint contributions from different BC source regions to the BC-induced hydroclimate effects over the Tibetan Plateau, which can provide important implications for an effective mitigation of BC emissions.

Bibliography

Adachi, K., and P. R. Buseck (2013), Changes of ns-soot mixing states and shapes in an urban area during calnex, *Journal of Geophysical Research: Atmospheres*, *118*(9), 3723–3730.

Adachi, K., S. H. Chung, and P. R. Buseck (2010), Shapes of soot aerosol particles and implications for their effects on climate, *Journal of Geophysical Research: Atmospheres*, *115*(D15).

Akagi, S. K., J. Craven, J. Taylor, G. McMeeking, R. Yokelson, I. Burling, S. Urbanski, C. Wold, J. Seinfeld, H. Coe, et al. (2012), Evolution of trace gases and particles emitted by a chaparral fire in california, *Atmospheric Chemistry and Physics*, *12*(3), 1397–1421.

Alexander, B., R. J. Park, D. J. Jacob, Q. Li, R. M. Yantosca, J. Savarino, C. Lee, and M. Thiemens (2005), Sulfate formation in sea-salt aerosols: Constraints from oxygen isotopes, *Journal of Geophysical Research: Atmospheres*, *110*(D10).

Allen, D. J., R. B. Rood, A. M. Thompson, and R. D. Hudson (1996a), Three-dimensional radon 222 calculations using assimilated meteorological data and a convective mixing algorithm, *JOURNAL OF GEOPHYSICAL RESEARCH-ALL SERIES-*, *101*, 6871–6881.

Allen, D. J., P. Kasibhatla, A. M. Thompson, R. B. Rood, B. G. Doddridge, K. E. Pickering, R. D. Hudson, and S.-J. Lin (1996b), Transport-induced interannual variability of carbon monoxide determined using a chemistry and transport model, *Journal of Geophysical Research: Atmospheres*, *101*(D22), 28,655–28,669.

Andermann, C., S. Bonnet, and R. Gloaguen (2011), Evaluation of precipitation data sets along the himalayan front, *Geochemistry, Geophysics, Geosystems*, *12*(7).

Anderson, T. L., and J. A. Ogren (1998), Determining aerosol radiative properties using the tsi 3563 integrating nephelometer, *Aerosol Science and Technology*, *29*(1), 57–69.

Aoki, T., K. Kuchiki, M. Niwano, Y. Kodama, M. Hosaka, and T. Tanaka (2011), Physically based snow albedo model for calculating broadband albedos and the solar heating profile in snowpack for general circulation models, *Journal of Geophysical Research: Atmospheres*, *116*(D11).

Aquila, V., J. Hendricks, A. Lauer, N. Riemer, H. Vogel, D. Baumgardner, A. Minikin, A. Petzold, J. Schwarz, J. Spackman, et al. (2011), Made-in: a new aerosol microphysics submodel for global simulation of insoluble particles and their mixing state, *Geoscientific Model Development*, *4*(2), 325.

Arakawa, A., and W. H. Schubert (1974), Interaction of a cumulus cloud ensemble with the large-scale environment, part i, *Journal of the Atmospheric Sciences*, *31*(3), 674–701.

Barnett, T. P., J. C. Adam, and D. P. Lettenmaier (2005), Potential impacts of a warming climate on water availability in snow-dominated regions, *Nature*, *438*(7066), 303–309.

Beegum, S. N., K. K. Moorthy, S. S. Babu, S. Satheesh, V. Vinoj, K. Badarinath, P. Safai, P. Devara, S. Singh, U. Dumka, et al. (2009), Spatial distribution of aerosol black carbon over india during pre-monsoon season, *Atmospheric Environment*, *43*(5), 1071–1078.

Bonasoni, P., P. Laj, A. Marinoni, M. Sprenger, F. Angelini, J. Arduini, U. Bonafè, F. Calzolari, T. Colombo, S. Decesari, et al. (2010), Atmospheric brown clouds in the himalayas: first two years of continuous observations at the nepal climate observatory-pyramid (5079 m), *Atmospheric Chemistry and Physics*, *10*(15), 7515–7531.

Bond, T. C., and R. W. Bergstrom (2006), Light absorption by carbonaceous particles: An investigative review, *Aerosol science and technology*, *40*(1), 27–67.

Bond, T. C., T. L. Anderson, and D. Campbell (1999), Calibration and intercomparison of filter-based measurements of visible light absorption by aerosols, *Aerosol Science & Technology*, *30*(6), 582–600.

Bond, T. C., D. G. Streets, K. F. Yarber, S. M. Nelson, J.-H. Woo, and Z. Klimont (2004), A technology-based global inventory of black and organic carbon emissions from combustion, *Journal of Geophysical Research: Atmospheres*, *109*(D14).

Bond, T. C., G. Habib, and R. W. Bergstrom (2006), Limitations in the enhancement of visible light absorption due to mixing state, *Journal of Geophysical Research: Atmospheres*, *111*(D20).

Bond, T. C., E. Bhardwaj, R. Dong, R. Jogani, S. Jung, C. Roden, D. G. Streets, and N. M. Trautmann (2007), Historical emissions of black and organic carbon aerosol from energy-related combustion, 1850–2000, *Global Biogeochemical Cycles*, *21*(2).

Bond, T. C., S. J. Doherty, D. Fahey, P. Forster, T. Berntsen, B. DeAngelo, M. Flanner, S. Ghan, B. Kärcher, D. Koch, et al. (2013), Bounding the role of black carbon in the climate system: A scientific assessment, *Journal of Geophysical Research: Atmospheres*, *118*(11), 5380–5552.

Born, M., and E. Wolf (1980), *Principles of optics: electromagnetic theory of propagation, interference and diffraction of light*, Elsevier.

Cachier, H., and M. H. Pertuisot (1994), Particulate carbon in arctic ice, analysis magazine, *Analusis Magazine*, *22*(1), 34–37.

Cappa, C. D., T. B. Onasch, P. Massoli, D. R. Worsnop, T. S. Bates, E. S. Cross, P. Davidovits, J. Hakala, K. L. Hayden, B. T. Jobson, et al. (2012), Radiative absorption enhancements due to the mixing state of atmospheric black carbon, *Science*, *337*(6098), 1078–1081.

Carrico, C. M., M. H. Bergin, A. B. Shrestha, J. E. Dibb, L. Gomes, and J. M. Harris (2003), The importance of carbon and mineral dust to seasonal aerosol properties in the nepal himalaya, *Atmospheric Environment*, *37*(20), 2811–2824.

Chen, D., Y. Wang, M. B. McElroy, K. He, R. M. Yantosca, and P. L. Sager (2009), Regional co pollution and export in china simulated by the high-resolution nested-grid geos-chem model, *Atmospheric Chemistry and Physics*, *9*(11), 3825–3839.

Chen, Y., and T. Bond (2010), Light absorption by organic carbon from wood combustion, *Atmospheric Chemistry and Physics*, *10*(4), 1773–1787.

Cheng, Y., M. Berghof, R. Garland, A. Wiedensohler, B. Wehner, T. Müller, H. Su, Y. Zhang, P. Achtert, A. Nowak, et al. (2009), Influence of soot mixing state on aerosol light absorption and single scattering albedo during air mass aging at a polluted regional site in northeastern china, *Journal of Geophysical Research: Atmospheres*, *114*(D2).

China, S., C. Mazzoleni, K. Gorkowski, A. C. Aiken, and M. K. Dubey (2013), Morphology and mixing state of individual freshly emitted wildfire carbonaceous particles, *Nature communications*, *4*.

China, S., B. Scarnato, R. C. Owen, B. Zhang, M. T. Ampadu, S. Kumar, K. Dzepina, M. P. Dziobak, P. Fialho, J. A. Perlinger, et al. (2015), Morphology and mixing state of aged soot particles at a remote marine free troposphere site: Implications for optical properties, *Geophysical Research Letters*, *42*(4), 1243–1250.

Chow, J. C., J. G. Watson, L.-W. A. Chen, W. P. Arnott, H. Moosmüller, and K. Fung (2004), Equivalence of elemental carbon by thermal/optical reflectance and transmittance with different temperature protocols, *Environmental Science & Technology*, *38*(16), 4414–4422.

Chung, C. E., V. Ramanathan, and D. Decremer (2012), Observationally constrained estimates of carbonaceous aerosol radiative forcing, *Proceedings of the National Academy of Sciences*, *109*(29), 11,624–11,629.

Chung, S. H., and J. H. Seinfeld (2002), Global distribution and climate forcing of carbonaceous aerosols, *Journal of Geophysical Research: Atmospheres*, *107*(D19).

Clarke, A., Y. Shinozuka, V. Kapustin, S. Howell, B. Huebert, S. Doherty, T. Anderson, D. Covert, J. Anderson, X. Hua, et al. (2004), Size distributions and mixtures of dust and black carbon aerosol in asian outflow: Physiochemistry and optical properties, *Journal of Geophysical Research: Atmospheres*, *109*(D15).

Cohen, J. B., and C. Wang (2014), Estimating global black carbon emissions using a top-down kalman filter approach, *Journal of Geophysical Research: Atmospheres*, *119*(1), 307–323.

Colbeck, S. (1982), An overview of seasonal snow metamorphism, *Reviews of Geophysics*, *20*(1), 45–61.

Cooke, W., C. Liousse, H. Cachier, and J. Feichter (1999), Construction of a 1×1 fossil fuel emission data set for carbonaceous aerosol and implementation and radiative impact in the echam4 model, *Journal of Geophysical Research: Atmospheres*, *104*(D18), 22,137–22,162.

Cozic, J., S. Mertes, B. Verheggen, D. J. Cziczo, S. Gallavardin, S. Walter, U. Baltensperger, and E. Weingartner (2008), Black carbon enrichment in atmospheric ice particle residuals observed in lower tropospheric mixed phase clouds, *Journal of Geophysical Research: Atmospheres*, *113*(D15).

Croft, B., U. Lohmann, and K. v. Salzen (2005), Black carbon ageing in the canadian centre for climate modelling and analysis atmospheric general circulation model, *Atmospheric chemistry and physics*, *5*(7), 1931–1949.

Dahe, Q., L. Shiyin, and L. Peiji (2006), Snow cover distribution, variability, and response to climate change in western china, *Journal of climate*, *19*(9), 1820–1833.

Dahneke, B. (1983), Simple kinetic theory of brownian diffusion in vapors and aerosols, *Theory of dispersed multiphase flow*, *2*, 97–133.

Dang, C., Q. Fu, and S. G. Warren (2016), Effect of snow grain shape on snow albedo, *Journal of the Atmospheric Sciences*, *73*(9), 3573–3583.

Decesari, S., M. Facchini, E. Matta, M. Mircea, S. Fuzzi, A. Chughtai, and D. Smith (2002), Water soluble organic compounds formed by oxidation of soot, *Atmospheric Environment*, *36*(11), 1827–1832.

Dentener, F., S. Kinne, T. Bond, O. Boucher, J. Cofala, S. Generoso, P. Ginoux, S. Gong, J. Hoelzemann, A. Ito, et al. (2006), Emissions of primary aerosol and precursor gases in the years 2000 and 1750 prescribed data-sets for aerocom, *Atmospheric Chemistry and Physics*, *6*(12), 4321–4344.

Dobbins, R. A., and C. M. Megaridis (1991), Absorption and scattering of light by polydisperse aggregates, *Applied Optics*, *30*(33), 4747–4754.

Donner, L. J., B. L. Wyman, R. S. Hemler, L. W. Horowitz, Y. Ming, M. Zhao, J.-C. Golaz, P. Ginoux, S.-J. Lin, M. D. Schwarzkopf, et al. (2011), The dynamical core, physical parameterizations, and basic simulation characteristics of the atmospheric component am3 of the gfdl global coupled model cm3, *Journal of Climate*, *24*(13), 3484–3519.

Draine, B. T., and P. J. Flatau (1994), Discrete-dipole approximation for scattering calculations, *JOSA A*, *11*(4), 1491–1499.

Dubovik, O., M. D. King, et al. (2000), A flexible inversion algorithm for retrieval of aerosol optical properties from sun and sky radiance measurements, *Journal of Geophysical Research*, *105*(D16), 20,673–20,696.

Efron, B., and R. Tibshirani (1986), Bootstrap methods for standard errors, confidence intervals, and other measures of statistical accuracy, *Statistical science*, pp. 54–75.

Emery, C., J. Jung, N. Downey, J. Johnson, M. Jimenez, G. Yarwood, and R. Morris (2012), Regional and global modeling estimates of policy relevant background ozone over the united states, *Atmospheric Environment*, *47*, 206–217.

Fairlie, T. D., D. J. Jacob, and R. J. Park (2007), The impact of transpacific transport of mineral dust in the united states, *Atmospheric Environment*, *41*(6), 1251–1266.

Fernandes, R., H. Zhao, X. Wang, J. Key, X. Qu, and A. Hall (2009), Controls on northern hemisphere snow albedo feedback quantified using satellite earth observations, *Geophysical Research Letters*, *36*(21).

Flanner, M., X. Liu, C. Zhou, J. E. Penner, and C. Jiao (2012), Enhanced solar energy absorption by internally-mixed black carbon in snow grains, *Atmospheric Chemistry and Physics*, *12*(10), 4699–4721.

Flanner, M. G., C. S. Zender, J. T. Randerson, and P. J. Rasch (2007), Present-day climate forcing and response from black carbon in snow, *Journal of Geophysical Research: Atmospheres*, *112*(D11).

Flanner, M. G., C. S. Zender, P. G. Hess, N. M. Mahowald, T. H. Painter, V. Ramanathan, and P. Rasch (2009), Springtime warming and reduced snow cover from carbonaceous particles, *Atmospheric Chemistry and Physics*, *9*(7), 2481–2497.

Flanner, M. G., K. Shell, M. Barlage, D. K. Perovich, and M. Tschudi (2011), Radiative forcing and albedo feedback from the northern hemisphere cryosphere between 1979 and 2008, *Nature Geoscience*, *4*(3), 151–155.

Fletcher, C. G., P. J. Kushner, A. Hall, and X. Qu (2009), Circulation responses to snow albedo feedback in climate change, *Geophysical Research Letters*, *36*(9).

Friedman, B., H. Herich, L. Kammermann, D. S. Gross, A. Arneth, T. Holst, and D. J. Cziczo (2009), Subarctic atmospheric aerosol composition: 1. ambient aerosol characterization, *Journal of Geophysical Research: Atmospheres*, *114*(D13).

Friedman, B., G. Kulkarni, J. Beránek, A. Zelenyuk, J. A. Thornton, and D. J. Cziczo (2011), Ice nucleation and droplet formation by bare and coated soot particles, *Journal of Geophysical Research: Atmospheres*, *116*(D17).

Fu, T.-M., J. Cao, X. Zhang, S. Lee, Q. Zhang, Y. Han, W. Qu, Z. Han, R. Zhang, Y. Wang, et al. (2012), Carbonaceous aerosols in china: top-down constraints on primary sources and

estimation of secondary contribution, *Atmospheric chemistry and physics*, *12*(5), 2725–2746.

Fuller, K. A. (1995), Scattering and absorption cross sections of compounded spheres. ii. calculations for external aggregation, *JOSA A*, *12*(5), 881–892.

Gangl, M., M. Kocifaj, G. Videen, and H. Horvath (2008), Light absorption by coated nano-sized carbonaceous particles, *Atmospheric Environment*, *42*(11), 2571–2581.

Ganguly, D., P. Ginoux, V. Ramaswamy, D. Winker, B. Holben, and S. Tripathi (2009a), Retrieving the composition and concentration of aerosols over the indo-gangetic basin using caliop and aeronet data, *Geophysical Research Letters*, *36*(13).

Ganguly, D., P. Ginoux, V. Ramaswamy, O. Dubovik, J. Welton, E. Reid, and B. Holben (2009b), Inferring the composition and concentration of aerosols by combining aeronet and mplnet data: Comparison with other measurements and utilization to evaluate gcm output, *Journal of Geophysical Research: Atmospheres*, *114*(D16).

Ghan, S. J., X. Liu, R. C. Easter, R. Zaveri, P. J. Rasch, J.-H. Yoon, and B. Eaton (2012), Toward a minimal representation of aerosols in climate models: Comparative decomposition of aerosol direct, semidirect, and indirect radiative forcing, *Journal of Climate*, *25*(19), 6461–6476.

Göbel, G., J. Kuhn, and J. Fricke (1995), Dependent scattering effects in latex-sphere suspensions and scattering powders, *Waves in random media*, *5*(4), 413–426.

Granier, C., B. Bessagnet, T. Bond, A. D'Angiola, H. D. van Der Gon, G. J. Frost, A. Heil, J. W. Kaiser, S. Kinne, Z. Klimont, et al. (2011), Evolution of anthropogenic and biomass burning emissions of air pollutants at global and regional scales during the 1980–2010 period, *Climatic Change*, *109*(1-2), 163.

Gu, Y., K. Liou, Y. Xue, C. Mechoso, W. Li, and Y. Luo (2006), Climatic effects of different aerosol types in china simulated by the ucla general circulation model, *Journal of Geophysical Research: Atmospheres*, *111*(D15).

Gu, Y., K. Liou, W. Chen, and H. Liao (2010), Direct climate effect of black carbon in china and its impact on dust storms, *Journal of Geophysical Research: Atmospheres*, *115*(D7).

Guenther, C. (2006), Estimates of global terrestrial isoprene emissions using megan (model of emissions of gases and aerosols from nature), *Atmospheric Chemistry and Physics*, *6*.

Hack, J., B. Boville, J. Kiehl, P. Rasch, and D. Williamson (1994), Climate statistics from the national center for atmospheric research community climate model ccm2, *J. Geophys. Res*, *99*(20), 785–20.

Hadley, O., C. Corrigan, T. Kirchstetter, S. Cliff, and V. Ramanathan (2010), Measured black carbon deposition on the sierra nevada snow pack and implication for snow pack retreat, *Atmospheric Chemistry and Physics*, *10*(15), 7505–7513.

Hadley, O. L., and T. W. Kirchstetter (2012), Black-carbon reduction of snow albedo, *Nature Climate Change*, *2*(6), 437–440.

Hall, A., and X. Qu (2006), Using the current seasonal cycle to constrain snow albedo feedback in future climate change, *Geophysical Research Letters*, *33*(3).

Hansen, J., and L. Nazarenko (2004), Soot climate forcing via snow and ice albedos, *Proceedings of the National Academy of Sciences of the United States of America*, *101*(2), 423–428.

Hansen, J. e., M. Sato, R. Ruedy, L. Nazarenko, A. Lacis, G. Schmidt, G. Russell, I. Aleinov, M. Bauer, S. Bauer, et al. (2005), Efficacy of climate forcings, *Journal of Geophysical Research: Atmospheres*, *110*(D18).

Harris, I., P. Jones, T. Osborn, and D. Lister (2014), Updated high-resolution grids of monthly climatic observations–the cru ts3. 10 dataset, *International Journal of Climatology*, *34*(3), 623–642.

He, C., Q. Li, K.-N. Liou, Y. Takano, Y. Gu, L. Qi, Y. Mao, and L. R. Leung (2014a), Black carbon radiative forcing over the tibetan plateau, *Geophysical Research Letters*, *41*(22), 7806–7813.

He, C., Q. Li, K. Liou, J. Zhang, L. Qi, Y. Mao, M. Gao, Z. Lu, D. Streets, Q. Zhang, et al. (2014b), A global 3-d ctm evaluation of black carbon in the tibetan plateau, *Atmospheric Chemistry and Physics*, *14*(13), 7091–7112.

He, C., K.-N. Liou, Y. Takano, R. Zhang, M. Levy Zamora, P. Yang, Q. Li, and L. R. Leung (2015), Variation of the radiative properties during black carbon aging: theoretical and experimental intercomparison, *Atmospheric Chemistry and Physics*, *15*(20), 11,967– 11,980.

He, C., Q. Li, K.-N. Liou, L. Qi, S. Tao, and J. P. Schwarz (2016a), Microphysics-based black carbon aging in a global ctm: constraints from hippo observations and implications for global black carbon budget, *Atmospheric Chemistry and Physics*, *16*(5), 3077–3098.

He, C., Y. Takano, K.-N. Liou, P. Yang, Q. Li, and D. W. Mackowski (2016b), Intercomparison of the gos approach, superposition t-matrix method, and laboratory measurements for black carbon optical properties during aging, *Journal of Quantitative Spectroscopy and Radiative Transfer*, *184*, 287–296.

Heintzenberg, J. (1989), Fine particles in the global troposphere a review, *Tellus B*, *41*(2), 149–160.

Heintzenberg, J., and D. Covert (1984), Size distribution of elemental carbon, sulphur and total mass in the radius range 10- 6 to 10- 4 cm, *Science of The Total Environment*, *36*, 289–297.

Holtslag, A., and B. Boville (1993), Local versus nonlocal boundary-layer diffusion in a global climate model, *Journal of Climate*, *6*(10), 1825–1842.

Huang, Y., S. Wu, M. Dubey, and N. French (2013), Impact of aging mechanism on model simulated carbonaceous aerosols, *Atmospheric Chemistry and Physics*, *13*(13), 6329.

Huffman, G. J., R. F. Adler, M. M. Morrissey, D. T. Bolvin, S. Curtis, R. Joyce, B. Mc-Gavock, and J. Susskind (2001), Global precipitation at one-degree daily resolution from multisatellite observations, *Journal of Hydrometeorology*, *2*(1), 36–50.

Immerzeel, W. W., L. P. Van Beek, and M. F. Bierkens (2010), Climate change will affect the asian water towers, *Science*, *328*(5984), 1382–1385.

Ishiniaru, A., and Y. Kuga (1982), Attenuation constant of a coherent field in a dense distribution of particles, *JOSA*, *72*(10), 1317–1320.

Iskander, M., H. Chen, and J. Penner (1991), Resonance optical absorption by fractal agglomerates of smoke aerosols, *Atmospheric Environment. Part A. General Topics*, *25*(11), 2563–2569.

Jacobson, M. Z. (2001), Strong radiative heating due to the mixing state of black carbon in atmospheric aerosols, *Nature*, *409*(6821), 695–697.

Jacobson, M. Z. (2004), Climate response of fossil fuel and biofuel soot, accounting for soot's feedback to snow and sea ice albedo and emissivity, *Journal of Geophysical Research: Atmospheres*, *109*(D21).

Jacobson, M. Z. (2006), Effects of externally-through-internally-mixed soot inclusions within clouds and precipitation on global climate, *The Journal of Physical Chemistry A*, *110*(21), 6860–6873.

Jacobson, M. Z. (2010), Short-term effects of controlling fossil-fuel soot, biofuel soot and

gases, and methane on climate, arctic ice, and air pollution health, *Journal of Geophysical Research: Atmospheres*, *115*(D14).

Jacobson, M. Z. (2014), Effects of biomass burning on climate, accounting for heat and moisture fluxes, black and brown carbon, and cloud absorption effects, *Journal of Geophysical Research: Atmospheres*, *119*(14), 8980–9002.

Jin, Z., T. P. Charlock, P. Yang, Y. Xie, and W. Miller (2008), Snow optical properties for different particle shapes with application to snow grain size retrieval and modis/ceres radiance comparison over antarctica, *Remote Sensing of Environment*, *112*(9), 3563–3581.

Johnson, K. S., B. Zuberi, L. Molina, M. J. Molina, M. J. Iedema, J. P. Cowin, D. J. Gaspar, C. Wang, and A. Laskin (2005), Processing of soot in an urban environment: case study from the mexico city metropolitan area, *Atmospheric Chemistry and Physics*, *5*(11), 3033–3043.

Kahnert, M., and A. Devasthale (2011), Black carbon fractal morphology and short-wave radiative impact: a modelling study, *Atmospheric Chemistry and Physics*, *11*(22), 11,745–11,759.

Kahnert, M., T. Nousiainen, and H. Lindqvist (2013), Models for integrated and differential scattering optical properties of encapsulated light absorbing carbon aggregates, *Optics express*, *21*(7), 7974–7993.

Kahnert, M., T. Nousiainen, and H. Lindqvist (2014), Review: Model particles in atmospheric optics, *Journal of Quantitative Spectroscopy and Radiative Transfer*, *146*, 41–58.

Kaiser, J., A. Heil, M. Andreae, A. Benedetti, N. Chubarova, L. Jones, J.-J. Morcrette, M. Razinger, M. Schultz, M. Suttie, et al. (2012), Biomass burning emissions estimated with a global fire assimilation system based on observed fire radiative power, *Biogeosciences*, *9*(1), 527.

Kaspari, S. D., M. Schwikowski, M. Gysel, M. Flanner, S. Kang, S. Hou, and P. A. Mayewski (2011), Recent increase in black carbon concentrations from a mt. everest ice core spanning 1860–2000 ad, *Geophysical Research Letters*, *38*(4).

Kasper, M., K. Siegmann, and K. Sattler (1997), Evaluation of an in situ sampling probe for its accuracy in determining particle size distributions from flames, *Journal of aerosol science*, *28*(8), 1569–1578.

Khalizov, A. F., R. Zhang, D. Zhang, H. Xue, J. Pagels, and P. H. McMurry (2009a), Formation of highly hygroscopic soot aerosols upon internal mixing with sulfuric acid vapor, *Journal of Geophysical Research: Atmospheres*, *114*(D5).

Khalizov, A. F., H. Xue, L. Wang, J. Zheng, R. Zhang, et al. (2009b), Enhanced light absorption and scattering by carbon soot aerosol internally mixed with sulfuric acid, *J. Phys. Chem. A*, *113*(6), 1066–1074.

Khalizov, A. F., M. Cruz-Quinones, and R. Zhang (2010), Heterogeneous reaction of no2 on fresh and coated soot surfaces, *The Journal of Physical Chemistry A*, *114*(28), 7516–7524.

Kim, D., C. Wang, A. M. Ekman, M. C. Barth, and P. J. Rasch (2008), Distribution and direct radiative forcing of carbonaceous and sulfate aerosols in an interactive size-resolving aerosol–climate model, *Journal of geophysical research: Atmospheres*, *113*(D16).

Kitoh, A., and S. Kusunoki (2008), East asian summer monsoon simulation by a 20-km mesh agcm, *Climate Dynamics*, *31*(4), 389–401.

Knox, A., G. Evans, J. Brook, X. Yao, C.-H. Jeong, K. Godri, K. Sabaliauskas, and J. Slowik (2009), Mass absorption cross-section of ambient black carbon aerosol in relation to chemical age, *Aerosol science and technology*, *43*(6), 522–532.

Koch, D., M. Schulz, S. Kinne, C. McNaughton, J. Spackman, Y. Balkanski, S. Bauer, T. Berntsen, T. C. Bond, O. Boucher, et al. (2009), Evaluation of black carbon estimations in global aerosol models, *Atmospheric Chemistry and Physics*, *9*(22), 9001–9026.

Koepke, P., M. Hess, I. Schult, and E. Shettle (1997), Global aerosol data set, *MPI Meteorologie Hamburg Rep*, *243*, 44.

Kokhanovsky, A. (1998), On light scattering in random media with large densely packed particles, *Journal of Geophysical Research: Atmospheres*, *103*(D6), 6089–6096.

Kokhanovsky, A. A., and E. P. Zege (2004), Scattering optics of snow, *Applied Optics*, *43*(7), 1589–1602.

Kondo, Y., H. Matsui, N. Moteki, L. Sahu, N. Takegawa, M. Kajino, Y. Zhao, M. Cubison, J. Jimenez, S. Vay, et al. (2011), Emissions of black carbon, organic, and inorganic aerosols from biomass burning in north america and asia in 2008, *Journal of Geophysical Research: Atmospheres*, *116*(D8).

Kopacz, M., D. Mauzerall, J. Wang, E. Leibensperger, D. Henze, and K. Singh (2011), Origin and radiative forcing of black carbon transported to the himalayas and tibetan plateau, *Atmospheric Chemistry and Physics*, *11*(6), 2837–2852.

Krekov, G. (1993), Models of atmospheric aerosols, *In: Aerosol effects on climate (A93-39529 15-42), p. 9-72.*, *1*, 9–72.

Kurokawa, J., T. Ohara, T. Morikawa, S. Hanayama, G. Janssens-Maenhout, T. Fukui, K. Kawashima, and H. Akimoto (2013), Emissions of air pollutants and greenhouse gases over asian regions during 2000–2008: Regional emission inventory in asia (reas) version 2, *Atmospheric Chemistry and Physics*, *13*(21), 11,019–11,058.

Lack, D. A., J. M. Langridge, R. Bahreini, C. D. Cappa, A. M. Middlebrook, and J. P. Schwarz (2012), Brown carbon and internal mixing in biomass burning particles, *Proceedings of the National Academy of Sciences*, *109*(37), 14,802–14,807.

Lamarque, J.-F., T. C. Bond, V. Eyring, C. Granier, A. Heil, Z. Klimont, D. Lee, C. Liousse, A. Mieville, B. Owen, et al. (2010), Historical (1850–2000) gridded anthropogenic and

biomass burning emissions of reactive gases and aerosols: methodology and application, *Atmospheric Chemistry and Physics*, *10*(15), 7017–7039.

Lana, A., T. Bell, R. Simó, S. Vallina, J. Ballabrera-Poy, A. Kettle, J. Dachs, L. Bopp, E. Saltzman, J. Stefels, et al. (2011), An updated climatology of surface dimethlysulfide concentrations and emission fluxes in the global ocean, *Global Biogeochemical Cycles*, *25*(1).

Lau, K.-M., and K.-M. Kim (2006), Observational relationships between aerosol and asian monsoon rainfall, and circulation, *Geophysical Research Letters*, *33*(21).

Lau, W. K., M.-K. Kim, K.-M. Kim, and W.-S. Lee (2010), Enhanced surface warming and accelerated snow melt in the himalayas and tibetan plateau induced by absorbing aerosols, *Environmental Research Letters*, *5*(2), 025,204.

Lee, W.-L., K. Liou, C. He, H.-C. Liang, T.-C. Wang, Q. Li, Z. Liu, and Q. Yue (2016), Impact of absorbing aerosol deposition on snow albedo reduction over the southern tibetan plateau based on satellite observations, *Theoretical and Applied Climatology*, pp. 1–10.

Li, G., Y. Wang, and R. Zhang (2008), Implementation of a two-moment bulk microphysics scheme to the wrf model to investigate aerosol-cloud interaction, *Journal of Geophysical Research: Atmospheres*, *113*(D15).

Li, K., H. Liao, Y. Mao, and D. A. Ridley (2016), Source sector and region contributions to concentration and direct radiative forcing of black carbon in china, *Atmospheric Environment*, *124*, 351–366.

Li, W., K. Stamnes, B. Chen, and X. Xiong (2001), Snow grain size retrieved from near-infrared radiances at multiple wavelengths, *Geophysical Research Letters*, *28*(9), 1699–1702.

Liao, H., D. K. Henze, J. H. Seinfeld, S. Wu, and L. J. Mickley (2007), Biogenic secondary organic aerosol over the united states: Comparison of climatological simulations with observations, *Journal of Geophysical Research: Atmospheres*, *112*(D6).

Lin, J.-T., and M. B. McElroy (2010), Impacts of boundary layer mixing on pollutant vertical profiles in the lower troposphere: Implications to satellite remote sensing, *Atmospheric Environment*, *44*(14), 1726–1739.

Lin, J.-T., D. Youn, X.-Z. Liang, and D. J. Wuebbles (2008), Global model simulation of summertime us ozone diurnal cycle and its sensitivity to pbl mixing, spatial resolution, and emissions, *Atmospheric Environment*, *42*(36), 8470–8483.

Lin, S.-J., and R. B. Rood (1996), Multidimensional flux-form semi-lagrangian transport schemes, *Monthly Weather Review*, *124*(9), 2046–2070.

Liou, K., Y. Takano, and P. Yang (2010), On geometric optics and surface waves for light scattering by spheres, *Journal of Quantitative Spectroscopy and Radiative Transfer*, *111*(12), 1980–1989.

Liou, K., Y. Takano, and P. Yang (2011), Light absorption and scattering by aggregates: Application to black carbon and snow grains, *Journal of Quantitative Spectroscopy and Radiative Transfer*, *112*(10), 1581–1594.

Liou, K., Y. Takano, C. He, P. Yang, L. Leung, Y. Gu, and W. Lee (2014), Stochastic parameterization for light absorption by internally mixed bc/dust in snow grains for application to climate models, *Journal of Geophysical Research: Atmospheres*, *119*(12), 7616–7632.

Liou, K.-N., and P. Yang (2016), *Light scattering by ice crystals: fundamentals and applications*, Cambridge University Press.

Liu, H., D. J. Jacob, I. Bey, and R. M. Yantosca (2001), Constraints from 210pb and 7be on wet deposition and transport in a global three-dimensional chemical tracer model

driven by assimilated meteorological fields, *Journal of Geophysical Research: Atmospheres*, *106*(D11), 12,109–12,128.

Liu, J., S. Fan, L. W. Horowitz, and H. Levy (2011), Evaluation of factors controlling long-range transport of black carbon to the arctic, *Journal of Geophysical Research: Atmospheres*, *116*(D4).

Liu, L., and M. I. Mishchenko (2007), Scattering and radiative properties of complex soot and soot-containing aggregate particles, *Journal of Quantitative Spectroscopy and Radiative Transfer*, *106*(1), 262–273.

Liu, L., M. I. Mishchenko, and W. P. Arnott (2008), A study of radiative properties of fractal soot aggregates using the superposition t-matrix method, *Journal of Quantitative Spectroscopy and Radiative Transfer*, *109*(15), 2656–2663.

Liu, X., J. E. Penner, and M. Wang (2009), Influence of anthropogenic sulfate and black carbon on upper tropospheric clouds in the ncar cam3 model coupled to the impact global aerosol model, *Journal of Geophysical Research: Atmospheres*, *114*(D3).

Louis, J.-F. (1979), A parametric model of vertical eddy fluxes in the atmosphere, *Boundary-Layer Meteorology*, *17*(2), 187–202.

Lu, Z., Q. Zhang, and D. G. Streets (2011), Sulfur dioxide and primary carbonaceous aerosol emissions in china and india, 1996–2010, *Atmospheric Chemistry and Physics*, *11*(18), 9839–9864.

Lu, Z., D. G. Streets, Q. Zhang, and S. Wang (2012), A novel back-trajectory analysis of the origin of black carbon transported to the himalayas and tibetan plateau during 1996–2010, *Geophysical Research Letters*, *39*(1).

Ma, L., T. Zhang, O. W. Frauenfeld, B. Ye, D. Yang, and D. Qin (2009), Evaluation of precipitation from the era-40, ncep-1, and ncep-2 reanalyses and cmap-1, cmap-2, and gpcp-2

with ground-based measurements in china, *Journal of Geophysical Research: Atmospheres*, *114*(D9).

Mackowski, D. (2014), A general superposition solution for electromagnetic scattering by multiple spherical domains of optically active media, *Journal of Quantitative Spectroscopy and Radiative Transfer*, *133*, 264–270.

Mackowski, D., and M. Mishchenko (2011), A multiple sphere t-matrix fortran code for use on parallel computer clusters, *Journal of Quantitative Spectroscopy and Radiative Transfer*, *112*(13), 2182–2192.

Mackowski, D. W., and M. I. Mishchenko (1996), Calculation of the t matrix and the scattering matrix for ensembles of spheres, *JOSA A*, *13*(11), 2266–2278.

Mao, Y., Q. Li, L. Zhang, Y. Chen, J. Randerson, D. Chen, and K. Liou (2011), Biomass burning contribution to black carbon in the western united states mountain ranges, *Atmospheric Chemistry and Physics*, *11*(21), 11,253–11,266.

Marks, D., T. Link, A. Winstral, and D. Garen (2001), Simulating snowmelt processes during rain-on-snow over a semi-arid mountain basin, *Annals of Glaciology*, *32*(1), 195–202.

Martins, J. V., P. Artaxo, C. Liousse, J. S. Reid, P. V. Hobbs, and Y. J. Kaufman (1998), Effects of black carbon content, particle size, and mixing on light absorption by aerosols from biomass burning in brazil, *Journal of Geophysical Research: Atmospheres*, *103*(D24), 32,041–32,050.

McMeeking, G., N. Good, M. Petters, G. McFiggans, and H. Coe (2011), Influences on the fraction of hydrophobic and hydrophilic black carbon in the atmosphere, *Atmospheric Chemistry and Physics*, *11*(10), 5099–5112.

Ménégoz, M., H. Gallée, and H. Jacobi (2013), Precipitation and snow cover in the himalaya: from reanalysis to regional climate simulations, *Hydrology and Earth System Sciences*, *17*(10), 3921–3936.

Menon, S., D. Koch, G. Beig, S. Sahu, J. Fasullo, and D. Orlikowski (2010), Black carbon aerosols and the third polar ice cap, *Atmospheric Chemistry and Physics*, *10*(10), 4559–4571.

Metcalf, A., J. Craven, J. Ensberg, J. Brioude, W. Angevine, A. Sorooshian, H. Duong, H. Jonsson, R. Flagan, and J. Seinfeld (2012), Black carbon aerosol over the los angeles basin during calnex, *Journal of Geophysical Research: Atmospheres*, *117*(D21).

Mikhailov, E., S. Vlasenko, L. Krämer, and R. Niessner (2001), Interaction of soot aerosol particles with water droplets: influence of surface hydrophilicity, *Journal of aerosol science*, *32*(6), 697–711.

Ming, J., H. Cachier, C. Xiao, D. Qin, S. Kang, S. Hou, and J. Xu (2008), Black carbon record based on a shallow himalayan ice core and its climatic implications, *Atmospheric Chemistry and Physics*, *8*(5), 1343–1352.

Ming, J., C. Xiao, H. Cachier, D. Qin, X. Qin, Z. Li, and J. Pu (2009a), Black carbon (bc) in the snow of glaciers in west china and its potential effects on albedos, *Atmospheric Research*, *92*(1), 114–123.

Ming, J., C. Xiao, Z. Du, and M. Flanner (2009b), Black carbon in snow/ice of west china and its radiave forcing, *Advances in Climate Change Research*, *5*(6), 328–35.

Ming, J., C. Xiao, J. Sun, S. Kang, and P. Bonasoni (2010), Carbonaceous particles in the atmosphere and precipitation of the nam co region, central tibet, *Journal of Environmental Sciences*, *22*(11), 1748–1756.

Ming, J., Z. Du, C. Xiao, X. Xu, and D. Zhang (2012), Darkening of the mid-himalaya glaciers since 2000 and the potential causes, *Environmental Research Letters*, *7*(1), 014,021.

Ming, J., C. Xiao, Z. Du, and X. Yang (2013), An overview of black carbon deposition in high asia glaciers and its impacts on radiation balance, *Advances in Water Resources*, *55*, 80–87.

Mishchenko, M. I., L. Liu, B. Cairns, and D. W. Mackowski (2014), Optics of water cloud droplets mixed with black-carbon aerosols, *Optics letters*, *39*(9), 2607–2610.

Moffet, R. C., and K. A. Prather (2009), In-situ measurements of the mixing state and optical properties of soot with implications for radiative forcing estimates, *Proceedings of the National Academy of Sciences*, *106*(29), 11,872–11,877.

Molod, A., L. Takacs, M. Suarez, J. Bacmeister, I.-S. Song, and A. Eichmann (2012), The geos-5 atmospheric general circulation model: Mean climate and development from merra to fortuna.

Moorthi, S., and M. J. Suarez (1992), Relaxed arakawa-schubert. a parameterization of moist convection for general circulation models, *Monthly Weather Review*, *120*(6), 978–1002.

Moorthy, K. K., S. N. Beegum, N. Srivastava, S. Satheesh, M. Chin, N. Blond, S. S. Babu, and S. Singh (2013), Performance evaluation of chemistry transport models over india, *Atmospheric environment*, *71*, 210–225.

Moteki, N., Y. Kondo, Y. Miyazaki, N. Takegawa, Y. Komazaki, G. Kurata, T. Shirai, D. Blake, T. Miyakawa, and M. Koike (2007), Evolution of mixing state of black carbon particles: Aircraft measurements over the western pacific in march 2004, *Geophysical Research Letters*, *34*(11).

Myhre, G., T. F. Berglen, M. Johnsrud, C. Hoyle, T. K. Berntsen, S. Christopher, D. Fahey, I. S. Isaksen, T. Jones, R. Kahn, et al. (2009), Modelled radiative forcing of the direct aerosol effect with multi-observation evaluation, *Atmos. Chem. Phys*, *9*(4), 1365–1392.

Nair, V. S., F. Solmon, F. Giorgi, L. Mariotti, S. S. Babu, and K. K. Moorthy (2012), Simulation of south asian aerosols for regional climate studies, *Journal of Geophysical Research: Atmospheres*, *117*(D4).

Naoe, H., S. Hasegawa, J. Heintzenberg, K. Okada, A. Uchiyama, Y. Zaizen, E. Kobayashi, and A. Yamazaki (2009), State of mixture of atmospheric submicrometer black carbon

particles and its effect on particulate light absorption, *Atmospheric Environment*, *43*(6), 1296–1301.

Nussenzveig, H., and W. Wiscombe (1980), Efficiency factors in mie scattering, *Physical Review Letters*, *45*(18), 1490.

Oshima, N., and M. Koike (2013), Development of a parameterization of black carbon aging for use in general circulation models, *Geoscientific Model Development*, *6*(2), 263.

Pagels, J., A. F. Khalizov, P. H. McMurry, and R. Y. Zhang (2009), Processing of soot by controlled sulphuric acid and water condensation—mass and mobility relationship, *Aerosol Science and Technology*, *43*(7), 629–640.

Painter, T. H., M. G. Flanner, G. Kaser, B. Marzeion, R. A. VanCuren, and W. Abdalati (2013), End of the little ice age in the alps forced by industrial black carbon, *Proceedings of the national academy of sciences*, *110*(38), 15,216–15,221.

Park, R. J., D. J. Jacob, M. Chin, and R. V. Martin (2003), Sources of carbonaceous aerosols over the united states and implications for natural visibility, *Journal of Geophysical Research: Atmospheres*, *108*(D12).

Park, R. J., D. J. Jacob, B. D. Field, R. M. Yantosca, and M. Chin (2004), Natural and transboundary pollution influences on sulfate-nitrate-ammonium aerosols in the united states: Implications for policy, *Journal of Geophysical Research: Atmospheres*, *109*(D15).

Park, R. J., D. J. Jacob, P. I. Palmer, A. D. Clarke, R. J. Weber, M. A. Zondlo, F. L. Eisele, A. R. Bandy, D. C. Thornton, G. W. Sachse, et al. (2005), Export efficiency of black carbon aerosol in continental outflow: Global implications, *Journal of Geophysical Research: Atmospheres*, *110*(D11).

Park, R. J., D. J. Jacob, N. Kumar, and R. M. Yantosca (2006), Regional visibility statistics in the united states: Natural and transboundary pollution influences, and implications for the regional haze rule, *Atmospheric Environment*, *40*(28), 5405–5423.

Pathak, B., G. Kalita, K. Bhuyan, P. Bhuyan, and K. K. Moorthy (2010), Aerosol temporal characteristics and its impact on shortwave radiative forcing at a location in the northeast of india, *Journal of Geophysical Research: Atmospheres*, *115*(D19).

Petzold, A., and M. Schönlinner (2004), Multi-angle absorption photometry—a new method for the measurement of aerosol light absorption and atmospheric black carbon, *Journal of Aerosol Science*, *35*(4), 421–441.

Popovicheva, O., N. Persiantseva, E. Kireeva, T. Khokhlova, and N. Shonija (2010), Quantification of the hygroscopic effect of soot aging in the atmosphere: laboratory simulations, *The Journal of Physical Chemistry A*, *115*(3), 298–306.

Pöschl, U., T. Letzel, C. Schauer, and R. Niessner (2001), Interaction of ozone and water vapor with spark discharge soot aerosol particles coated with benzo [a] pyrene: O3 and h2o adsorption, benzo [a] pyrene degradation, and atmospheric implications, *The Journal of Physical Chemistry A*, *105*(16), 4029–4041.

Prasad, A. K., K.-H. S. Yang, H. el Askary, and M. Kafatos (2009), Melting of major glaciers in the western himalayas: evidence of climatic changes from long term msu derived tropospheric temperature trend (1979-2008).

Prenni, A. J., M. D. Petters, S. M. Kreidenweis, P. J. DeMott, and P. J. Ziemann (2007), Cloud droplet activation of secondary organic aerosol, *Journal of Geophysical Research: Atmospheres*, *112*(D10).

Pu, Z., L. Xu, and V. V. Salomonson (2007), Modis/terra observed seasonal variations of snow cover over the tibetan plateau, *Geophysical Research Letters*, *34*(6).

Qi, L., Q. Li, Y. Li, and C. He (2017), Factors controlling black carbon distribution in the arctic, *Atmospheric Chemistry and Physics*, *17*(2), 1037–1059.

Qian, Y., W. I. Gustafson, L. R. Leung, and S. J. Ghan (2009), Effects of soot-induced snow albedo change on snowpack and hydrological cycle in western united states based on

weather research and forecasting chemistry and regional climate simulations, *Journal of Geophysical Research: Atmospheres*, *114*(D3).

Qian, Y., M. Flanner, L. Leung, and W. Wang (2011), Sensitivity studies on the impacts of tibetan plateau snowpack pollution on the asian hydrological cycle and monsoon climate, *Atmospheric Chemistry and Physics*, *11*(5), 1929–1948.

Qian, Y., T. J. Yasunari, S. J. Doherty, M. G. Flanner, W. K. Lau, J. Ming, H. Wang, M. Wang, S. G. Warren, and R. Zhang (2015), Light-absorbing particles in snow and ice: Measurement and modeling of climatic and hydrological impact, *Advances in Atmospheric Sciences*, *32*(1), 64–91.

Qin, Y., and S. Xie (2012), Spatial and temporal variation of anthropogenic black carbon emissions in china for the period 1980–2009, *Atmospheric Chemistry and Physics*, *12*(11), 4825–4841.

Qiu, C., A. F. Khalizov, and R. Zhang (2012), Soot aging from oh-initiated oxidation of toluene, *Environmental science & technology*, *46*(17), 9464–9472.

Qu, W. J., X. Y. Zhang, R. Arimoto, D. Wang, Y. Q. Wang, L. W. Yan, and Y. Li (2008), Chemical composition of the background aerosol at two sites in southwestern and northwestern china: potential influences of regional transport, *Tellus B*, *60*(4), 657–673.

Qu, X., and A. Hall (2014), On the persistent spread in snow-albedo feedback, *Climate dynamics*, *42*(1-2), 69–81.

Ram, K., M. Sarin, and P. Hegde (2010a), Long-term record of aerosol optical properties and chemical composition from a high-altitude site (manora peak) in central himalaya, *Atmospheric Chemistry and Physics*, *10*(23), 11,791–11,803.

Ram, K., M. Sarin, and S. Tripathi (2010b), A 1 year record of carbonaceous aerosols from an urban site in the indo-gangetic plain: Characterization, sources, and temporal variability, *Journal of Geophysical Research: Atmospheres*, *115*(D24).

Ramanathan, V., and G. Carmichael (2008), Global and regional climate changes due to black carbon, *Nature geoscience*, *1*(4), 221–227.

Ramanathan, V., C. Chung, D. Kim, T. Bettge, L. Buja, J. Kiehl, W. Washington, Q. Fu, D. Sikka, and M. Wild (2005), Atmospheric brown clouds: Impacts on south asian climate and hydrological cycle, *Proceedings of the National Academy of Sciences of the United States of America*, *102*(15), 5326–5333.

Ramanathan, V., M. V. Ramana, G. Roberts, D. Kim, C. Corrigan, C. Chung, and D. Winker (2007), Warming trends in asia amplified by brown cloud solar absorption, *Nature*, *448*(7153), 575–578.

Randerson, J., Y. Chen, G. Werf, B. Rogers, and D. Morton (2012), Global burned area and biomass burning emissions from small fires, *Journal of Geophysical Research: Biogeosciences*, *117*(G4).

Riemer, N., H. Vogel, and B. Vogel (2004), Soot aging time scales in polluted regions during day and night, *Atmospheric Chemistry and Physics*, *4*(7), 1885–1893.

Saathoff, H., K.-H. Naumann, M. Schnaiter, W. Schöck, O. Möhler, U. Schurath, E. Weingartner, M. Gysel, and U. Baltensperger (2003), Coating of soot and (nh 4) 2 so 4 particles by ozonolysis products of α-pinene, *Journal of Aerosol Science*, *34*(10), 1297–1321.

Samset, B., G. Myhre, M. Schulz, Y. Balkanski, S. Bauer, T. Berntsen, H. Bian, N. Bellouin, T. Diehl, R. C. Easter, et al. (2013), Black carbon vertical profiles strongly affect its radiative forcing uncertainty, *Atmospheric Chemistry and Physics*, *13*(5), 2423.

Santoro, R., H. Semerjian, and R. Dobbins (1983), Soot particle measurements in diffusion flames, *Combustion and Flame*, *51*, 203–218.

Sato, M., J. Hansen, D. Koch, A. Lacis, R. Ruedy, O. Dubovik, B. Holben, M. Chin, and T. Novakov (2003), Global atmospheric black carbon inferred from aeronet, *Proceedings of the National Academy of Sciences*, *100*(11), 6319–6324.

Scarnato, B., S. Vahidinia, D. Richard, and T. Kirchstetter (2013), Effects of internal mixing and aggregate morphology on optical properties of black carbon using a discrete dipole approximation model, *Atmospheric Chemistry and Physics*, *13*(10), 5089–5101.

Scarnato, B., S. China, K. Nielsen, and C. Mazzoleni (2015), Perturbations of the optical properties of mineral dust particles by mixing with black carbon: a numerical simulation study, *Atmospheric Chemistry and Physics*, *15*(12), 6913–6928.

Schmid, H., L. Laskus, H. J. Abraham, U. Baltensperger, V. Lavanchy, M. Bizjak, P. Burba, H. Cachier, D. Crow, J. Chow, et al. (2001), Results of the "carbon conference" international aerosol carbon round robin test stage i, *Atmospheric Environment*, *35*(12), 2111–2121.

Schulz, M., C. Textor, S. Kinne, Y. Balkanski, S. Bauer, T. Berntsen, T. Berglen, O. Boucher, F. Dentener, S. Guibert, et al. (2006), Radiative forcing by aerosols as derived from the aerocom present-day and pre-industrial simulations, *Atmospheric Chemistry and Physics*, *6*(12), 5225–5246.

Schwarz, J., J. Spackman, D. Fahey, R. Gao, U. Lohmann, P. Stier, L. Watts, D. Thomson, D. Lack, L. Pfister, et al. (2008), Coatings and their enhancement of black carbon light absorption in the tropical atmosphere, *Journal of Geophysical Research: Atmospheres*, *113*(D3).

Schwarz, J., J. Spackman, R. Gao, L. Watts, P. Stier, M. Schulz, S. Davis, S. C. Wofsy, and D. Fahey (2010), Global-scale black carbon profiles observed in the remote atmosphere and compared to models, *Geophysical Research Letters*, *37*(18).

Schwarz, J., B. Samset, A. Perring, J. Spackman, R. Gao, P. Stier, M. Schulz, F. Moore, E. A. Ray, and D. Fahey (2013), Global-scale seasonally resolved black carbon vertical profiles over the pacific, *Geophysical research letters*, *40*(20), 5542–5547.

Sedlacek, A. J., E. R. Lewis, L. Kleinman, J. Xu, and Q. Zhang (2012), Determination of and evidence for non-core-shell structure of particles containing black carbon using the single-particle soot photometer (sp2), *Geophysical Research Letters*, *39*(6).

Seinfeld, J., and S. Pandis (2006), Atmospheric chemistry and physics: from air pollution to climate change.

Shen, Z., J. Liu, L. Horowitz, D. Henze, S. Fan, D. Mauzerall, J.-T. Lin, S. Tao, et al. (2014), Analysis of transpacific transport of black carbon during hippo-3: implications for black carbon aging, *Atmospheric Chemistry and Physics*, *14*(12), 6315–6327.

Shiraiwa, M., Y. Kondo, N. Moteki, N. Takegawa, Y. Miyazaki, and D. Blake (2007), Evolution of mixing state of black carbon in polluted air from tokyo, *Geophysical Research Letters*, *34*(16).

Shiraiwa, M., Y. Kondo, T. Iwamoto, and K. Kita (2010), Amplification of light absorption of black carbon by organic coating, *Aerosol Science and Technology*, *44*(1), 46–54.

Singh, H., W. Brune, J. Crawford, F. Flocke, and D. J. Jacob (2009), Chemistry and transport of pollution over the gulf of mexico and the pacific: spring 2006 intex-b campaign overview and first results, *Atmospheric Chemistry and Physics*, *9*(7), 2301–2318.

Skorupski, K., J. Mroczka, N. Riefler, H. Oltmann, S. Will, and T. Wriedt (2013), Impact of morphological parameters onto simulated light scattering patterns, *Journal of Quantitative Spectroscopy and Radiative Transfer*, *119*, 53–66.

Stratmann, F., M. Bilde, U. Dusek, G. Frank, T. Hennig, S. Henning, A. Kiendler-Scharr, A. Kiselev, A. Kristensson, I. Lieberwirth, et al. (2010), Examination of laboratory-generated coated soot particles: An overview of the lacis experiment in november (lexno) campaign, *Journal of Geophysical Research: Atmospheres*, *115*(D11).

Strawa, A., K. Drdla, G. Ferry, S. Verma, R. Pueschel, M. Yasuda, R. Salawitch, R. Gao, S. Howard, P. Bui, et al. (1999), Carbonaceous aerosol (soot) measured in the lower stratosphere during polaris and its role in stratospheric photochemistry, *Journal of Geophysical Research: Atmospheres*, *104*(D21), 26,753–26,766.

Streets, D. G., T. Bond, G. Carmichael, S. Fernandes, Q. Fu, D. He, Z. Klimont, S. Nelson, N. Tsai, M. Q. Wang, et al. (2003), An inventory of gaseous and primary aerosol emissions in asia in the year 2000, *Journal of Geophysical Research: Atmospheres*, *108*(D21).

Stroeve, J., J. E. Box, F. Gao, S. Liang, A. Nolin, and C. Schaaf (2005), Accuracy assessment of the modis 16-day albedo product for snow: comparisons with greenland in situ measurements, *Remote Sensing of Environment*, *94*(1), 46–60.

Stroeve, J., J. E. Box, Z. Wang, C. Schaaf, and A. Barrett (2013), Re-evaluation of modis mcd43 greenland albedo accuracy and trends, *Remote Sensing of Environment*, *138*, 199–214.

Takano, Y. (1989), Radiative transfer in cirrus clouds. i. single scattering and optical properties of hexagonal ice crystals., *J. Atmos. Sci.*, *46*, 3–20.

Takano, Y., K. Liou, M. Kahnert, and P. Yang (2013), The single-scattering properties of black carbon aggregates determined from the geometric-optics surface-wave approach and the t-matrix method, *Journal of Quantitative Spectroscopy and Radiative Transfer*, *125*, 51–56.

Textor, C., M. Schulz, S. Guibert, S. Kinne, Y. Balkanski, S. Bauer, T. Berntsen, T. Berglen, O. Boucher, M. Chin, et al. (2006), Analysis and quantification of the diversities of aerosol life cycles within aerocom, *Atmospheric Chemistry and Physics*, *6*(7), 1777–1813.

Toon, O. B., and T. Ackerman (1981), Algorithms for the calculation of scattering by stratified spheres, *Applied Optics*, *20*(20), 3657–3660.

Toon, O. B., J. B. Pollack, and B. N. Khare (1976), The optical constants of several atmospheric aerosol species: Ammonium sulfate, aluminum oxide, and sodium chloride, *Journal of Geophysical research*, *81*(33), 5733–5748.

Tsang, L., and A. Ishimaru (1987), Radiative wave equations for vector electromagnetic propagation in dense nontenuous media, *Journal of Electromagnetic Waves and Applications*, *1*(1), 59–72.

Van der Werf, G. R., J. T. Randerson, L. Giglio, G. Collatz, M. Mu, P. S. Kasibhatla, D. C. Morton, R. DeFries, Y. v. Jin, and T. T. van Leeuwen (2010), Global fire emissions and the contribution of deforestation, savanna, forest, agricultural, and peat fires (1997–2009), *Atmospheric Chemistry and Physics*, *10*(23), 11,707–11,735.

Videen, G., D. Ngo, and P. Chỳlek (1994), Effective-medium predictions of absorption by graphitic carbon in water droplets, *Optics letters*, *19*(21), 1675–1677.

Voisin, N., A. W. Wood, and D. P. Lettenmaier (2008), Evaluation of precipitation products for global hydrological prediction, *Journal of Hydrometeorology*, *9*(3), 388–407.

Walcek, C., R. Brost, J. Chang, and M. Wesely (1986), So2, sulfate and hno3 deposition velocities computed using regional landuse and meteorological data, *Atmospheric Environment (1967)*, *20*(5), 949–964.

Wang, B., and Q. Ding (2008), Global monsoon: Dominant mode of annual variation in the tropics, *Dynamics of Atmospheres and Oceans*, *44*(3), 165–183.

Wang, C. (2004), A modeling study on the climate impacts of black carbon aerosols, *Journal of Geophysical Research: Atmospheres*, *109*(D3).

Wang, Q., D. J. Jacob, J. A. Fisher, J. Mao, E. Leibensperger, C. Carouge, P. L. Sager, Y. Kondo, J. Jimenez, M. Cubison, et al. (2011), Sources of carbonaceous aerosols and deposited black carbon in the arctic in winter-spring: implications for radiative forcing, *Atmospheric Chemistry and Physics*, *11*(23), 12,453–12,473.

Wang, Q., D. J. Jacob, J. R. Spackman, A. E. Perring, J. P. Schwarz, N. Moteki, E. A. Marais, C. Ge, J. Wang, and S. R. Barrett (2014a), Global budget and radiative forcing of black carbon aerosol: Constraints from pole-to-pole (hippo) observations across the pacific, *Journal of Geophysical Research: Atmospheres*, *119*(1), 195–206.

Wang, R., S. Tao, W. Wang, J. Liu, H. Shen, G. Shen, B. Wang, X. Liu, W. Li, Y. Huang, et al. (2012a), Black carbon emissions in china from 1949 to 2050, *Environmental science & technology*, *46*(14), 7595–7603.

Wang, R., S. Tao, H. Shen, X. Wang, B. Li, G. Shen, B. Wang, W. Li, X. Liu, Y. Huang, et al. (2012b), Global emission of black carbon from motor vehicles from 1960 to 2006, *Environmental science & technology*, *46*(2), 1278–1284.

Wang, R., S. Tao, P. Ciais, H. Shen, Y. Huang, H. Chen, G. Shen, B. Wang, W. Li, Y. Zhang, et al. (2013), High-resolution mapping of combustion processes and implications for co 2 emissions, *Atmospheric Chemistry and Physics*, *13*(10), 5189–5203.

Wang, R., S. Tao, Y. Balkanski, P. Ciais, O. Boucher, J. Liu, S. Piao, H. Shen, M. R. Vuolo, M. Valari, et al. (2014b), Exposure to ambient black carbon derived from a unique inventory and high-resolution model, *Proceedings of the National Academy of Sciences*, *111*(7), 2459–2463.

Wang, Y., D. J. Jacob, and J. A. Logan (1998), Global simulation of tropospheric o3-no x-hydrocarbon chemistry: 1. model formulation, *Journal of Geophysical Research: Atmospheres*, *103*(D9), 10,713–10,725.

Warren, S. G. (2013), Can black carbon in snow be detected by remote sensing?, *Journal of Geophysical Research: Atmospheres*, *118*(2), 779–786.

Warren, S. G., and R. E. Brandt (2008), Optical constants of ice from the ultraviolet to the microwave: A revised compilation, *Journal of Geophysical Research: Atmospheres*, *113*(D14).

Warren, S. G., and W. J. Wiscombe (1980), A model for the spectral albedo of snow. ii: Snow containing atmospheric aerosols, *Journal of the Atmospheric Sciences*, *37*(12), 2734–2745.

Warren, S. G., and W. J. Wiscombe (1985), Dirty snow after nuclear war, *Nature*, *313*(6002), 467–470.

Weingartner, E., H. Burtscher, and U. Baltensperger (1997), Hygroscopic properties of carbon and diesel soot particles, *Atmospheric Environment*, *31*(15), 2311–2327.

Weingartner, E., H. Saathoff, M. Schnaiter, N. Streit, B. Bitnar, and U. Baltensperger (2003), Absorption of light by soot particles: determination of the absorption coefficient by means of aethalometers, *Journal of Aerosol Science*, *34*(10), 1445–1463.

Wen, B., L. Tsang, D. P. Winebrenner, and A. Ishimaru (1990), Dense medium radiative transfer theory: Comparison with experiment and application to microwave remote sensing and polarimetry, *IEEE Transactions on Geoscience and Remote Sensing*, *28*(1), 46–59.

Wesely, M. (1989), Parameterization of surface resistances to gaseous dry deposition in regional-scale numerical models, *Atmospheric Environment (1967)*, *23*(6), 1293–1304.

Willis, M. D., R. M. Healy, N. Riemer, M. West, J. M. Wang, C.-H. Jeong, J. C. Wenger, G. J. Evans, J. P. Abbatt, and A. K. Lee (2016), Quantification of black carbon mixing state from traffic: implications for aerosol optical properties, *Atmospheric Chemistry and Physics*, *16*(7), 4693–4706.

Wiscombe, W. J., and S. G. Warren (1980), A model for the spectral albedo of snow. i: Pure snow, *Journal of the Atmospheric Sciences*, *37*(12), 2712–2733.

Wofsy, S. C. (2011), Hiaper pole-to-pole observations (hippo): fine-grained, global-scale measurements of climatically important atmospheric gases and aerosols, *Philosophical Transactions of the Royal Society of London A: Mathematical, Physical and Engineering Sciences*, *369*(1943), 2073–2086.

Wu, Q., and Y. Liu (2004), Ground temperature monitoring and its recent change in qinghai–tibet plateau, *Cold Regions Science and Technology*, *38*(2), 85–92.

Wu, Y., T. Cheng, L. Zheng, and H. Chen (2015a), A study of optical properties of soot aggregates composed of poly-disperse monomers using the superposition t-matrix method, *Aerosol Science and Technology*, *49*(10), 941–949.

Wu, Y., T. Cheng, L. Zheng, H. Chen, and H. Xu (2015b), Single scattering properties of semi-embedded soot morphologies with intersecting and non-intersecting surfaces of absorbing spheres and non-absorbing host, *Journal of Quantitative Spectroscopy and Radiative Transfer*, *157*, 1–13.

Wu, Y., T. Cheng, L. Zheng, and H. Chen (2016), Effect of morphology on the optical properties of soot aggregated with spheroidal monomers, *Journal of Quantitative Spectroscopy and Radiative Transfer*, *168*, 158–169.

Xie, P., and P. A. Arkin (1997), Global precipitation: A 17-year monthly analysis based on gauge observations, satellite estimates, and numerical model outputs, *Bulletin of the American Meteorological Society*, *78*(11), 2539–2558.

Xie, P., M. Chen, S. Yang, A. Yatagai, T. Hayasaka, Y. Fukushima, and C. Liu (2007), A gauge-based analysis of daily precipitation over east asia, *Journal of Hydrometeorology*, *8*(3), 607–626.

Xu, B., T. Yao, X. Liu, and N. Wang (2006), Elemental and organic carbon measurements with a two-step heating–gas chromatography system in snow samples from the tibetan plateau, *Annals of Glaciology*, *43*(1), 257–262.

Xu, B., J. Cao, J. Hansen, T. Yao, D. R. Joswia, N. Wang, G. Wu, M. Wang, H. Zhao, W. Yang, et al. (2009), Black soot and the survival of tibetan glaciers, *Proceedings of the National Academy of Sciences*, *106*(52), 22,114–22,118.

Xue, H., A. F. Khalizov, L. Wang, J. Zheng, and R. Zhang (2009), Effects of dicarboxylic acid coating on the optical properties of soot, *Physical Chemistry Chemical Physics*, *11*(36), 7869–7875.

Yang, P., and K. Liou (1996), Finite-difference time domain method for light scattering by small ice crystals in three-dimensional space, *JOSA A*, *13*(10), 2072–2085.

Yang, P., and K. Liou (1997), Light scattering by hexagonal ice crystals: solutions by a ray-by-ray integration algorithm, *JOSA A*, *14*(9), 2278–2289.

Yasunari, T., P. Bonasoni, P. Laj, K. Fujita, E. Vuillermoz, A. Marinoni, P. Cristofanelli, R. Duchi, G. Tartari, and K.-M. Lau (2010), Estimated impact of black carbon deposition during pre-monsoon season from nepal climate observatory–pyramid data and snow albedo changes over himalayan glaciers, *Atmospheric Chemistry and Physics*, *10*(14), 6603–6615.

Yu, F., and G. Luo (2009), Simulation of particle size distribution with a global aerosol model: contribution of nucleation to aerosol and ccn number concentrations, *Atmospheric Chemistry and Physics*, *9*(20), 7691–7710.

Zhang, J., J. Liu, S. Tao, and G. Ban-Weiss (2015), Long-range transport of black carbon to the pacific ocean and its dependence on aging timescale, *Atmospheric Chemistry and Physics*, *15*(20), 11,521–11,535.

Zhang, Q., D. G. Streets, G. R. Carmichael, K. He, H. Huo, A. Kannari, Z. Klimont, I. Park, S. Reddy, J. Fu, et al. (2009), Asian emissions in 2006 for the nasa intex-b mission, *Atmospheric Chemistry and Physics*, *9*(14), 5131–5153.

Zhang, R., A. F. Khalizov, J. Pagels, D. Zhang, H. Xue, and P. H. McMurry (2008a), Variability in morphology, hygroscopicity, and optical properties of soot aerosols during atmospheric processing, *Proceedings of the National Academy of Sciences*, *105*(30), 10,291–10,296.

Zhang, R., A. Khalizov, L. Wang, M. Hu, and W. Xu (2011), Nucleation and growth of nanoparticles in the atmosphere, *Chemical Reviews*, *112*(3), 1957–2011.

Zhang, X., Y. Wang, X. Zhang, W. Guo, and S. Gong (2008b), Carbonaceous aerosol composition over various regions of china during 2006, *Journal of Geophysical Research: Atmospheres*, *113*(D14).

Zhao, T., and C. Fu (2006), Comparison of products from era-40, ncep-2, and cru with station data for summer precipitation over china, *Advances in Atmospheric sciences*, *23*(4), 593–604.

Zhou, G., T. Yao, S. Kang, J.-c. Pu, L.-d. Tian, and W. Yang (2007), Mass balance of the zhadang glacier in the central tibetan plateau, *J. Glaciol. Geocryol*, *29*(3), 360–365.

Zuberi, B., K. S. Johnson, G. K. Aleks, L. T. Molina, M. J. Molina, and A. Laskin (2005), Hydrophilic properties of aged soot, *Geophysical research letters*, *32*(1).